Universitat Autònoma de Barcelona
Campus de la UAB, E-08193 Bellaterra

Institut de Ciència de Materials de Barcelona -CSIC
Campus de la UAB, E-08193 Bellaterra

(001) and (110) $La_{2/3}Ca_{1/3}MnO_3$ epitaxial ferromagnetic electrodes: a comparative study

Elèctrodes epitaxials ferromagnètics (001) i (110) $La_{2/3}Ca_{1/3}MnO_3$: un estudi comparatiu

Ingrid Cañero Infante

Programa de Doctorat en Ciència de Materials - Departament de Física
Facultat de Ciències – Universitat Autònoma de Barcelona

Directors: Prof. Josep Fontcuberta i Griñó
Dr. Florencio Sánchez Barrera
Tutor: Prof. Jordi Pascual Gainza

Membres del jurat:

Prof. Agnès Barthélémy	(President)
Dr. Javier Rodríguez Viejo	(Secretari)
Dr. Etienne Snoeck	(Vocal)
Dr. Riccardo Bertacco	(Vocal)
Prof. Pedro A. Algarabel	(Vocal)
Dra. Francesca Peiró	(Suplent)
Dr. Gervasi Herranz	(Suplent)

Memòria presentada per a l'obtenció de la titulació de Doctor

Barcelona, Abril 2008

Aquesta tesi s'ha dut a terme al Laboratori de Materials Magnètics i Òxids Funcionals de l'Institut de Ciència de Materials de Barcelona (ICMAB-CSIC) dins del programa de Formación del Profesorado Universitario (FPU) del Ministerio de Educación y Ciencia del govern espanyol. La recerca s'ha emmarcat dins dels projectes MAT2002-04551-C03-01, NAN2004-9094-C03-01, MAT2005-05656-C04-01 i NANOSELECT CSD2007-00041.

A mis padres

“Eppur si muove”
Galileo Galilei

Abstract

Oxides can display a wide variety of electronic and magnetic properties. Among them, we can find insulators but also superconductors of high transition temperature. Some oxides are ferromagnets and some ferroelectrics, and even the coexistence of both ferromagnetism and ferroelectricity is found in a few of them (biferroics). These are noteworthy examples that account for the interest of the research community in these materials. Making use of these newly appearing oxides and of the techniques required to multilayer deposition and lithography, new devices have been designed and fabricated. Nevertheless, the functional properties of these devices, as well as those of the bare oxide films, appear to be highly sensitive to some effects of the epitaxial growth, which include crystal lattice distortions, electronic inhomogeneities or chemical redistribution. A deeper knowledge in this field is thus necessary to obtain fully functional oxide devices.

Spintronics is the new electronics which exploits not only the charge but also the spin character of the carriers in these oxides. As an example, magnetic tunnel junctions (MTJs) are functional devices based on two ferromagnetic metallic electrodes separated by a thin insulating layer. The manganese perovskites $R_{1-x}A_xMnO_3$, where R is a trivalent rare earth ion and A is a divalent alkaline earth, have been considered as electrodes in MTJs. The physics of these materials is based on the effect of the x doping with A^{2+} ions on the 3d levels of Mn ions, causing the appearance of (x) Mn^{4+} ions, with 3 electrons in $t_{2g}(3)e_g(0)$ configuration, coexisting with (1-x) Mn^{3+} Jahn-Teller ions, with 4 electrons into $t_{2g}(3)e_g(1)$ configuration. Tuning the x doping in this structure, ferromagnetism and metallicity can be obtained due to the itinerancy of the e_g electrons among Mn^{3+} and Mn^{4+} sites. For instance, in the La^{3+} manganites the metallicity and

ferromagnetism is found in the Sr^{2+} or Ca^{2+} substituted series at doping levels of $x \sim 0.3$, being the ferromagnetic to paramagnetic order transition temperature (Curie temperature: T_C) of ~ 360 K and ~ 270 K, respectively. Using these manganite electrodes in MTJs, it is repetitively observed that the tunnel magnetoresistance (TMR) of these devices drops at lower temperature that the T_C of bare manganite electrodes. Among the possible explanations to these depleted properties, it has been suggested the stabilization of the e_g electron in the Mn^{3+} ion caused by the Jahn-Teller distortion, promoting a cationic redistribution localized at the interfaces. These studies also address an important role to the strain induced by the epitaxy, but the actual relevance of the chemical, electronic and strain effects remains undisclosed.

Analyzing the problem on MTJs based on manganite electrodes, we notice that in all these devices only cubic (001) lattice orientation is used for the heteroepitaxial growth. Aiming to understand and solve the problem of MTJs functionality, we present in this work the study of alternative film growth orientation: (110). We were motivated by a previous analysis of the nature of (001) and (110) planes that suggested differences in their elastic properties and in the polarity of these planes that may influence in film properties. With this objective, we have grown $La_{2/3}Ca_{1/3}MnO_3$ (LCMO) films onto $SrTiO_3$ (STO) substrate, which is a cubic insulating perovskite, having two different orientations: (001) and (110), and we have compared the corresponding film properties.

In this thesis, we prove the existence of different growth mechanisms in (001) films compared to those of (110) ones, which is a key for further heterostructural growth. We achieve a fine control of (001) surfaces and identify the growth mechanisms acting in (110) ones. We have measured film magnetic properties, and remarkably higher T_C and saturation magnetization have been obtained for (110) than for (001) ones. Thus, taking care of the observed different structural deformation of (001) and (110) films, the hypothesis of different elastic response for (001) and (110) planes is proved and it has been correlated with the film magnetic properties (T_C and magnetic anisotropy). We have found that the substrate-induced lattice strain can not fully explain the different properties of these (001) and (110) films, and thus we have investigated other possible origins that could cause these dissimilar results. Added to the known electronic phase separation occurring in (001) films, we also show the development of a cationic redistribution. In contrast, conclusive evidences of the electronic and chemical homogeneity and robust magnetism of (110) films are obtained.

For the future exploitation of these manganite electrodes, the understanding and control of the magnetic and transport properties are necessary. With this objective, we have identified the main driving force of the magnetic anisotropy of (001) and (110) films, finding it to be connected to the elastic properties of the (001) and (110) planes. We have also demonstrated the influence of the in-plane magnetic anisotropy into the transport phenomena of (001) and (110) films, which plays a relevant role in the uniaxial (110) ones. The in-plane magnetoresistance has been studied as a function of the angular position of the applied magnetic field (strong enough to saturate the magnetization), so-called anisotropic magnetoresistance (AMR). We have found that the AMR, measured for the (001) and (110) films within the (001) and (110) planes, depends on the crystallographic direction of current flow. We argue that, comparing (001) and (110) films, the AMR sign and amplitude change due to the orbital arrangement within these planes.

With the objective of applying these (001) and (110) LCMO electrodes into MTJs, we have prepared bilayers with LCMO electrodes and nanometric STO layers on top. First, in order to optimize the complex process of performance of MTJs, we have used the conducting atomic force microscopy to test the quality of the insulating barriers which is a big step into the performance of fully functional MTJs. On the other hand, and wanting to investigate the newly created (001) and (110) STO layer/LCMO electrode interfaces, we have studied the effect of the STO layer on the magnetic properties and electronic phase separation occurring at the LCMO electrodes. The obtained experimental evidences signal the increase of electronic phase separation in (001) capped LCMO electrodes compared to uncapped (001) ones. Contrasting with these results, (110) capped and uncapped LCMO electrodes present a steady magnetic and electronic state. We analyze the possible mechanisms that can originate these effects, taking into consideration the different polarity appearing among insulating STO layers and LCMO electrodes depending on the interface orientation.

This strategy based on the comparative study of (001) and (110) manganite films and bilayers allows us to dig into a wide variety of physical phenomena related to the film growth, the structural deformation, the magnetic and electronic properties, or the chemical segregations. The usefulness of this approach based on the change of film orientation has been proved, and it can be considered as a possible way to tune the properties of other oxide heterostructures.

0 Contents

Contents

1 Introduction

In this chapter, we present basic concepts related to the materials studied in this thesis, half metallic ferromagnetic manganites; we will specially focus on their properties when grown in thin film form. We will introduce the existing theory of the dependence of their ferromagnetic transition temperature on lattice strain. We will describe afterwards the integration of these materials into magnetic tunnel junctions. The properties of these junctions will be analyzed, emphasizing in the decay of TMR that limits their use. Since junctions are fabricated with (001) oriented films, we discuss on the possible relevance of the crystal orientation on film properties in view of exploring the (110) oriented films as an alternative.

1.1 The physics of ferromagnetic metallic manganites: from bulk to thin films

Perovskite manganites of general formula $R_{1-x}A_xMnO_3$ (Figure 1.1a), where R is a trivalent rare earth ion (La, Nd…) and A is a divalent alkaline earth (Ca, Sr, Ba), present very interesting properties. For the case of La manganites, the undoped parent $LaMnO_3$ is an antiferromagnetic insulator [1] with Mn^{3+} ions in $3d^4$ electronic configuration. The crystal field induced by the oxygen ions in the perovskite structure splits the 3d levels into a low energy t_{2g} triplet and a high energy e_g doublet (see Figure 1.1b). As the strength of the crystal field spitting is weaker than the Hund coupling (J_H), three electrons occupy the t_{2g} levels and one electron the e_g level, and all they have parallel spin (S = 2). Besides, a more favorable energetic configuration is achieved by losing the degeneration of these e_g levels occurring the so-called Jahn-Teller distortion.

This non-degeneration localizes the e_g electrons into a filled sub-band and makes $LaMnO_3$ to be an insulator. The cooperative Jahn-Teller effect leads then to a three-dimensional orbital order, and due to superexchange magnetic interactions among the Mn^{3+} ions, A-type antiferromagnetism develops in this material [2].

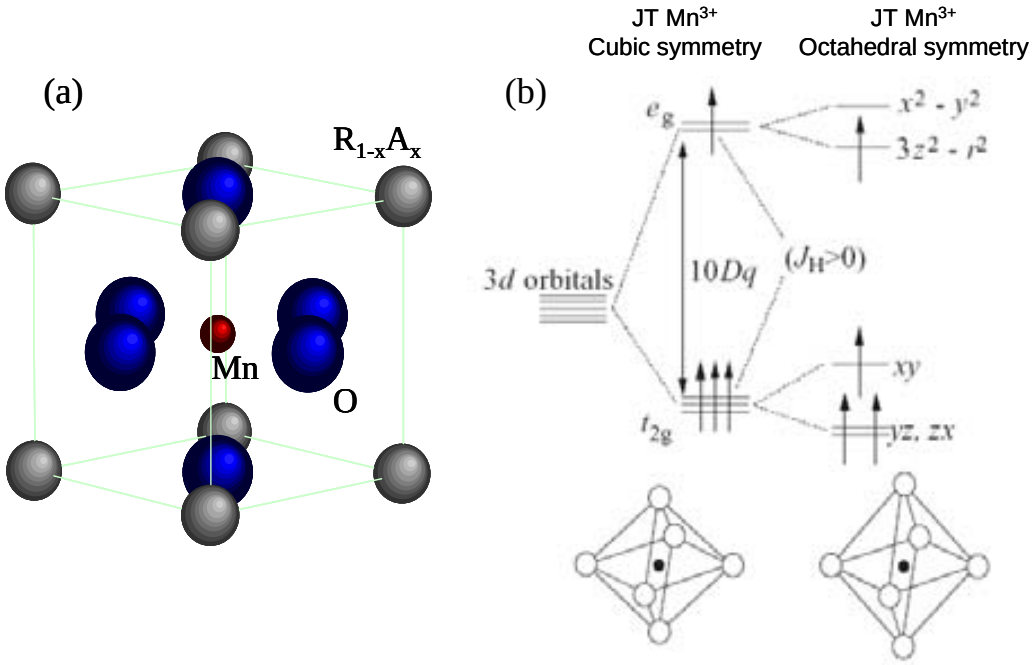

Figure 1.1(a) Schematic view of the $R_{1-x}A_xMnO_3$ perovskite pseudocubic unit cell. (b) *3d* orbitals in Mn^{3+} (solid symbols) with different oxygen coordination (open symbols). Note that, caused by the cubic crystal field, a 10*Dq* energy splitting between t_{2g} and e_g levels (left) appears and in octahedral crystal field symmetry (right) the JT distortion breaks the degeneracy of these levels.

Upon doping (x) with divalent alkaline ions (Ca, Sr…), La^{3+} ions are substituted by these Ca^{2+} (Sr^{2+}) ions. This substitution changes the Mn ionic state and the number of e_g electrons, appearing an amount of x-Mn^{4+} ions coexisting with (1-x)-Mn^{3+} ions and reducing the number of e_g electrons. A metallic state occurs for x = 0.20 (0.15) with delocalized e_g electrons with the spin parallelly aligned to that of the t_{2g} electrons. Within these conditions, mediated by these delocalized e_g electrons, ferromagnetic interactions are possible among the Mn ions through the double-exchange mechanism, as described latter.

The phase diagram of these manganites is quite complex. For the Ca (Sr) substituted ones, optimal doping is achieved for $x \approx 0.33$ with Curie temperature (T_C) of ≈ 270 K [3] (≈ 360 K [4]). As an example, the phase diagram of the $La_{1-x}Ca_xMnO_3$ compounds is shown in Figure 1.2. Approaching T_C, the resistivity (ρ) of these compounds drops notably, and in most of them it develops an electronic transition from

insulator (paramagnetic) to metal (ferromagnetic) state. The application of a magnetic field, which strengthens the spin coupling, also affects the value of ρ, making it to drop. Large values of negative magnetoresistance [(ρ(H) - ρ(0)/ ρ(0)] are obtained and the phenomenon is referred as colossal magnetoresistance effect, which is especially high at temperatures close to T_C where the magnetic order of manganites is much sensitive.

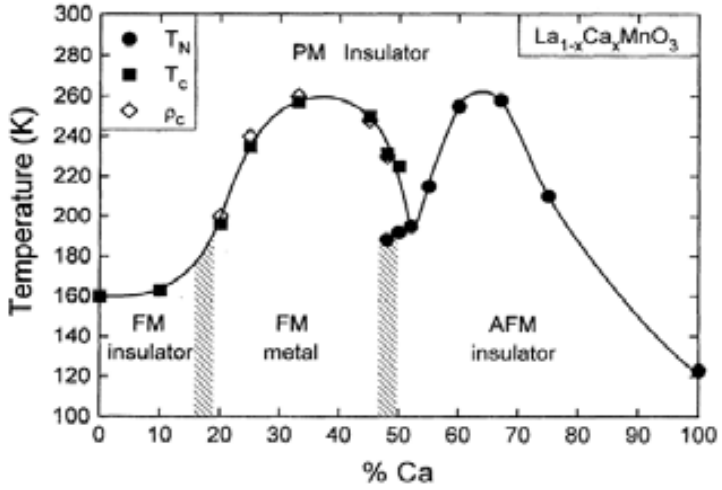

Figure 1.2. Phase diagram of $La_{1-x}Ca_xMnO_3$ compounds, from Ref. 3. The corresponding magnetic transition temperatures indicated are for the antiferromagnetic phases (AFM), the Néel temperature (T_N), and for the ferromagnetic phases (FM), the Curie temperature (T_C), both towards paramagnetic phases (PM). It is also shown the insulator to metal transition (ρ_C) where necessary.

The ferromagnetism of manganites at the $x \approx 1/3$ doping level [5] occurs by the called double-exchange mechanism. It is based in the coexistence of Mn^{3+} and Mn^{4+} ions with $t_{2g}(3)e_g(1)$ and $t_{2g}(3)e_g(0)$ electronic configurations, respectively. The energy of t_{2g} electrons lies far from the conduction band, thus they do not contribute to the transport properties. However, it is relevant that all t_{2g} electrons have parallel spin, thus defining a shell of S = 3/2. In the conduction band we find e_g electrons, which are simultaneously shared by Mn and O sites. In this energy band extended throughout all the material, the simultaneous transfer of e_g electrons from Mn^{3+} towards O^{2-} and from O^{2-} towards Mn^{4+} happens (Figure 1.3). This hopping of e_g electrons creates degenerated couples of $Mn^{3+/4+}$-O^{2-}-$Mn^{4+/3+}$ and due to the strong coupling among e_g electrons and t_{2g} electrons, the spin orientation is preserved in all the Mn sites and ferromagnetism arises. Thus, in the ferromagnetic metallic phase ($T < T_C$), it is expected a fully spin polarization of the conduction band, which make these materials so interesting to Spintronics. For instance, in $La_{1-x}Ca_xMnO_3$ theoretical predictions by

Pickett and Singh [6] indicate that only majority bands are occupied at the Fermi level at x = 1/3.

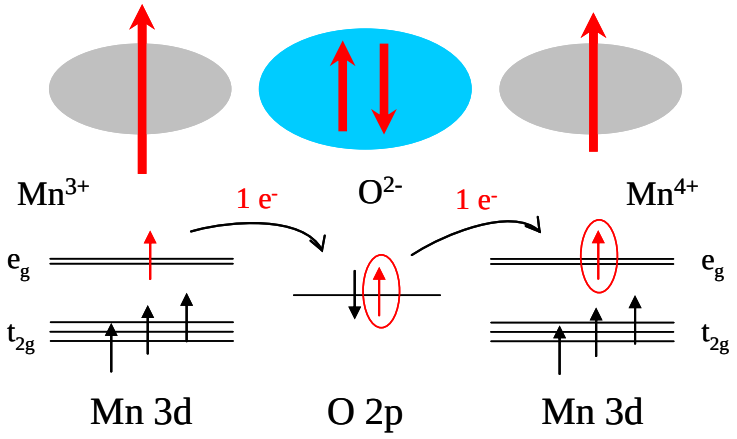

Figure 1.3. Sketch of the double-exchange mechanism showing the hopping of e_g electrons between Mn 3d and O 2p bands.

Further study of the conductivity of these e_g carriers highlights the relevance of the Mn-O-Mn bonding characteristics. The energy width of this e_g band (bandwidth, W) is directly related to the overlapping of Mn-O orbitals, which is optimum for a 180 deg bond angle, and it is also influenced by the Mn-Mn distance. Experiments inducing structural distortions by the use of different trivalent and divalent ions in manganites [7] clearly show that as W decreases, the conductivity drops and the T_C decreases. Indeed, double-exchange mechanism competes with the intrinsic tendency of isolated Mn^{3+} and Mn^{4+} ions to be antiferromagnetically coupled. Thus, by reducing the orbital overlapping, that is, the strength of the ferromagnetic double-exchange mechanism, the system evolves to antiferromagnetic order.

To integrate these fully spin polarized materials into functional devices, epitaxial thin film and heterostructures of these materials are necessary. However, the properties of these thin films are usually found to be depressed compared to those of their bulk counterparts. Several studies in single manganite films [8][9][10] and heterostructures [11][12] show that, at reduced thickness, the conductivity, T_C and saturation magnetization drop, and even in thinner films the ferromagnetism and conductivity can be suppressed (Figure 1.4). This phenomenon is commonly attributed to the existence of a dead layer, non-ferromagnetic and insulator one. The thickness of this dead layer is estimated around few nm and, for a given manganite layer, it depends on the substrate, which is a fact that signals the interface origin of this effect. A useful technique to study the existence of a dead layer and more exactly the electronic state of the Mn ions is

^{55}Mn nuclear magnetic resonance (NMR). The capability to detect the electronic environment of Mn ions has allowed relating the reduced properties on these manganite films to the nucleation of regions with different magnetic and electronic states, which make the film magnetically and electronically inhomogeneous [8][13]. This electronic phase separation was already theoretically predicted by Dagotto *et al.* [14], concluding that manganites are very sensitive materials to disorder. Possible sources of this disorder are: the jump on the stacking sequence of the combined perovskite materials, the presence of oxygen vacancies in the manganite layers and the loss of coordination in the Mn-O-Mn bond happening at the interfaces. Combining surface and bulk sensitive techniques, the occurrence of the loss of magnetism at the surface or at the interface of manganite layers have been proved [15][16], as shown in Figure 1.5. Moreover, theoretical calculus on manganite and insulator heterostuctures predicts a similar result: within the manganite electrode and near the interface, regions presenting depleted ferromagnetic and metallic properties are expected [17].

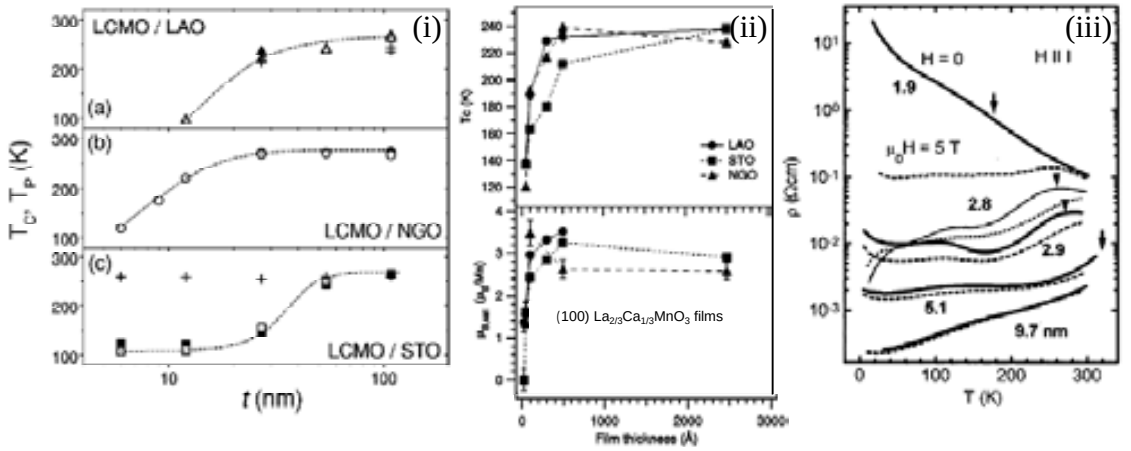

Figure 1.4. [(i) and (ii)]: Different studies on the magnetic properties of $La_{2/3}Ca_{1/3}MnO_3$ films as a function of film thickness and substrate: (a) T_C (solid symbols) and metal to insulator transition T_P (open symbols) [8]; (b) T_C and saturation moment $\mu_{B\ sat}$ [10]. (iii): Resistivity of multilayers of $[La_{0.7}Sr_{0.3}MnO_3/SrTiO_3]$ for thicknesses of the manganite layers as indicated in the figure under magnetic field of 0 T (straight line) and 5 T (dash line) [12].

These results signal the appearance of reduced ferromagnetism and conductivity and of electronic phase separation related to the interfaces. This localization of the e_g electrons and the decrease in the double exchange mechanism have been suggested to arise from the distortion on the Mn-O-Mn bonds at the interface. However, the exact origin of these depressed properties and the strategies to control them remain still undisclosed.

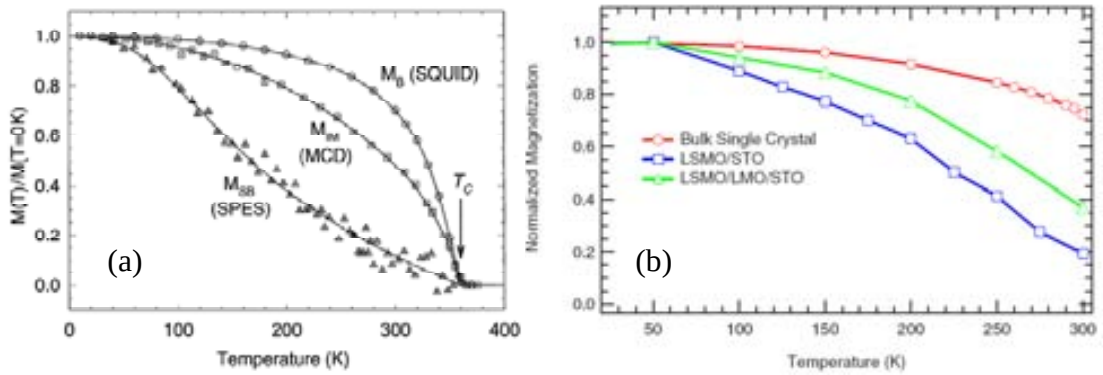

Figure 1.5. Temperature dependence of magnetization on: (a) $La_{0.7}Sr_{0.3}MnO_3$ (001) films using three techniques with different sensisitivity to surface magnetism, here we refer the depth scale with the origin at the film surface: by SQUID, bulk sample magnetization (M_B), by X-ray magnetic circular dichroism (MCD), intermediate depth magnetization of ~ 5 nm (M_{IM}), and by spin polarized electron spectroscopy (SPES), the surface boundary ~ 0.5 nm (M_{SB}) [15]; (b) $La_{2/3}Sr_{1/3}MnO_3/SrTiO_3$ (001) films and $La_{2/3}Sr_{1/3}MnO_3/LaMnO_3/SrTiO_3$ heterostructures, showing only the intermediate depth magnetization (M_{IM}) measured from the MCD peak height. Also the bulk LSMO single crystal magnetization is plotted [16].

1.2 Magnetic tunnel junctions based on manganites: (001) oriented electrodes

Magnetic tunnel junctions are spintronics devices composed by two ferromagnetic conductors (electrodes) separated by a ultrathin insulating layer (barrier). Applying a low electrical potential to these electrodes, the electrons may tunnel through the barrier, being the effective tunneling current dependent on the relative magnetic configuration of the electrodes. From the orientation of the corresponding magnetizations, two different working configurations are defined: parallel (P) and antiparallel (AP). From these different functional regimes, an operating ratio for the MTJs can be defined, which is the so-called tunnel magnetoresistance (TMR)

$$TMR = \frac{R_{AP} - R_P}{R_P} \qquad [1.1]$$

where R_{AP} and R_P account for the junction resistance in the different magnetic states. In Figure 1.6 (main panel) a sketch of the resistance as a function of the applied magnetic field in an ideal MTJs is plotted. The swept from high field (in absolute value), where both electrodes have magnetization pointing to the same direction, towards lower fields, where the magnetization vector rotates, defines a device with a binary behavior between P and AP configurations.

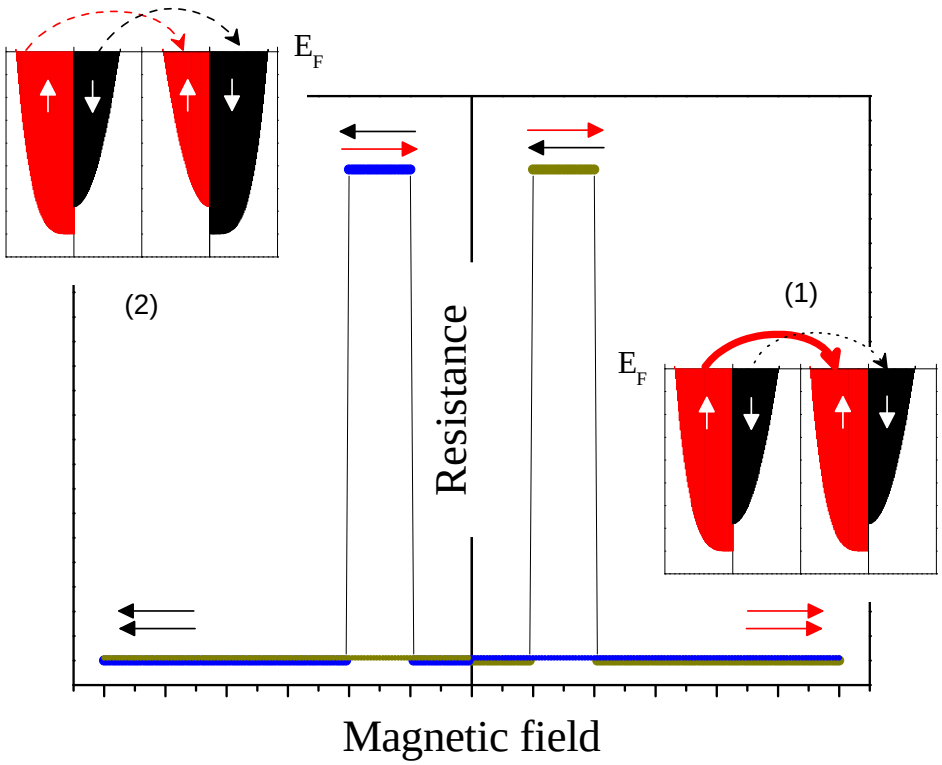

Figure 1.6. Main panel: Junction resistance versus magnetic applied field measurement on a MTJ with decoupled ferromagnetic electrodes. Two different states are expected for parallel (P) and antiparallel (AP) electrode magnetization. Insets: Sketch of the density-of-states near the Fermi level (E_F) for two identical electrodes. (1) represents the P configuration and (2) the AP one. Note that in (1) [P configuration] the available electronic states in both electrodes are those of majority spin bands whereas for (2) [AP configuration] the tunneling may happen between majority and minority bands for each electrode, thus the current in AP configuration decreases leading to higher R_{AP}.

Following the Jullière model [18], in the tunneling process it is assumed that the spin of the electrons is preserved through the tunneling and that the tunnel conductivity between two ferromagnetic electrodes which are in P and AP states is proportional to the product of the corresponding density-of-states for majority and minority spin. Being $n_\uparrow$ the density-of-states of majority spin electrons and $n_\downarrow$ the density-of-states of minority spin electrons in a ferromagnetic electrode, the spin polarization (P) is thus described by:

$$P = \frac{n_\uparrow - n_\downarrow}{n_\uparrow + n_\downarrow} \qquad [1.2]$$

According to eq. 1.2, TMR expression (eq. 1.1) can be then rewritten in terms of the polarization of the ferromagnetic electrodes (P_1 and P_2) as:

$$TMR = \frac{2P_1P_2}{1 - P_1P_2} \qquad [1.3]$$

Thus, within this model, TMR is proportional to the difference in density-of-states of majority spin (n↑) and minority spin (n↓) bands for each electrode (labeled 1 and 2):

$$TMR \sim \left(n_{1\uparrow} - n_{1\downarrow}\right)\left(n_{2\uparrow} - n_{2\downarrow}\right) \qquad [1.4]$$

However, this prediction cannot explain the experimental observation of the TMR dependence on barrier thickness, height and also in her nature. Accounting for the existence of other contributing effects, as impurities in the barrier or depolarizing effects at the electrode-barrier interfaces, other more complex models have been developed [19]. Still, Jullière's simple model is useful for the evaluation of the polarization of ferromagnetic electrodes in MTJs at low temperature.

The use of manganite materials and other half-metallic ferromagnetic conductors as electrodes in MTJs opens the possibility of obtaining optimal TMR response of such devices due to the expected fully spin-polarization of the electrons at the Fermi level. First MTJs were performed using $La_{0.67}Sr_{0.33}MnO_3$ (LSMO) electrodes grown on (001) $SrTiO_3$ (STO) substrates with a relatively thick insulating layer of STO of 5 nm as barrier [20]. Resistance curves versus applied magnetic field at different temperature are shown in Figure 1.7a. The low temperature TMR value of this LSMO/STO/LSMO trilayer device was 100 %, which considering identical LSMO electrodes leads to a spin polarization, through the use of eq. 1.3, of P_{LSMO} = 58 %, which is quite lower than the ideal 100 % expected for a half-metallic ferromagnet. The development of photolithographic techniques and other lithographic process for the performance of MTJs have lead to the improvement of device and thus of the TMR response. MTJs using other substrates and barriers, as orthorhombic $NdGaO_3$ (NGO), and other manganites, as $La_{0.7}Ca_{0.3}MnO_3$ (LCMO), have lead to TMR ratios as high as ~ 86 % at low temperature, which using eq. 1.3 corresponds to a LCMO spin polarization of P_{LCMO} = 55% (Figure 1.7b)[21]. The orientation of the NGO substrates and thus of these heterostructures was (110) one in orthorhombic notation, which means a (001) orientation in cubic notation.

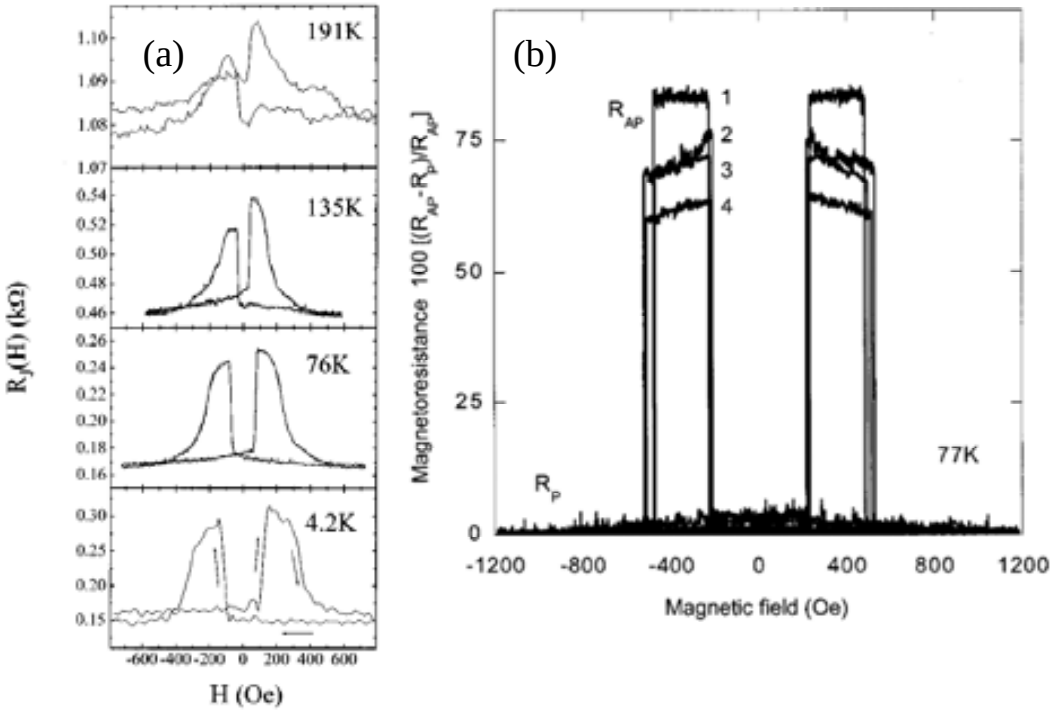

Figure 1.7. TMR curves of (a) a LSMO/STO/LSMO//STO(001) pillar at different temperatures [20] and (b) four LCMO/NGO/LCMO//NGO(110) junctions at 77 K [21].

However, a clear disadvantage of these MTJs appears when studying the temperature dependence of the TMR ratio. As shown in Figure 1.8, the TMR ratios of symmetric LSMO/STO/LSMO (a) [22] and LCMO/NGO/LCMO (b) [21] junctions vanish at temperatures lower than the corresponding Curie temperature of the electrodes. Several combinations of manganites and insulating materials into MTJs [20][21][22][23][24][25][26][27] has been tested. Within these experiments, the nature of the electrode-insulator interfaces have been changed in different ways: by choosing insulators of perovskite or rutile structure, by using perovskite insulators with different structural mismatch with the electrode, by varying the nominal charge of the insulator planes, etc. For instance, experiments with the rutile insulator TiO_2, which presents an oxygen lattice much different from the perovskite one, compared to those performed with the perovskite insulator $LaAlO_3$ indicate a preferential lowering of the TMR ratio in the TiO_2-manganite system [25]. The direct measurement of the TMR ratio as a function of the interface nature together with the existing studies on surface and interface magnetization [15][16][17], claim that the interface phenomena dominate the depleted TMR ratio as a function of temperature.

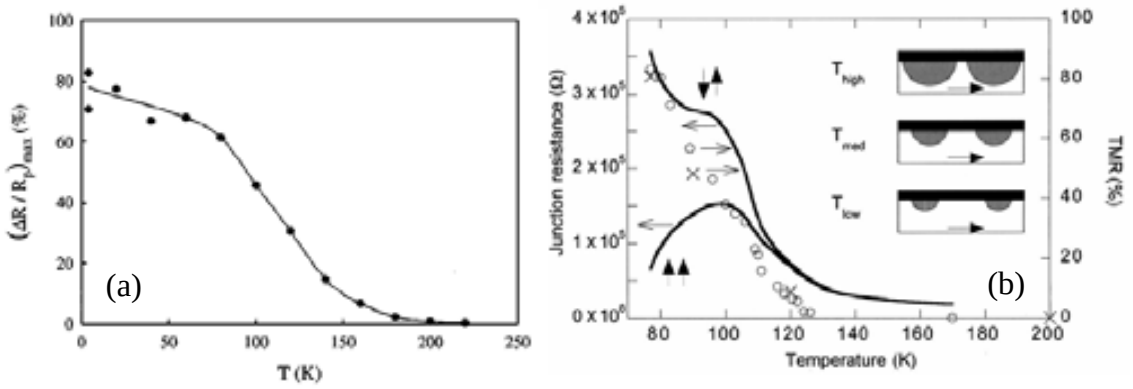

Figure 1.8. Temperature dependence of (a) the TMR ratio in LSMO/STO/LSMO//STO(001) junctions [21], being the T_C of the LSMO electrodes of ~347 K and (b) junction resistance for AP and P configuration (lines) and corresponding TMR ratio (symbols) of LCMO/NGO/LCMO//NGO(110) junctions, being the T_C of LCMO electrodes ~265 K [22].

Lastly reported values of TMR in manganite based MTJs are clearly higher (TMR ~ 1850 %) [28] than the equivalent preliminary results (TMR ~ 100 %) [20], and in some cases not only high values of TMR have been measured at low temperature but also at temperatures closer to the Curie temperature of the used electrodes (TMR around the T_C of the LSMO electrodes ~ 300 K) [25]. In all these studies, only (001) oriented heterostructures (in the cubic notation) are used. MTJs exploiting other orientations are few, and it can be highlighted the work of Ruotolo *et al*. [29], who have integrated $Ni_{80}Fe_{20}$/LSMO//STO(110) bilayers into MTJs. They have achieved to measure a value of TMR of ~ 1.2 % at low temperature which may be that low because of the use of the manganite dead layer as the spacer between the two ferromagnetic $Ni_{80}Fe_{20}$ and LSMO electrodes.

1.3 Elastic and electronic characteristics of (001) and (110) interfaces

The growth of thin film heterostructure based on perovskite materials, such as the La-manganites, implies the necessary choice of appropriate substrates that are structurally and chemically compatible. Commonly used substrates of manganite films are insulating perovskites as $LaAlO_3$, $NdGaO_3$ or $SrTiO_3$, which due to the low lattice mismatch with the manganite films (from virtually 0 % to 2.3 %, depending on the manganite and substrate) allow the performance of complex epitaxial heterostructures [30]. Nevertheless, tuning the lattice mismatch is not the only approach to induce a different unit cell deformation. *A priori*, the elastic properties of different planes of

growth can be used to tune the unit cell deformation with the same nominal lattice mismatch. On the other hand, the chemical and electronic characteristics of a given plane, either in the manganites or in the insulating perovskites, is expected to influence the properties of the manganite layer at least at the near interface.

(001) (cubic notation) substrates have been extensively exploited and fewer attention has been driven to other orientation. However, as already mentioned, the substrate and interface orientation is a most relevant factor as they may alter manganite magnetic properties through the induced unit cell deformation of the growing layers (elastic and plastic deformation) or electronic and chemical effects through the interface. In the following, some of the more relevant elastic and electronic considerations arising from the use of (001) and (110) substrates and interfaces are described.

1.3.1 Elastic properties

An analysis of the elastic properties of (001) and (110) epitaxial films grown on this substrate may commence studying those of the bare substrates. With this purpose, we take as the starting point the cubic perovskite $SrTiO_3$ (STO) (cubic parameter a_{STO} = 3.905 Å). The investigation of the atomic arrangement along the main in-plane crystal directions in (001) and (110) planes clearly signals relevant differences (Figure 1.9): concerning the 3d metal (Ti) the same Ti-O-Ti sequence is observed along the [100] and [010] directions in the (001) plane whereas in the (110) plane along the [001] direction is Ti-O-Ti and along [1-10] direction is Ti-Ti. Thus, the different atomic sequences and bonding among Sr, Ti and O atoms within (001) and (110) planes can influence the elastic properties of these planes. In a general approach to the evaluation of the elastic properties of a given cubic crystal, it is necessary to acknowledge the elastic stiffness constants c_{ij} of the crystal. Here, c_{ij} account for elastic stiffness matrix elements defined following the Voigt notation: diagonal elements are then c_{11} and c_{44} and off-diagonal ones c_{12} [31]. Taking these c_{ij} values and appropriate elastic expressions [32] we can evaluate the Young moduli Y_{hkl} along the crystal directions present in the (001) and (110) planes. Along a given [hkl] direction, from the Y_{hkl} values we can obtain the elastic effects of an applied strain ε_{hkl} on the crystal by quantifying the crystal mechanical stress σ_{hkl} as $\sigma_{hkl} = Y_{hkl}\ \varepsilon_{hkl}$. Therefore, for the elastic study of (001) and (110) planes it is necessary to obtain the Young moduli along [100] and [110] directions (Y_{100} and Y_{110}) which are actually contained in these planes.

The Young modulus expressions for [100] and [110] directions are [32]:

$$Y_{100} = c_{11} + c_{12} - \frac{c_{12}\left(c_{11} + 3c_{12} - 2c_{44}\right)}{\left(c_{11} + c_{12} + 2c_{44}\right)} \quad [1.5]$$

$$Y_{110} = \frac{\left(c_{11} + 3c_{12} + 2c_{44}\right)}{4} - \frac{\left(c_{11} + c_{12} - 2c_{44}\right)}{2} \frac{c_{11} + 3c_{12} - 2c_{44}}{c_{11} + c_{12} + 2c_{44}} \quad [1.6]$$

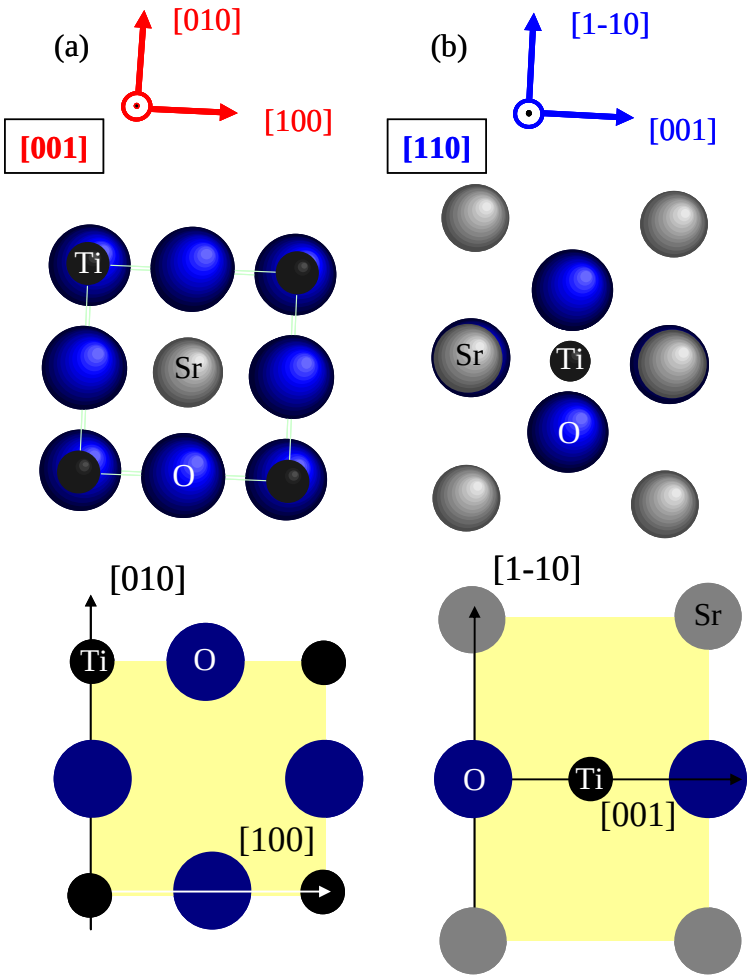

Figure 1.9. Projections of $SrTiO_3$ cubic crystal on (a) (001) and (b) (110) planes. Crystallographic directions are indicated for each orientation (top) and each atom is identified by their atomic symbol. Bottom: Sketches of (a) TiO_2 and (b) SrTiO planes.

Turning to the STO crystal, Bell and Rupprecht [33] reported c_{ij} values of c_{11} = 317 GPa, c_{12} = 102 GPa and c_{44} = 123 GPa. Using these c_{11}, c_{12} and c_{44} into eqs. 1.5 and 1.6, the Young moduli of STO are calculated to be Y_{100} = 361 GPa and Y_{110} = 385 GPa. Focusing the investigation onto the (001) and (110) STO planes (Figure 1.9), for the (001) plane we observe that for two orthogonal directions, for instance [100] and [010] directions, equal Young modulus is expected, with $Y_{100} = Y_{010}$ = 361 GPa and $Y_{110} = Y_{1\text{-}10}$ = 385 GPa, and thus the plane presents four-fold stress symmetry. Quite different is the case of the (110) plane, where the orthogonal

[001] and [1-10] directions define a two-fold stress symmetry, with higher Young modulus along [110] direction, Y_{110} = 385 GPa, than along [001] direction, Y_{001} = 361 GPa. To have a clear experimental evidence of the different mechanical behavior of STO crystal planes, in Figure 1.10 there are shown atomic force microscopy (AFM) images of (001) and (110) STO surfaces after nanoindentations with a conical tip were performed. A comparison of the shape of the surface imprints highlights the isotropic deformation of (001) plane (circular imprint in Figure 1.10a) and an anisotropic deformation occurring on the (110) plane (elliptical imprint Figure 1.10b), with preferential deformation along [001] direction.

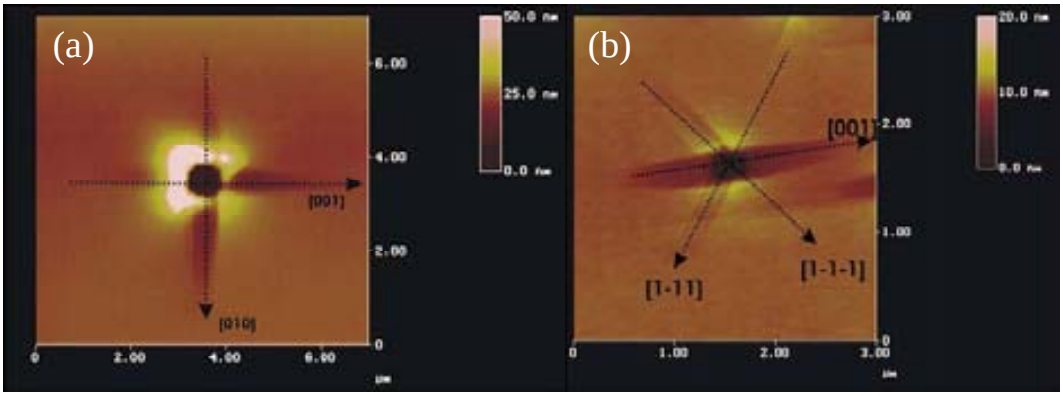

Figure 1.10. AFM images of nanoindentations performed in $SrTiO_3$ single crystals using a conical tip, corresponding to (a) (001) and (b) (110) substrates [34].

After an analysis of the (001) and (110) STO elastic properties, we should consider the case of epitaxial manganite thin films grown on them. The similarity of the crystal structure of the La-manganites to STO and the low mismatch between their lattice parameters suggest that the elastic properties of manganite films are likely to be similar to those of the STO substrates. The manganite unit cell is characterized by its lattice parameters, which can be experimentally measured. To evaluate and map the elastic deformation of the film unit cell, we can calculate the epitaxial strain values ε_{hkl} for a given [*hkl*] direction (being *h*, *k*, *l* the Miller indices) as:

$$\varepsilon_{hkl} = \frac{d_{hkl}^{film} - d_{hkl}^{bulk}}{d_{hkl}^{bulk}} \qquad [1.7]$$

where d^{film}_{hkl} and d^{bulk}_{hkl} are the film and bulk interplanar distances along the [*hkl*] direction. To determine the mechanical stress of the manganite unit cell, it is necessary to use the strain values ε_{hkl}, the elastic stiffness constants c_{ij} and to calculate for a given [*hkl*] direction the epitaxial stress σ_{hkl} as:

$$\sigma_{hkl} = Y_{hkl}\varepsilon_{hkl} \qquad [1.8]$$

The different crystallographic directions contained within the (001) and (110) planes are expected to influence the manganite film mechanical stress, and the film functional properties may be consequently affected.

1.3.2 Electronic properties

In the ABO_3 perovskites, the formal terminating planes along [001] direction are AO and BO_2 and along [110] direction are ABO and O_2. Assuming that there are no electronic and structure reconstructions, the relative charge of these planes depend on their chemical composition (A, B, O). Considering $SrTiO_3$ (STO) as the preferable material to be substrate and insulating layer in La-manganite ($La_{1-x}A_xMnO_3$) heterostructures, in STO the A site is occupied by Sr and the B site by Ti. For the La-manganites, A perovskite site is occupied by both La and the doping alkaline earth (A), whereas the B site is filled by Mn atoms.

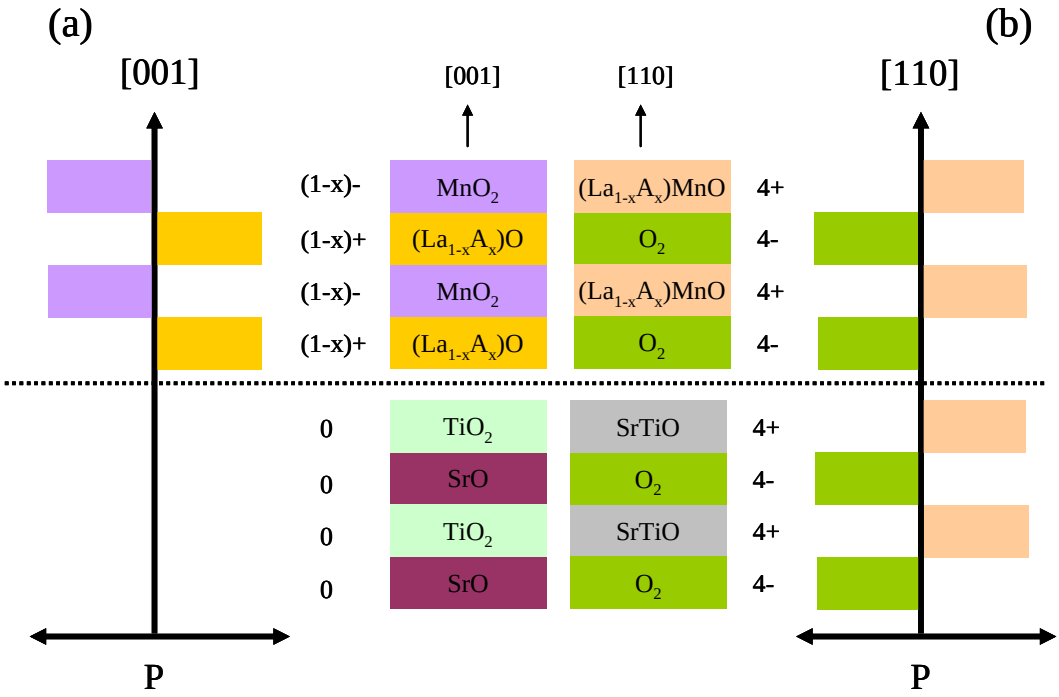

Figure 1.11. Schematic view of $SrTiO_3$ and $La_{1-x}A_xMnO_3$ layers depending on the plane orientation: (a) (001) and (b) (110). Assuming an ionic picture, the corresponding electric polarization (P) and charge are shown for each case.

In a simple ionic image, heterostructures based on La-manganites and STO grown with (001) and (110) orientation present an electronic distribution as seen in Figure 1.11. Focusing firstly on the (001) planes (Figure 1.11a), (001) STO planes are charge neutral due to the charge balance at the SrO [$Sr^{2+}O^{2-}$] and TiO_2 [$Ti^{4+}O^{2-}{}_2$] planes. On the other hand, (001) La-manganite film planes present a net electronic charge of (1-

x)+ for the $(La_{1-x}A_x)O$ $[(La^{3+}_{1-x}A^{2+}_{x})O^{2-}]$ planes and (1-x)- for the MnO_2 $[Mn^{3+}_{1-x}Mn^{4+}_{x}O^{2-}_{2}]$ planes. Thus, in (001) heteostructures, neutrally charged (001) STO planes are put in contact to (001) La-manganite charged ones. In contrast, the case of (110) planes is much different (Figure 1.11b) and is characterized by presenting STO and La-manganite polar planes. In concrete, within (110) STO planes a net 4- electronic charge is found in O_2 $[O^{2-}_{2}]$ and a 4+ charge is located at the SrTiO $[Sr^{2+}Ti^{4+}O^{2-}]$ planes. For the (110) La-manganites, similarly to the (110) STO case, O_2 $[O^{2-}_{2}]$ planes with 4- electronic charge coexist with 4+ charged $(La_{1-x}A_x)MnO$ $[(La^{3+}_{1-x}A^{2+}_{x})Mn^{3+}_{1-x}Mn^{4+}_{x}O^{2-}]$ planes, independently of the amount of x doping. Therefore, the charge of the (110) planes oscillates among 4+ and 4- in a similar way in both (110) STO and (110) La-manganite layers.

The striking conclusions of this simple analysis of the electronic properties of (001) and (110) La-manganite and STO layers highlight the disruption of the net charge distribution between (001) La-manganite and STO layers and the continuity of the oscillating charge distribution between (110) ones. In fact, the polarity nature of (001) and (110) STO surfaces have been reported to be weakly polar for the (001) STO surfaces and polar for the (110) STO surfaces [35]. Within the framework of these reports and from the simple ionic evaluation, relevant electronic differences arise between (001) and (110) STO and La-manganite layers that are expected to influence the properties of the (001) and (110) La-manganite films and STO-La-manganite interfaces.

1.4 Outline of the thesis

This thesis is focused in the development of half-metallic ferromagnetic (110) $La_{2/3}Ca_{1/3}MnO_3$ (LCMO) electrodes and their integration into functional magnetic tunnel junctions. The parallel study of the more used (001) LCMO electrodes allows directing the research into three main fields:

(a) Comparative study of the growth mechanisms of LCMO films onto $SrTiO_3$ (STO) substrates with (001) and (110) orientation. The precise knowledge of the film unit cell parameters and of the Mn electronic state and chemical distribution of the cations help to understand the effect of the orientation in the crystal deformation and on the appearance of electronic and chemical inhomogeneities in (001) films.

(b) Comparative study of the magnetic properties of (110) and (001) LCMO half-metallic ferromagnetic electrodes. It turns out that the robustness of ferromagnetic properties of (110) LCMO films is extended to a wide range of film thickness, letting us argue about the origin of the depressed properties of (001) LCMO films. We connect the structural, electronic and magnetic properties of these films and we discuss the possible origins of the observed charge distribution on the basis of different polarization and elastic properties of (001) and (110) planes. Furthermore, the elastic properties are found to be the driving force of the magnetic anisotropy of both (001) and (110) LCMO films through the magnetoelastic energy.

(c) The development of magnetic tunnel junctions based on (001) and (110) LCMO electrodes using STO barriers. After the STO/LCMO//STO bilayer growth, fundamental and practical studies on these heterostructures are performed. The investigation of the phenomena located at the functional top STO/LCMO interfaces signals the electronic sensitivity of (001) interfaces, whereas slight changes are seen in (110) interfaces. We link this topic to the previous study on single LCMO films, achieving a deeper understanding of the physical origin of these interfacial effects. The STO/LCMO//STO bilayers are finally integrated into magnetic tunnel junctions, thus we test the insulating character of our STO barrier and create useful devices obtaining preliminary positive results on the tunneling using STO/LCMO//STO(110) heterostructures.

Chapter 2. A general description of the physical phenomena as well as the experimental system related to the thin film deposition, characterization tools and lithographic procedures are presented.

Chapter 3. The growth mechanisms of LCMO films of different thickness on STO (001) and (110) are identified, from analysis of topographic images obtained by atomic force microscopy (AFM). Discussion on the strategies to control the film morphology is presented.

Chapter 4. The structural characterization of LCMO films was performed mainly by X-ray diffraction methods, being of especial relevance the use of reciprocal space maps. These experiments show not only the epitaxy of these ones on STO (001) and (110), but also an interesting different strain state between (001) and (110). For (110) films, it is found an anisotropic in-plane strain. High resolution transmission microscopy (HRTEM) images confirm the good quality of films and interfaces and the absence of major lattice defects. Manganese valence states of both kinds of films are investigated by nuclear magnetic resonance (NMR). Other techniques, X-photoelectron spectroscopy (XPS), electron energy loss spectroscopy (EELS) and X-ray absorption spectroscopy, have been also used to study the electronic state and cation distribution in these films.

Chapter 5. Magnetic properties of LCMO films were studied mainly by SQUID magnetometry. The magnetic properties were found to be very sensitive to substrate orientation. Particularly, it will be presented the dependence of the Curie temperature on the film strain from a wide range of film thickness, and the dependence will be analyzed using magnetoelastic theory. High in-plane uniaxial magnetic anisotropy is found in (110) films, with a clear dependence on the film strain. In the (001) case, a similar influence of the magnetoelastic energy on the magnetic anisotropy confirms that the mechanical stress dominates the magnetic anisotropy of LCMO films independently of their orientation. Magnetotransport measurements were performed on (001) and (110) films using a PPMS system, some of these fims being lithographed allowing the measurement of longitudinal and transverse resistance. Higher transition temperatures and lower resistivities are measured for (110) films compared to (001) ones, and in the lithographed films the anisotropic magnetoresistance and planar Hall effect are observed

to show the effects of a different spin scattering depending on the in-plane current direction and on the plane orientation.

Chapter 6. The growth and characterization of bilayers of STO thin barriers on LCMO (001) and (110) electrodes are presented. Bilayer crystal quality, magnetic and electronic properties and the top STO/LCMO interfaces were carefully studied by means of SQUID, XPS, NMR and HRTEM-EELS. We observed the influence of the growth orientation on the magnetic and electronic properties, and found important conclusions for the fundamental understanding of the (001) and (110) interface phenomena. Further test of the functionality of bilayers was done by Conducting AFM (CAFM), and from these measurements we evaluated the barrier height energy involved in these heterostructures. Magnetic tunnel junctions based on (110) LCMO electrodes were performed and first results on the transport measurements of these devices are shown.

Appendix I. Results on magnetotransport measurements carried on (110) oriented films of $La_{0.95}Ag_{0.05}MnO_3$ signals the occurrence of similar effects on anisotropic magnetoresistance to those observed as measured in LCMO(110) films.

Appendix II. Results on $La_{2/3}Sr_{1/3}MnO_3$ (LSMO) films grown by pulsed laser deposition (PLD) onto STO (001) and (110) substrates. Studying the effect of the oxygen pressure in the PLD chamber during the LSMO deposition, we have studied the surface morphology by AFM and the structure and magnetic properties. We analyze the influence of both the plane of growth and the deposition oxygen pressure on the magnetic properties within the framework of the results obtained from LCMO (001) and (110) films.

References

[1] E.O. Wollan and W.C. Koehler, Phys. Rev. **100** 545 (1955)

[2] J. Goodenough, Phys. Rev. **100,** 564 (1955)

[3] P. Schiffer, A. P. Ramírez, W. Bao, and S.-W. Cheong, Phys. Rev. Lett. **75**, 3336 (1995)

[4] A. Urushibara, Y. Moritomo, T. Arima, A. Asamitsu, G. Kido, and Y. Tokura, Phys. Rev. B **51**, 14103 (1995)

[5] C. Zener, Phys. Rev. **82**, 403 (1951); P. de Gennes, Phys. Rev. **118**, 141 (1960)

[6] W. E. Pickett and D. J. Singh, Phys. Rev. B **53**, 1146 (1995)

[7] J. Fontcuberta, B. Martínez, A. Seffar, S. Piñol, J. L. García-Muñoz, and X. Obradors, Phys. Rev. Lett. **76**, 1122 (1996); J. L. García-Muñoz, J. Fontcuberta, M. Suaaidi, and X. Obradors, J. Phys.: Condens. Matter **8,** L787 (1996)

[8] M. Bibes, S. Valencia, Ll. Balcells, B. Martínez, J. Fontcuberta, M. Wojcik, S. Nadolski, and E. Jedryka, Phys. Rev. B **66**, 134416 (2002)

[9] M. Izumi, Y. Konishi, T. Nishihara, S. Hayashi, M. Shinohara, M. Kawasaki, and Y. Tokura, Appl. Phy. Lett. **73**, 2497 (1998); M. Ziese, H. C. Semmelhack, and K. H. Kan, Phys. Rev. B **68**, 134444 (2003)

[10] J. Dvorak, Y. U. Idzerda, S. B. Ogale, Sanjay Shinde, Tao Wu, T. Venkatesan, R. Godfrey, and R. Ramesh, J. Appl. Phys. **97**, 10C102 (2005)

[11] M. Izumi, Y. Ogimoto, Y. Okimoto, T. Manako, P. Ahmet, K. Nakajima, T. Chikyow, M. Kawasaki, and Y. Tokura, Phys. Rev. B **64**, 64429 (2001)

[12] K. Dörr, T. Walter, M. Sahana, K.-H. Muller, K. Nenkov, K. Brand, and L. Schultz, J. Appl. Phys. **89**, 6973 (2001)

[13] M. Bibes, LL. Balcells, S. València, J. Fontcuberta, M. Wojcik, E. Jedryka, and S. Nadolski, Phys. Rev. Lett. **87**, 67210 (2001); A. A. Sidorenko, G. Allodi, R de Renzi, G. Balestrino, and M. Angeloni, Phys. Rev. B **73**, 54406 (2006)

[14] E. Dagotto, T. Hotta and A. Moreo, Phys. Rep. **344**, 1 (2001)

[15] J.-H. Park, E. Vescovo, H.-J. Kim, C. Kwon, R. Ramesh, and T. Venkatesan, Phys. Rev. Lett. **81**, 1953 (1998)

[16] J. J. Kavich, M. P. Warusawithana, J. W. Freeland, P. Ryan, X. Zhai, R. H. Kodama, and J. N. Eckstein, Phys. Rev. B **76**, 014410 (2007)

[17] L. Brey, Phys. Rev. B **75**, 104423 (2007)

[18] M. Jullière, Phys. Lett. **54A**, 225 (1975)

[19] J. C. Slonczewski, Phys. Rev. B **39**, 6995 (1989); J. M. MacLaren, X.-G. Zhang, and W. H. Butler, Phys. Rev. B **56**, 11827 (1997)

[20] J. Z. Sun, W. J. Gallagher, P. R. Ducombe, L. Krusin-Elbaum, R. A. Altman, A. Gupta, Yu Lu, G. Q. Gong, and Gang Xiao, Appl. Phys. Lett. **69**, 3266 (1996)

[21] Moon-Ho Jo, N. D. Mathur, N. K. Todd, and M. G: Blamire, Phys. Rev. B **61**, R14905 (2000)

[22] Yu Lu, X. W. Li, G. Q. Gong, Gang Xiao, A. Gupta, P. Lecoeur, J. Z. Sun, Y. Y. Wang, and V. D. Dravid, Phys. Rev. B **54**, R8357 (1997)

[23] M. Viret, M. Drouet, J. Nassar, J.-P. Contour, C. Fermon, and A. Fert, Europhys. Lett. **39**, 545 (1997)

[24] M. Bibes, K. Bouzehouane, M. Besse, A. Barthélémy, S. Fusil, M. Bowen, P. Seneor, J. P. Contour, and A. Fert, Appl. Phys. Lett. **83** 2629 (2003)

[25] V. Garcia, M. Bibes, A. Barthélémy, M. Bowen, E. Jacquet, J.-P. Contour, and A. Fert, Phys. Rev. B **69**, 052403 (2004)

[26] V. Garcia, M. Bibes, J.-L. Maurice, E. Jacquet, J.-P. Contour, and A. Barthélémy, Appl. Phys. Lett. **87**, 212501 (2005)

[27] Y. Ishii, H. Yamada, H. Sato, H. Akoh, M. Kawasaki, and Y. Tokura, Appl. Phys. Lett. **87**, 22509 (2005)

[28] M. Bowen, M. Bibes, A. Barthélémy, J. P. Contour, A. Anane, Y. Lemaître, and A. Fert, Appl. Phys. Lett. **82,** 233 (2003)

[29] A. Ruotolo, A. Oropallo, F. Miletto Granozio, G. P. Pepe, P. Perna, and U. Scotti di Uccio, Appl. Phys. Lett. **88**, 252504 (2006)

[30] Y. Lu, J. Klein, C. Höfener, B. Wiedenhorst, J. B. Philipp, F. Herbstritt, A. Marx, L. Alff, and R. Gross, Phys. Rev. B **62**, 15806 (2000); H. Yamada, M. Kawasaki, Y. Ogawa, and Y. Tokura, Appl. Phys. Lett. **81**, 4793 (2002); L. M. Wang, and Chih-Chian Gou, Appl. Phys. Lett. **87**, 172503 (2005)

[31] D. Sander, Rep. Prog. Phys. **62**, 809 (1999)

[32] W. D. Nix, Metall. Trans. A **20**, 2217 (1989)

[33] R. O. Bell and G. Rupprecht, Phys. Rev. **129**, 90 (1963)

[34] P.Paufler, B. Bergk, M. Reibold, A. Belger, N. Pätzke, and D. C. Meyer, Solid State Sci. **8**, 782 (2006)

[35] J. Goniakowski, F. Finocchi, and C. Noguera, Rep. Prog. Phys. **71**, 016501 (2007)

2 Experimental techniques

2.1 Growth of thin films and heterostructures

2.1.1 RF sputtering

LCMO films and STO/LCMO bilayers were grown by RF magnetron sputtering at the Institut de Ciència de Materials de Barcelona (ICMAB).

This deposition technique is based in the bombardment of a target with ions from a plasma. A sintered stoichiometric target of $La_{2/3}Ca_{1/3}MnO_3$ (or $SrTiO_3$) chemical composition was used. The expelled particles are generated in a plasma with a typical value of rf power of 15 W and deposited onto the substrate, which is faced to the target few centimeters away (6 cm). The substrate, (001) or (110) STO single crystals (or both simultaneously), were silver-pasted to a Ni plate and heated by a commercial thermocoax heater. Substrate temperature is controlled by a thermocouple connected to Ni plate.

Ar is the gas used for creating the plasma (a picture scheme is shown in Figure 2.1a. For LCMO (or STO) deposition a mixture of Ar and O was used in order to provide oxygen to the growing film. The pressure was set to be 0.44 mbar. Rotatory and turbomolecular (of variable speed) pumps were used to create the vacuum and to fix the growth pressure.

Before each deposition process, targets are pre-sputtered during 20 min to clean their surface and to stabilize the plasma conditions. The heater with the sample holder is situated away from the sputtering gun during this pre-sputtering to prevent deposition in this stage. Plasma ionization occurs by the application of RF radiation of frequency

13.56 MHz. After a transient time, under a negative voltage applied to the target respect to the substrate, Ar^+ ions are accelerated against the target. To enhance the sputtering rate by increasing the Ar gas ionization, ring-like magnets (magnetrons) generate a magnetic field between the center and the edge of the target.

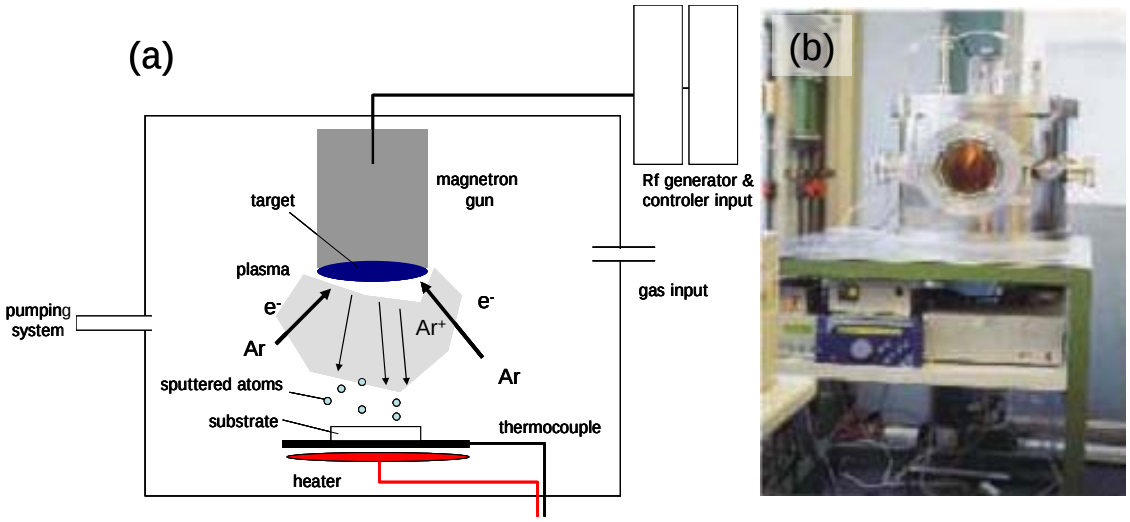

Figure 2.1. (a) Picture scheme of the sputtering set-up and process. (b) Photography of the actual rf magnetron sputtering deposition set-up.

Additional details about the experimental deposition set-up can be found in the thesis of M. Bibes [1]. Actual image of the sputtering set-up can be seen in Figure 2.1b.

The deposition process is fully automated, and the computer control allows the setting, modification, monitorization, and recording of the processing parameters. A base pressure in the range of 10^{-7} mbar is set in the chamber. Fluxmeters of Ar and O allow the control of gas flow, and one electro-valve permits a massive entry of oxygen during the *in-situ* annealing of the samples. Substrates are heated up to the deposition temperature, 750-800ºC, although most samples were deposited at 800ºC. Combining the speed of the turbomolecular pump and Ar and O flux rates, the pressure at film deposition was set to 0.44 mbar with an incoming proportion of 80 % Ar and 20 % O. The deposition time for each deposition is set from previous calibrated growth rate (through thickness measurement by X-ray reflectometry measurements) in order to obtain the desired film thickness. In most cases, after film deposition, the samples are *in-situ* annealed under a 466 mbar oxygen pressure during 60 min at 800ºC to ensure the stoichiometric oxygen contents.

2.1.2 Pulsed laser deposition (PLD)

$La_{2/3}Sr_{1/3}MnO_3$ films were grown by pulsed laser deposition (PLD) using the equipment of the group of Prof. M. Varela at the Dept. Física Aplicada i Òptica of the Universitat de Barcelona. The PLD system uses a KrF excimer laser that emits light pulses of 34 ns duration at the wavelength of $\lambda = 248$ nm. The optical alignments of the beam is performed using a HeNe laser ($\lambda = 632.8$ nm), mounted in the rear of the excimer laser. The laser pulse frequency can be varied up to 50 Hz, being the range of typical frequencies 1 to 10 Hz. The laser beam is directed onto the target inside the deposition chamber at a 45 deg angle. A scheme of the PLD system is shown in Figure 2.2.

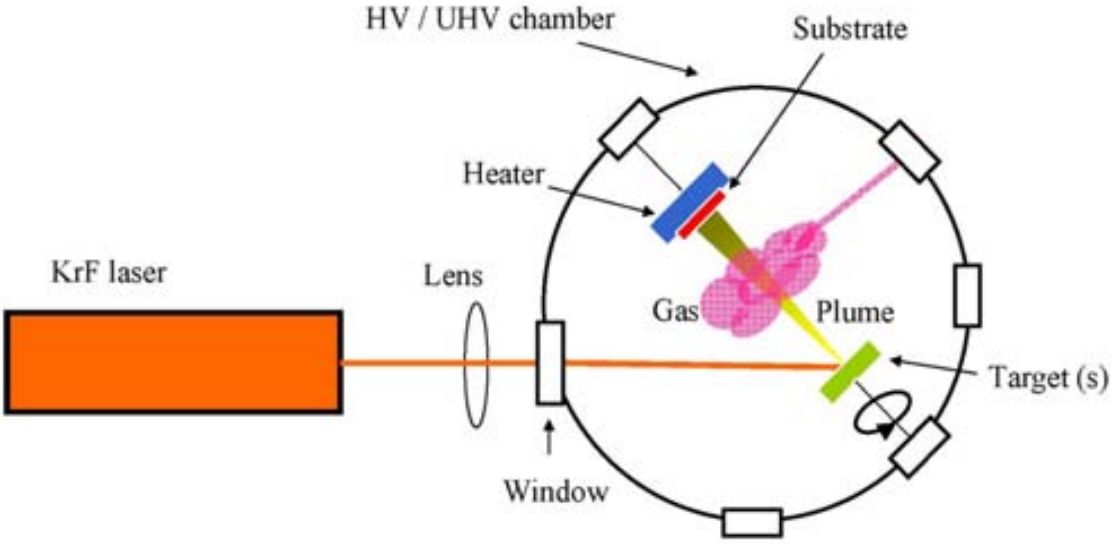

Figure 2.2. Schematic top view of the PLD system at the Dept. Física Aplicada i Òptica of the Universitat de Barcelona.

The PLD technique is based on the interaction between laser and matter, which results in the formation of a plasma made of the atomic species from the target. First, the laser pulse enters the vacuum chamber through a window and impinges the target, which is mounted into a holder that can be rotated by a motor to allow the laser erosion of the target to be uniform. The target holder allows placing up to four targets. The energy fluence of the pulse depends on the pulse energy and the position of the optical lens, being typically in the 2-4 J/m^2 range. The laser pulse irradiates a small area of the target (a few mm^2), during the time length of the pulse (34 ns). This time is much shorter than the time between pulses (0.1-1 s). Optical absorption of most of materials is very high at a wavelength of 248 nm, and thus the energy is absorbed in the very top

layer of the target. Moreover, since the pulse length is very short, the thermal diffusion length is also low. Although the ablation mechanisms can be very complex and they depend on the material, the most important issue is that all the laser energy is confined in a very small volume during a very short time. It produces a very high pressure plasma with the same composition that the ablated volume. The plasma expands fast from an initial volume much shorter in the normal direction, and in consequence the velocity of expansion is much higher in this direction. Since the plasma is very directional, the substrate is placed exactly perpendicularly to the target, at only few centimetres (typically ~5 cm) from the target. The substrate is heated to a temperature between 650 and 750ºC, and a flow of O_2 gas is introduced during the deposition, varied to obtain a chamber pressure of 0.1 and 0.4 mbar, in order to avoid loss of oxygen in the film. After the deposition, the oxygen pressure is increased progressively during the cooling down, and at 530 ºC a pressure of 1.013 bar of oxygen is introduced. At some fixed deposition conditions, film thickness is controlled by the number of laser pulses and an accurate measurement of film thickness is afterwards obtained by X-ray reflectometry.

2.2 Surface characterization

2.2.1 Atomic Force Microscopy (AFM)

The topographic AFM images were obtained by a PicoSPM® (Molecular Imaging) microscope at the ICMAB working in dynamic mode by M.-J. Polo and Dr. A. Pérez del Pino.

AFM is one of the scanning probe microscopes which operates by measuring interaction forces between a tip and the sample surface. In dynamic mode, the tip alternatively contacts the surface, following the resonant frequency of the tip located the end of a cantilever. As raster-scan drags the tip over the sample, using a laser source and photoelectrons, it is measured the vertical deflection of the cantilever, which indicates the local sample height. During tapping mode operation, the cantilever oscillation amplitude is maintained constant by a feedback loop.

Images were analyzed using the software packages WSxM 3.0 Develop 9.3, from Nanotec Electronica S.L. [2] and also Mountains® Technology v4.1 from Digital Surf [3].

2.2.2 Conducting-AFM

Conducting AFM (C-AFM) uses the same device as ordinary AFM but using conducting tips. C-AFM operates in contact mode and it records at each point the electrical current (or resistance) through the sample when a voltage is applied between it and the tip. The surface morphology is simultaneously recorded.

C-AFM measurements were carried out in a modified Digital Instruments Nanoscope III Multimode AFM [4] (Figure 2.3) at the CNRS-Thales (Palaiseau, Paris). The modifications allowed obtaining resistance maps in the wide range of 100 to 10^{12} Ω under a bias voltage ranging from 0.1 to 10 V, which was applied to the tip, and grounding the sample. The accuracy of the measurement is of around 5 %

The conducting tips were Si_3N_4 ones, with spring constant of 40 N/m coated by Boron-doped polycrystalline diamond. The macroscopic tip radius is about 100 nm, but roughness in the coating due to diamond crystallites induce a nanoroughness which leads to a local radius of less than 10 nm.

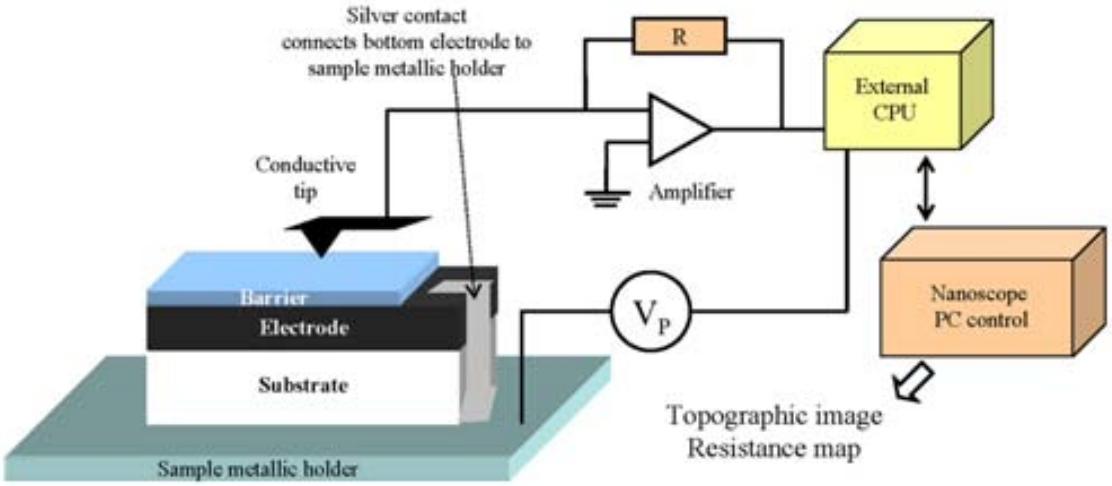

Figure 2.3. Schematic diagram showing the Conducting-AFM set-up (CNRS-Thales).

2.2.3 X-Photoelectron Spectroscopy (XPS)

XPS technique (also known as electron spectroscopy for chemical analysis ESCA) is based in the photoelectric effect: the surface of a material is irradiated by a X-ray beam and the system collects the escaping electrons. It is measured both the amount of electrons as their kinetic energy (KE), and thus not only the chemical elements on a surface are detected, but also the amount of each one.

The physical process for the photoelectron emission energy analysis takes into account that for a given photon energy (E_ν), it has been inverted in extracting an electron from its binding site (binding energy: BE), in sending it to the vacuum (work function: Φ) and finally in keeping the electron in movement (kinetic energy: KE).

$$BE = E_\nu - KE - \Phi \qquad [2.1]$$

Eq. 2.1 summarizes the process previously explained. E_ν is fixed by the radiation source, KE is the measured magnitude and Φ is a known referenced value for the given material. The collected electrons will provide information about the characteristic BE that accomplish the energy expression:

$$BE < E_\nu - \Phi \qquad [2.2]$$

The BE represents the strength of the interaction of the electrons at different atomic (core) levels with the nuclear charge. In Figure 2.4a it is shown an scheme of the XPS measurement within other techniques, and in Figure 2.4b a simple view of the electron energy configuration and the possible effects caused by X-ray photon incidence.

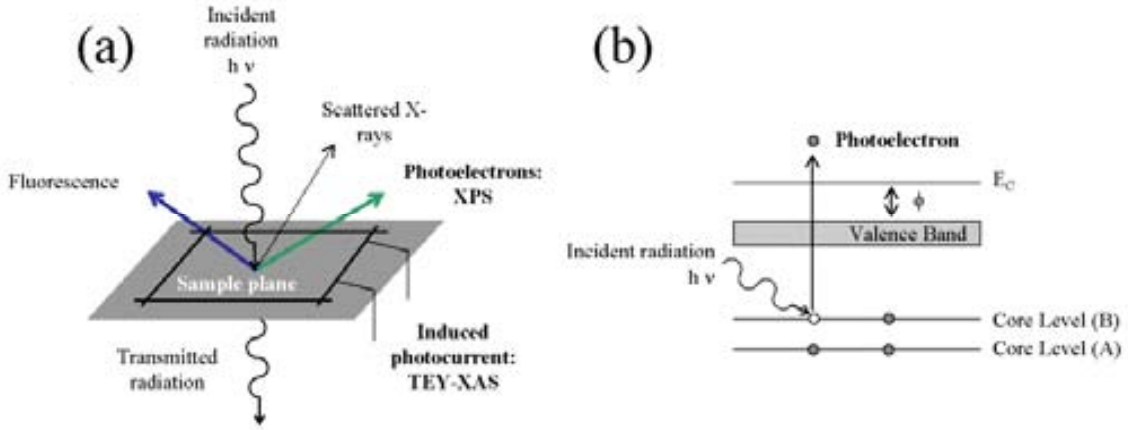

Figure 2.4. (a) Scheme of processes after irradiation of a sample by an X-ray beam of energy hν. (b) Energy diagram of a photoelectronic emission process involving the energy of the incident photons (hν), the core levels of the atom and the valence and conduction (E_C) bands. The work-function ϕ of the atom is also indicated.

The dependency of the BE on the atomic number *n* and on the orbital and spin moment is characteristic of a given atom and thus it provides information about the composition of the inspected surface as well as on the electronic state. In an ideal approximation, the BE of a photoemitted electron which leaves an atom of *N* electrons is equal to difference between the atomic final state (with (*N*-1) electrons) and the initial state (with *N* electrons), following Koopmans' approximation. Nevertheless, the

experimental BE value differs from this approximation and different effects should be taken into account when interpreting the XPS spectra. We comment here some of the effects to consider:

1. Surface charging: good insulators cannot dissipate the positive charge generated by the created holes, and an excess of positive charge in the material is translated into an energy shift towards higher in the evaluated BE. This effect can be prevented using appropriate metallic contacts on the insulator to dissipate the charge or using an electron beam (neutralizer).

2. Initial and final states: the orbital and spin moments (also *n* atomic number) of the initial and final states determines the appearance of single peaks, doublets, triplets, etc. corresponding to the interaction allowed transitions. For instance, in Figure 2.5 some XPS spectra from Mn, Co and Bi compounds are shown.

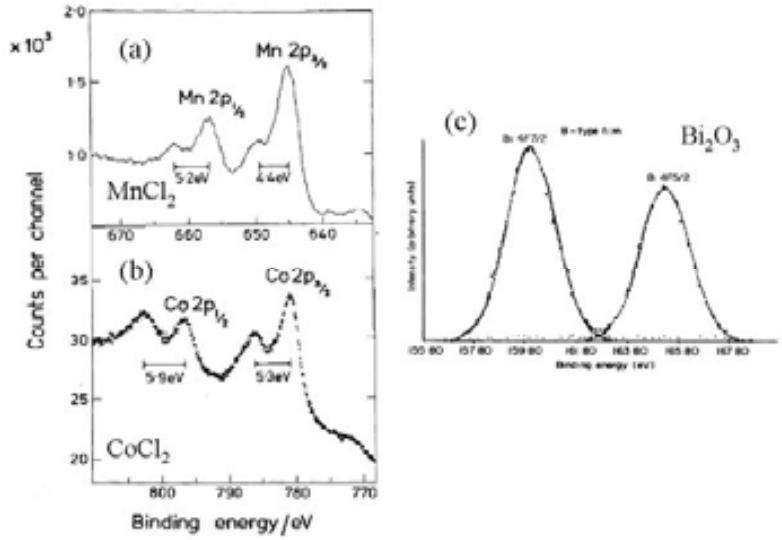

Figure 2.5. Experimental X-ray photoemission spectra obtained for $MnCl_2$ (a) and $CoCl_2$ (b) compounds extracted from Ref. [5], and for Bi_2O_3 compound (c), after Ref. [6]

Inspecting the examples of Figure 2.5, the Mn and Co [(a) and (b)] 2p core levels are characterized by two possible spin states: high spin 3/2 and low spin 1/2, as indicated in the figures, separated by the spin-orbit splitting energy (~ 15-20 eV, depending of the atom). For the case of Bi (c), inspection of the 4f core level indicates the presence of the spin-orbit splitting into 7/2 and 5/2 spin states with an energy separation of ~ 6 eV. On the other hand, the spectra can give information of the valence of these atoms. In Mn2p and Co2p spectra [(a) and (b)], the low intensity peaks appearing at higher BE are a signature of multiple final states which happens in Mn^{2+} [$3d^5$] and Co^{2+} [$3d^7$] ions. The multiplicity of states is caused by the existence of 3d

shells with 5 or more electrons, which allow the occurrence of final states with excited ions and thus the measured BE can be different from that of the ground state. However, in the case of Bi (c), only two peaks from the two final spin states are observed due to the fact that Bi^{3+} [$4f^{14}5d^{10}6s^2$] ions present close shells and recombination into different final states as in the Mn^{2+} and Co^{2+} case is not possible.

X-ray photoelectron emission spectra were recorded with two different equipments at room temperature. An ESCALAB 210 spectrometer fitted with a hemispherical energy analyzer working at a constant pass-energy of 30 eV is the system situated at the Instituto de Ciencia de Materiales de Sevilla. The experiments were performed and analyzed by Dr. J. P. Espinós and they were focused on the chemical compositional analysis of single LCMO film surfaces. The base pressure of the analysis chamber was about 10^{-10} mbar. Unmonochromatized AlKα radiation (1486.6 eV) was used as excitation source. Survey spectra and the following core levels were recorded: La $3d_{5/2}$, Ca 2p, Mn 2p, O 1s and C1s. Binding energy calibration of the spectra was done by referencing the recorded peaks to the $Au4f_{7/2}$ core level of a very thin layer (0.1 monolayers) of gold deposited onto the samples. Intensity ratios for the different photoelectron emission signals have been calculated by estimating the area of the elastic photoelectron emission peaks and by referring the obtained values to their relative sensitivity factors [7]. Sputtering with Ar^+ ions (2 keV, 60º grazing incidence, 3.5 minutes) onto the sample was used to remove surface contamination.

The second equipment is a PHI 5500 Multitechnique System (Physical Electronics) located at the Serveis Cientificotècnics of the Universitat de Barcelona. It has been used for the study of STO capped LCMO electrodes, that is, in STO/LCMO bilayers. The system has a monochromatic X-ray source (Al-K_α) placed perpendicular to the hemispherical analyzer axis. The analyzer pass energy was 23.5 eV and the base pressure of the analysis chamber was 7 10^{-9} mbar. Survey spectra and the following core levels were recorded: La 3d, Ca 2p, Mn 2p, Mn 3s, Ar 2p and C 1s at 45 deg grazing incidence. Binding energy calibration was done by referencing the recorded peaks to the $La3d_{5/2}$ at 834.9 eV. Ar^+ ion etching at 4 keV (6 seconds) was used to remove surface contamination on bilayers. Multipak v6.0 (Physical Electronics) package was used for the spectrum fitting.

For both equipments, working at a constant pass-energy for the analyzer of 30 eV (ESCALAB) and 23.5 eV (Multitechnique System), the detectors are set to fixed energy resolutions that depending on the characteristics of the samples can be of

≤ 0.5 eV. The pass-energy influences in the energy resolution, with higher resolution for lower pass-energy, although it has to be taken into account that the amount collected photoelectrons diminishes as the pass-energy decreases.

2.2.4 X-ray Absorption Spectroscopy (XAS)

XAS is based on the interaction of the oscillating electromagnetic field of X-ray radiation with the electrons bound in an atom. Either the radiation will be scattered by these electrons or absorbed and excite the electrons, depending on the energy of the radiation and of the available core levels. From all the possible measurements resulting of X-ray interaction presented in Figure 2.4a, XAS allows obtaining information about the fine structure of the ions of a solid by indirectly measuring the effect of the absorbed radiation on the atoms. For the XAS experiments, different working modes are possible, as the fluorescence mode, where the fluorescent photons are inspected, and the total electron yield mode (TEY), where the sample is connected to the ground and the induced photoelectron current on the sample surface is monitored. In a synchrotron facility, and using a series of lenses and monochromator, highly monochromatic X-ray beam provides a range of photon energies from 100 eV to 100 keV.

In XAS experiments, and working near the absorption energy edge of a given core level of an atom of the sample, a slight variation of the photon energy will cause a high increase in the absorption of the X-ray beam. At this edge, the interaction of a photon and an electron in a core level gives rise to an excited electron that consequently abandons its core state. The excited electron is then so-called photoelectron, and it finally evolves to a state in the continuum, that is, to an unoccupied state above the Fermi level. In this single particle view, the transition probability σ of a given electron in an initial core state $|\psi_i>$ to relax into a final state $|\psi_f>$ is given by the Golden Rule:

$$\sigma = \sum \left| \left\langle \Psi_f \left| \mathbf{Ap} \right| \Psi_i \right\rangle \right|^2 \delta\left(h\nu + E_i - E_f\right) \qquad [2.3]$$

where **A** and **p** are the electromagnetic vector potential and the momentum operator acting on the electron, respectively, and E_i the initial state energy and E_f corresponds to the final state energy, which can run over all the available states. The angular part (orbital momentum **l**) of the created matrix elements gives rise to the dipole selection rule, which allows only transitions where $\Delta l = \pm 1$. Therefore, the final state of the photoelectron is determined by both the available states $|\psi_f>$ and the dipole selection rule applied to the $|\psi_i>$ and $|\psi_f>$ states.

The X-ray absorption spectroscopy (XAS) experiments were performed and analyzed by Dr. M. Abbate at the SGM beam line in the LNLS (located at Campinhas, Brazil). The base pressure in the experimental chamber was in the low 10^{-9} mbar range. The mean-probing-depth of the total-electron-yield (TEY) method is about 20–50 Å [8]. The energy resolution of the spherical grating monochromator was approximately 0.5–0.6 eV. For the measurement carried out in LCMO films, the energy scale was calibrated using the peak positions in the parent $LaMnO_3$ compound. The spectra were normalized to the maximum after a constant background subtraction.

2.3 Structural characterization

2.3.1 X-ray Reflectometry (XRR)

XRR measurements on LCMO and STO thin films were carried out in the Rigaku Rotaflex RU-200B diffractometer, located at the ICMAB.

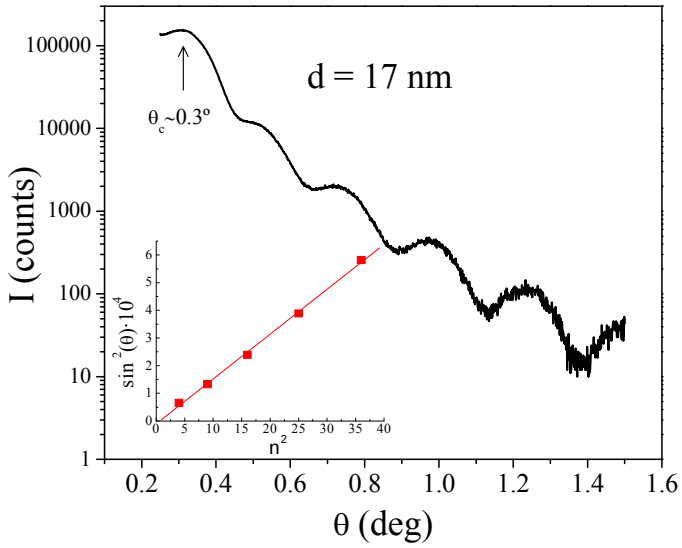

Figure 2.6. XRR spectrum of a thin LCMO film showing the oscillations of the interference pattern. In the inset, minimum positions was linearly fitted to minima order to calculate film thickness following eq. 2.4.

With this technique, it is possible to calculate from an acquired X-ray spectrum (Figure 2.6) the thickness of a thin film. XRR method involves monitoring the intensity of the x-ray beam reflected by a sample at grazing angles. Monochromatic X-ray beam irradiates a sample at a low angle $\omega = \theta$ and the reflected intensity at an angle 2θ is recorded. Thus, operating mode on the diffractometer is coupled ω-2θ mode. Working

on thin films, XRR takes advantage of two relevant physical principles: the dependency of surface reflection on the different electron densities of the materials and the optical interference between the incident beam at the top and at the bottom of the thin film. The first effect determines the minimum angle at which radiation X-rays can be reflected (the so-called critical angle θ_c), while the second is observed from the oscillation caused by the difference light path of reflected top and bottom beams. The collected data is affected by another effect, as it is the surface and interface roughness. The scattering on rough surfaces causes a loss of the collected X-ray radiation within an exponential rate.

The general expression to describe measured XRR spectra is:

$$\sin^2(\theta_n) = \sin^2(\theta_C) + n^2\left(\frac{\lambda}{2d}\right)^2 \qquad [2.4]$$

where θ_n is the angle at which the interference of order *n* appears, λ is the X-ray emission energy and *d* accounts for the film thickness. In this interference profile, distinguishable minima and maxima develop and they can be used as reference values for a numerical evaluation of the thickness *d* of the film. Extracting the minima (or maxima) from the experimental XRR spectrum, which can be referred as θ_n values, and computing the corresponding $\sin^2(\theta_n)$, from eq. 2.4 a linear dependence between $\sin^2(\theta_n)$ and the order n of the interference is expected. As an example, in Figure 2.6 the XRR spectrum of a 17 nm sample show the interference pattern and in the inset a plot for the minima of the $\sin^2(\theta_n)$ *vs* n values present the expected linear dependence. The linear fit of these values will provide information about the critical angle (θ_c) from the ordinate [$\sin^2(\theta_c)$] and about the film thickness *d* from the slope [$(\lambda/2d)^2$].

2.3.2 X-ray Diffraction (XRD)

X-ray diffraction measurements were performed using four different diffractomers: on a four-circle MRD Philips diffractometer located at the Serveis Científico-Tècnics of the Universitat de Barcelona; on another four-circle one, a Bruker D8-General Area Detector Diffraction System (GADDS); on two different two circle diffractometers: Rigaku Rotaflex RU-200B and Siemens D-5000 located at the ICMAB. These diffractometers work with Cu X-ray sources, with an emission spectrum characterized by two main lines: $k_{\alpha 1}$ = 1.5406 Å and $k_{\alpha 2}$ = 1.5444 Å, with relative intensity 2:1. Appropriate Ni-filters are used to eliminate the lower length emission lines (k_β).

For X-ray measurements, depending on the kind of diffractometer, one can vary different angles of the sample and so one can get different information. A schematical view and the nomenclature of the angles can be seen in Figure 2.7a, corresponding to:

ω Angle between the direction of the incoming beam and sample plane. It can be modified by a rotation of the goniometer around an axis normal to the plane of incidence.

2θ Angle between the incoming light direction and the inspected diffraction direction. It is modified by the displacement of the detector.

φ Angle defining the rotation around an axis normal to the sample plane.

χ Angle of the tilt obtained by rotating around a horizontal axis within the goniometer plane and contained within the plane of incidence.

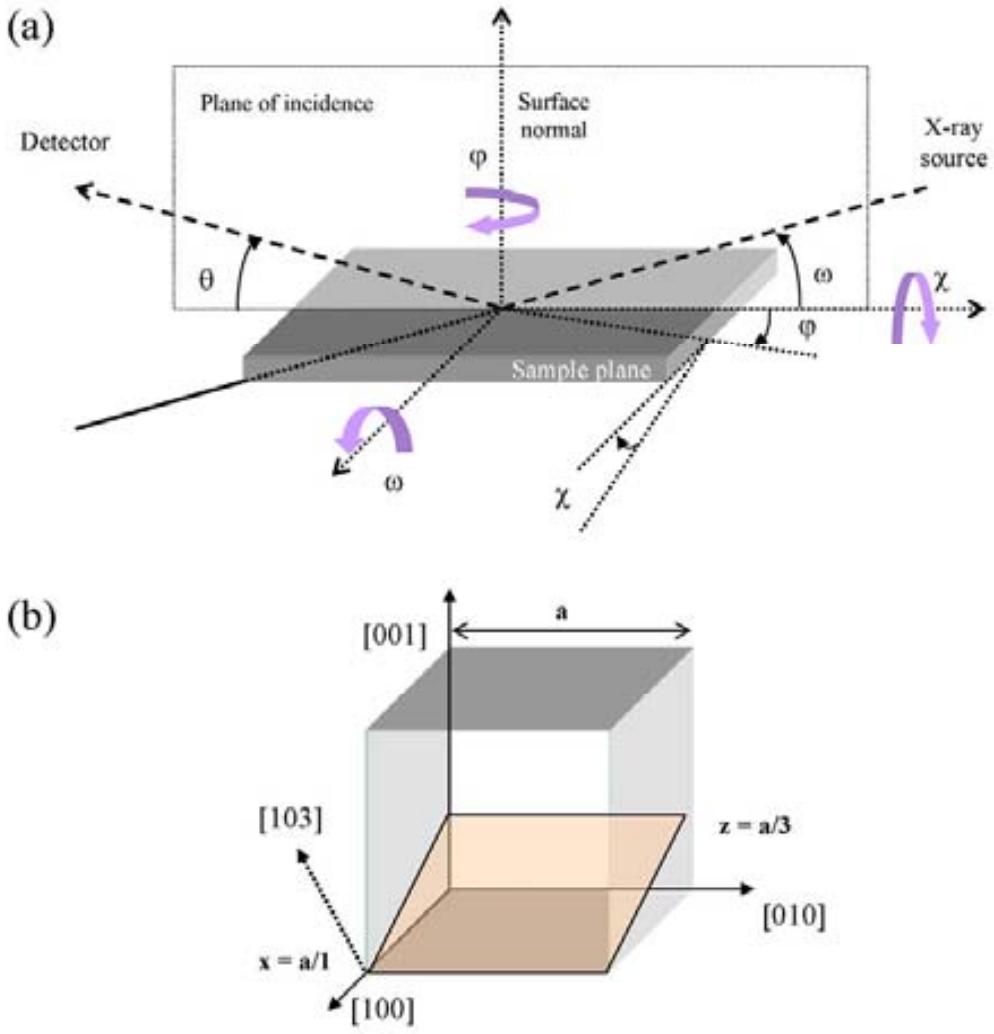

Figure 2.7. (a) Schematic view of the different angles and their relationship to sample surface for XRD measurements. (b) Sketch of an ideal cubic unit cell of parameter *a* indicating the position of the [103] plane and its relationship to the crystal axes.

We can use two possible diffraction conditions depending on the coupling of the angular setting. If $\omega = \theta$ and $\chi = 0$, we work in a symmetric configuration, that is, the inspected reflections are symmetric with respect the surface normal. The diffraction planes that can be explored are parallel to the film surface and for a given (*hkl*) plane, the diffraction condition or Bragg law is directly applicable:

$$2d_{hkl}\sin\theta = \lambda \qquad [2.5]$$

where d_{hkl} are the (hkl) interplanar distance and λ is the wavelength of the incoming radiation.

On the other hand, asymmetric reflections are defined as those obtained when the explored planes are not parallel to the surface, and thus other angular configurations are necessary. Two typical methods are used:

1. Decoupling ω angle from θ angle, and thus the diffracting planes are not parallel to the film surface, but still the diffraction vector is in the diffraction plane.

2 Tilting the sample through a rotation of the φ and χ and keeping $\omega = \theta$.

Asymmetric reflections provide information about all the unit cell parameters, as from the in-plane components of the explored planes we can investigate the in-plane unit cell parameter. A general description of the used X-ray techniques will be done here, and much detail will be presented when analyzing experimental results:

θ-2θ scans: Detector (2θ) and the rotation of the goniometer (ω) are coupled, that is, for symmetric reflections it is accomplished $\omega = \theta$. Film texture and out-of-plane lattice parameters can be evaluated from these scans. They have been performed mainly in the Rigaku and Siemens system.

ω-scans: Keeping the detector fixed, it is changed ω in order to evaluate the misorientation of the out-of-plane axis around a symmetric reflection.

φ-scans (pole figures): Performed for asymmetric reflections, the rotation of φ at fixed ω and θ angles allow the observation of substrate and film reflections containing in-plane components. Combining the φ-scans at different values of χ allows obtaining two dimensional maps including the explored reflections and their symmetry (pole figures). Therefore, the in-plane film texture can be deduced. Bruker setup was used for the φ-scans and pole figures.

Reciprocal space maps (RSMs): Performing a series of ω-2θ scans at fixed φ and χ around particular asymmetric reflections, we can get through a complete area of

the reciprocal space. Thus, it is possible to obtain a map of the reciprocal space. The measurements were carried out in the MRD Philips and also in the Bruker setup.

The methodology of a RSM is based on breaking with the coupling of ω and θ and fixing new angular conditions, in concrete the expected relationship between ω and θ values will provide the χ-value of the explored planes:

$$\chi = \theta - \omega \qquad [2.5]$$

being $\chi \neq 0$ as it is an asymmetric reflection. Then, from the value of χ, ω is calculated through eq. 2.5 in order to experimentally work at $\chi = 0$ and decouple ω from 2θ.

Given a pseudocubic lattice with real space vectors **u**, **v**, and **w**, the reciprocal space lattice vectors **u***, **v***and **w***are related to the real ones by:

$$\mathbf{u}^* \,//\, \mathbf{u} \quad ; \quad \mathbf{v}^* \,//\, \mathbf{v} \quad ; \quad \mathbf{w}^* \,//= \mathbf{w} \qquad [2.6]$$

$$\left\|\mathbf{u}^*\right\| = \left\|\frac{1}{\mathbf{u}}\right\| \quad ; \quad \left\|\mathbf{v}^*\right\| = \left\|\frac{1}{\mathbf{v}}\right\| \quad ; \quad \left\|\mathbf{w}^*\right\| = \left\|\frac{1}{\mathbf{w}}\right\| \qquad [2.7]$$

Depending on the experimental condition, we can easily evaluate the **u***, **v***and **w*** from the given ω, 2θ, φ and χ angles. Finding with eq. 2.5 the value of χ for given pair of ω and θ, we can change the value of ω in order to work $\chi = 0$ and that eq. 2.5 still remains true. At these conditions, we can obtain a two-dimensional map of the reciprocal soace, built using the wave vectors $q_{//}$ and $q_{\perp}$ which correspond to:

$$q_{//} = \frac{2}{\lambda}\sin(\theta)\sin(\theta - \omega) \qquad [2.8]$$

$$q_{\perp} = \frac{2}{\lambda}\sin(\theta)\cos(\theta - \omega) \qquad [2.9]$$

where λ is the wavelength of the incident X-ray beam and $q_{//}$ and $q_{\perp}$ are the equivalent reciprocal space distances on the equivalent real space distances. The wave vectors $q_{//}$ and $q_{\perp}$ are measured respective to the sample surface, and to obtain the unit cell parameters it is necessary to know the relationship of the reciprocal and real space lattices. As an example, in Figure 2.7b it is shown the [103] plane in a cubic unit cell of parameter *a* in a (001)-oriented crystal. In the real space, this plane is determined by its intersection with the crystal axes [100], [010] and [001] indicated from its Miller indices [*hkl*]. The intersections are at x = a/h = a/1 and z = a/l = a/3 as seen in Figure 2.7b. Then, studying this [103] reflection in the reciprocal space, from the angular position of the peak we obtain the wave vectors $q_{//}$ and $q_{\perp}$ which correspond to the [100]

and [001] direction (q_{100} and q_{001}, respectively). From this ideal case, the experimental parameters are thus calculated using the Miller indices of the peak: $a_{exp} = h/q_{100} = 1/q_{100}$ and $c_{exp} = l/q_{001} = 1/q_{001}$, where a_{exp} and c_{exp} denote the in-plane and out-of-plane experimental parameters of the crystal.

Absolute values of unit cell parameters for films with any orientation can be extracted from the position of the peaks. More information on these calculations will be provided within the experimental results.

2.3.3 Transmission Electron Microscopy (TEM)

Electron microscope allows, as in the case of their optical counterparts, obtaining images of the explored material but at a nanometric scale. The physical concept uses the wave-like character of electrons. Electrons are generated by thermoionic discharge in a cathode, or by field emission; and afterwards they are accelerated by an electric field, typically in the 100-300 kV range, achieving equivalent electronic wavelengths of $\lambda \sim 10^{-12}$ m. Using different operating modes in these microscopes is possible to get into the crystal structure of the studied materials. In Figure 2.8, schemes on two operating modes are presented. The diffraction mode (Figure 2.8a) allows observing the diffraction pattern of the studied material, and thus information about the unit-cell can be deduced. In imaging mode (Figure 2.8b), a preliminary image of the sample is formed in the back image plane of the objective lens. Through further magnification and using intermediated and projector lenses, the final imgae is formed in the screen. To introduce contrast in the image, an aperture is placed in the back focal plane of the objective lens. Depending on the orientation of the sample and the diameter of the aperture, we can work in different operation modes as high resolution, two-beam bright field or dark field imaging, among others. To switch from image mode to diffraction mode, the strength of the intermediate lens is changed in order to focus the back focal plane of the objective lens instead of the back image plane of the objective lens.

In STEM mode the electron beam is focused on the surface to form a sub-nanometer incident probe and the resulting images are produced by the scanning of the probe on the studied region.

The HRTEM experiments were performed and analyzed by S. Estradé, Dr. J. Arbiol and Dr. F. Peiró. TEM samples were prepared in cross section (XT) geometry both by conventional method, in which the thin foil specimens were mechanically

polished down to ~ 30 μm and then were further thinned by ion milling at 5 kV and 7 deg down to achieve electro-transparency, and by focused ion beam (FIB).

The used microscopes were a Jeol J2010F FEG (Serveis Científico-Tècnics of the Universitat de Barcelona) operating at an electron accelerating voltage of 200 kV and a VG 501 cold FEG dedicated STEM (LPS Orsay, France) operating at 100 kV.

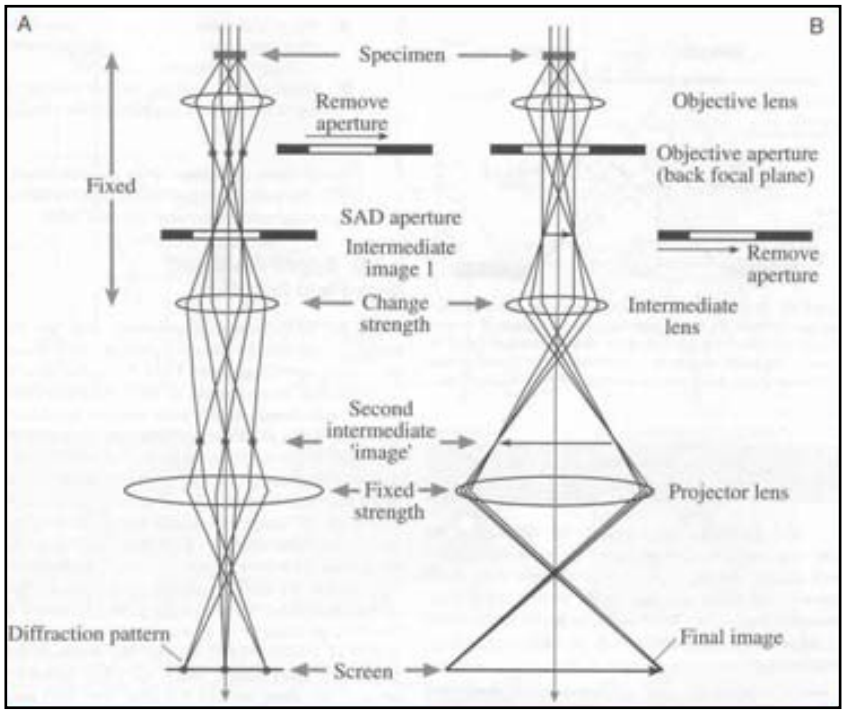

Figure 2.8. Schematic views of TEM operating modes: (a) diffraction mode (b) imaging mode.

2.3.4 Electron energy loss spectroscopy (EELS)

EELS measurements were carried out and analyzed by S. Estradé, Dr. J. Arbiol and Dr. F. Peiró using the Jeol 2010F (S)TEM with a Gatan GIF detector, which energy resolution is about 0.8 eV, and also the VG 501 dedicated STEM of the LPS at Orsay, France, working at 100 kV with a final spot size of 0.5 nm and an energy resolution of 0.3 eV

TEM specimens prepared in XT geometry were subjected to chemical analysis by focusing the e-beam spot into different regions of the sample and analyzing the transmitted electrons. In short, the physical principle of the EELS technique is based on the inelastic scattering of the incident electrons by the electrons in the sample. In this process, the incident electron loses a given amount of energy, which can be characteristic of an atomic transition, or some solid-state effect. In a typical EELS spectrum, the main contribution to the collected electrons is due to those that have not

undergone any inelastic scattering, forming the so-called Zero Loss Peak. Information about the sample properties is obtained from the collected scattered electrons and the final analysis using an electron spectrometer allows interpreting the nature of the atoms found in the sample and their ionization state.

2.3.5 ^{55}Mn Nuclear Magnetic Resonance (NMR)

NMR spectra were acquired and analyzed by Dr. M. Wojcik at the Institute of Physics, Polish Academy of Sciences, Warszawa, Poland.

The physical principle used in this technique explodes the intrinsic magnetic moment of a given nucleus [9]. Arising from the magnetic moment of the protons and neutrons of the nucleus, the nuclear magnetic moment is measured in nuclear magnetons M_N:

$$M_N = \frac{\mu_0 e\hbar}{2m_p} \qquad [2.10]$$

From the spin angular momentum *I*, measured in units of $\hbar$, the gyromagnetic constant *g* appears naturally as the ratio of the nuclear magnetic moment of the nucleus *M* and the spin angular momentum *I*, as:

$$g = \frac{M / M_N}{I / \hbar} \qquad [2.11]$$

Upon the application of an external magnetic field ($\mathbf{H_0}$), the nuclear moment *M* aligns towards the direction of $\mathbf{H_0}$ appearing a Zeeman splitting of the nuclear levels given by:

$$\Delta E = gM_N I_z H_0 \qquad [2.12]$$

where I_z is the component of *I* along the $\mathbf{H_0}$ direction (z-axis). This gap separates into two populations, parallel and anti-parallel nuclear moment relative to $\mathbf{H_0}$, the energy levels on the explored nuclei. Exploding this intrinsic property of the nuclei, in this technique a static and an alternating magnetic field (in the rf range) are combined to control the alignment of the nuclear spins. The spin-echo NMR experiment is based in the application of a series of rf pulses perpendicular to the static field $\mathbf{H_0}$. This rf field can cause the resonance of nuclear spins, which absorb energy and rotate in a plane perpendicular to $\mathbf{H_0}$ but that finally precess along $\mathbf{H_0}$ axis. In ferromagnetic materials, due to the large internal field caused by the magnetization, it exists a coupling of the electronic and nuclear spins through the hyperfine interactions. The strength of this hyperfine field H_{hf} depends on the electronic spin *S* and on the hyperfine tensor (A). the

NMR signal is thus sensitive to the bare electronic spin *S* and also to the mobility of the electronic charge around the nuclei, providing information of the magnetic and electronic state of the atoms.

NMR signals without the application of the static field $\mathbf{H_0}$ can be obtained in ferromagnetic materials. Working at $H_0 = 0$, the resonant frequency ω depends only on the internal magnetic field *H* and on the nuclear magnetic moment through:

$$\omega = g\frac{M_N}{\hbar}H \qquad [2.13]$$

The spin echo NMR signals were collected by means of a broadband phase-sensitive spin-echo spectrometer. The experiments were performed at 4.2 K, in zero external magnetic field and several values of the excitation rf field in order to optimize the signal intensity at each frequency. The ^{55}Mn NMR spectra of single LCMO films and STO/LCMO bilayers were obtained in the frequency range of 300-450 MHz by plotting every 1 MHz, with optimized spin echo signal intensity being corrected with frequency dependent enhancement factor η and ω^2 dependent sensitivity, as described in detail in Ref. [10].

2.4 Functional characterization

2.4.1 SQUID magnetometry

Magnetometry measurements were carried out on a Superconducting Quantum Interference Device (SQUID) of Quantum design (MMPS system) located at the ICMAB).

Measurements were carried out with magnetic field applied in-plane or out-of-plane. In all cases, samples were introduced at low temperature from the disordered paramagnetic state. Magnetic hysteresis loops were measured applying starting with high positive field (typically 30-50 kOe) and lowering the intensity in wide steps (5 kOe) towards low positive field. Between 1 kOe and -1 kOe the field step is decreased and the measurement is recorded in no overshoot mode to not overcome the target field during the measurement and stabilizes the field. The intensity of the negative field is then increased in a similar way as in the high field regime on the positive part of the loop. After saturating the sample at high negative field, the procedure undertaken is similar to that explained from the high positive fields. After the magnetic hysteresis loop is performed and high positive field is stable (30-50 kOe), a static 5 kOe magnetic

field, high enough to obtain magnetic signal for the small and thin used samples, was set for the magnetization dependence on temperature. For LCMO samples, temperature scans of 10 K to 300 K were performed, at a warming rate of 2 K/min.

The contribution of diamagnetic STO substrate was subtracted by experimentally measuring in the hysteresis loops the high field slope. From sample size and thickness, absolute value of magnetization was calculated.

2.4.2 Ferromagnetic resonance (FMR)

FMR spectra were acquired and analyzed by A. Brandlmaier and Dr. S. T. B. Goennenwein at the Walther-Meißner-Institut (Bayerische Akademie der Wissenschaften) at Garching (Germany).

FMR technique basically exploits the magnetic moment of the electrons in atoms of a sample. Like in NMR measurements, the existing magnetic moment precesses around the direction of a static magnetic field, and upon the application of an alternating (rf) field perpendicular to the static one the material absorbs energy when the frequency of the rf field is equal to that of the precession.

In Figure 2.9a the experimental FMR setup is shown. The ferromagnetic sample is placed under a strong magnetic field, and the rf transverse field is generated by a microwave source. The use of a resonant cavity enhances the signal to noise ratio of the FMR measurement. First, the effect of the static magnetic field (H_0) is to align the spin vectors (**S**) into a single orientation along the direction of H_0, changing the energy levels of the electrons due to the Zeeman splitting into:

$$\Delta E = g\mu_B S_z H_0 \qquad [2.14]$$

where g is the gyromagnetic constant, μ_B is the Bohr magneton and S_z is the component of the total spin vector **S** along the direction of $\mathbf{H_0}$. The strength of the static magnetic field is changed gradually modifying the energy levels of the electronic states. Meanwhile, the sample also is subjected to the rf field from the microwave radiation. When the energy difference between two excited states is equal to the energy of the incident microwave photons, the microwave radiation will be resonantly absorbed by the ferromagnetic material.

In a macroscopic view, the FMR resonance happens when the precession frequency of the magnetic moment vector and that of the rf field are the same (Figure 2.9b). The effective magnetic field $\mathbf{H_{eff}}$ acting on the electronic spins depends not only

on the external field $\mathbf{H_0}$ but also in the internal magnetic created by the sample magnetic anisotropy. Thus, the precession of the electrons and their relaxation process is influenced by the magnetic anisotropy. FMR measurements are performed tuning the intensity and direction of the static field $\mathbf{H_0}$ and analyzing the dynamics of $\mathbf{M}$ through the Landau-Lifschitz-Gilbert equation:

$$\frac{\partial \mathbf{M}}{\partial t} = -\gamma \mathbf{M} \times \mathbf{H}_{\mathbf{eff}} + \frac{\alpha}{M_S} \mathbf{M} \times \frac{\partial \mathbf{M}}{\partial t} \qquad [2.15]$$

where α is the damping constant ($\alpha > 0$), M_S is the saturation magnetization and γ is the gyromagnetic ratio. The magnetic anisotropy of the material is monitored by the effective field $\mathbf{H_{eff}}$ as long as $\mathbf{H_{eff}}$ is related to the energy E of the system through:

$$\mathbf{H}_{\mathbf{e_{ff}}} = -\frac{\partial E}{\partial \mathbf{M}} \qquad [2.16]$$

E includes the different magnetic energy terms, as the magnetostatic, Zeeman and magnetic anisotropy energies. Thus, finding the resonance field $\mathbf{H_r}$ that equals the effective field Heff we can obtain information about the magnetic anisotropy of the samples.

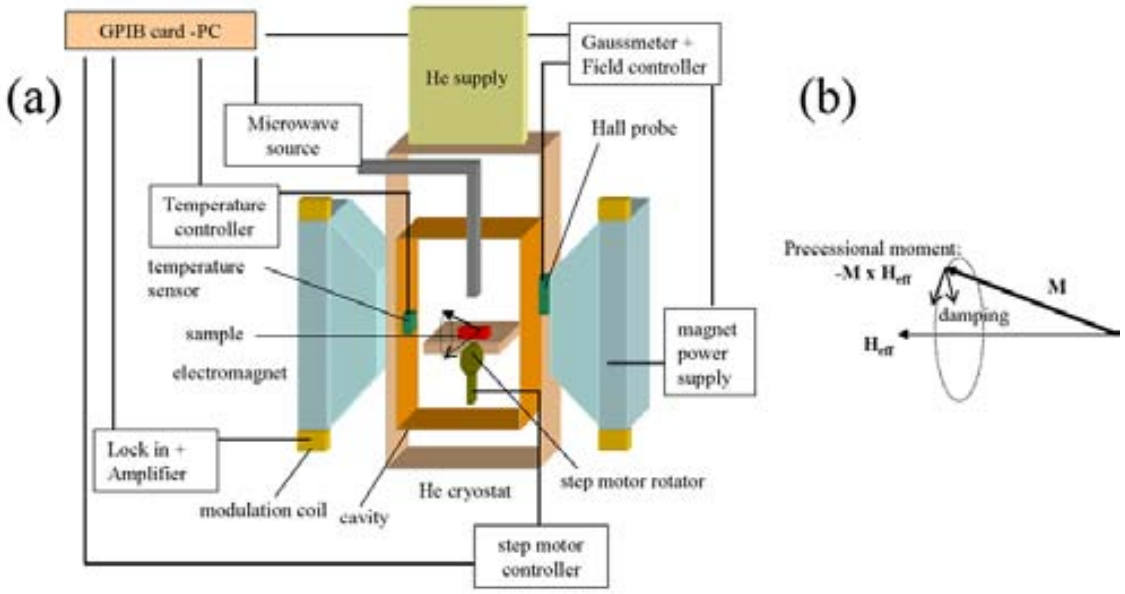

Figure 2.9. (a) Schematic view of the low temperature FMR setup. (b) Precessional motion of magnetization $\mathbf{M}$ around the effective magnetic field $\mathbf{H_{eff}}$.

For the series of experiments in (001) and (110) LCMO films, two different angular configurations has been used, depending on the applied magnetic field position and sample rotation. In the out-of-plane configuration the magnetic field is rotated within a plane perpendicular to the sample surface and in the in-plane configuration it is

rotated within the sample plane. The FMR spectra were measured in an X-band (9.3 GHz) electron spin resonance setup, being applied a static magnetic field H generated by an electromagnet and using an alternating magnetic field working at a frequency of 100 kHz with an amplitude of $\Delta H = 32$ Oe. A liquid-He flow cryostat allows controlling the sample temperature in the range of 4.2 K to 300 K and 90 spectra are recorded per plane.

2.4.3 Magnetotransport (PPMS)

Magnetotransport measurements were performed at the ICMAB by means of a PPMS (Physical Properties Measurements System, Quantum Design). This system allows reaching temperatures down to 1.8 K. A superconductive coil allows to reach magnetic fields up to 90 kOe. The resistance is measured by injecting current within a range of 5 nA-5 mA, and the experimental resolution is about 10^{-8} V.

The resistivity and rotator sample holders are shown in Ch5, explained in more detail there together with the methodological process followed for measuring bare and lithographed films.

2.5 Fabrication of defined pads by optical lithography

Micrometric pads and contacts on LCMO films are defined by using optical lithography, and from the design and application of special masks, it was possible to control the direction of the applied current and measured voltage. The experiments were carried out at the clean room facilities of the Universitat Autònoma de Barcelona with the aid of Dr. M. Benítez and R. Palencia.

Optical lithography is based on the interaction of ultraviolet (UV) light and photosensitive materials, referred as photoresists. Two types of photoresists exist: those with photoactive components that can be removed using a developer (positive) and those with photoactive components that stay on the sample (negative). The experiments presented here were performed using a positive photoresist (Shipley Microposit 1813) and the corresponding developer.

As a first step of the procedure, sample surface is dried in a convection oven at 120 ºC for 20 min. Working with (5x5) mm^2 samples, by spin-coating, 2-3 drops of photoresists is homogeneously deposited on the sample surface at optimal spinner conditions. The photoresist is then soft baked at 95 ºC for 30 min. A mask for the photolithography was created by printing at high-resolution the design on a transparent

photolitho, as shown in Figure 2.10a. The photolitho is (4x4) mm^2 to be scaled to the sample size [(5x5) mm^2]. The sample covered by the photoresist is attached to the sample holder of a Karl Süss MA750 aligner that allows positioning the mask to the sample edges. This system works with a Hg lamp operating in the mid UV wavelengths (~ 310 nm). The sample holder and photolitho are under a primary vacuum to the distance between photolitho and photoresist and enhance the resolution of the lithographic process.

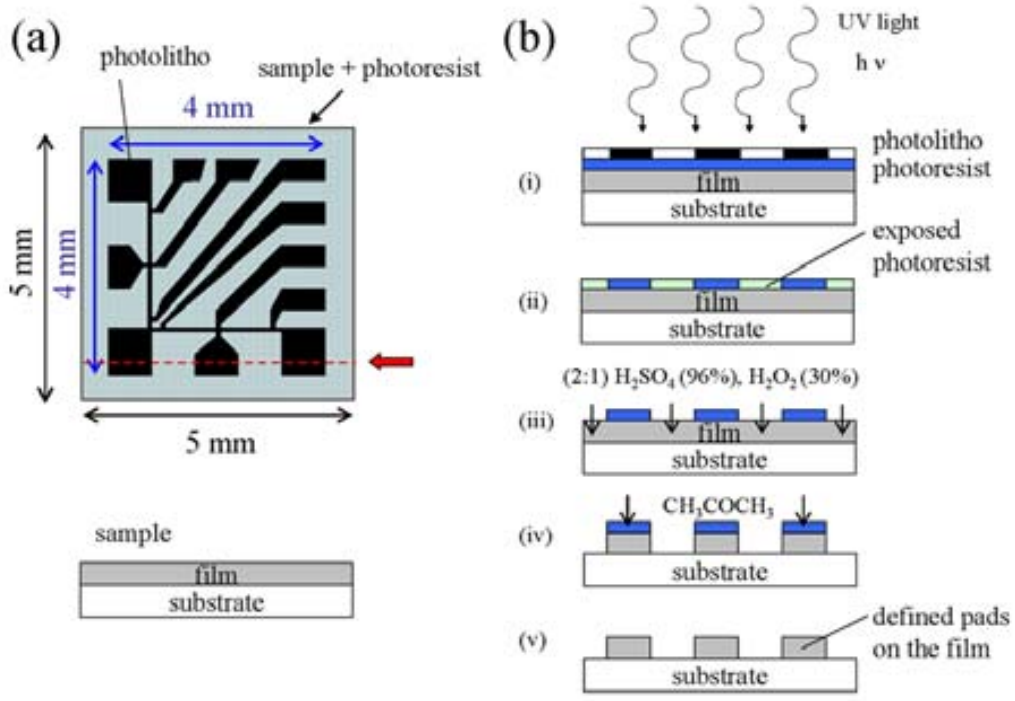

Figure 2.10. (a) Schematic view of the mask used for the optical photolithography compared to the size of the sample. The arrow marks the transversal area inspected in (b). (b) Main steps followed in the lithography process: (i) UV exposure of the photoresist through the photolitho; (ii) exposed regions in the photoresist coexist with non-exposed ones; (iii) chemical attack of the film; (iv) chemical attack of the resist; (v) final sample with defined pattern.

The next steps of the photolithographic procedure are sketched in Figure 2.10b. The UV exposure (typically for 6-10 sec) through the photolitho (i) is masked by the shadow areas defined in Figure 2.10a, and after the exposure (ii) regions with exposed photoresist are identified. Dipping the sample in the developer (typically 60 sec), the exposed photoresist leaves the sample surface. At this step, the contrast between regions with and without photoresist should be enough to allow the inspection of the defined pattern by an optical microscope in order to correct if necessary some of the parameters of the lithography process. A final treatment of the remaining photoresist includes a hard bake at 105 ºC for 30 min. Dipping the sample on a bath of 2:1 sulphuric acid (96

% H_2SO_4) and hydrogen peroxide (30 % H_2O_2) the film is attacked (iii). The combination of these acids breaks the oxygen bonds on the oxide and destroys the complex oxide structure. In order to control the attack of the sample, the 2:1 solution is diluted into distilled water in a 1:10 proportion. Before dipping the lithographed sample, a film of controlled thickness is dipped in the solution to evaluate the reaction velocity. The reactivity of this diluted solution in LCMO films is approximately 0.56 nm/min. The dipping time is thus fixed according to the film thickness, and the attack is stopped by dipping the sample into a distilled water bath. The remaining photoresist is removed using an organic solvent, typically acetone (CH_3COCH_3) (iv). The final pattern on the LCMO film (v) follows the photolitho mask shown in Figure 2.10a.

2.6 Fabrication of magnetic tunnel junctions (MTJs)

2.6.1 MTJs by e-beam lithography

E-beam lithography is based on the interaction of an electron beam with an electron-sensitive material. For this kind of lithography, it is very useful the scanning electron microscope (SEM) when equipped with a lithographic tool (consisting of a specific control software and computer requirements) to perform well defined scans with the e-beam. In short, the lithographic process starts with the electrons being emitted from the electron source of the SEM, expelled towards the sample surface following the electron lenses through a vacuum column. The electron beam can be focalised and controlled to define a pattern using the lithographic tools, being shuttered when necessary. The electron-sensitive materials are organic polymers (resists) that after electron exposure change their molecular structure. Some of them break into smaller molecules, which are called positive resists, and some others react creating more complex molecules, which are called negative resists. Thus, after the exposure, the electron-exposed and the non-exposed parts of the resist are formed by different molecules. Exploiting the different solubility of these molecules in organic solvents, they can be selectively removed from the surface. A thermal treatment allows strongly reducing or even stopping the electron sensitivity of the resist.

The e-beam lithography experiments were performed by M. Rubio as part of his PhD thesis under the supervision of Prof. E. Bertrán from the FEMAN group at the Universitat de Barcelona. A JEOL JSM-840 equipped with a RAITH Elphy Plus tool located at the Serveis Científico-tècnics of the Universitat de Barcelona was used for

performing e-beam lithography on STO/LCMO bilayers. The electron source is a W filament and the magnification is 10x to 300 000x. Acceleration voltage range is 200 V to 40 kV and electron beam current can vary between 10^{-12} and 10^{-5} A. The optimum vacuum to operate is 10^{-6} mbar. The used resists were polymethylmethacrylate (PMMA) and the combination of PMMA and the copolymer [methacrylic acid, P(MMA-MAA)] [11]. Due to the lower density of PMMA and the presence of methacrylic acid in the copolymer, a copolymer layer is more sensitive than the PMMA to electrons. Therefore, being fixed the e-beam exposure conditions, a copolymer layer is much effectively attacked than a PMMA layer. Exploiting the different electron sensitivity of PMMA and copolymer, layers of PMMA and copolymer can be stacked in bilayer structures, as shown in Figure 2.11a and b. By spin-coating, homogeneous PMMA and copolymer layers are deposited onto the sample, being each layer baked treated at optimal conditions (typically 170 ºC for the PMMA and 140 ºC for the copolymer in a convection oven for 30 min). After the e-beam exposure and final development of the resist, the gate (hole) structure is defined depending on the stacking order of the layers: copolymer/PMMA/sample stacking defines a T-gate (Figure 2.11a) and PMMA/copolymer/sample defines an inverted T-gate (Figure 2.11b). Tuning the e-beam parameters (acceleration voltage, e-beam current, nominal dose factor) and the stacking of resist layers, different holes can be defined. An example of a hole obtained in an inverted T-gate is shown in Figure 2.11c, showing that from the total resist layer thickness (280 nm), the defined holes are open down to the underneath sample (hole depth ~ 280 nm).

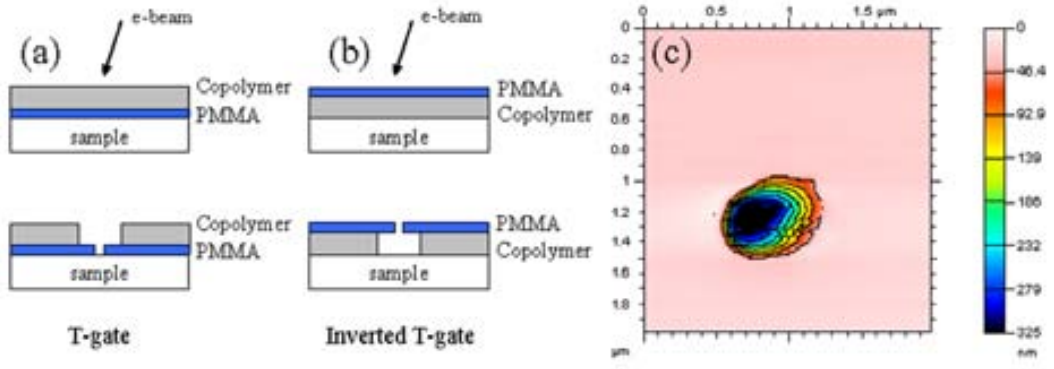

Figure 2.11. [(a) and (b)] Sketch of the stacking of PMMA and copolymer layer and final pattern obtained after e-beam exposure, being open the contact to the sample through (a) a T-gate or (b) an inverted T-gate. (c) Topography image obtained from using a profilemeter on an inverted T-gate obtained (80 nm PMMA/200 nm copolymer) at a voltage 20 kV, current of 46 pA and nominal dose factor of 25x. The width of the hole is $\phi \sim 500$ nm and the depth ~ 280 nm

After the optimal conditions for the e-beam lithography are found, the definition of inverted T-gates with resist layers of PMMA(80 nm)/copolymer(200 nm) onto STO/LCMO//STO samples is performed. Circular holes on the resist of diameter $\phi \sim 400$ nm diameter are obtained for 20 kV of acceleration voltage, 46 pA of electron beam current with a dose factor of 20x, being the x-dose x = 150 $\mu C/cm^2$. Previously to the definition of top electrodes, a soft oxygen plasma attack is performed inside a sputtering chamber during 30 sec at a dc power of 10 W through a W mask leaving one half of the sample exposed to the plasma and the other half protected. The top electrodes are arranged into a (4x4) matrix, being deposited through a metallic mask allowing the matching of the matrix of holes and electrodes to fit (Figure 2.12). The nominal dose factor for the holes was previously changed from column to column to create holes of different sizes. Besides, one column on top electrodes is directly deposited onto the resists in order to have a reference of the conductivity of the resists.

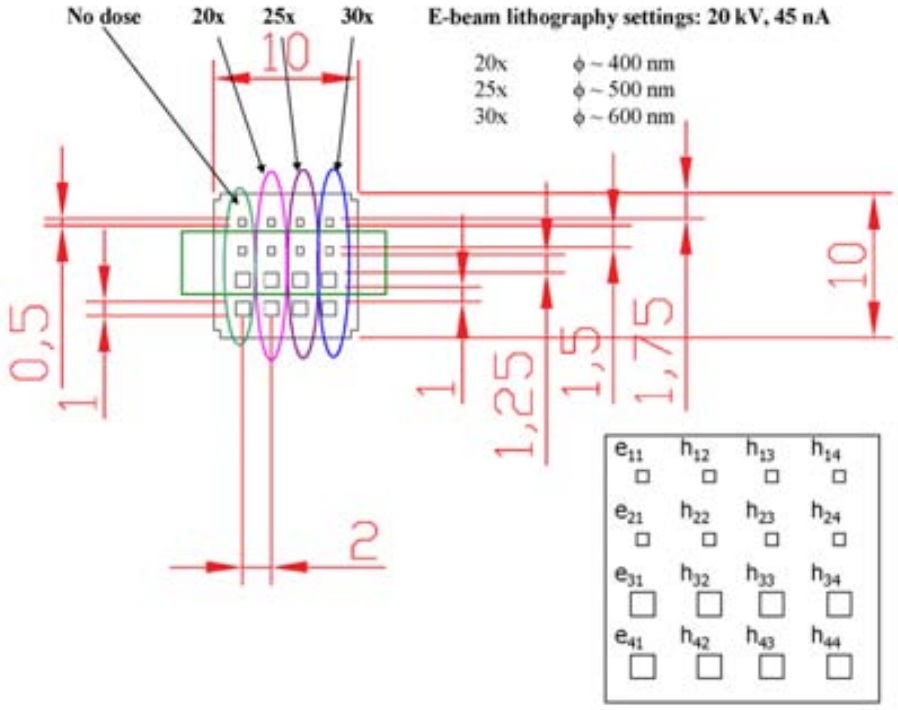

Figure 2.12. Sketch of the matrix defining top electrodes (left) and their corresponding nomenclature (right). Sizes are in mm. Left column electrodes are performed directly onto the resist without litographied hole (e_{ij}). (h_{ij}) indicate an electrode with an underneath hole. The rectangular area marked on the left sketch indicates the area on the samples that was attacked with the soft oxygen plasma. The e-beam doses for each array of motifs are also indicated as well as the nominal diameter (ϕ) of 20x dose holes.

Co top electrodes were deposited using either dc sputtering or evaporation at the Dept. Física Aplicada i Òptica of the Universitat de Barcelona by M. Rubio. Co

thickness was controlled by measuring the height step of the Co layer deposited onto a masked STO single crystal surface. Typical thickness was 6-30 nm. The deposition was made using a metallic mask that defines a (4x4) matrix of (0.5x0.5) mm^2 and (1x1) mm^2 electrodes as seen in Figure 2.12.

2.6.2 MTJs by nanoindentation

The basic principle of this procedure exploits the Conducting AFM (C-AFM) technique and its possibility to measure in real time the conduction (resistance) through between the conductive tip and a given sample. It is necessary to previously measure the resistance value of the sample surface. Then, when the C-AFM tip proceeds to indent the insulating resist, the monitoring of the resistance allows stopping the indentation process when the tip measures the reference value of sample surface. We used epitaxial bilayers of thin STO barriers deposited on LCMO electrodes, and magnetic tunnel junctions were created by defining nanometric holes with the C-AFM tip and afterwards depositing top ferromagnetic electrodes. The nanolithography tasks were developed at the Unité Mixte de Physique CNRS-Thales under the supervision of Dr. K. Bouzehouane and Dr. S. Fusil. The procedure can be described as the following:

1. Characterization of the surface resistance by C-AFM. This step allows knowing the base resistance (R_S) of the sample surface at some fixed conditions (polarization voltage, tip force).

2. Deposition by spin coating of the first resist on the sample surface, followed by a thermal treatment to optimize resist hardness. Afterwards, a second photosensitive resist is deposited on top of the previous one. Using an appropriate mask, a classical photolithographic process is carried out to remove the second resist only in some small areas. The design of the mask allows allocating these small areas easily with an optic microscope (Figure 2.13a).

3. Nanolithography using the C-AFM setup. As described in detail in Ref.[4], appropriately positioning the conductive tip to touch one of the motifs, the tip approaches the sample surface covered by the resist(s). Once the surface is touched, the piezoelectric deflection starts to evolve from its zero reference value of non-contact towards higher values as the tip penetrates the resist. A schematic view of the tip-sample state is shown in Figure 2.13b. Simultaneously to the tip penetration on the resist, the tip-sample resistance is monitored. The base resistance of the free sample surface R_S is known from previous C-AFM measurements on bare surface samples. To

ensure the success of the nanoindentation process, the resistance at which the tip returns is fixed in a range close to that of the bare sample surface: $[\log(R_S) - 0.5] \leq R_S \leq [\log(R_S) + 0.5]$. Thus, different nanoholes are defined depending on the resistance set point but also on the resist inhomogeneous coverage. In Figure 2.14, two sets of deflection and resistance curves recorded during two nanoindentation processes in the same sample are shown. Following the resistance curve, it is clear that a great change of resistance happens when the thin resist is finally penetrated and the tip touches the sample surface (arrows).

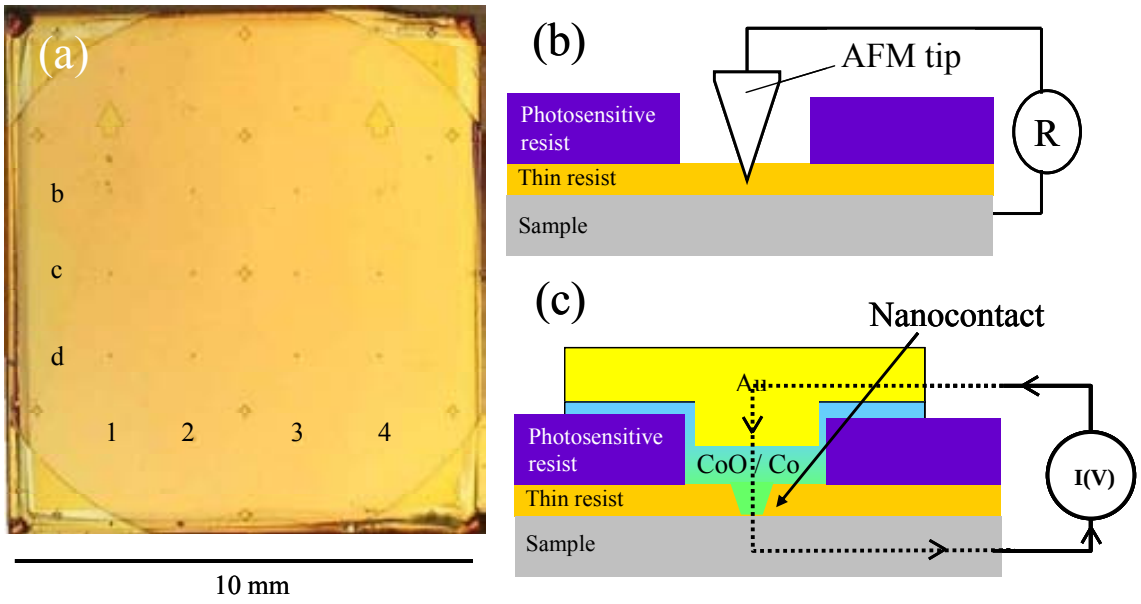

Figure 2.13. (a) Photograph of a (10x10) mm^2 crystal after the classical UV photolitographic process has been performed on the photoresist. Arrows are used to orient the matrix of lithographed nanoholes. (b) Schematic view of the C-AFM tip nanoindenting the thin resist on the sample. (c) Schematic view of the final magnetic tunnel junction after the deposition of top Au/CoO/Co electrode.

4. Using a dc sputering setup, the deposition of the top ferromagnetic electrode (Co) by dc sputtering is performed. After a complete layer of 15 nm is grown, a short oxidation allows obtaining a 3.5 nm top CoO antiferromagnetic layer. Finally, a thick Au electrode (100 nm) is deposited for electric contacting.

5. To define the final top electrodes, selective ion beam etching (IBE) is performed onto the Au/CoO/Co/STO/LCMO sample. An IBE setup equipped with a secondary ion mass spectrometer (SIMS) allows monitoring the Au and Co signal when the etching of the surface is performed. Previously to proceed to the IBE, polymethylmethacrylate (PMMA) is deposited on top of the Au/CoO/Co area with nanoholes are underneath. Thermally treating the PMMA, this resist becomes

insensitive to the ion beam and protects the Au/CoO/Co from the ion beam. Therefore, the continuous Au/CoO/Co electrodes are selectively attacked by the IBE and top separated top electrodes are defined. The IBE is used at 300 V and during 6 to 9 min. Au and Co signals are followed by the SIMS and the attack is stopped when the Co signal disappears. A sketch of the final device is shown in Figure 2.13c.

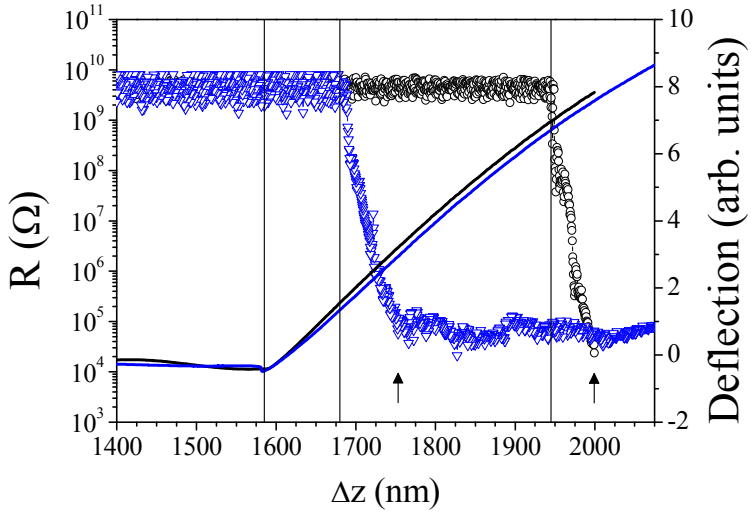

Figure 2.14. Change of the tip-sample resistance (symbols, left axis) and of the cantilever deflexion (lines, right axis) as a function of the displacement of the piezoelectric crystal during the indentation process. From the highly insulating resist (10^{10} Ω) a great change of resistance in the tip-sample occurs when the free sample surface is touched (10^5 Ω, marked by arrows). For the same base resistance $\log R_S = 5$, both nanoindentations used the same resistance setpoint to return ($\log R = 4.5$).

References

[1] M. Bibes, Elaboration et étude de couches minces de manganites à valence mixte, PhD thesis, Universitat Autònoma de Barcelona – ICMAB-CSIC (2001)

[2] Nanotec Electronica S.L.: http://www.nanotec.es/

[3] Digital Surf webpage for Mountains analysis software: http://www.digitalsurf.fr/en/mntas.htm

[4] F. Houzé, R. Meyer, O. Schneegans, and L. Boyer, Appl. Phys. Lett. **69**, 1975 (1996)

[5] B. Wallbank, I. G. Main, and C. E. Johnson, J. Spect. Relat. Phenom. **5**, 259 (1974)

[6] V. S. Dhramadhikari, S. R. Sainkar, S. Badrinarayan, and A Goswami, J. Spect. Relat. Phenom. **25**, 181 (1982)

[7] C. D. Wagner, L. E. Davis, M. V. Zeller, J. A. Taylor, R. H. Raymond, and L. H. Gale, Surf. Interf. Anal. **3**, 211 (1981)

[8] M. Abbate, J. B. Goedkoop, F. M. F. de Groot, M. Grioni, J. C. Fuggle, S. Hofmann, H. Petersen, and M. Sacchi, Surf. Interf. Anal. **18**, 65 (1992)

[9] S. Chikazumi, *Physics of Ferromagnetism*, Oxford University Press Inc., Second Edition, 1999, pag. 85-88

[10] P. Panissod, M. Malinowska, E. Jędryka, M. Wojcik, S. Nadolski, M. Knobel, and J. E. Schmidt, Phys. Rev. B 63, 14408 (2000); Panissod, C. Mény, M. Wójcik, and E. Jędryka "Magnetic properties and structure of metallic multilayers investigations by NMR", in J. G. Tobin ed. Proc. Mat. Res. Soc. Symp. 475, 157 (1997)

[11] MicroChem polymethil methacrylate (PMMA), used with Co-PMMA (mixture of PMMA and 8.5% of methacrylic acid), allows designing T-gates. Website of MicroChem products: http://www.microchem.com/products/index.htm

3 Growth mechanisms in LCMO films

Understanding the phenomena of crystal growth from a vapor phase is a key issue in surface science, as well as, from a technological point of view, it is also necessary to control the defects in thin films and heterostructures. Research of crystal growth from a vapor phase has been mainly focused in systems involving semiconducting or metallic materials. The growth mechanisms of oxides, and of transition metal oxides in particular, has received less attention because their novelty, complexity, and preparation difficulties. Nevertheless, the epitaxial growth of a complex oxide needs to be understood to optimize and even tune the functional properties through the film nanostructure, and to develop self-organized low-dimensional oxide structures for future devices [1].

In the case of CMR manganites, epitaxial films with well controlled surface morphology are essential for most promising applications. For example, magnetic tunnel junctions with manganite electrodes that allow large tunnelling magnetoresistance require very smooth surfaces. However, the growth phenomena of manganite epitaxies is far to be completely comprehended. Atomically smooth surfaces of manganites thin films have been observed [2][3][4][5], even in films 100 nm thick [3][4][6], but also rough surfaces are common in high quality epitaxial manganite films [7][8][9][10]. Although systematic studies of roughening are not available, it appears that there is a progressive surface roughening as the film thickness increases [10][11] and it has been recently claimed [12] that film roughness is mainly controlled by

substrate induced strains. Therefore, the investigation, knowledge and control of the epitaxy of manganites (and of oxides in general) have become emerging fields that require much more research.

In this work, detailed investigation of the surface roughening process of LCMO films deposited by rf magnetron sputtering on $SrTiO_3$(001) substrates has been carried out. It is finally demonstrated that roughness develops above a critical thickness. We have identified the rough structures and the growth mechanisms that originate them. These structures are multilayered mounds caused by the kinetic growth instability associated to an anisotropic adatom current flow due to the energy barriers formed at step-edges of two dimensional (2D) islands. There will be shown that mound formation can be controlled by adjusting substrate miscut angle and growth temperature, and we propose also a possible series of additional strategies to control the growth mechanisms and the morphology. We also present a characterization of the growth of LCMO on STO (110). Although the study was not so complete as in the case of the (001) films, we have clearly identified the growth trend, quite different from the (001) case. We have observed the development of film faceted three dimensional (3D) islands. The 3D islands are favored thermodynamically and its existence leads to rougher (110) surfaces compared to the (001) ones, which depict 2D islands. A description of the topography of these (110) surfaces and a discussion on the strategies to reduce roughness or prevent crystal formation are presented.

Detailed information on structural properties of the films will be presented in Ch4. We want to mention that the films are epitaxial, with cube-on-cube epitaxial relationship with the substrate (for both cases, films on (001) and on (110) substrates). LCMO (001) ones grow coherently with the substrate, whereas LCMO(110) films undergo progressive relaxation, which is found to be anisotropic.

3.1 Growth mechanisms and morphology of (001) LCMO films

Several (001)LCMO films with thicknesses in the range of 23 to 80 nm were grown on STO (001) substrates at different growth conditions and on substrates with different miscut angles. The films were deposited at fixed chamber conditions and following the same deposition procedure as described in Ch2, changing only in some of

the experiments the substrate temperature during deposition. The list of samples is included in Table 3.1.

Table 3.1. List of (001)LCMO samples used for the morphology study together with the information about the substrate miscut angle, film thickness and deposition temperature (T_d). The AFM images from samples marked * and ** were granted by Dr. U. Luders and Dr. L. Abad, respectively.

Sample	Substrate	Miscut angle (deg)	Film thickness (nm)	T_d (C)
LCMO-01*	STO(001)	0.15	23	800
LCMO-05**	STO(001)	0.15	27	800
LCMO-04*	STO(001)	0.15	48	800
LCMO-03*	STO(001)	0.15	62	800
020603**	STO(001)	0.15	80	800
150704C	STO(001)	0.5	80	800
241103C	STO(001)	0.05	30	750
201103C	STO(001)	0.05	30	800
191103C	STO(001)	0.05	30	825

We have first studied the evolution of the surface morphology of films as thickness increases at fixed substrate miscut angle and deposition temperature. In Figure 3.1 the surface morphology of films deposited at substrate temperature of 800 ºC on 0.15 deg miscut STO (001) substrates, with thicknesses ranging 23 to 62 nm, is shown. For thinner films, t = 23 nm and 27 nm, (Figure 3.1a and b) there are holes and 2D islands, but the underneath structure of terraces and steps of the substrate is evidenced. However, terraces cannot be resolved in the t = 48 nm film (Figure 3.1c), as the surface is mainly covered by irregularly shaped 2D islands, some of them showing other ones nucleated on their surface.

A thicker film, t = 62 nm, (Figure 3.1d) does not show 2D structures, but 3D grain-like units. Therefore, whereas we have not detected any degradation of the crystalline quality upon increasing film thickness, the surface evolves from flat to rough. Interestingly, the topography of the thinnest films (Figure 3.1a, b, and c) demonstrates that the grain-like rough surface in Figure 3.1d does not form from a 3D nucleation, but from a 2D nucleation. Grain-like morphology is widely found in manganite epitaxy [8][9][10], thus it is highly interesting the study of its formation.

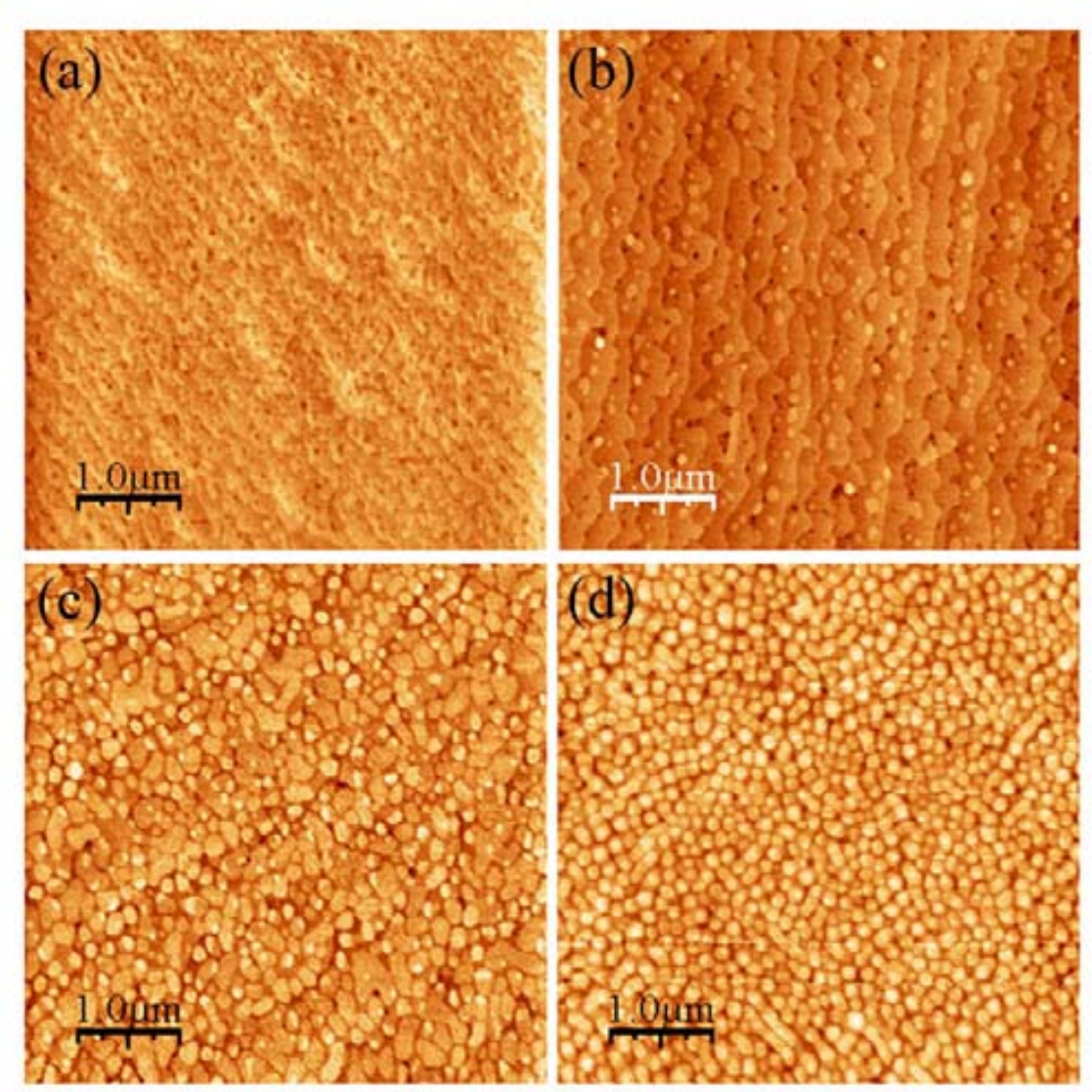

Figure 3.1. AFM topographic images (5x5) μm^2 of films grown on 0.15 deg miscut (001) STO. The thickness of the films is, correspondingly, (a) t = 23 nm, (b) t = 27 nm, (c) t = 48 nm, and (d) t = 62 nm.

High-resolution AFM images shown in Figure 3.2 of films of 23 to 80 nm thickness were analyzed in order to get insight on the roughening process.

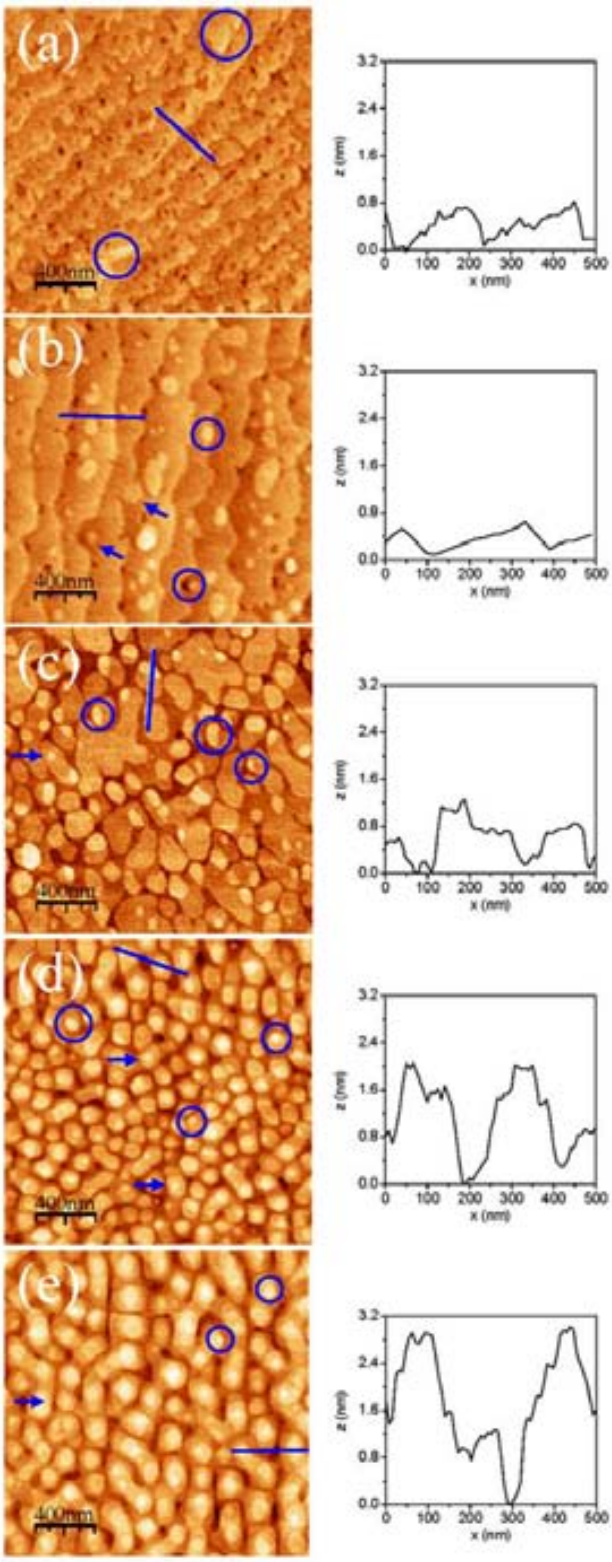

Figure 3.2. AFM topographic images (2x2) μm^2 of films grown on 0.15 deg miscut (001) STO. Film thickness is (a) t = 23 nm, (b) t = 27 nm, (c) t = 48 nm, (d) t = 62 nm, and (e) t = 80 nm. Height profiles at the right correspond to the marked lines on the each image. With circles, 2D islands are marked either if: (a) and (b) they have nucleated at the steps on upper terraces; (c), (d) and (e) the nucleation occurred at the edge of holes or at the edge of lower islands.

The morphology of terraces and steps in films thinner than 30 nm is shown in detail (Figure 3.2a and b). Height profiles indicate that most of the steps are 1, 1 and ½, or 2 unit cells (u.c.) high, and the miscut angle of the substrate is determined to be around 0.15 deg. In the t = 23 nm film (Figure 3.2a), the presence of 2D holes on the terraces signals an incomplete layer coalescence. Then, layer-by-layer is the main growth mechanism, although certainly a part of the adatoms can also stick to the steps during growth. There are some 2D islands that have nucleated at the steps, on the upper terrace part. Two of these islands are encircled in the Figure 3.2a; one is a very small one (top circle), whereas the other (bottom left part of the image) is a large 2D island. On the other hand, in the t = 27 nm film (Figure 3.2b) there are less holes and more islands. Two islands are encircled in Figure 3.2b; one located at a step between terraces and other that has nucleated at the edge of a hole. It can be also appreciated that both holes and 2D islands affect –and they are also affected by- the steps between the terraces. It is observed that practically all the holes are in contact with the steps. Moreover, the nucleation of 2D islands can be influenced by the step profile. An example located at the left bottom of the image is marked by an arrow. It points out that growth does not proceed exclusively by layer-by-layer but also by step flow. On the other hand, it is to be noted that the presence of large 2D islands can destabilize the morphology of terraces and steps. As an example, we have marked (see the arrow close to the center of Figure 3.2b) an island that is close to merge to the step. After merging, meandering of the step will increase, and the upper terrace will be much wider and narrow.

With further growth, the terrace and steps morphology was no longer observed, as evidenced the 48 nm thick films (Figure 3.2c). This scan shows that the morphology of this film is dominated by large 2D islands. In the right panel, the height profile depicts a quite different shape compared to those corresponding to the vicinal surfaces found in the thinnest films, where the morphology of terraces and steps was still noticeable. The height profiles along the islands nucleated on top of larger ones reveal that all islands are 2D, and that they are ½ to 2 u.c. high, most of them exactly 1 u.c. Considering the whole area in Figure 3.2c, height variations are within only 3 u.c. range. The upper layer corresponds to the lastly formed islands, and their spatial location suggests their possible origin. Some of them (as the one marked by an arrow) have nucleated at the middle of the lower island, but most of them have done it at the edges (as the encircled ones). The probability of nucleation of a stable island depends

on the adatom supersaturation, so the inhomogeneous island distribution is likely to be a result of an inhomogeneous adatom density. This is outstanding; and it implies that during the growth the adatom supersaturation was higher close to the edges of the 2D islands than in their center part, that is, far from the edges. However, as the arrival of atoms from the gas phase to the film surface is homogeneous, the inhomogeneous adatom density has to be caused by a constraint in the adatoms flow. The physical origin is a barrier of energy (Erlich-Schwoebel barrier-ES) [13][14][15] that hinders adatoms to jump from an upper to a lower terrace, since the jump involves a transitory state of lower coordination (Figure 3.3). The effect has been widely identified in metal and semiconductor epitaxies. The ES barrier causes the loss of the straightness of the steps (step meandering) and also multilayered islands (mounds) when the film follows a step flow or a layer-by-layer growth mode, respectively [13][14][15][16][17][18]. Here, it is demonstrated that this kinetic instability has a critical destabilizing effect in the epitaxy of oxides.

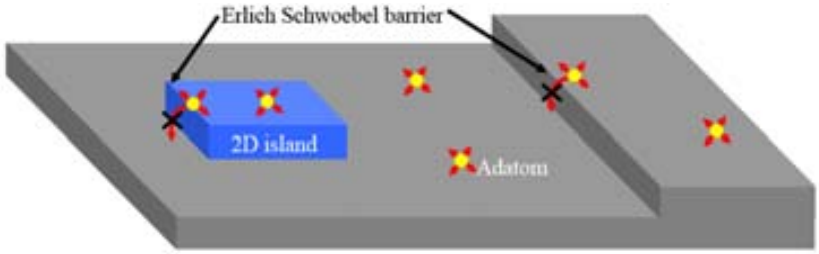

Figure 3.3. Squematic view of film growth in the presence of an Erlich-Schwoebel barrier. In this case, adatoms avoid low coordination states, as those of passing from the edges of 2D islands or substrate terraces to a lower layer or substrate terrace (marked by arrows).

Indeed, the kinetic restriction is the cause of the roughening evolution with thickness that have produced the 3D grain-like units in the nominally 62 nm film, as showed in Figure 3.2d. The profile displayed at the right panel covers height variations of 5 u.c., whereas a maximum height variation of 6 u.c. was found in other profiles. The nucleation of the majority of top layers occurs at the island edges (two examples are encircled), although others (marked with arrows) are in the middle part. Increasing the thickness of the film to 80 nm, as seen in Figure 3.2e, the peak-valley distances increase. From the extracted profile of this image, height variations are even 8 u.c., and still we can find the presence of upper 2D islands nucleated at the edges or in the middle part of the lower terraces (marked by circles and arrows, respectively). The topographic images in Figure 3.2d and e show that these units are multilayered islands being the upper ones of smaller area than those underneath. In Figure 3.4, the derivative image of

the topography demonstrates that the grain units are multilayered islands (wedding cake like), as it illustrates the sketch in Figure 3.4c.

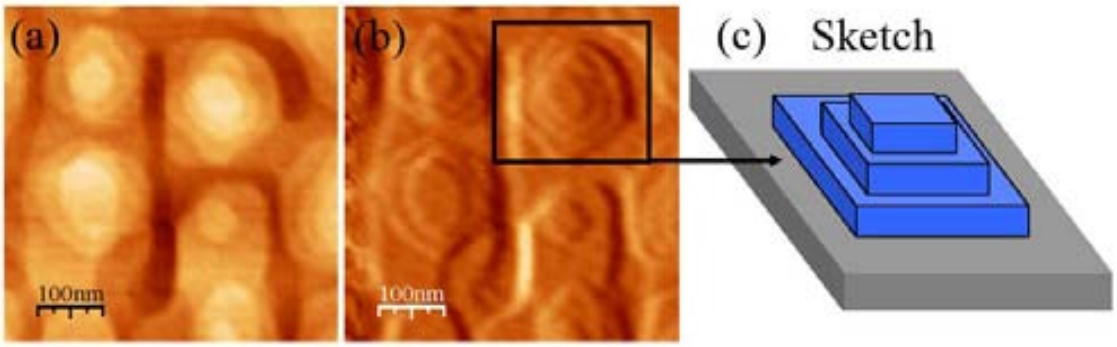

Figure 3.4. (a) Detail of the topographic image of 80 nm film shown in Figure 3.2e. (b) Corresponding derivative of image shown at (a), reflecting the formation of multilayered islands with the shape of wedding cake. (c) 3D sketch of the morphology of the multilayered islands.

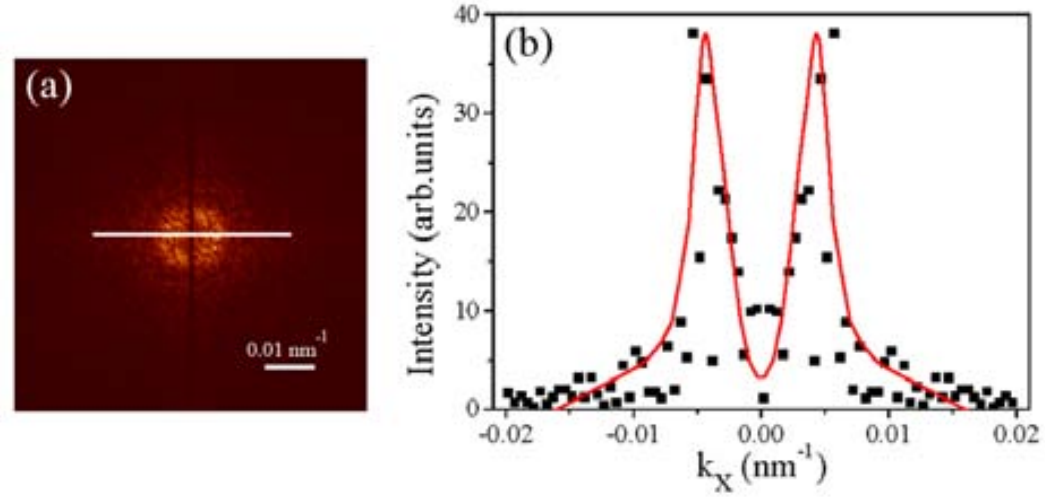

Figure 3.5. (a) Fast Fourier transform of the topographic image shown in Figure 3.2e. (b) Intensity profile along the marked line in (a). The line is a guide to the eye.

As mounds increase in height, their lateral size increases too, as a comparison of Figure 3.2d and e evidences. On the other hand, films seem to self-organize during growth, as it is deduced from the uniform separation of mounds and from the slight indication of spatial order in thickest film (Figure 3.2e). To investigate the self-organization, we have calculated the fast Fourier transform (FFT) of this later AFM topographic image and the resulted function is plotted in Figure 3.5a. Together with the FFT image, we include in Figure 3.5b a quantification study on this FFT by extracting an intensity profile along the horizontal direction. The average mound separation can be

properly calculated from peak positions. The determined average separation is around 225 nm, and therefore the mound density is close to $2 \cdot 10^9$ mounds/cm^2.

To analyze quantitatively the topography, height histograms from each image in Figure 3.1 have been extracted and finally plotted in Figure 3.6a. The distributions represent the number of events of height within an interval as a function of height, and they have been normalized to allow the comparison of different samples. The normalization is performed by dividing by the maximum number of events in the studied distribution and shifting the origin of height (z = 0) to center all the histograms.

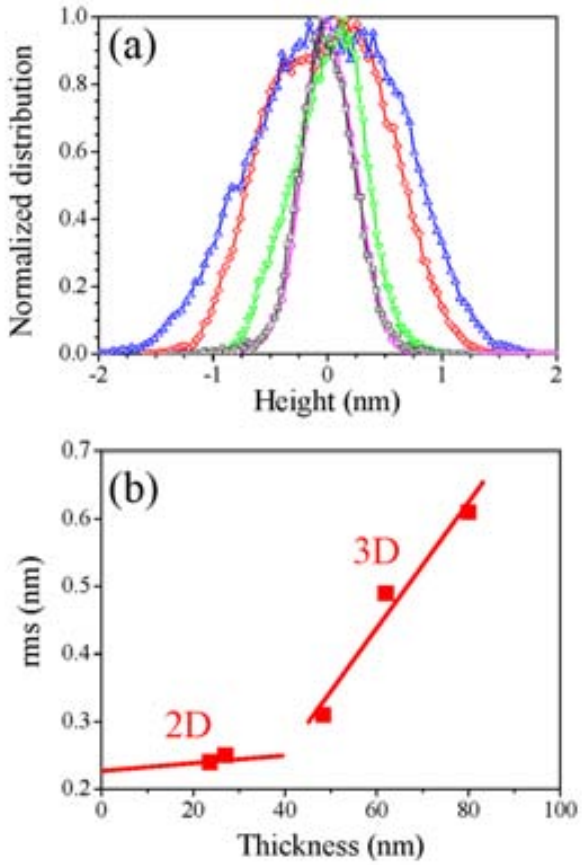

Figure 3.6. (a) Normalized histograms of height corresponding to the scans shown in Figure 3.2 (more details in the text). Symbols: circles (t = 23 nm), squares (t = 27 nm), down triangles (t = 48 nm), diamonds (t = 62 nm), and up triangles (t = 80 nm). (b) Root-mean-square surface roughness as a function of the film thickness.

Relevant comments on these histograms have to be addressed to the different growth as film thickness increases. Thinnest films showed morphology of terrace and steps (Figure 3.2a and b), and their histograms are almost coincident (in Figure 3.6a, they correspond to circles and squares). The t = 48 nm film (Figure 3.2c) presented a morphology far from that of terraces and steps, although the surface was still almost 2D (height variations were in a 3 u.c. range). According to this morphology, the histogram

in Figure 3.6a broads only slightly (down triangles). However, the histograms of the two thicker films show distinct shapes and are much broader since the multilayered mounds involve a larger range of height variations. The set of histograms certainly evidences the roughening process as the initially flat 2D surfaces turn progressively into rough 3D ones. As a natural consequence of this process, the root-mean-square (rms) surface roughness increases (Figure 3.6b) as the film undergoes the morphology transformation.

As it has been pointed out, multilayered mounds are believed to form in layer-by-layer growth conditions when an Erlich-Schwoebel barrier reduces the probability of the adatoms on a 2D island to jump to the lower terrace [14][15][16]. Therefore, the formation and characteristics of the 2D islands are determinant to the growth and evolution of mounds. The morphology progression just described has evidenced that at early stages growth proceeds not only by layer-by-layer but also by step flow mechanism. It should be possible then to tune the relative importance of both mechanisms by using substrates of varied miscut angle, since it determines the terrace width. To verify it, deposition of new films at the same growth conditions but on substrates of much reduced miscut angle (0.05 deg instead of 0.15 deg) was done. In Figure 3.7a, the surface morphology of a t = 30 nm film grown on the almost singular (0.05 deg miscut angle) substrate, has a clear grain-like appearance. The analysis of higher resolution images and height profiles confirms that islands are multilayered mounds, as it can be seen in Figure 3.7b in a (1x1) μm^2 topographic image where solid lines denote the equiheight contours with $\Delta z = 1$ u.c. It is outstanding that such high roughening has occurred at a low thickness (t = 30 nm), since mound formation in films on the 0.15 deg miscut substrates requires a thickness above t = 50 nm. The impact of the substrate vicinality on surface roughening is well illustrated in the normalized histograms plotted in Figure 3.7c. The narrow histogram (down triangles) corresponds to the t = 48 nm film on the 0.15 deg miscut substrate (topography in Figure 3.2c), whereas the broad histogram corresponds to the image displayed in Figure 3.7b (t = 30 nm film on 0.05 deg miscut substrate). Clearly, the almost singular surface of the 0.05 deg miscut substrate favors an earlier formation of large 2D islands that turn fast into multilayered mounds.

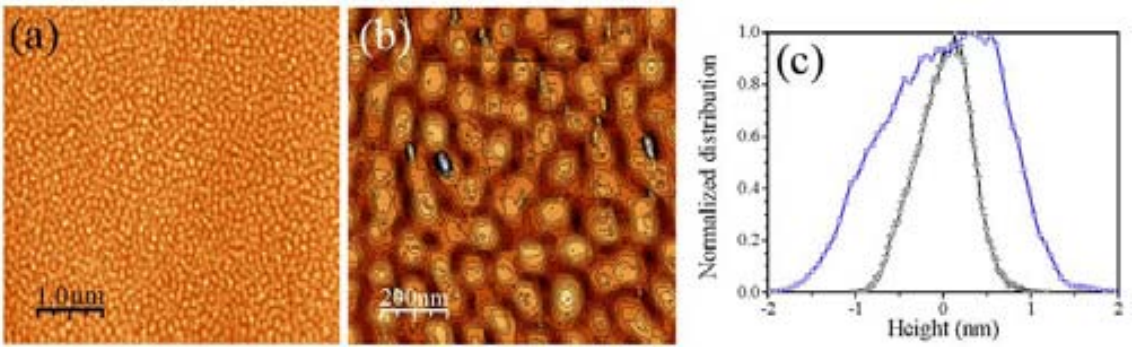

Figure 3.7. (a) AFM topographic image (5x5) μm^2 of a t = 30 nm film grown on 0.05 deg miscut STO (001). (b) Detailed (1x1) μm^2 of the image in (a), with superposed equiheight lines (height difference = 1 u.c.). (c) Normalized histograms of height corresponding to this t = 30 nm film (squares) and to the t = 48 nm film on 0.15 deg miscut STO (down triangles, topographic image in Figure 3.2a).

Opposed to the almost singular substrates, and in order to suppress mound formation, we can increase the vicinality of the substrates used in the film growth. The width of terraces can be thus reduced by the higher angular miscut angle, and the adatom flow is though to be highly sensitive to the reduction of nucleation sites. The impact of higher substrate vicinality on the morphology is evaluated by comparing the morphology of the t = 80 nm film deposited on 0.5 deg vicinal substrate (Figure 3.8a) with that one of the simultaneously grown film in Figure 3.2e. In the film grown on the more vicinal substrate there are no mounds but a corrugated surface with trenches oriented along a single direction. This morphology contrasts with the grain-like surface developed in the film grown on 0.15 deg miscut substrate of Figure 3.2e. Most of the trenches seen in Figure 3.8a do not extent more than one micron, and in their perpendicular direction they are in average around 240 nm apart, which is close to five times the terrace width of the 0.5 deg miscut substrate. With the aid of the image shown in Figure 3.8b and with the corresponding 3D view (Figure 3.8c), a deeper study on this corrugated morphology can be done. It is observed that there are terraces of different width, being some of them of ~ 50 nm width but also existing some much more wide. The trenches (arrow labeled 1) are at the border of the wide terraces with ascending narrow ones. There are other trenches, having a shorter length, running perpendicular to the steps (arrow 2). These short trenches separate the terraces that show a very prominent in-phase meandering (the steps at both sides of the trench). In fact, steps can develop two morphological instabilities, step bunching and step meandering, as it has reported to occur in the epitaxy of semiconductors and metals [19][20]. The presence of an ES barrier hinders the kinetic formation of step bunching, but strongly favors step

meandering [21]. The ES barrier that originates mounds on non-intentionally miscut substrates, also provokes the meandering instability on vicinal surfaces. Besides, the meandering of steps reduces the uniformity in the step separation, and terraces are much wider in some regions than in others. Where wider terraces are found, trenches and also 2D nucleation is possible, as the presence of some incipient mounds (arrow 3) demonstrates. Nevertheless, the surface is quite smooth, with rms roughness around 0.4 nm. In Figure 3.8d, the height histogram of this film is compared to that of the film of equal thickness grown on the 0.15 deg miscut substrate (Figure 3.2e). Comparing the corresponding FWHM of the histograms of the 0.5 deg film (triangles) and 0.15 deg one (squares), we obtain a value of 0.78 nm (equivalent to 2 u.c.) for the first one while and for the second one 1.6 nm, which indicate the higher roughness associated to the low miscut angle. This remarkable difference illustrates the impact of the substrate vicinality on the surface roughness on these films.

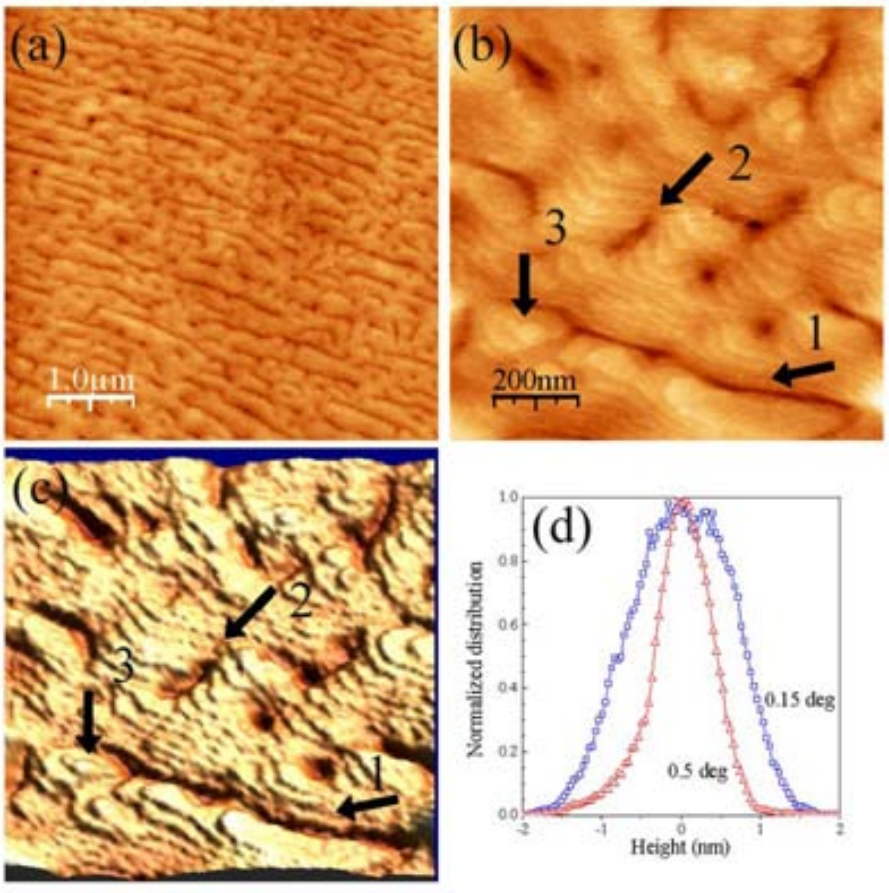

Figure 3.8. (a) Topographic AFM image (5x5) μm^2 of a t = 80 nm film grown on a ~ 0.5 deg miscut STO (001) substrate; (b) Image from a (1x1) μm^2 scan size of (a). (c) 3D view of the image in (b). (d) Normalized histograms of height corresponding to this film (narrow histogram, triangles) and to the t = 80 nm film (wider histogram, squares) on the 0.15 deg miscut substrate.

The deposition temperature is other relevant processing parameter. It fixes adatoms diffusivity and their capability to overcome any energy barrier during their diffusion. Aiming to investigate the influence of the growth temperature, a set of films of the same thickness t = 30 nm were grown on 0.05 deg miscut substrates at varied temperatures. In Figure 3.9 AFM topographic images of films grown at 750, 800 and 825ºC are shown. First, we comment that we observe a lower number of mounds while increasing the growth temperature, although slight variation in height is measured, as it is seen in the extracted profiles shown in the right panels. It has to be noted that these films were grown on the almost singular substrates (0.05 deg miscut), meaning that large 2D islands are believed to form at the earlier stages. Thus, from this growth temperature study, the diffusion of adatoms on a surface is enhanced at high temperature, which results in the observed lower island density.

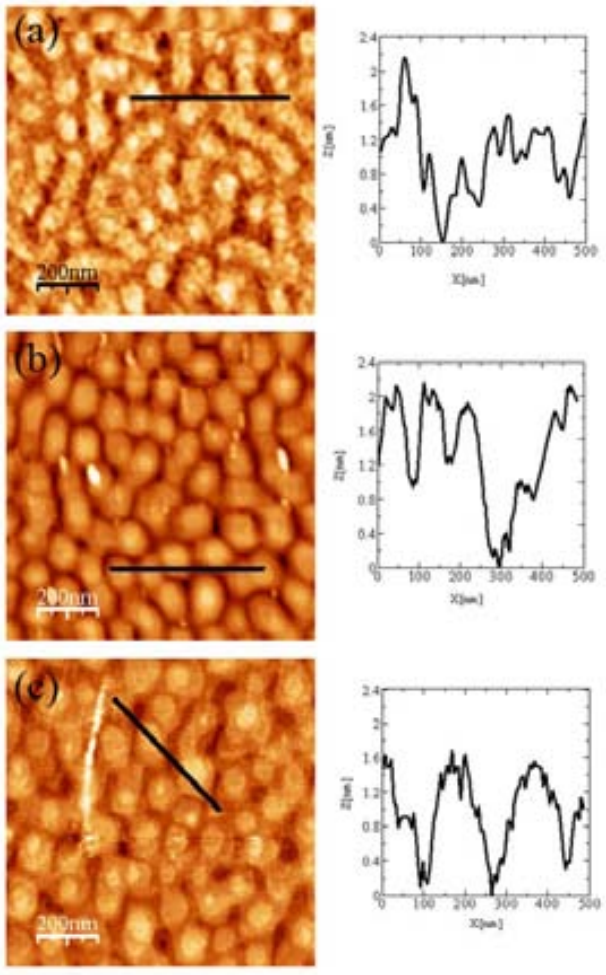

Figure 3.9. (1x1) μm^2 AFM topographic images of t = 30nm LCMO films grown on 0.05 deg miscut STO (001) as a function of the substrate temperature: (a) 750ºC, (b) 800ºC, and (c) 825ºC. The height profiles at the right of each image were taken along marked lines on the correspondent image on the left.

All the previous work proves that both the growth temperature and the film thickness offer a certain degree of control on the mound separation. A statistical quantification of the mound separation that allows comparing it in different samples have been performed by means of the calculated autocorrelation functions of the topographic images. The 2D height-height correlation function is defined as [22]:

$$C(\mathbf{r}) = \langle h(\mathbf{r}_0) h(\mathbf{r} + \mathbf{r}_0) \rangle \qquad [3.1]$$

where **r** is a shift from the center of the image, < ... > means an average over all possible positions defined by $\mathbf{r_0}$, and h($\mathbf{r_0}$) is the height at the position $\mathbf{r_0}$ relative to the mean height. Radial profiles of C(r)'s from some of films are plotted in Figure 3.10.

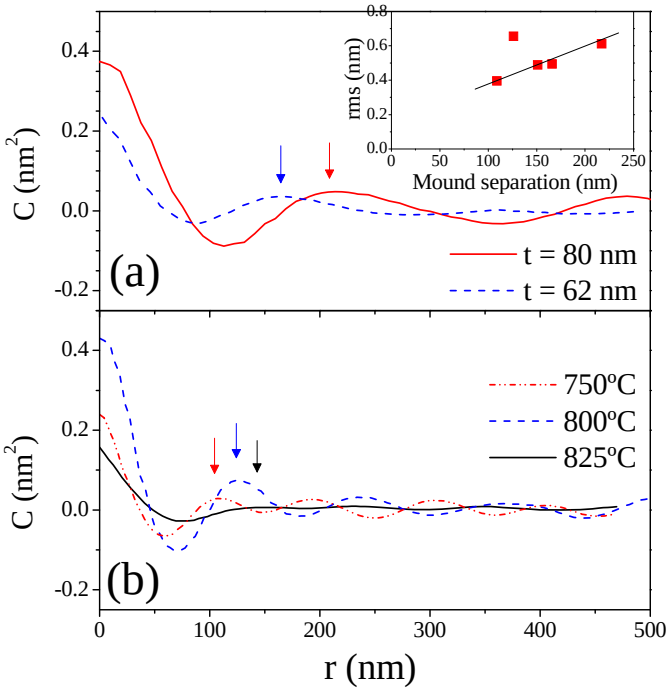

Figure 3.10. Autocorrelation along a radial direction for (a) t = 62 nm and 80 nm films grown at 800ºC on 0.15 deg miscut substrates, and (b) t = 30 nm films grown at 750, 800 and 825ºC on 0.05 deg miscut substrates. Arrows mark the position of the first maximum in each curve. Inset: rms plotted against average mound separation for all films in (a) and (b).

The C(**r**) profiles of two films of different thickness, t = 62 nm and t = 80 nm, grown on the 0.15 deg miscut substrates are compared in Figure 3.10a, whereas in Figure 3.10b the profiles corresponding to t = 30 nm films grown on the 0.05 deg miscut substrate at various temperatures are plotted. A first comment on these profiles has to be addressed to the observed oscillations of the intensity in all the profiles. The oscillations, absent in self-affine surfaces [23], is here a signature of the well-defined mound separation length characteristic of each sample surface. The average mound

separation and thus its lateral size can be properly determined from the position of the first maximum of the experimental C(**r**) curve [24], calculated by means of eq. 3.1. The positions of the maxima for the different curves in Figure 3.10 ranging from 110 to 220 nm are denoted by arrows. It is clear that the increase of either the film thickness (Figure 3.10a) or the growth temperature (Figure 3.10b) implies the formation of larger mounds. At this point, it is interesting to compare the rise on the lateral dimension and the rms roughness, being the last number a way to quantify the height dimension. The rms values of these five films -being grown on two different miscut substrates, at different temperatures, and having different thicknesses- are all plotted in the inset of Figure 3.10a against the mound separation, which was previously determined from the maxima indicated by arrows on the corresponding C(**r**)'s function shown in Figure 3.10a and b. All samples except one fall on a straight line, though the linearity dependence is understood as arising from the increase in lateral size of mounds accompanied by an increase of the mound height (and in the measured rms). Thus, it implies that when the mounds increase in size (base area) more 2D layers are grown at their surface rather than obtaining wider terraces.

To sum up, it has been demonstrated that substrate miscut and growth temperature have an impact on the mound morphology. Firstly, the vicinality of the substrates can allow tuning the critical thickness for mound formation, but even to prevent them to be formed. If the miscut angle is high enough, terraces can be narrower than the adatom diffusion length and then growth could proceed exclusively by step flow mechanism. Secondly, the control of growth temperature makes possible not only to tune the density of 2D islands, but it also favors step flow mechanism since it determines the adatom diffusion length. Moreover, as mounds form due to the ES barrier, its efficiency should decrease at a high enough temperature, since adatom energy could be enough to overcome the barrier. Thirdly, although the influence of the growth rate has not been investigated in the present work, it has to be remarked that this is an important processing parameter as it determines the size of the critical 2D nucleus. Then, both growth supersaturation and temperature are determinant factors to allow step flow mechanism, also determining the density of 2D islands in the case of layer-by-layer mode. Finally, multilayered mounds can be avoided in layer-by-layer mode if the 2D islands are below a critical size [25][26], because the probability that an adatom deposited on a 2D island jump to the lower terrace is likely to increase with the number

of attempts, which should be higher if the island is smaller. Then, in order to suppress the roughening process previously described, the alternative solution to step flow is based in achieving the film growth by layer-by-layer, that is, by obtaining high super-saturation and/or working at low temperature in order to reduce the 2D island size.

To end, a comment of the expected differences in film morphology if the common technique of pulsed laser deposition (PLD) was been used is in order. Whereas films deposited by rf magnetron sputtering grow at a constant rate, in PLD there is a higher instantaneous rate with each laser pulse. Then, 2D islands can be smaller and thus the PLD technique could favor the suppression of the roughening process.

3.2 Growth mechanisms and morphology of LCMO (110) films

The general surface morphology of (110) films of different thickness grown at 800ºC is presented in Figure 3.11. The films were grown at different rate from 0.18 to 0.43 nm/min, as indicated in Table 3.2.

Table 3.2. List of (110)LCMO samples used for the morphology study together with the information about film thickness, growth rate and rms roughness.

Sample	Substrate	Film thickness (nm)	Growth rate (nm/min)	Rms (nm)
050704B	STO(110)	19	0.18	2.7
230204B	STO(110)	63	0.37	3.1
210604B2	STO(110)	80	0.26	3.7
200204B	STO(110)	85	0.43	3.0
050406B	STO(110)	150	0.28	5.8

In Figure 3.11a, the topography corresponds to the thinnest film of 19 nm and it signals the presence of some 3D structures over the film. The objects have an elongated base, as it can be clearly observed in the zoom displayed at the right. Some of the structures are taller than the rest, and they appear as bright spots in the image. Interestingly, it is also observed that some objects are associated two-by-two by means of other objects positioned perpendicularly, and then defining a singular H-shaped base. The elongated objects are oriented along a single direction, which was found to be the [001] by means of X-ray diffraction measurements.

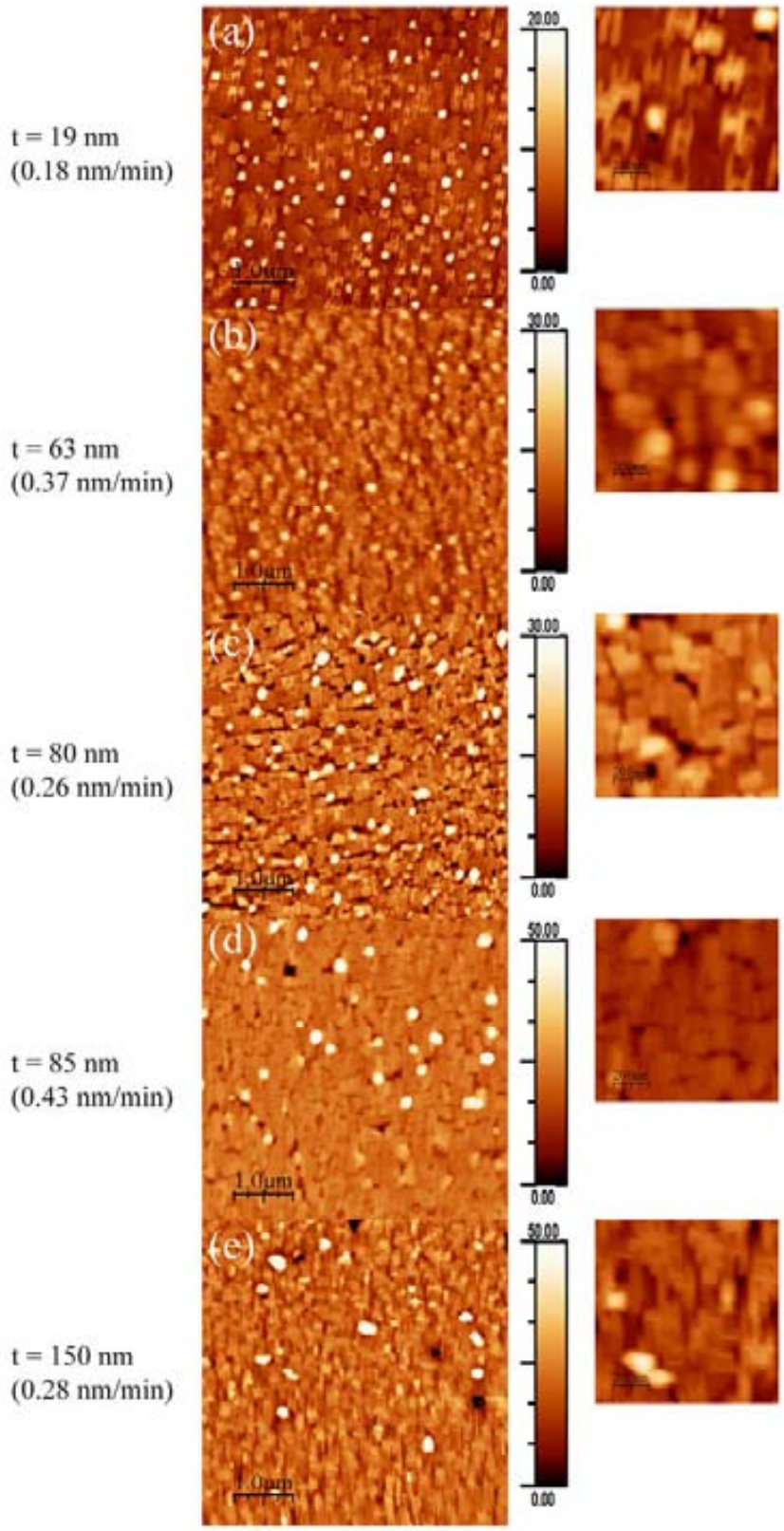

Figure 3.11. Topographic (5x5) μm^2 images of (110) films of different thickness: (a) 19 nm, (b) 63 nm, (c) 80 nm, (d) 85 nm and (e) 150 nm. The rate at which each film is grown is indicated. On the right part of each image, corresponding z-scale (in nm) and a (1x1) μm^2 zoom of them are shown. Roughness values are extracted from (1x1) μm^2 images.

The morphology of films with thickness in the t = 62-80 nm range and deposited at rates in the 0.26-0.43 nm/min range is shown in Figure 3.11b-d. The singular H-shaped base crystallites are not observed in these films, but they show similar rectangular crystallites elongated too along the [001] in-plane crystallographic direction. The morphology of the thickest film (t = 150 nm) is shown in Figure 3.11e. It is remarkable the 3D objects maintain a high guided order, with the elongated side parallel to the [001] direction. Although the morphology is very similar to that of the thinnest film shown in Figure 3.11a, the object height is much higher, and the film rms is 5.8nm, whereas in the case of the film 19 nm thick the rms is 2.7 nm, a much lower value.

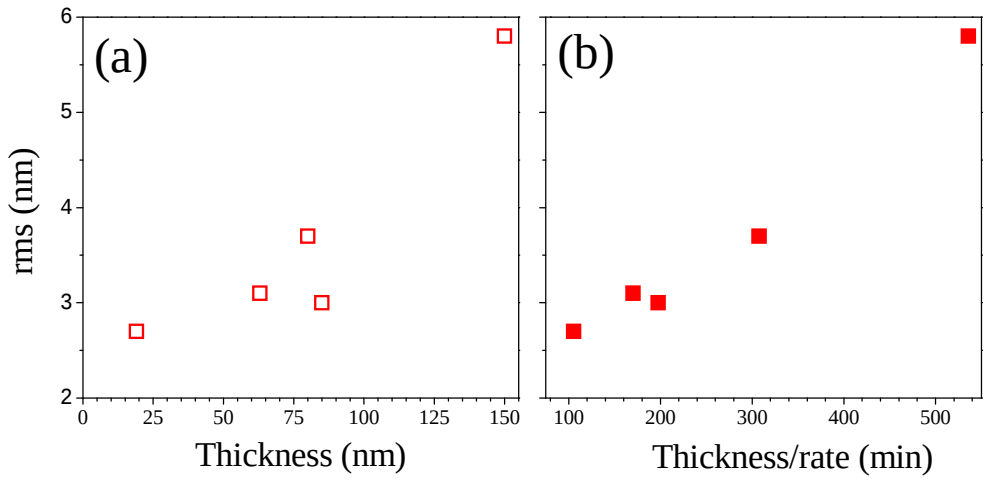

Figure 3.12. Root-mean-square (rms) surface roughness as a function of (a) film thickness or (b) thickness/rate.

A roughness analysis of all the (1x1) μm^2 AFM images of Figure 3.11 is presented in Figure 3.12. As previously noted, 3D growth happens in the (110) film, and it leads to a roughness increase with thickness (Figure 3.12a). However, for *t* = 63 nm film and especially for *t* = 85 nm film the expected tendency seems to be broken. The roughness of these films is lower than the expected according the trend suggested by the other films. It has to be noted that the two films were grown at the highest deposition rates: at 0.37 nm/min the t = 63 nm film and at 0.43 nm/min the t = 85 nm film. Then, the results indicate that roughness increases with thickness and decreases with growth rate. Or, alternatively, that roughness increases with both the thickness and the reciprocal of the growth rate. A plot of the rms roughness *vs* thickness/(growth rate) is

in Figure 3.12b. It is observed that the rms increases roughly linearly with thickness/(growth rate), confirming the mentioned dependences.

The faceted shape of the 3D objects strongly suggests that they do not form kinetically but thermodynamically. Different thermodynamically driving forces can provoke the formation of crystallites in the epitaxial growth of a film. One is the relief of elastic energy that occurs close to the edges of the islands. The paradigmatic example is the formation of SiGe quantum dots [27]. But this does not seem to be what occurs in our case, since the LCMO (110) crystals do not show abrupt changes with thickness, as it occurs in the case of SiGe dots, mainly when dislocations start to form on the dots [28]. Other driven force is caused by the presence of dislocations that promote the 3D object to nucleate and to grow, since dislocated objects have a lower energy [29]. But (110) films show a progressive lattice relaxation (described in Ch4) and it should have an impact in the island density, which is not observed. Other case corresponds to the mechanism known as Volmer-Weber [30]. It occurs when the surface energy of the substrate is lower than the sum of the surface energy of the film and the interface energy, thus making the wetting of the substrate surface unfavorable. Even if the substrate surface is wet by the film, islands can develop with additional coverage if the surface energy of the film is highly anisotropic, making favorable a large area of low energy planes than a smaller area of high energy planes. This occurs commonly in some metals, and then clusters are formed instead of flat films [31]. In oxides, the anisotropy uses to be much more reduced, except in some cases as for spinels [32]. The fact that these objects present the same shape in all films clearly indicates that the anisotropy in the surface energy of LCMO plays a relevant role. However, the results do not allow distinguishing if islands nucleate on the bare substrate or on a wetting layer.

In summary, LCMO (110) films are observed to tend to become rough by developing facetted crystals, possibly influenced by the anisotropy of the surface energy. However, it does not mean that flat LCMO (110) surfaces could not be obtained. On the one hand, steps are preferential sites for adatom accommodation, thus if adatom diffusion length is higher than the terrace width, which depends on the substrate miscut angle, and it allows step flow growth mode, flat metastable surfaces are likely to form. On the other hand, it is important to remark that in 3D islands there is always an additional positive contribution to the energy due to the presence of edges and corners where the atoms coordination is lower. It implies that very small islands

will be not stable. Thus, growth at high super-saturation and/or low substrate temperature could lead to metastable flat films. Indeed, the observation that roughness decreases with growth rate (Figure 3.11 and Figure 3.12) supports this hypothesis.

References

[1] E.W. Plummer, Ismail, R. Matzdorf, A.V. Melechko, J.P. Pierce, J. Zhang, Surf. Sci. **500**, 1 (2002)

[2] V. A. Vas'ko, C. A. Nordman, P. A. Kraus, V. S. Achutharaman, A. R. Ruosi, and A.M. Goldman, Appl. Phys. Lett. **68**, 2571 (1996)

[3] M. Izumi, Y. Konishi, T. Nishihara, S. Hayashi, M. Shinohara, M. Kawasaki, Y. Tokura, Appl. Phys. Lett. **73**, 2497 (1998)

[4] J. F. Bobo, D. Magnoux, R. Porres, B. Raquet, J.C. Ousset, A.R. Fert, Ch. Roucau, P. Baulès, M. J. Casanove, and E. Snoeck, J. Appl. Phys. **87**, 6773 (2000)

[5] Z. H. Wang, H. Kronmüller, O. I. Lebedev, G. M. Gross, F. S. Razavi, H. U. Habermeier, and B. G. Shen, Phys. Rev. B **65**, 054411 (2002)

[6] M. Bibes, Ll. Balcells, S. Valencia, S. Sena, B. Martínez, J. Fontcuberta, S. Nadolski, M. Wojcik, and E. Jedryka, J. Appl. Phys. **89**, 6686 (2001)

[7] J. Z. Sun, D. W. Abraham, R. A. Rao, and C. B. Eom, Appl. Phys. Lett. **74**, 3017 (1999)

[8] L. M. Berndt, V. Balbarin, and Y. Suzuki, Appl. Phys. Lett. 77, 2903 (2000)

[9] M. E. Hawley, G.W. Brown, P.C. Yashar, C. Kwon, J. Cryst. Growth 211, 86 (2000)

[10] M. Ziese, H.C. Semmelhack, and K.H. Han, Phys. Rev. B **68**, 134444 (2003)

[11] M. Paranjape, A. K. Raychaudhuri, N. D. Mathur, and M. G. Blamire, Phys. Rev. B **67**, 214415 (2003)

[12] J. Mitra, M. Paranjape, A.K. Raychaudhuri, N.D. Mathur, and M.G. Blamire, Phys. Rev. B 71, 094426 (2005)

[13] M. G. Lagally and Z. Zhang, Nature **417**, 907 (2002)

[14] P. Politi, G. Grenet, A. Marty, A. Ponchet, and J. Villain, Phys. Rep. **324**, 271 (2000)

[15] J. Krug, Phys. A **313**, 47 (2002)

[16] J. E. van Nostrand, S. Jay Chey, M. A. Hasan, D. G. Cahill, and J. E. Greene, Phys. Rev. Lett. **74**, 1127 (1995)

[17] J. A. Stroscio, D. T. Pierce, M. D. Stiles, A. Zangwill, and L. M. Sander, Phys. Rev. Lett. **75**, 4246 (1995)

[18] G. Apostolopoulos, J. Herfort, L. Däweritz, K. H. Ploog, and M. Luysberg, Phys. Rev. Lett. **84**, 3358 (2000)

[19] V. A. Shchukin and D. Bimberg, Rev. Mod. Phys. **71**, 1125 (1999)

[20] N. Néel, T. Maroutian, L. Douillard, and H.-J. Ernst, Phys. Rev. Lett. **91**, 226103 (2003)

[21] G.S. Bales and A. Zangwill, Phys. Rev. B **41**, 5500 (1990)

[22] C. Teichert, Phys. Rep. **365**, 335 (2002)

[23] A.L. Barabási and H.E. Stanley, *Fractal Concepts in Surface Growth*, Cambridge University Press, Cambridge, Great Britain (1995)

[24] M. Raible, S. Linz, and P. Hänggi, Phys. Rev. E **62**, 1691 (2000)

[25] R. Kunkel, B. Poelsema, L.K. Verheij, and G. Comsa, Phys. Rev. Lett. **65**, 733 (1990)

[26] J. Tersoff, A.W. Denier van der Gon, and R.M. Tromp, Phys. Rev. Lett. **72**, 266 (1994)

[27] Y.W. Mo, D.E. Savage, B.S. Swartzentruber, M. G. Lagally, Phys. Rev. Lett. **65**, 1020 (1990)

[28] M. Goryll, L. Vescan, K. Schmidt, S. Mesters, H. Lüth, K. Szot, Appl. Phys. Lett. **71**, 410 (1997)

[29] M. Zinke-Allmang, L.C. Feldman, and M. H. Grabow, Surf. Sci. Rep. **16**, 377 (1992)

[30] M. Ohring, *The Materials Science of Thin Films*, Academic Press

[31] F. Silly and M. R. Castell, Phys. Rev. Lett. **96**, 086104 (2006)

[32] U. Lüders, F. Sánchez, and J. Fontcuberta, Phys. Rev. B **70**, 045403 (2004); U. Lüders, F. Sánchez, G. Herranz, I. C. Infante, J. Fontcuberta, M. V. García-Cuenca, C. Ferrater, and M. Varela, Nanotechnology **16**, S190 (2005)

4 Thin LCMO films: structure and composition

The source of structural data presented here is mainly X-ray diffraction (XRD) measurements. Complementary high-resolution transmission electron microscopy (HRTEM) images, nuclear magnetic resonance (NMR) spectra, electron energy loss spectroscopy (EELS) measurements, X-ray photoelectron spectroscopy (XPS) and X-ray absorption spectroscopy (XAS) measurements are presented.

We present detailed XRD measurements of LCMO films with a range of thickness of 8 nm to 150 nm grown on (001) and (110) STO. The films present a cube-on-cube epitaxial relationship with the substrate and from reciprocal space maps (RSMs) we have determined unit cell parameters and evaluated the unit cell volume.

Cross section HRTEM images have provided an overlook of the microstructure and have shown the absence of remarkable defects in the observed regions. Using EELS experiments, we have analyzed the distribution of Ca and La ions through the films, as well as the electronic state of Mn ions. Besides to EELS, NMR experiments on a series of films of different thickness have allowed investigating in detail the ionic state of Mn atoms ($Mn^{3+/4+}$ mixed states, and Mn^{3+} and Mn^{4+} localized states). The cationic differences between (001) and (110) films exposed surface has been studied by (XPS), signaling a significant superficial segregation of Ca in the (001) films. XAS experiments revealed the presence of $Mn^{3+/4+}$ state and no traces of spurious Mn^{2+}, Mn^{3+} or Mn^{4+} phases are found on the film surface.

4.1 Epitaxy of LCMO films: Structural properties

The orthorhombic LCMO can be also approximately described by a cubic cell. The lattice parameter of the pseudocubic LCMO is 3.863 Å, very close to the lattice parameter of STO substrates (cubic, 3.905 Å). The lattice mismatch is then small, $f = (a_{STO} - a_{LCMO}) / a_{LCMO} = + 1.1$ %, thus epitaxial growth with cube-on-cube epitaxial relationships is expected. Since the unit cell of the LCMO film is smaller than that of the substrate ($a_{LCMO} < a_{STO}$), films will suffer a tensile epitaxial stress, and then before lattice relaxation, in-plane parameters will be tensily strained.

We present in this section the studies focused on the crystalline characteristics of LCMO films grown on (001) and (110) substrates:

1. Using θ-2θ scans, the texture and the out-of-plane unit cell parameter are determined.
2. With ω-scans (rocking curves) the spread of out-of-plane axis.
3. Pole figures and φ-scans are used to deduce film epitaxial relationships.
4. Both in-plane and out-of-plane unit cell parameters, and thus the unit cell volume, are obtained with reciprocal space maps (RSMs) in samples of different thickness.

The results shown in this section are extracted from the samples listed in Table 4.1, where we include also the corresponding thickness and substrate.

Table 4.1. List of LCMO samples used for this section.

Sample	Substrate	Sample	Substrate	Thickness (nm)
280504A	STO(001)	280504B	STO(110)	8
070704A	STO(001)	070704B	STO(110)	14
180304AA	STO(001)	180304BB	STO(110)	17
240204A	STO(001)	240204B	STO(110)	43
230204A	STO(001)	230204B	STO(110)	63
290504A	STO(001)	290504B	STO(110)	80
200204A	STO(001)	200204B	STO(110)	85
270504A	STO(001)	270504B	STO(110)	93
090704A	STO(001)	090704B	STO(110)	110
050406A	STO(001)	050406B	STO(110)	150

4.1.1 θ-2θ scans: LCMO texture and out-of-plane unit cell parameter

The first study of the crystal structure of LCMO films was performed by investigating symmetrical reflections. In Figure 4.1, representative θ-2θ scans of a pair of (001) and (110) samples are shown. All the peaks correspond to diffraction from the

STO substrate and $La_{0.67}Ca_{0.33}MnO_3$ film. For all the possible (*hkl*) diffraction peaks, where *h*, *k*, *l* correspond to the Miller indices, the appearance of only (00*l*) peaks for films grown on (001) STO substrate ensures the alignment of STO and LCMO c-axis, and thus the (001) texture is confirmed in these films. For that grown on (110) STO substrates, (110) texture occurs, as it is seen from the observed (*hk*0) peaks, with $h = k$. Thus, the films are fully textured and there are no impurity crystalline phases within experimental resolution. It has to be noted that film peaks occur at higher angles than those expected for the bulk material, indicating smaller out-of-plane lattice distances (d_{001} and d_{110}, respectively) than those of the bulk. This results from the tensile strain imposed by the substrate on the basal plane of LCMO.

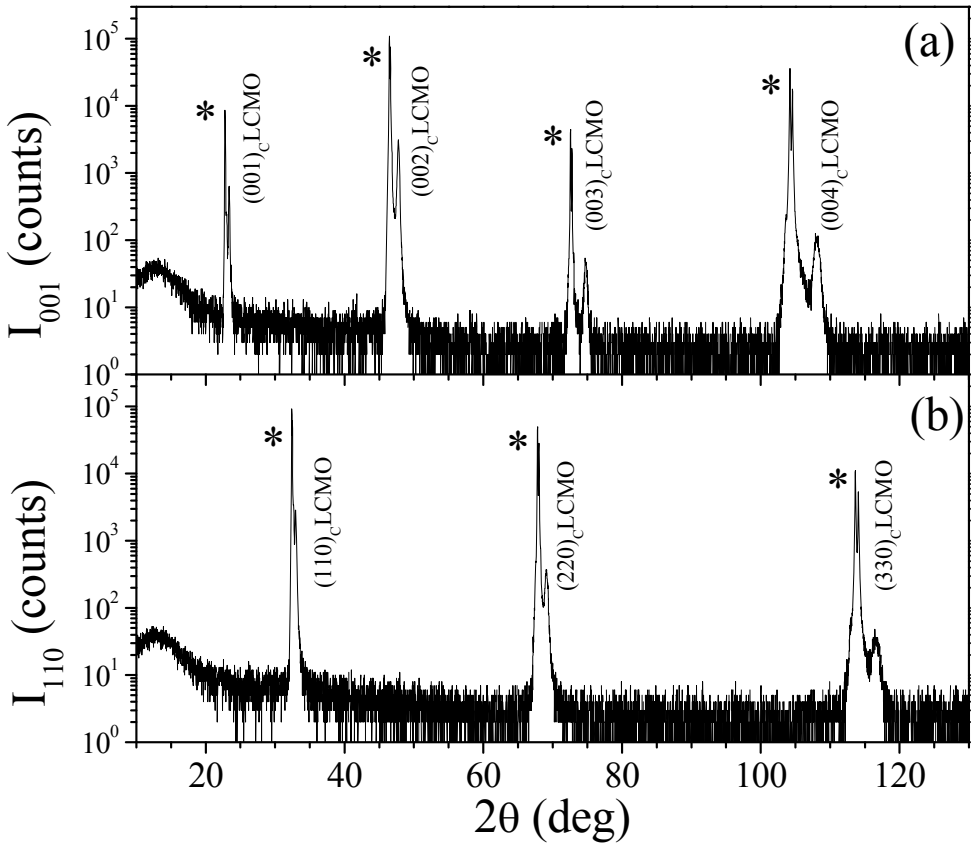

Figure 4.1. θ-2θ scans (step = 0.02 deg) of simultaneously grown LCMO film on (a) STO (001) and (b) STO (110) substrates). Films thickness is 85 nm. The scans show for (001) and (110) substrates the corresponding film texture, with (00*l*) peaks for (001) films and (*hk*0) peaks with $h = k$ for (110) ones. No parasite phases are found. Substrate peaks are marked by asterisks (*).

The out-of-plane parameter of (001) and (110) films was calculated from θ-2θ scans. The high angle reflections, which present a wider angular separation of the substrate and film reflections, were used. The zooms of the θ-2θ scans are shown in Figure 4.2, being in the range of 100 deg-120 deg for the (001) films and 110 deg-130 deg for the (110) ones, which include the substrate and film (004) peaks for (001) samples and (330) peaks for (110) ones. It is expected that the thicker the film, the higher the tendency of the unit cell parameters to approach its bulk values. Under the tensile strain induced by the STO substrate on the LCMO unit cell, the out-of-plane parameter is compresed. For the (001) films with thickness from 8 nm to 150 nm only a minor variation in the position of the (004) peak towards lower angles is appreciated (see the arrow in Figure 4.2a).

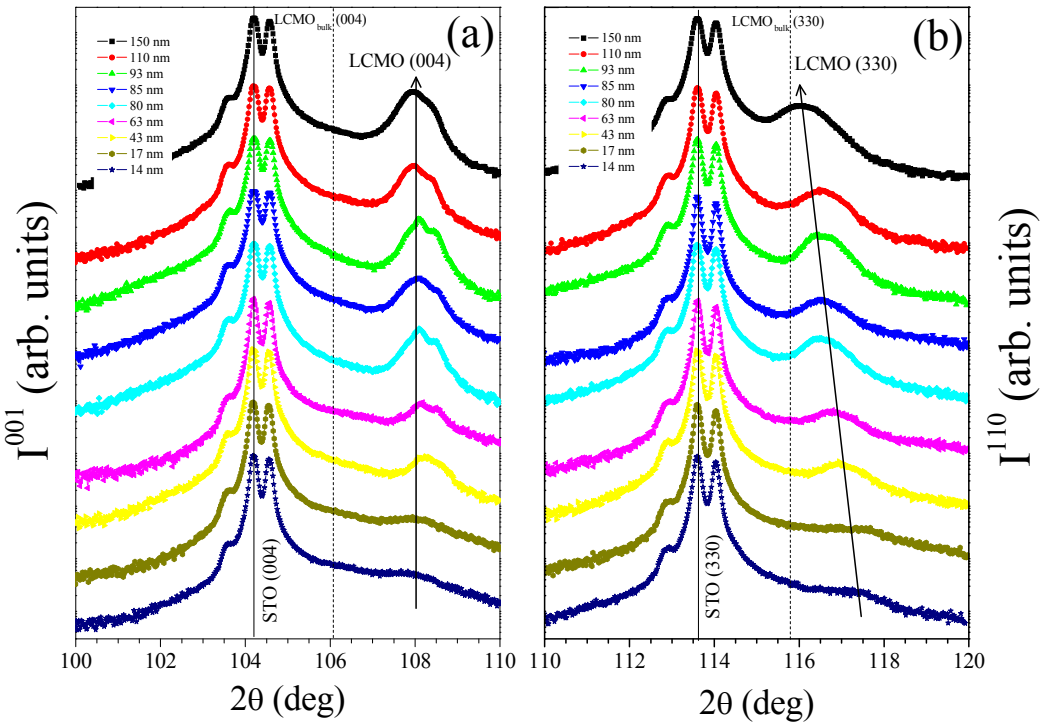

Figure 4.2. θ-2θ scans from samples ranging 14 nm to 150 nm thickness: (a) (001) films, and (b) (110) films. For both series of spectra, STO (004) and STO (330) peak positions were corrected correspondingly. As references for (001) and (110) film spectra, the dash lines indicate the position of bulk (004) LCMO and (330) LCMO bulk peaks, respectively.

For the case of (110) films (Figure 4.2b), the shift of the (330) peak towards lower 2θ values with increasing thickness is more relevant (see the arrow). The

progressive relaxation of out-of-plane parameter of (110) films is then deduced from this shift.

For the calculation of the out-of-plane parameter from the θ-2θ scans, each θ-2θ curve was first shifted as much as necessary to achieve the STO reference angle (θ_{004} = 104.17 deg, θ_{330} = 113.60 deg). After the correction, the calculation of the lattice parameter was done as explained by means of the case of the 43 nm films (Figure 4.3). The out-of-plane parameter can be extracted from a single peak or can be determined more accurately by a method which consists in approximately defining film peak position or either by fitting to appropriate pseudo-Voigt curves. In case of using the approximate method, from the experimental data, the mean value ($2\theta_{hkl}$) at which the film peak maximum appears is determined and with the average wavelength of the Cu emission spectrum [$\lambda(K_{\alpha\,av})$ = 1.54187 Å], applying Bragg diffraction law:

$$2d_{hkl}\,\mathbf{sin}\,\theta_{hkl} = \lambda \qquad [4.1]$$

where d_{hkl} is the out-of-plane interplanar distance with pseudocubic lattice parameter *d*, being $d_{hkl} = d/\sqrt{(h^2+k^2+l^2)}$.

In Figure 4.3, the film reflections are marked with arrows. Peak positions and interplanar distances for the (001) film (Figure 4.3a) are $2\theta_{004}$ = 108.38 deg and thus d_{001} = 3.803 Å, while for the (110) film (Figure 4.3b) $2\theta_{330}$ = 116.97 deg and thus $\sqrt{2}d_{110}$ = 3.837 Å.

For the second method, the process is slightly more complicated due to the fits to pseudo-Voigt functions, each of one with a general expression of:

$$y = y_0 + A\left(\mu\frac{2}{\pi}\left(\frac{\omega}{4(x-x_c)^2+\omega^2}\right)-(1-\mu)\left(\frac{\sqrt{4\ln 2}}{\sqrt{\pi}\omega}\right)\exp\left(-\frac{4\ln 2}{\omega^2}(x-x_c)^2\right)\right) \qquad [4.2]$$

where y_0 is the offset, A is the amplitude, μ means the relative importance of Gaussian and Lorentz components ($0 \le \mu \le 1$, being μ = 0 pure Gaussian and μ = 1 pure Lorentz), ω is the function width, and x_c corresponds to the centre of the curve. Two are the main wavelengths of the Cu emission spectrum: $\lambda(K_{\alpha1})$ = 1.5406 Å and $\lambda(K_{\alpha2})$ = 1.5444 Å. It means that considering both the substrate and film reflections, four pseudo-Voigt functions are needed. Besides, the angular relation of each pair of reflections will be determined by Bragg diffraction law (eq. 4.1) applied to Cu emission wavelengths $\lambda(K_{\alpha1})$ and $\lambda(K_{\alpha2})$. Thus, the angular relation will be $\sin\theta_1 / \sin\theta_2 = \lambda(K_{\alpha1}) / \lambda(K_{\alpha2})$ between corresponding substrate and film pair of peaks.

The results are shown in the lower panel of Figure 4.3. The final out-of-plane parameters calculated from the $K_{\alpha 1}$ peaks are d_{001} = 3.803(5) Å and $\sqrt{2}d_{110}$ = 3.836(6) Å.

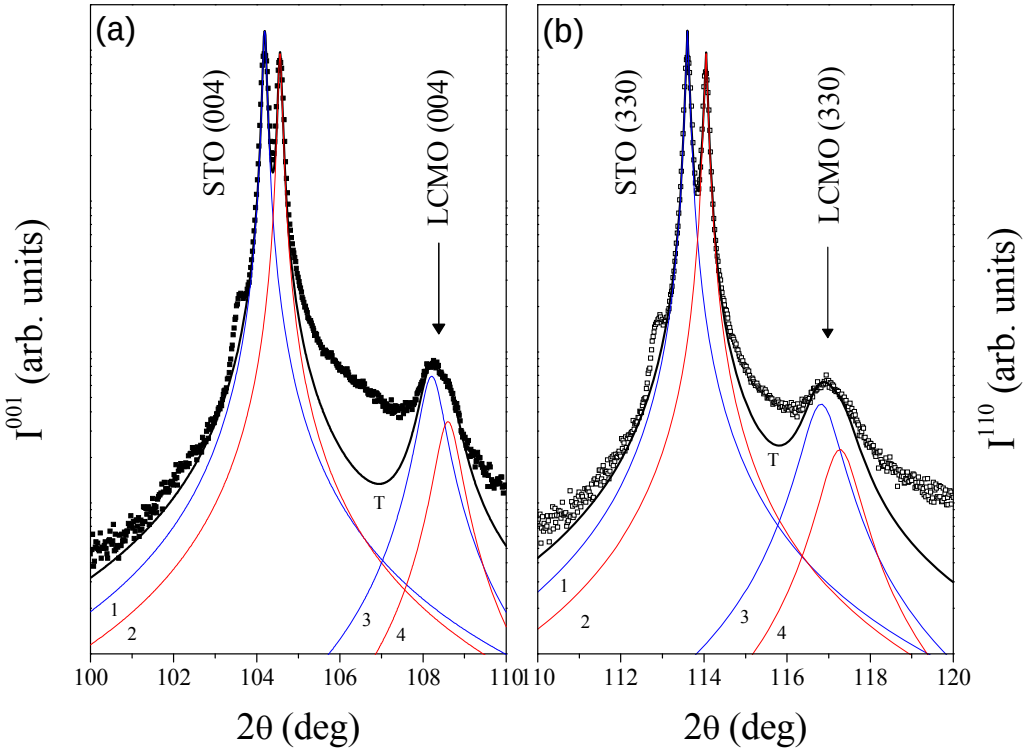

(a)

y0	0		
STO λ($K\alpha_1$)		LCMO λ($K\alpha_1$)	
xc1	104.19	xc3	108.21
A1	2100	A3	65
ω1	0.1	ω3	0.6
μ1	1	μ3	1
STO λ($K\alpha_2$)		LCMO λ($K\alpha_2$)	
xc2	104.56	xc4	108.6
A2	1500	A4	32.5
ω2	0.1	ω4	0.6
μ2	1	μ4	1

(b)

y0	0		
STO λ($K\alpha_1$)		LCMO λ($K\alpha_1$)	
xc1	113.61	xc3	116.82
A1	2100	A3	64
ω1	0.1	ω3	0.9
μ1	1	μ3	1
STO λ($K\alpha_2$)		LCMO λ($K\alpha_2$)	
xc2	114.05	xc4	117.28
A2	1500	A4	32
ω2	0.1	ω4	0.9
μ2	1	μ4	1

Figure 4.3. Zoomed θ-2θ scans of (a) (004) reflection (close symbols) and (b) (330) one (open symbols) obtained from 43 nm films. The arrows mark the mean angular positions of corresponding LCMO (330) peaks. Numbered curves 1 and 2 (lines) correspond to λ($K_{\alpha 1}$) and λ($K_{\alpha 2}$) pseudo-Voigt fits to the STO reflection, respectively. Similarly, numbered curves 3 and 4 (lines) are pseudo-Voigt fits to the LCMO reflection. The total fitting curve (sum of pseudo-Voigt contributions from STO and LCMO) is indicated in by T. Fitting parameter values are shown in lower panel; the units of x_c and ω are deg.

The agreement of the results of both methods in these couple of 43 nm films and in other samples of different thickness (not shown) allowed us to extensively use the

approximate method as a less time-consuming and adequate procedure to extract the out-of-plane parameters.

Finally, from θ-2θ scans of Figure 4.2, and using the approximate method, the calculated out-of-plane parameters are shown in Table 4.2, with the quotient c / a_{LCMO}. All the samples with the same thickness are placed side by side, although there were slight variations on thickness measured from XRR (see Ch2). A clear conclusion is achieved after the comparison of (001) and (110) data in Table 4.2: the out-of-plane parameter is more compressed in (001) films, compared to that of (110) films of the same thickness.

Table 4.2. Out-of-plane pseudocubic parameter calculated from θ-2θ scans and their corresponding percentage of pseudocubic a_{LCMO} that each one represents

Thickness (nm)	(001)		(110)	
	d_{001} (Å)	d_{001}/a_{LCMO} (%)	$\sqrt{2}d_{110}$ (Å)	$\sqrt{2}d_{110}/a_{LCMO}$ (%)
14	3.810	98.63	3.829	99.12
17	3.809	98.60	3.824	98.99
43	3.803	98.45	3.837	99.33
63	3.805	98.50	3.840	99.39
80	3.806	98.53	3.844	99.51
85	3.806	98.52	3.845	99.52
93	3.807	98.55	3.844	99.52
110	3.809	98.60	3.842	99.46
150	3.812	98.68	3.856	99.82

4.1.2 ω-scans: out-of-plane axis dispersion

Another study of the film crystal structure was focused on quantifying the texture by measuring the dispersion from the growth direction. With ω-scans (rocking curves) taken from symmetric reflections, it is obtained the spread of film out-of-plane crystal axis, being the rocking curve corresponding to the substrate measured to account for the instrumental width. For (001) films, the (002) reflection was selected and for (110) films the (220) one. Some examples of these rocking curves are presented in Figure 4.4. Normalized experimental data from films of 17 to 85 nm thickness are shown together with the corresponding pseudo-Voigt fitting curves. Full width at half maximum (FWHM) allows quantifying the misorientation of out-of-plane crystal axis of the films.

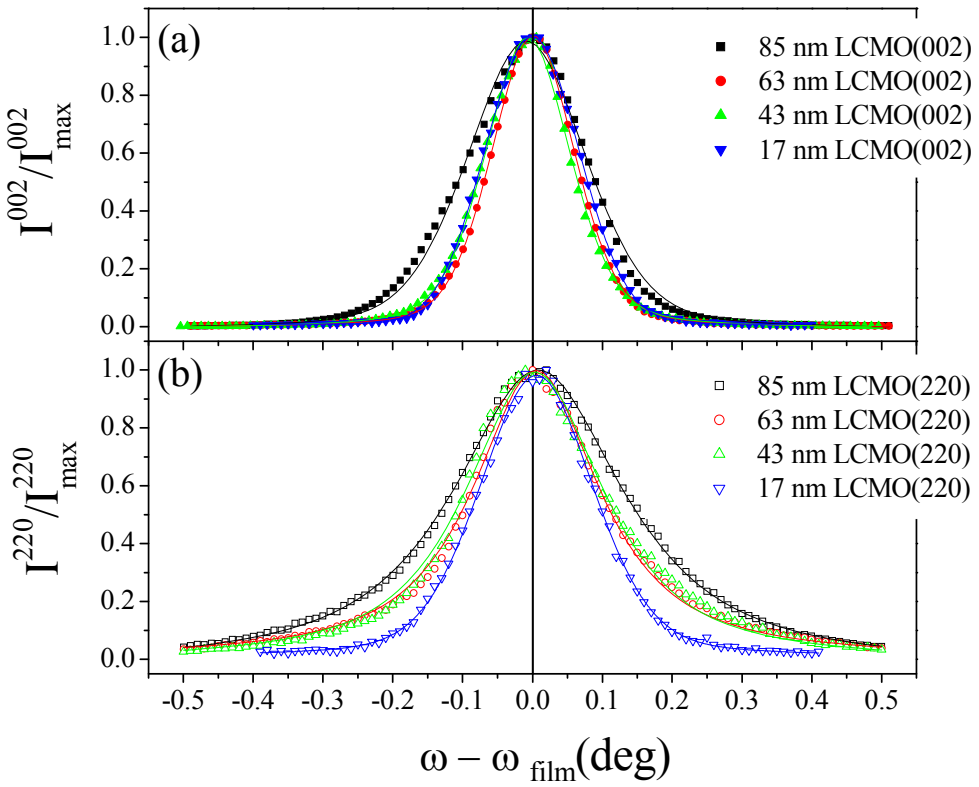

Figure 4.4. Rocking curves from ly 17 nm, 43 nm, 63 nm and 85 nm thick (a) (001) films (closed symbols) and (b) (110) ones (open symbols). The corresponding reflections are (002) for (001) films and (220) for (110) films. Lines are pseudo-Voigt fits to the raw data.

Table 4.3. Experimental FWHM obtained from LCMO rocking curves of Figure 4.4 and corresponding STO substrates.

Thickness (nm)	$FWHM_{STO(002)}$ (deg)	$FWHM_{LCMO(002)}$ (deg)	$FWHM_{STO(220)}$ (deg)	$FWHM_{LCMO(220)}$ (deg)
17	0.143	0.159	0.210	0.193
43	0.126	0.142	0.156	0.227
63	0.119	0.141	0.131	0.208
85	0.142	0.198	0.164	0.277

An inspection of Table 4.3 with values of FWHM from both the films (curves in Figure 4.4) and substrates (not shown) allows quantifying the crystal quality (concerning texture) of the film. The reference substrate peak has FWHM range of 0.12 deg to 0.16 deg due to instrumental limitations. From the curves depicted in Figure 4.4 and values shown in Table 4.3 it is derived that (110) films present a larger spread of the out-of-plane crystal axis. Besides, it exists in both kind of films a thickness

dependence of this c-axis spread. The increase in FWHM recalls the fact that at higher thickness the film lattice progressively suffers a slight misorientation.

4.1.3 Pole figures and φ-scans: epitaxy

It is also of major importance to determine the in-plane orientation of the films in order to verify if they have grown epitaxially and if they present the expected cube-on-cube epitaxial relationship with the substrate. Asymmetric reflections (poles) provide information about the in-plane parameters. The criterion to select the appropriate reflection is based on using those poles involving a simple analysis. With this purpose, the used poles correspond to planes with in-plane component parallel to one of the main crystallographic directions. For each orientation, and working in pseudocubic notation, we describe the crystal lattice using three orthogonal real space vectors, two of them contained in the growth plane, referred as $\mathbf{u} = (u_x, u_y, u_z)$ and $\mathbf{v} = (v_x, v_y, v_z)$, and one vector perpendicular to it, referred as $\mathbf{w} = (w_x, w_y, w_z)$. For the (001) films, the used in-plane directions are [100] and [010] and the out-of-plane one [001], whereas for the (110) films, the in-plane directions are [-110] and [001] and the the out-of-plane one [110]. Once the base of vectors is established, for a given (*hkl*) plane, characterized by the real space direction [*hkl*], where *h*, *k*, *l* are the Miller indices, we deduce the linear combination of the vectors from the real space base which leads to the [*hkl*] direction, as follows:

$$[hkl] = a[u_x u_y u_z] + b[v_x v_y v_z] + c[w_x w_y w_z] \qquad [4.3]$$

being a, b and c scalars. In Figure 4.5 we present a scheme of the plane arrangement for the (001) (a) and (110) (b) unit cell as well as some examples of the crystal planes inspected.

Starting with the (001) case, the (202) plane provides a pole with pure in-plane component as shown in Figure 4.5a. Equivalent poles to (202) correspond to the (022), (-202) and (0-22) planes. In Table 4.4 we summarize the construction of these planes from the used base of vectors. As a reference, the angular position of these poles is calculated using the unit cell parameter of the STO. The (202) family of planes provides a total of four poles separated in φ by 90 deg. Thus, fixing the angles ω, 2θ, and χ and scanning on φ, a total of four poles can be recorded for the (202) and equivalent planes for (001) films. Continuing with the selected planes for the (110) case, the (-130) plane has pure in-plane component along [-110] direction as shown in Figure 4.5b, similarly

to the equivalent (3-10) plane. In Table 4.4 the construction of these planes from the used base of vectors is included. Fixing all the angles and scanning φ, we expect to find a pole figure with two contributions appearing paralelly to the in-plane [-110] direction, thus separated in φ by 180 deg.

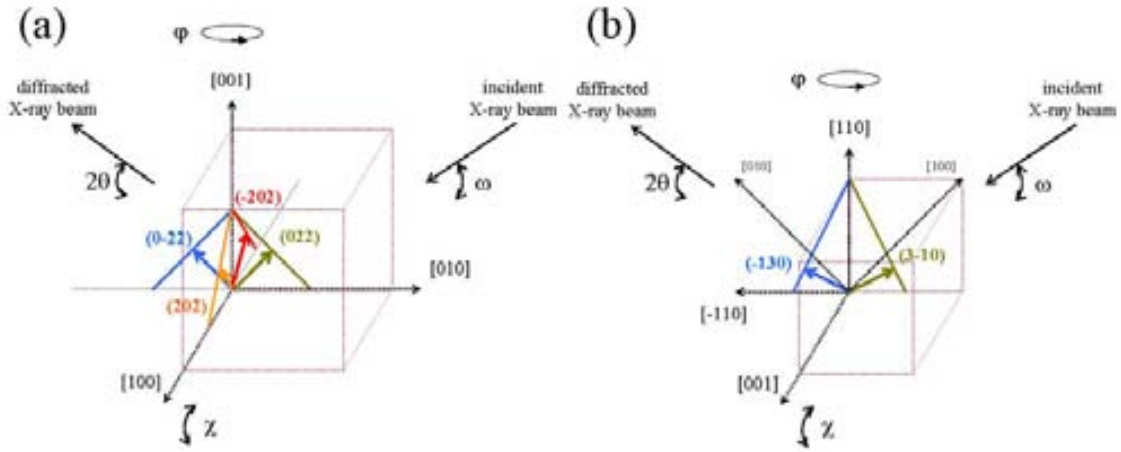

Figure 4.5. Schematic view of a pseudocubic (a) (001)-oriented and (b) (110)-oriented unit cell. For the (001) case, the planes indicated are the (202), (022), (-202) and (0-22) ones and for the (110) case, the (-130) and (3-10) ones. The in-plane and out-of-plane vectors for each case are also shown.

Table 4.4. Explored poles from the (*hkl*) planes from the (001) and (110) samples. The construction based on the linear combination of the corresponding vectors in-plane **u** and **v** vectors and out-of-plane **w** vector and using the scalars a, b and c. More details, in the text. 2θ values are calculated using the unit cell parameter of the STO substrate.

(001)	**h**	**k**	**l**	a	u_x	u_y	u_z	b	v_x	v_y	v_z	c	w_x	w_y	w_z	2θ (deg)	χ (deg)	φ (deg)
	2	**0**	**2**	2	1	0	0	0	0	1	0	2	0	0	1	67.83	45.00	0
	0	**2**	**2**	0	1	0	0	2	0	1	0	2	0	0	1	67.83	45.00	90
	-2	**0**	**2**	-2	1	0	0	0	0	1	0	2	0	0	1	67.83	45.00	180
	0	**-2**	**2**	0	1	0	0	-2	0	1	0	2	0	0	1	67.83	45.00	270

(110)	**h**	**k**	**l**	a	u_x	u_y	u_z	b	v_x	v_y	v_z	c	w_x	w_y	w_z	2θ (deg)	χ (deg)	φ (deg)
	-1	**3**	**0**	2	-1	1	0	0	0	0	1	1	1	1	0	77.19	63.43	0
	3	**-1**	**0**	-2	-1	1	0	0	0	0	1	1	1	1	0	77.19	63.43	180
	0	**3**	**1**	1.5	-1	1	0	1	0	0	1	1.5	1	1	0	77.19	47.87	25.24
	3	**0**	**1**	-1.5	-1	1	0	1	0	0	1	1.5	1	1	0	77.19	47.87	154.76
	3	**0**	**-1**	-1.5	-1	1	0	-1	0	0	1	1.5	1	1	0	77.19	47.87	205.24
	0	**3**	**-1**	1.5	-1	1	0	-1	0	0	1	1.5	1	1	0	77.19	47.87	334.76

We used Bruker diffractometer to perform the pole figures measurement. The system includes a bidimensional detector (GADDS), which allows recording at different

2θ and χ in a range of ± 15 deg for fixed ω. For obtaining pole figures of the substrate and the film, we need only to scan φ. The starting angular conditions, which correspond to the angular settings of the center of the detector, were for the (001) samples ω = 34.05 deg and 2θ = 68.01 deg (related to the (220) family of planes) and χ = 45 deg, and for the (110) samples ω = 38.5 deg and 2θ = 77 deg (related to the (-130) planes) and χ = 55 deg.

Examples of pole figures of (001) and (110) films of 110 nm thickness are shown in Figure 4.6 and Figure 4.7, respectively. For the (001) case, in Figure 4.6 both a simulation of the pole figure (a) and the experimental data (b) are presented. Exploring the 30 deg ≤ χ ≤ 60 deg and at 2θ = 68.9 deg, we observe in Figure 4.6b the (202), (022), (-202) and (0-22) poles of the LCMO film appearing at χ = 45 deg and separated by Δφ = 90 deg, in agreement with the simulated pole figure of Figure 4.6a. The pole figure of the STO substrate is obtained for 2θ = 67.9 deg and present (202) and equivalent poles at the same φ values.

Turning to the (110) case, in Figure 4.7 we plot the simulated (a) and experimental data (b) the poles appearing in the 40 deg ≤ χ ≤ 70 deg range. At 2θ = 78.2 deg, we observe the reflections of the two families of poles of the film: one family corresponds to the poles appearing at χ = 63.6 deg (two poles) and another family appear at χ = 47.7 deg (four poles) (Table 4.4). At χ = 63.6 deg, the (-130) and (3-10) poles present only [-110] in-plane component, which is very useful to determine the orientation of the sample with respect to the sample edges. The poles at χ = 47.7 deg, appear at φ = 25 deg from the [-110] direction (positive and negative side), which agrees with the predicted values (Table 4.4), and correspond to (031) and equivalent planes. For the STO substrate, the corresponding pole figure was measured at 2θ = 77.2 deg and presents the same features as those of the film with two families of poles presented at the same φ values than those of the film.

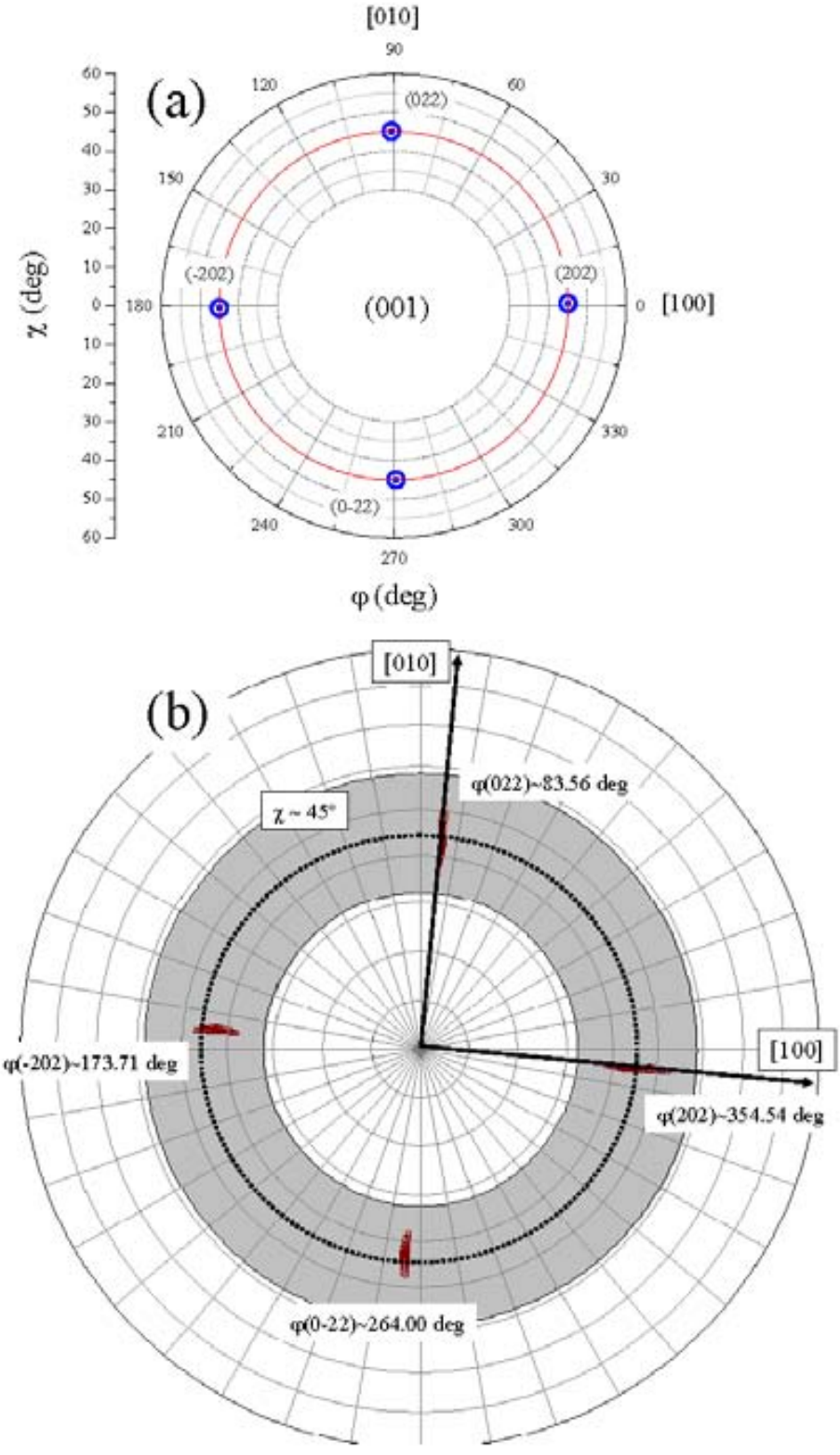

Figure 4.6. (a) Simulated pole figure of a (001) oriented film and (b) experimental pole figure obtained at $\omega = 34.05$ deg and $2\theta = 68.9$ deg. The in-plane directions are [100] and [010], being φ referred to [100] direction. The range of χ for both simulated and experimental data is 30-60 deg. In (b), χ and φ are referred as in (a) and for each pole the φ value is indicated.

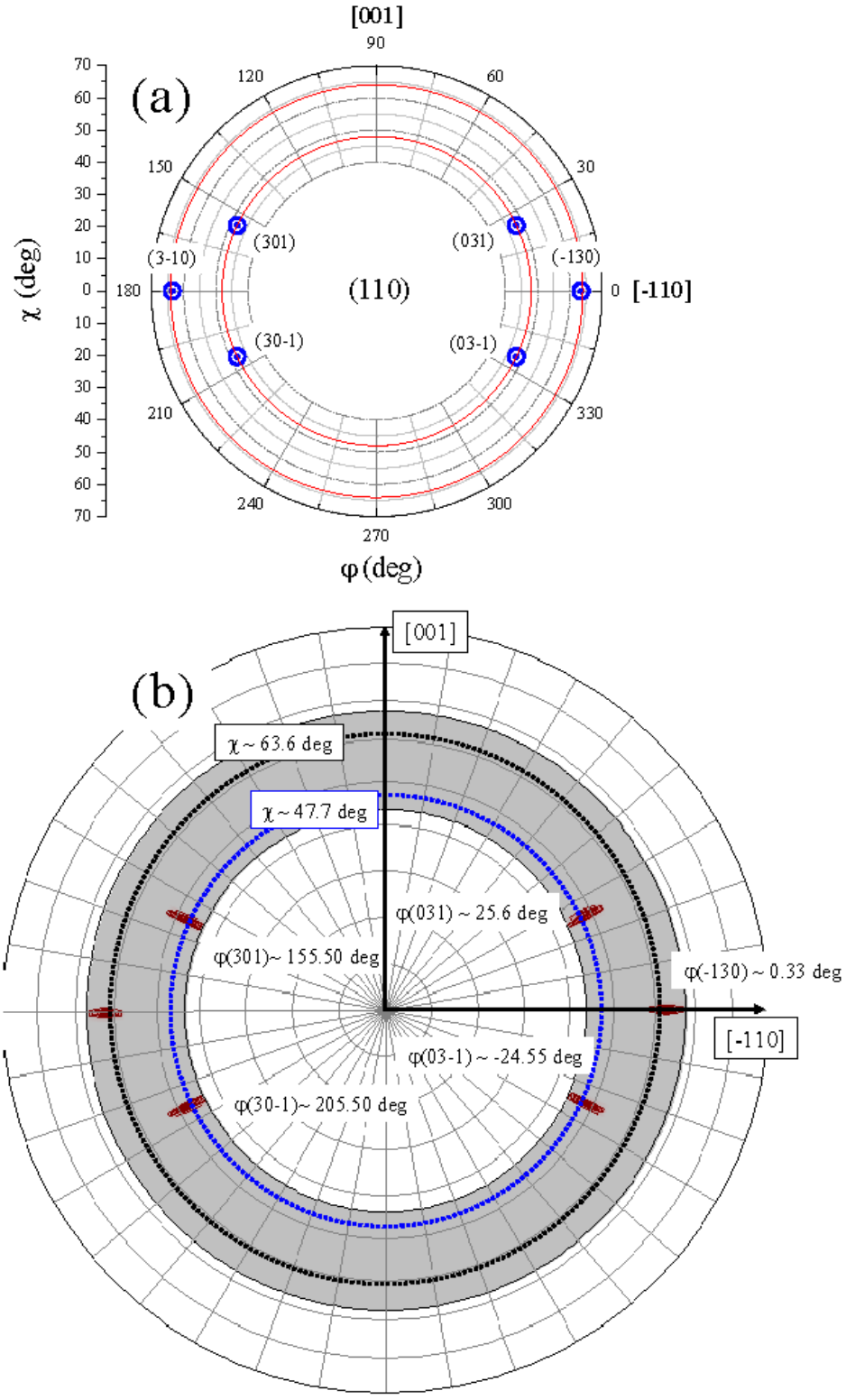

Figure 4.7. (a) Simulated pole figure of a (110) oriented film and (b) experimental pole figure obtained at ω = 38.5 deg and 2θ = 78.2 deg. The in-plane directions are [100] and [010], being φ referred to [100] direction. The range of χ for both simulated and experimental data is 40-70 deg. In (b), χ and φ are referred as in (a) and for each pole the φ value is indicated.

We recall that since the Bruker diffractometer is provided with a two-dimensional detector, we can obtain in a simultaneous measurement a range of ± 15 deg in 2θ and χ at a give φ value. Thus, a φ-scan can be extracted from the recorded pole figures if we can separate into the substrate and film peaks in the total pole figure measurement. With these scans, we can determine the epitaxial relationship of the in-plane parameters of film and substrate. First, we show examples of the angular separation in 2θ of substrate and film peaks in Figure 4.8a. For the (001) sample, we present the data around the (202) peak and for the (110) sample, the (-130) one. Using the acquired pole figure, we integrate for a given width of χ ($\Delta\chi \sim 5$ deg) the total recorded intensity as a function of 2θ for each φ value in a total range of $\Delta\varphi = 3$ deg around the film peak. In Figure 4.8a, the data corresponding to (001) and (110) samples allows separating the high intensity peak of the STO substrate from the low intensity peak of the LCMO film, although it is much clear in the (001) case. We note that in both cases the LCMO peak intensity is affected by the tail of the STO substrate, being more relevant in the data obtained from the (110) sample. As the peaks from the substrate and film have been identified, we can define the integration regions in χ working at the corresponding optimum values of 2θ (indicated by dashed lines in Figure 4.8a). The resulting φ-scans are shown in Figure 4.8b and c.

The φ-scan in Figure 4.8a, corresponding to the (001) film, was extracted from the pole figure recorded at $\omega = 34.05$ deg, $2\theta = 68.9$ deg and $\chi = 43.9$ deg with (202) and equivalent poles. The φ-scan of the (001) STO substrate corresponds to $\omega = 34.05$ deg, $2\theta = 67.9$ deg and $\chi = 44.6$ deg and to the same poles. The φ-scans of the (110) film and the (110) STO substrate are shown in Figure 4.8c. For the film, the angular settings were $\omega = 38.5$ deg, $2\theta = 78.2$ deg and $\chi = 63.1$ deg, thus focused only in the (-130) and (3-10) planes. The same reflections from the STO substrate were also observed at $\omega = 38.5$ deg, $2\theta = 77.2$ deg and $\chi = 63.9$ deg and similar φ values. The φ-scans indicate single crystal in-plane orientation for both (001) and (110) films with LCMO(001)[100]//STO(001)[100] and LCMO(110)[1-10]//STO(110)[1-10] epitaxial relationships, respectively.

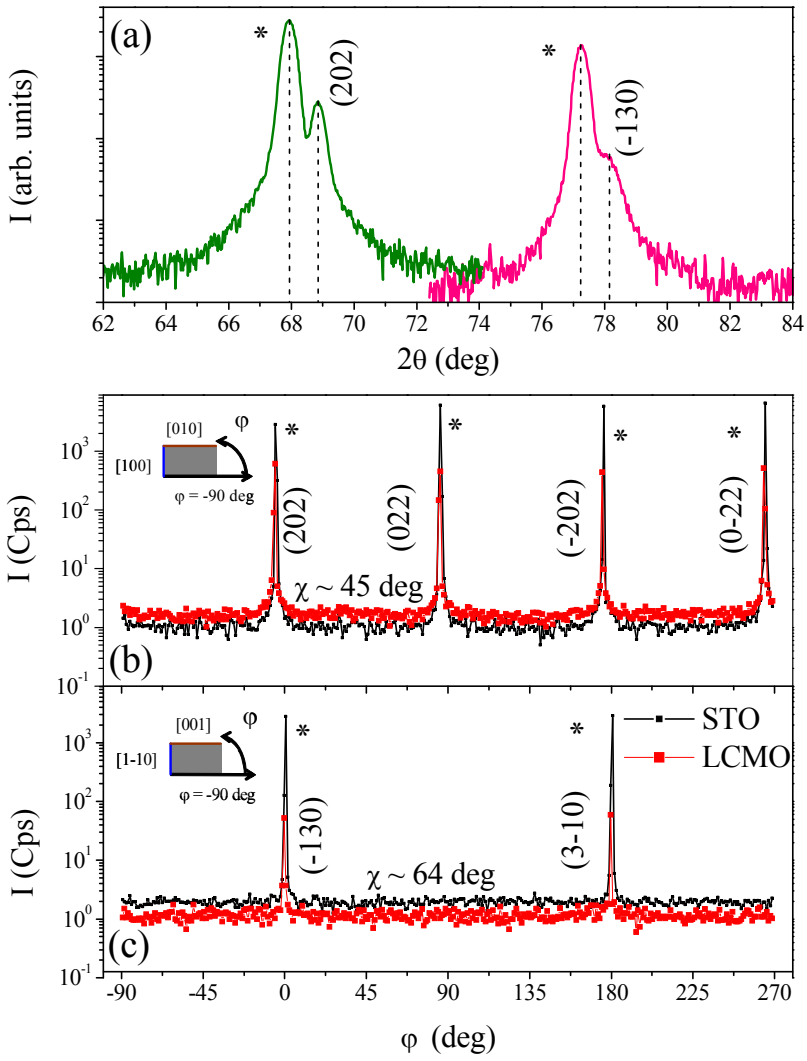

Figure 4.8. (a) Integrated intensity for Δφ = 3 deg as a function of 2θ for the (202) reflection of the (001) sample (left) and for the (-130) reflection of the (110) sample (right), showing the substrate [asterisks (*)] and the film peaks. [(b) and (c)] φ-scans extracted from complete pole figures (b) of the (001) film and (c) of the (110) one. From the analysis of peak position, sample crystal axes can be deduced and identified with respect to the sample borders. The χ value is written on the graph. In the insets, schemes of the sample shape showing the crystallographic axes.

4.1.4 Reciprocal space maps: unit cell parameters

In order to accurately obtain the in-plane unit cell parameters, reciprocal space maps (RSMs) were performed. With the RSMs, both out-of-plane and in-plane lattice strain can be studied. We have previously observed that the out-of-plane parameters

(obtained from θ-2θ scans, results in Table 4.2) increase (and thus relax) when increasing thickness (*t*) for $t > 20$ nm. This fact signals a thickness dependence of the lattice parameters. Then, RSMs are necessary to study in detail the complete unit cell. The experiments were performed using a four circle MRD Philips diffractometer provided of a point detector.

The first decision to take concerns the proper reflections to map, which depends on the angular separation of film and substrate peaks and intensity of the asymmetric reflection. Similarly to the analysis performed for the pole figures, from the in-plane and out-of-plane directions of the (001) and (110) samples we built the asymmetric reflections planes explored by RSMs. A series of 3 reflections were used in this work: one for (001) samples and two for (110) ones. In the analysis and discussion of RSMs, we describe the crystallographic directions using the pseudocubic notation:

(i) (001) samples: in-plane vectors **u** = (100) and **v** = (010), out-of-plane vector **w** = (001)

(ii) (110) samples: in-plane vectors **u** = (1-10) and **v** = (001), out-of-plane vector **w** = (110)

We note that for the RSMs measurements we used for the (110) films the in-plane direction **u** = (1-10) instead of the equivalent one (-110) used for the pole figures. The reflections were selected in order to simplify the analysis allowing extracting one of the in-plane components with no mixing of the other in-plane component. The chosen reflections are: the (103) reflection for the (001) samples, and the (130) and (222) reflections for the (110) samples,. The construction of the used reflections as a function of the vectors for (001) and (110) samples is included in Table 4.5. We note that the explored asymmetric reflections were measured fixing $\chi = 0$ and using a value of ω calculated from $\omega = \theta - \chi$. The final ω values are included in Table 4.5. Working at these conditions, the reciprocal space is described using only two angular variables ω and θ, that can be translated into orthogonal wave vectors: an in-plane (or parallel) component $q_{//}$, and an out-of-plane (perpendicular) components, $q_{\perp}$. The expressions to calculate $q_{//}$ and $q_{\perp}$ from the values of ω and θ are described in Ch2 and recalled here:

$$q_{//} = \frac{2}{\lambda}\sin(\theta)\sin(\theta - \omega) \qquad [4.3]$$

$$q_{\perp} = \frac{2}{\lambda}\sin(\theta)\cos(\theta - \omega) \qquad [4.4]$$

where λ corresponds to the wavelength of the incident X-ray beam.

Table 4.5. Explored reflections corresponding to the (*hkl*) planes from the (001) and (110) samples. The construction is based on the linear combination of the in-plane **u** and **v** vectors and out-of-plane **w** vector, using the scalars a, b and c. More details, in the text. ω and 2θ values are calculated using the unit cell parameter of the STO substrate.

	h	**k**	**l**	a	u_x	u_y	u_z	b	v_x	v_y	v_z	c	w_x	w_y	w_z	ω (deg)	2θ (deg)	χ (deg)	φ (deg)
(001)	**1**	**0**	**3**	1	1	0	0	0	0	1	0	3	0	0	1	20.16	77.19	18.43	0
(110)	**1**	**3**	**0**	-1	1	-1	0	0	0	0	1	2	1	1	0	12.03	77.19	26.57	180
	2	**2**	**2**	0	1	-1	0	2	0	0	1	2	1	1	0	7.84	86.21	35.26	90

The procedure to obtain the unit cell parameters starts by determining the angular ω and 2θ values of the film and substrate reflections in the RSM of the (*hkl*) reflection. Using eqs. 4.3 and 4.4, we calculate the in-plane and out-of-plane wave vectors $q^{hkl}_{//}$ and $q^{hkl}_{\perp}$ which correspond to the studied reflection. We recall that to simplify the analysis, we have chosen reflections with pure in-plane **u** or **v** components. To pass from the reciprocal space lattice ($q^{hkl}_{//}$ and $q^{hkl}_{\perp}$ values) to the real space ones, we need to convert the $q^{hkl}_{//}$ and $q^{hkl}_{\perp}$ values to the real space and apply the corresponding scalars that relates the studied (*hkl*) reflection to the real space vectors **u**, **v**, and **w**. Following Table 4.5, for the (001) samples we have studied the (103) reflection, which correspond to the in-plane d_{100} distance and to the out-of-plane d_{001} one; using the a and c values for this reflection (Table 4.5), the final interplanar distances are calculated as follows:

$$d_{100} = \frac{a}{q_{//}^{103}} = d_{010} \qquad [4.5]$$

$$d_{001} = \frac{c}{q_{\perp}^{103}} \qquad [4.6]$$

For the (110) samples, the asymmetric reflections explored are (130) and (222). We extract the interplanar distances $d_{1\text{-}10}$, d_{001} and d_{110} similarly to the (001) case but applying the corresponding a, b and c scalars (Table 4.5):

$$d_{1\text{-}10} = \frac{|a|}{q_{//}^{130}} \qquad [4.7]$$

$$d_{001} = \frac{b}{q_{//}^{222}} \qquad [4.8]$$

$$d_{110} = \frac{c}{q_{\perp}^{130}} \; ; \; d_{110} = \frac{c}{q_{\perp}^{222}} \qquad [4.9]$$

Some RSMs from (103) reflection of the series of (001) films are plotted in Figure 4.9. Even for thinner films (Figure 4.9a), both the substrate and film peaks can be clearly identified. As it corresponds to smaller unit cell parameters, LCMO peak in the RSMs is found at higher q_{001} values than that of the substrate. In-plane unit cell parameters of all (001) films are completely clamped to those of the substrate, seen from the coincident value of q_{100} for both film and substrate peaks. The d_{100} (d_{010}) and d_{001} parameters are calculated using eqs. 4.5 and 4.6, respectively, and the resulting values are included in Table 4.6. The obtained d_{001} are similar to those previously showed in Table 4.2 calculated from θ-2θ scans. Thus, (001) films are fully strained with a slight variation of out-of-plane parameter which leads to a variation of unit cell volume, as it will be commented later on.

A selection of RSMs for (110) films is presented in Figure 4.10. In this case, as previously stated, two different reflections are needed, (130) and (222). As it happened for (001) films (Figure 4.9), substrate peak appears at lower $q_{1\text{-}10}$, q_{001} and q_{110} values. In the series of RSMs shown in Figure 4.10, it is remarkable that for thinner films (8 nm, Figure 4.10a and b) the in-plane parameters are almost the same as those of the STO. An increase in thickness triggers the progressive relaxation of both in-plane parameters towards lower values, closer to bulk ones, although along [1-10] direction the process becomes quicker. Thus, from a general inspection of the RSMs from (130) and (222) reflections signals that a relaxation process takes place in (110) films as the in-plane $q_{1\text{-}10}$ and q_{001} film wave vectors tend to higher values than those of the substrate. Moreover, the relaxation rate followed of $q_{1\text{-}10}$ and q_{001} is different. Thus, an anisotropic relaxation process is detected in (110) films as the film thickness increases. Using the values of the in-plane $q_{1\text{-}10}$ and q_{001} and out-of-plane q_{110} wave vectors and using eqs. 4.7-4.9, we evaluated the in-plane $d_{1\text{-}10}$ and d_{001} and out-of-plane d_{110} distances. The results are included in Table 4.6. The d_{110} values have been compared to those previously obtained by θ-2θ scans (Table 4.2) and they are found to be completely coherent.

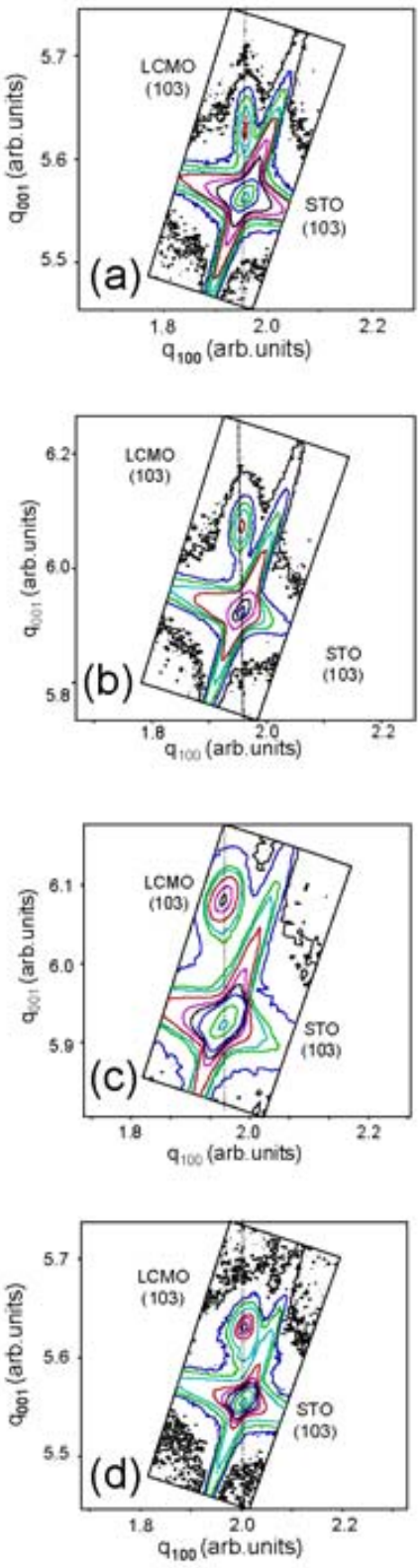

Figure 4.9. RSMs from STO (103) and LCMO (103) reflection from LCMO (001) films of thickness (a) 8 nm, (b) 17 nm, (c) 43 nm, and (d) 80 nm. Each line is a guide for the eye, signaling the vertical alignment of STO and LCMO peaks.

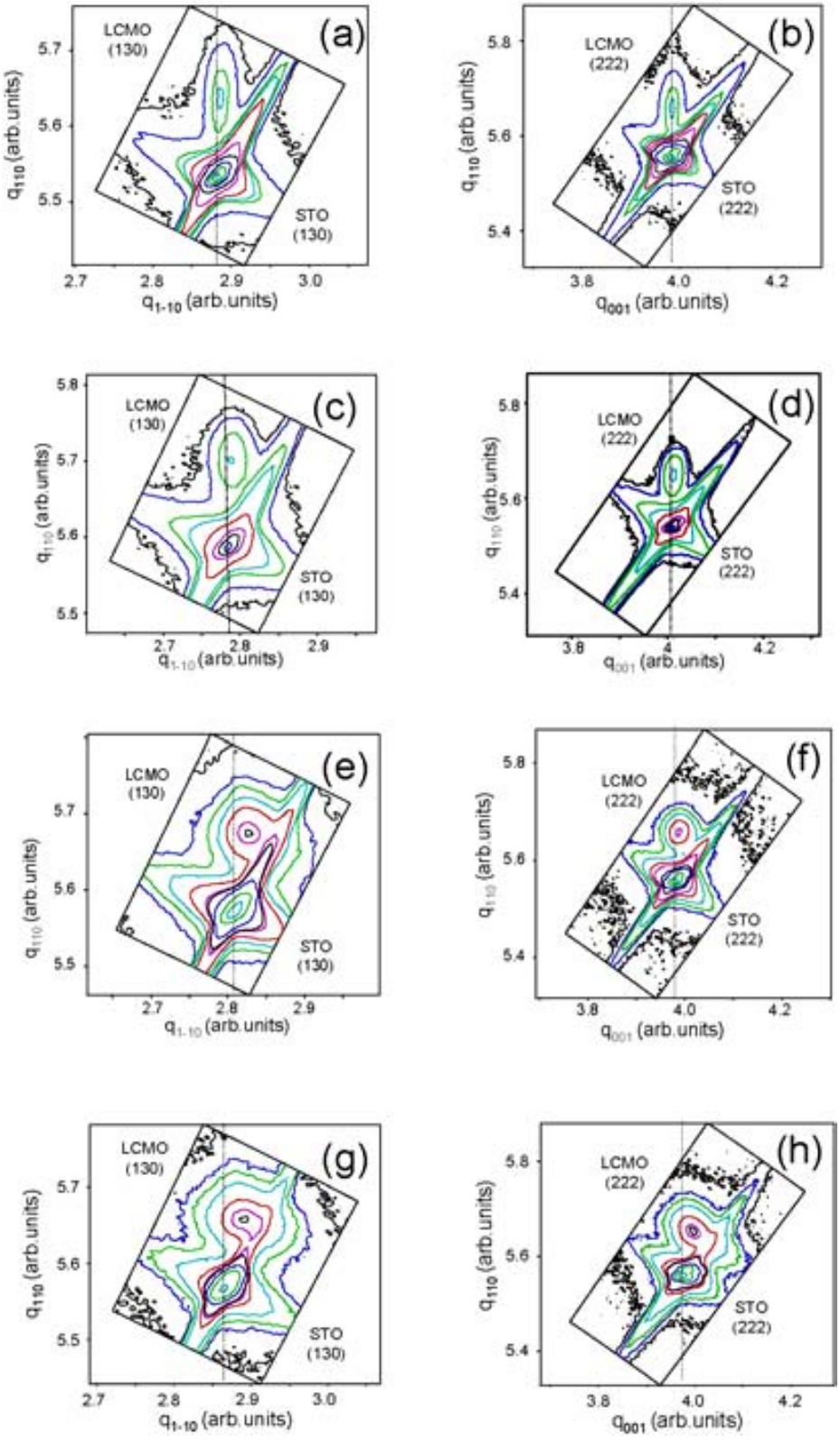

Figure 4.10. RSMs from STO (130) and LCMO (130) reflections (left column) and STO (222) and LCMO (222) ones(right column) from LCMO(110) films corresponding to film thickness of 8 nm [(a) and (b)], 17 nm [(c) and (d)], 43 nm [(e) and (f)], and 80 nm [(g) and (h)]. The lines are guides for the eye. Note the evolution of q_x from thinner to thicker films to higher values, a sign of relaxation of the in-plane parameter.

The summary of all the calculated in-plane and out-of-plane interplanar distances for (001) and (110) films with thickness in the 8 to 150 nm range are collected in Table 4.6 and plotted as a function of film thickness in Figure 4.11a. Focusing first in (001) films data (solid symbols), virtually no relaxation occurs for the in-plane interplanar distance d_{100} (solid triangles), which remains clamped to the substrate. The out-of-plane d_{001} distance (solid rhombi) displays a non-monotonic behavior: it contracts for films up to a critical thickness $t_c \approx 20$ nm and expands slightly for the $t > 40$ nm films, remaining well below the bulk value (indicated by the dashed line) even for $t \approx 150$ nm. The persistence of a strained state in LCMO (and other manganites) epitaxial thin films has been already reported [1][2].

Table 4.6. Unit cell parameters and volume per Mn ion of (001) and (110) films of thickness between 8 and 150 nm.

Thickness (nm)	(001)			(110)			
	$d_{100} = d_{010}$ (Å)	d_{001} (Å)	V_{001}/Mn (Å^3)	$\sqrt{2}d_{1\text{-}10}$ (Å)	d_{001} (Å)	$\sqrt{2}d_{110}$ (Å)	V_{110}/Mn (Å^3)
8	3.905	3.818	58.23	3.897	3.901	3.839	58.35
14	3.905	3.815	58.18	3.897	3.902	3.827	58.19
17	3.905	3.809	58.10	3.891	3.901	3.830	58.13
43	3.905	3.806	58.05	3.877	3.896	3.832	57.88
63	3.905	3.806	58.05	3.880	3.891	3.838	57.93
80	3.905	3.805	58.04	3.877	3.888	3.843	57.93
85	3.905	3.807	58.07	3.876	3.887	3.844	57.90
93	3.905	3.808	58.08	3.876	3.886	3.846	57.92
110	3.905	3.808	58.09	3.877	3.884	3.844	57.88
150	3.903	3.810	58.05	3.860	3.866	3.858	57.58

Still in Figure 4.11a, (110) films (open symbols) present a gradual structural relaxation for both in-plane directions [001] and [1-10] as well as the out-of-plane one [110]. For the in-plane directions, the relaxation process occurs at different rates, being [1-10] faster than [001]. Even when comparing with (001) films, the in-plane distances d_{001} and $d_{1\text{-}10}$ relax much faster than the in-plane distance d_{100} in (001) films. At thicker films (150 nm thick) the relaxation is almost complete. About anisotropy in strain relaxation for oxide films grown on STO(110), only a few references [3] report on it. Concerning the out-of-plane distance, d_{110}, it displays a non-monotonic behavior similar to the one observed in (001) films: it contracts up to a critical thickness of $t_c \approx 20$ nm and it expands for further increase of thickness, approaching the bulk values for thickest film $t = 150$ nm.

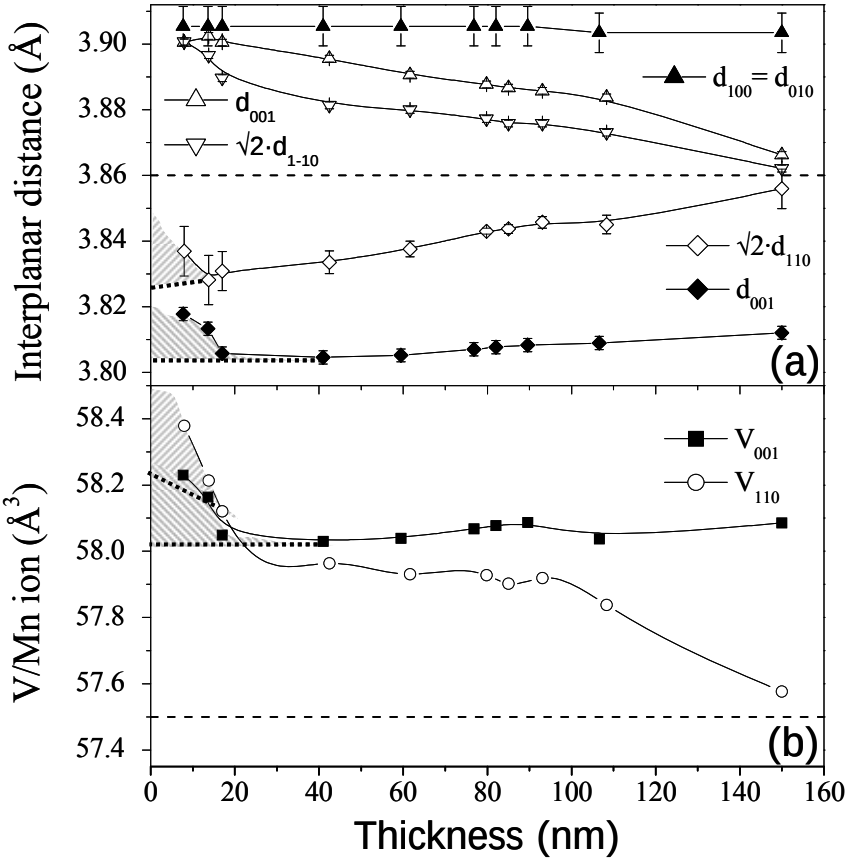

Figure 4.11. Thickness dependence of (a) interplanar distances and (b) unit cell volume for the (001) and (110) films. The dashed lines indicate the pseudocubic (a) unit cell parameter and (b) unit cell volume of bulk LCMO. To make interplanar distances comparable, for (001) films we plot d_{100} and d_{001} and for (110) films $\sqrt{2}d_{1\text{-}10}$, d_{001} and $\sqrt{2}d_{110}$.

Therefore, the response of (001) and (110) films to the identical lattice mismatch imposed by the substrate is qualitative and quantitatively different; however, a common trend is identified, namely the evidence of a critical thickness t_c that separates the well-defined regions in the thickness dependence of the out-of-plane interplanar distance. The data corresponding to the low thickness films ($t < t_c$) cannot be explained with arguments related to an elastic or a plastic deformation of the unit cell with thickness. In order to emphasize the existence of two different regions, linear extrapolation of the out-of-plane cell parameter has been performed as a function of thickness from $t > t_c$ towards $t \rightarrow 0$. Dashed areas in Figure 4.11a indicate a range of thicknesses where out-of-plane cell parameters are substantially larger from what could be expected from the monotonic variation observed above t_c.

Unit cell volume values of (001) (close symbols) and (110) (open symbols) films with thickness are also included in Table 4.6 and depicted in Figure 4.11b. Important remarks should be addressed from the analysis of these data:

(i) The unit cell volume of the (001) and (110) films (V_{001} and V_{110} respectively) are substantially larger than the bulk value V_{LCMO} (indicated by a dashed line in Figure 4.11b): $V_{001}, V_{110} \geq V_{LCMO}$

(ii) Upon increasing thickness, V_{001} changes slightly, remaining above the bulk value even for the thickest film: $V_{001} \approx$ constant

(iii) The gradual reduction of the unit cell volume is clearly pronounced for the (110) films: for $t > 30$ nm, $V_{110} < V_{001}$ and at $t \approx 150$ nm, V_{110} reaches the bulk value.

Remembering that it is widely assumed that the strain effects cause the film unit cell volume to be conserved, experimental data in Figure 4.11b clearly do not support this assumption. Moreover, these data also reveal that for films with thickness below t_c, the unit cell volume displays a rapid expansion which is more pronounced than what could be expected from a simple linear extrapolation towards $t \rightarrow 0$. Dashed areas in Figure 4.11b illustrate the anomalous unit cell volume regions for (001) and (110) films, mimicking the corresponding regions in the out-of-plane interplanar distance evolution shown in Figure 4.11a.

In summary, the analysis of XRD measurements performed on epitaxial LCMO films grown on (001) and (110) STO substrates reveal the occurrence of (001) and (110) texture and of cube-on-cube epitaxy in both families of films. The accurate study of unit cell parameters in these films signals a different strain state in (001) and (110) films, which evolves dissimilarly with thickness, being in the case of (110) films associated to a faster and anisotropic unit cell relaxation.

4.2 Epitaxy of LCMO films: microstructure by HRTEM

For an accurate structural study of the substrate-film interface, cross section transmission electron microscopy (XTEM) images have been studied. This work was performed by S. Estradé, from the Universitat de Barcelona, and it is included in her PhD thesis. More details on sample preparation are described in Ch2. The samples used for this study are included in Table 4.7.

Table 4.7. List of samples for HRTEM experiments.

Sample	Substrate	Sample	Substrate	Thickness (nm)
050329A	STO(001)	050329B	STO(110)	8

Low magnification XTEM images from (001) and (110) films of $t = 8$ nm are presented in Figure 4.12. The images do not show the presence of defects. Other authors have reported in thick $La_{0.7}Ca_{0.3}MnO_3$ films grown either under tensile strain, on (001) STO, or under compressive strain, on (001) $LaAlO_3$, the development of secondary phases [4]. Besides, Lebedev et *al.*[5] found in $La_{0.7}Ca_{0.3}MnO_3$ films on (001) STO not only columnar defects but also islands of LCMO in the free surface of thinner films: Their conclusion is that these islands should be a mechanism of relieve of elastic energy in the system. Our actual TEM images of thin LCMO fully strained films (Figure 4.12 and Figure 4.13) signal the absence of islands or columnar defects.

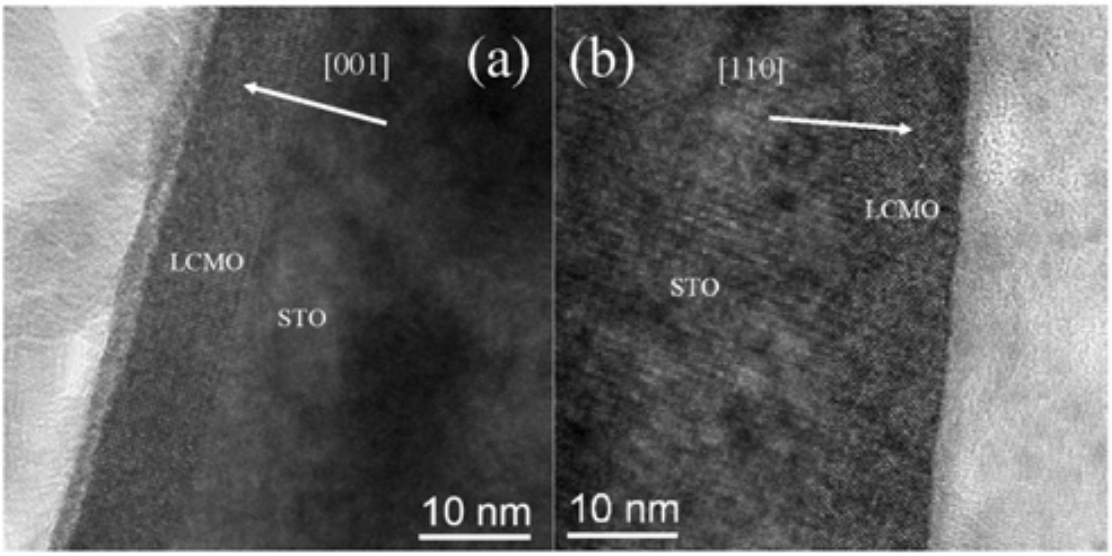

Figure 4.12. Low magnification TEM images from 8 nm films with (a) (001) and (b) (110) orientation. The corresponding growth direction is indicated by arrows.

In order to investigate film microstructure and film-substrate interface, high resolution XTEM images are taken and shown in Figure 4.13. With the purpose of evaluating the crystallographic features in these films, the corresponding fast Fourier transforms (FFTs) (Figure 4.13i and ii for (001) sample and Figure 4.13v and vi for (110) sample) of these images have been performed in both substrate and film areas. Besides, to enlighten the quality of the interface region, detailed zooms around this area

have been selected and carefully studied (Figure 4.13iii and iv for (001) sample and Figure 4.13vii and viii for (110) sample).

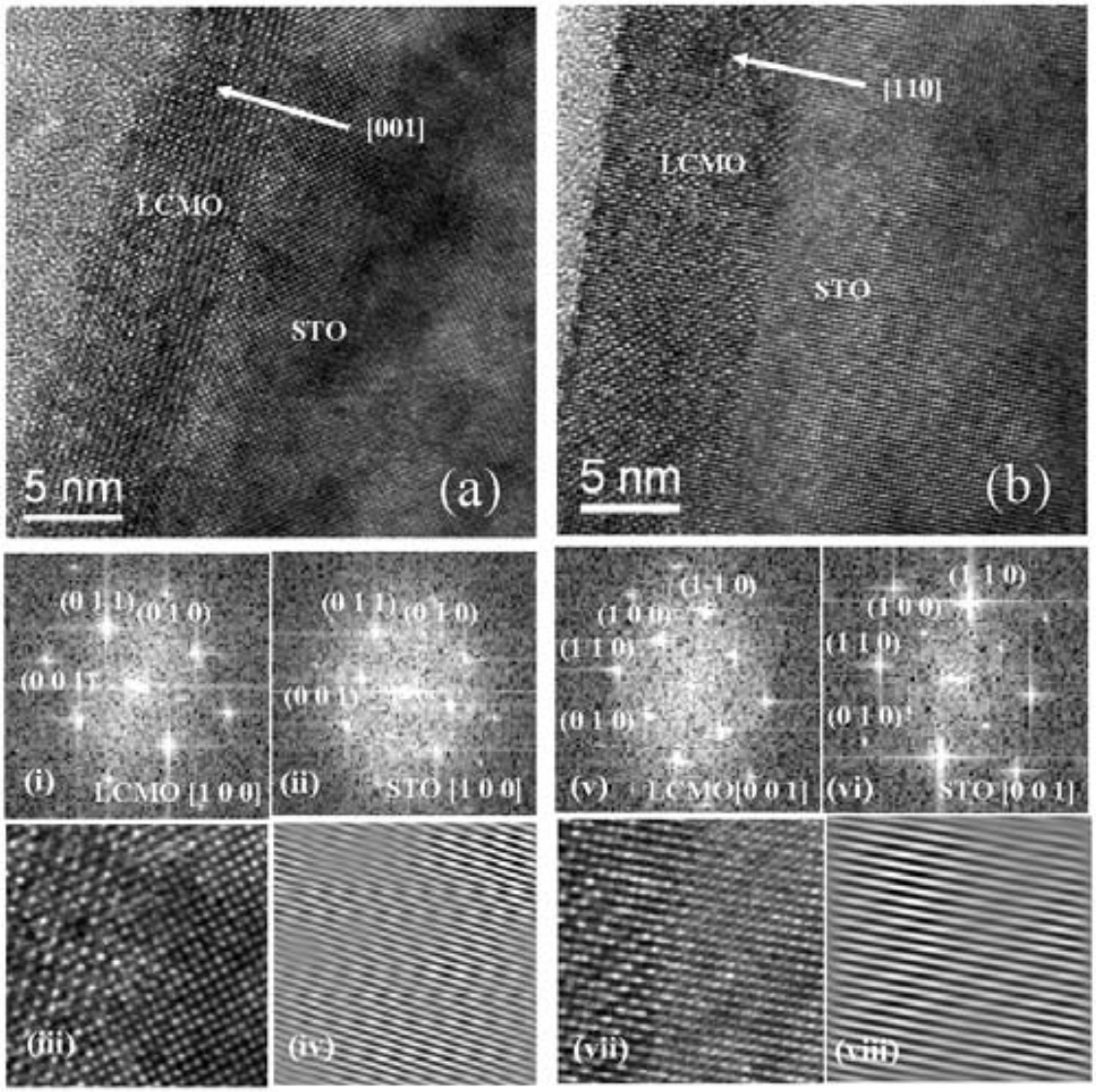

Figure 4.13. High resolution XTEM images of STO/LCMO interfaces: (a) (001) interface along the [100] zone axis and (b) (110) interface along the [001] zone axis. The FFTs calculated from LCMO and STO areas are shown for the (001) sample in (i) and (ii) and for the (110) sample in (v) and (vi), respectively. Zooms of the (001) and (110) interfaces [(iii) and (vii), respectively] are studied by filtering in the corresponding FFTs (not shown) for the in-plane directions and reconstructing the images [(iv) and (viii), respectively].

About the crystallographic orientation of LCMO film grown on STO (001), the epitaxial relationship is deduced from electron diffraction patterns (not shown) and FFTs (Figure 4.13i and ii) calculated from the high resolution XTEM image (Figure 4.13a), being LCMO(001)[100]//STO(001)[100]. This result agrees with the XRD measurements presented in this chapter. On the other hand, in the examined area of the XTEM image, it is confirmed the abruptness of the film-substrate interface, with no

misfit dislocations. Besides, the lattice parameters extracted from the FFTs are similar to those extracted from XRD data, confirming the coherent growth of the (001) LCMO film on (001) STO substrate. An equivalent analysis of the XTEM images of LCMO film grown on STO (110) has been performed. The epitaxial relationship deduced from calculations on FFTs spots (Figure 4.13v and vi) on these XTEM images (Figure 4.13b) performed along the [001] zone axis is LCMO(110)[001]//STO(110)[001]. The lattice parameters extracted from the FFTs agree with those of XRD within the experimental error.

The comparison of (001) and (110) film XTEM images in Figure 4.13 does not reveal relevant differences except for a greater roughness at the (110) interface. In fact, rougher (110) interfaces can be expected on the basis of the polar nature of the (110) STO surface and its inherent tendency to reconstruction [6]. No misfit dislocations have been observed in the considered region, as expected since (110) films of this thickness (8 nm) were found to be fully strained by XRD measurements.

The sharp contrast across the interface suggests, in both cases, the absence of interdiffusion. In bottom panels in Figure 4.13 show clear images of the different atomic arrangement along the [100] zone axis in the (001) interface (Figure 4.13a) and along the [001] zone axis in the (110) interface (Figure 4.13b). Zoomed interface regions extracted from the images shown in Figure 4.13a and b are presented in Figure 4.13iii and vii, respectively. To study the possible existence of dislocations, we performed FFTs (not shown) of these zooms and filtered for the corresponding in-plane direction. Therefore, for the (001) interface (Figure 4.13a), the filtering is done for the [010] direction and for the (110) interface (Figure 4.13b) the filtering is done for the [1-10] direction. The reconstructed images are shown in Figure 4.13iv and viii, respectively. The high fringe parallelism of both filtered images signals: (1) the good matching of in-plane parameters for both (001) and (110) films with respect the STO substrate, and (2) the absence of misfit dislocations, at least at this thickness. This analysis reinforces the already achieved conclusions from direct observation of low magnification and high resolution XTEM images.

To sum up, cross section HRTEM images and their analysis have confirmed the complete epitaxial growth of LCMO films onto (001) and (110) STO, showing as relevant features the slightly rougher interface in the (110) case.

4.3 Epitaxy of LCMO films: electronic and chemical phase separation by NMR, EELS, XPS and XAS

Four complementary characterization techniques have been used to investigate the ionic state and the chemical composition of the films:

1. A study of the mixed valence $Mn^{3+/4+}$ state and the appearance of the localized Mn^{m+} states, by Nuclear Magnetic Resonance (NMR) measurements carried out in a series of samples of different thickness.

2. The distribution of La and Ca cations in the films as well as the Mn electronic state is investigated by electron energy loss spectroscopy (EELS).

3. The ratios of the different cations in the surface by X-Photoelectron Spectroscopy (XPS).

4. The ionic environment of Mn and O in the film surface by X-ray Absorption Spectroscopy (XAS).

As previously explained in Ch1, the conductive double-exchange ferromagnetism in $La_{2/3}Ca_{1/3}MnO_3$ films arises from the quick migration of holes and electrons in the neighborhood of Mn^{3+}-Mn^{4+} ions mediated by the presence of O^{2-}. Any change in the ionic environment caused by a chemical or an electronic phase separation would probably change the functional properties of the films. More relevantly, if these segregations are located at the film surface, they would strongly affect the top interface properties, being a critical factor if the single layers are used in oxide heterostructures [7].

The objectives of present studies were on the one hand to precisely determine in (001) and (110) LCMO films the ionic states of Mn ions in the whole film by NMR measurements. Moreover, EELS experiments carried in cross section samples allows measuring the cationic distribution through the film as well as the electronic state of the Mn ions. The investigation of the film surface was performed using two surface-sensitive techniques: XPS and XAS. With XPS and XAS we have explored the Mn ionic states, and also the XPS measurements served to obtain information about the surface chemical composition.

4.3.1 ^{55}Mn NMR experimental results: electronic phase separation

The ^{55}Mn NMR experiments were carried out and analyzed by Dr. M. Wojcik at the Institute of Physics, Polish Academy of Sciences (Warszawa). The inspected series of samples were (001) and (110) films of different thickness, listed in Table 4.8.

Table 4.8. List of samples included in this section.

Sample	Substrate	Sample	Substrate	Nominal thickness (nm)
050929A4	STO(001)	180304BB	STO(110)	17
070110A1	STO(001)	070109B1	STO(110)	39
240204A	STO(001)	240204B	STO(110)	43
		050406BB	STO(110)	60
200204A	STO(001)	200204B	STO(110)	85

Two sets of the collected NMR spectra corresponding to (001) and (110) films 85, 43 and 17 nm thick are shown in Figure 4.14a, b and c, respectively. The inspection of these NMR spectra signals the appearance of a dominant line (around 375-380 MHz) related to the mixed valence $Mn^{3+/4+}$ state. This resonant line corresponds to the ^{55}Mn hyperfine field averaged due to double-exchange driven fast motion of electron-holes over manganese sites Mn^{4+}-Mn^{3+}. Consequently, the frequency of this line is determined by the ratio of Mn^{3+} to Mn^{4+} and varies proportionally with charge carrier density in the conducting band [8]. In Figure 4.14, the solid vertical lines indicate the value of the resonant frequency $\nu(Mn^{3+/4+})$ for each film. A noticeable shift of $\nu(Mn^{3+/4+})$ towards higher values is observed when increasing film thickness. Moreover, the value of the $\nu(Mn^{3+/4+})$ depends on the film orientation: it is larger for (110) films than for (001) ones at each thickness, being for instance for the 85 nm films $\nu(Mn^{3+/4+})^{001} = 376$ MHz and $\nu(Mn^{3+/4+})^{110} = 380$ MHz. Similar trend agrees with the results presented in Ref. [2], where an increase of $\nu(Mn^{3+/4+})$ happens when film thickness increases simultaneously to the increase of the Curie temperature (T_C) of the films. The relationship between the value of the resonant frequency of $Mn^{3+/4+}$ line and the T_C is of main interest since it connects compositional and functional properties. In present work, from the higher values of $\nu(Mn^{3+/4+})^{110}$ compared to $\nu(Mn^{3+/4+})^{001}$ ones, more robust ferromagnetic interactions, represented by higher T_C, is expected for the (110) films than for the (001) ones of the same thickness.

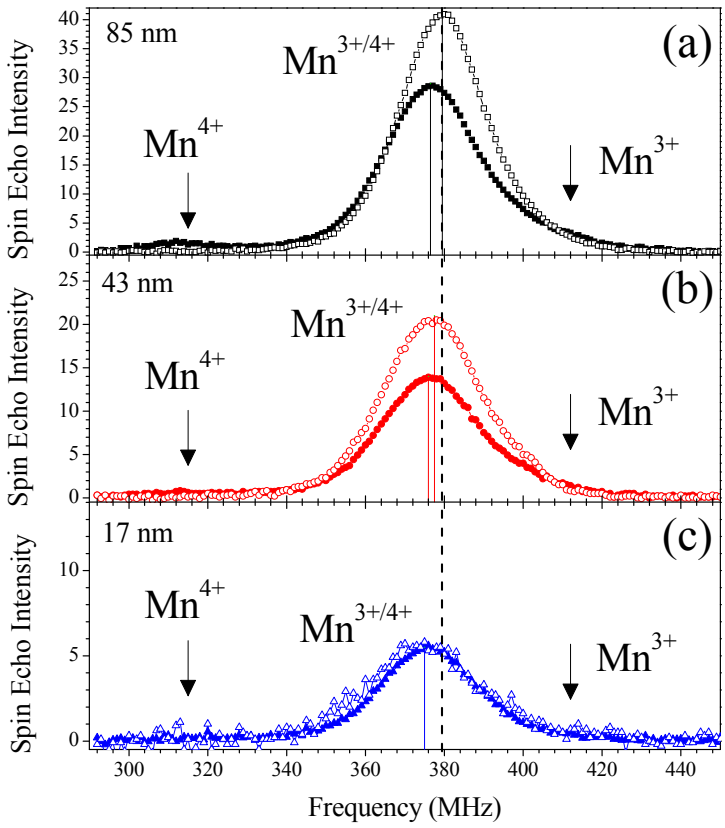

Figure 4.14. ^{55}Mn NMR spectra of the (001) (solid symbols) and (110) (open symbols) films of thickness (a) 85 nm, (b) 43 nm and (c) 17 nm, measured at T = 4.2 K and at zero magnetic field. Vertical solid lines indicate the resonant frequency deduced from each spectra and dashed line corresponds to the resonant frequency of the 85 nm (110) film.

On the other hand, the inspection of the spectra of (001) films shown in Figure 4.14 (close symbols) reveals the occurrence of other Mn resonances. These resonances are more clearly observed in the low intensity zooms depicted in Figure 4.15 (close symbols). A broad peak of reduced intensity appears at lower frequency (around 315 MHz) and features a high value of NMR enhancement factor characteristic for ferromagnetic phase. Lower resonant frequency indicate lower magnetic moment, which can eventually be related to a change from $Mn^{3+/4+}$ ions to Mn^{4+}. The presence of hole-trapped (localized) ferromagnetic Mn^{4+} state has been previously attributed to be at the origin of this feature [2]. Moreover, in the present experiment, a clear, albeit tiny, asymmetry is observed on the high frequency side of the $Mn^{3+/4+}$ line revealing the presence of additional Mn state giving rise to the NMR Mn^{3+} state producing a NMR signal in this frequency range. The frequency of this resonance (~ 400-420 MHz)

corresponds to a Mn^{3+} state [8] and thus it identifies the presence of localized ferromagnetic Mn^{3+} ions in the (001) film. A sizable amount of localized Mn^{4+} and Mn^{3+} ions in (001) films detected by ^{55}Mn NMR evidences the presence of ferromagnetic insulating phase with localized charges and consequently it can be considered as a signature of electronic phase separation taking place in these films [2]. Charge localization implies weakening of the double exchange coupling, and thus a reduction of the T_C is foreseen for (001) films. Remarkably, the NMR spectrum of the (110) films does not show these localized Mn^{3+} or Mn^{4+} states, and thus the phase separation can be considered to be absent or, at least, much less abundant; accordingly, the T_C (and magnetization) should approach ideal, bulk-like values, which is a fact that will be shown in Ch5.

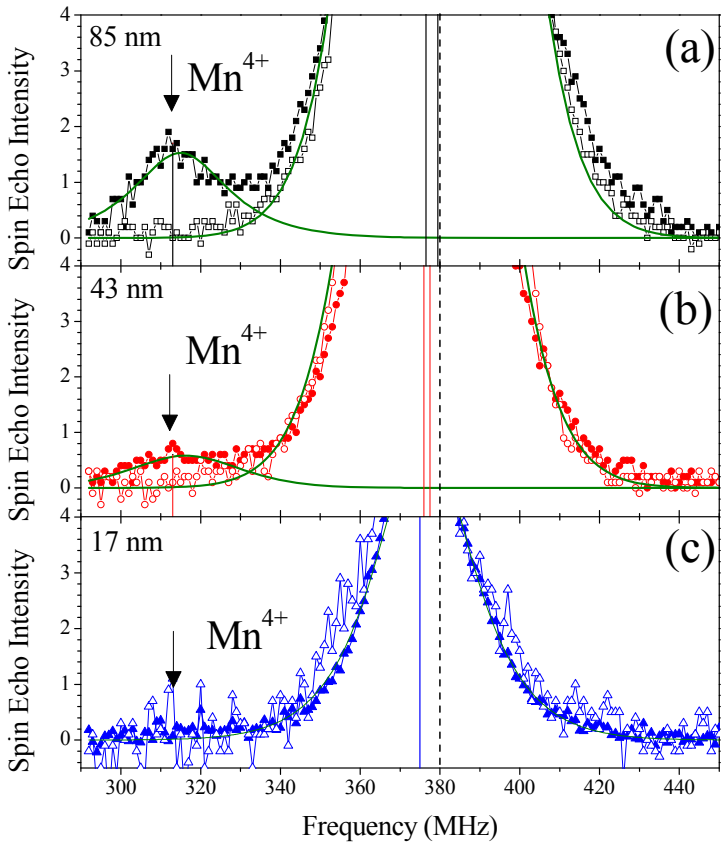

Figure 4.15. Zooms of the ^{55}Mn NMR spectra of the presented spectra of Figure 4.14. Vertical lines in the low frequency region indicate the resonant frequency of Mn^{4+} ions and solid vertical lines around ν=380MHz correspond to the resonant frequency for each film. The vertical dashed line corresponds to the resonant frequency of the 85 nm (110) film. The Lorentzian-Gaussian fits to the experimental data Mn^{4+} and Mn^{3+4+} peaks are also shown (lines).

Under the appropriate measurement conditions, the total area under the NMR spectra is determined by the fraction of magnetic ions in the sample [9]. The integrated area under the spectra for (001) and (110) samples of various thicknesses have been measured and these values are collected in Table 4.9 and plotted in Figure 4.16a as a function of film thickness.

Table 4.9. Total intensity of the NMR spectra [I(total)] extracted from the NMR spectra obtained on the (001) and (110) samples, together with the intensities of the Mn^{4+} [I(Mn4+)] peak measured on the (001) samples. The calculated ratios [Ratio(Mn4+)] of the Mn^{4+} and total intensities of the NMR spectra of (001) samples are also included.

Nominal thickness (nm)	(001)			(110)
	I(total) (arb. units)	I(Mn4+) (arb. units)	Ratio(Mn4+) (%)	I(total) (arb. Units)
17	81.00	2.97	3.66	98.44
39	235.00	10.10	4.30	287.70
43	235.13	9.07	3.86	323.44
60				384.38
85	472.97	14.50	3.07	581.72

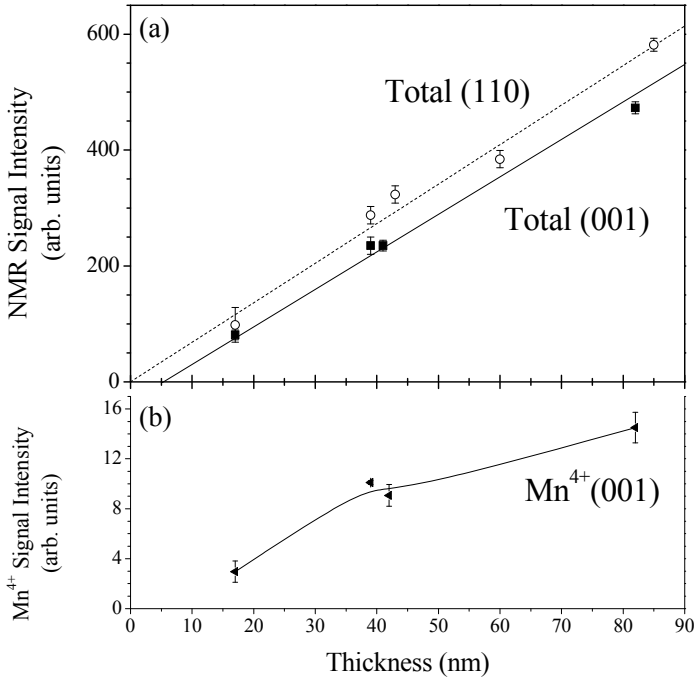

Figure 4.16. Thickness dependence (a) of the total integrated intensity of the NMR spectra for (001) (solid symbols) and (110) (open symbols) films and (b) of the Mn^{4+} intensity of (001) films, measured at T = 4.2 K.

There is a gradual increase of the NMR intensity at T = 4.2 K as a function of thickness for both series of samples, which was expected from the larger amount of ferromagnetic material. However, there is a striking difference: the NMR intensity is always larger for the (110) samples than for the (001) ones. This observation clearly indicates that the ferromagnetic fraction in the (110) samples is always larger than that of the (001) ones. Remarkably, the missing intensity can be related to Mn^{m+} ions either antiferromagnetically coupled or paramagnetic, characterized by a very low NMR enhancement. Thus, these Mn ions contribute with a negligible intensity to the NMR spectrum of strong ferromagnetic signals. Extrapolating to zero thickness the experimental NMR intensity, it can be evaluated the thickness of the non-ferromagnetic layer (t_c), being for (001) films t_c^{001} = 5.5 nm, whereas for (110) ones it is virtually zero, t_c^{110} = 0 nm. The thickness dependence of the Mn^{4+} intensity for the NMR spectra of the (001) films is presented in Figure 4.16b. We note that the Mn^{4+} intensity increases with film thickness, and calculating the intensity ratio Ratio(Mn^{4+}) = I(Mn^{4+})/I(Total) for each (001) film (Table 4.9), we obtain ratios that moderately depend on film thickness. The more remarkable feature of this thickness dependence of the Mn^{4+} ratio arises from the observation that thicker (001) film (85 nm) presents a lower Ratio(Mn^{4+}) than those the 17-43 nm films, which can be interpreted as a signature of a limited amount of Mn^{4+} ions formation. In fact, upon the increase of film thickness, the number of Mn^{4+} ions may increase up to a limited value, and once the maximal amount of Mn ions is surpassed (at a critical thickness), the formation of Mn^{4+} is less promoted, or it may be even suppressed. The results presented here on Mn4+ signal are comparable to those reported by Bibes *et al*. [2] in LCMO(001) films.

The observation of a ferromagnetic charge-localized signal in the NMR spectra of $La_{1-x}Ca_xMnO_3$ manganites has been viewed [10] as a signature of the presence of ferromagnetic insulating regions with A-type orbital ordering. In Ch5 we will discuss in detail these results in the framework of the strain-induced reinforcement of orbital ordering happening in (001) films.

To sum up, the comparative of (001) and (110) films leads to concluding that stronger ferromagnetism is expected in (110) films, with higher T_C and possible absence of a dead magnetic layer, which has been clearly found in (001) ones.

4.3.2 EELS experimental results: chemical distribution and electronic phase separation

EELS experiments were carried out on 85 nm films of (001) and (110) orientation (see Table 4.10) by S. Estradé, from the University of Barcelona, and the data and their analysis is included in her PhD thesis. Samples were prepared in cross section geometry, and the used VG STEM microscope allows performing probe displacements in a step down to 0.2 nm.

Table 4.10. List of samples for EELS experiments.

Sample	Substrate	Sample	Substrate	Nominal thickness (nm)
200204A	STO(001)	200204B	STO(110)	85

The Ca $L_{3,2}$ (~ 345-355 eV), O K (~ 525-550 eV), Mn $L_{3,2}$ (~ 630-660 eV) and La $M_{5,4}$ (~ 830-860 eV) EELS core edges have been inspected at room temperature, recording the spectra throughout the sample along a direction perpendicular to the interface from the substrate to the free film surface following the paths shown in Figure 4.17a and Figure 4.17b. Two examples of the O K and Mn $L_{3,2}$ spectra recorded at the central area of the (001) and (110) LCMO films are shown in Figure 4.17c and d. In these spectra, the energy lost by incident electrons is transferred to core-level electrons that jump to unoccupied energy states in the conduction band above the Fermi level. EELS core edges are very narrow in energy, thus providing a first order approximation of the density of states immediately above the Fermi level, i.e. the density of empty states in the conduction band.

Using the recorded Ca $L_{3,2}$ and La $M_{5,4}$ spectra, the distribution of Ca and La cations through the films has been studied. Normalizing to 1 the quotient between the total intensity of Ca $L_{3,2}$ edge to that of La $M_{5,4}$ edge at the interface for each film (the nominal Ca/La ratio is ½), the Ca/La normalized ratios extracted from (001) and (110) films are shown in Figure 4.18. An analysis of these results highlights that upon increasing the distance from the substrate-film interface, Ca/La ratio in the (001) films increases whereas in the (110) film the ratio remains constant. Thus, no cation migration is observed in (110) films. Using EELS, the Ca segregation towards the top interface of (001)-oriented $La_{2/3}Ca_{1/3}MnO_3/SrTiO_3/La_{2/3}Ca_{1/3}MnO_3$ heterostructures has been previously reported [7][11].

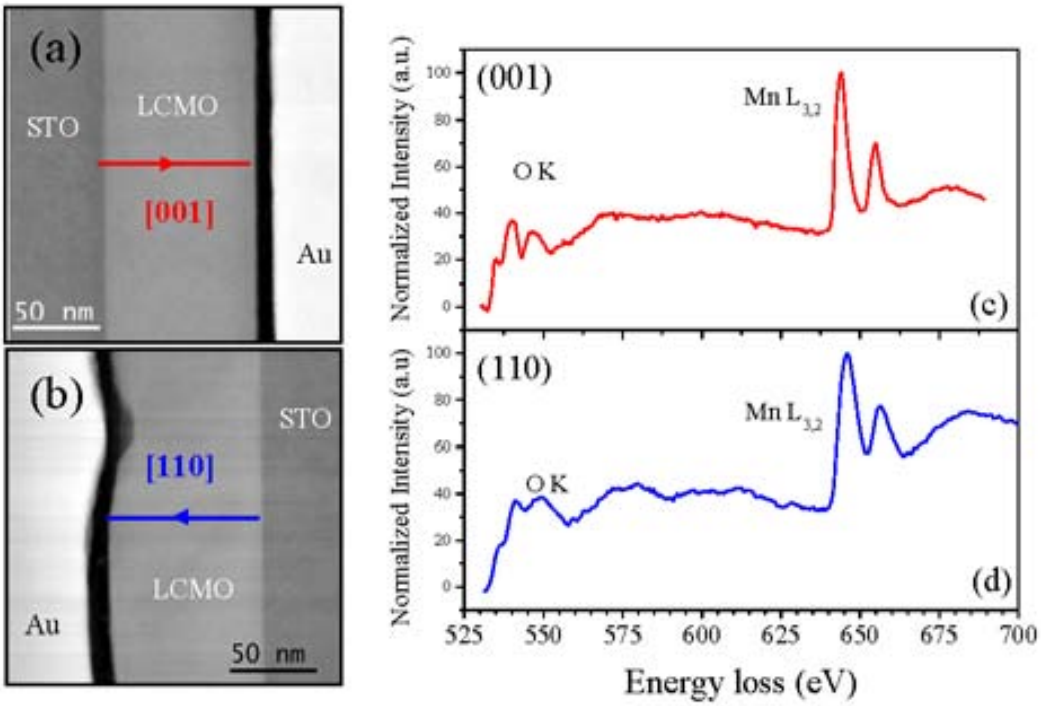

Figure 4.17. [(a) and (b)] Low magnification XTEM images of 85 nm films with (a) (001) and (b) (110) orientation. The arrows indicate the followed path for the focalization of EELS probe. [(c) and (d)] EELS espectra of the O_K and Mn-$L_{3,2}$ edges from the center area of the films shown in (a) and (b), corresponding (c) to the (001) film and (d) to the (110) one.

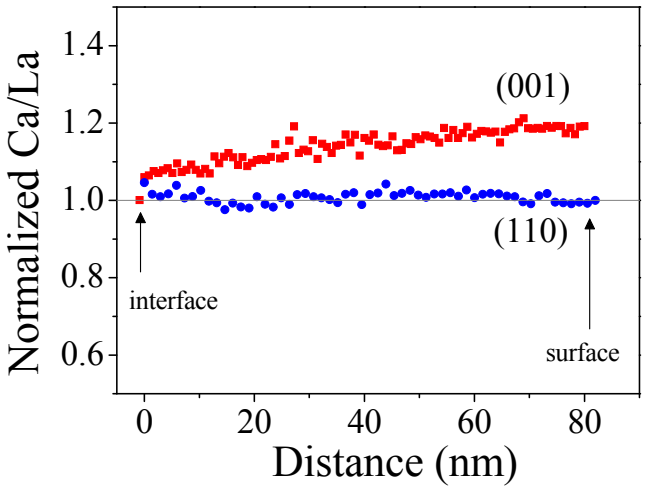

Figure 4.18. Normalized Ca/La quantification obtained along the line displayed in (a) and (b) for (001) and (110) films, respectively.

Turning to Mn $L_{3,2}$ edges, Mn oxidation state can be determined from either the ratio between the L_3 and L_2 peaks or from the Mn L_3 onset energy. Using the home-made Matlab routine "ManganitaS" described in Ref. [12], the L_3/L_2 ratios and the Mn

L_3 onset energies of (001) and (110) films have been calculated. The results are plotted in Figure 4.19. The L_3/L_2 ratio and Mn L_3 energy references for the different oxidation states of Mn are obtained from Ref. [13]. An analysis of (001) and (110) results signals that, accordingly to the Ca migration to the (001) surface observed in Figure 4.18, Mn oxidation state varies through the (001) film (Figure 4.19a and b), being most preferably Mn^{3+} near the substrate interface up to ~ 15 nm from it and Mn^{4+} close to the free surface. On the other hand, Mn oxidation state in the (110) film (Figure 4.19c and d) is constant with a mixed valence value related to the $2/3Mn^{3+}$-$1/3Mn^{4+}$ stoichiometric population.

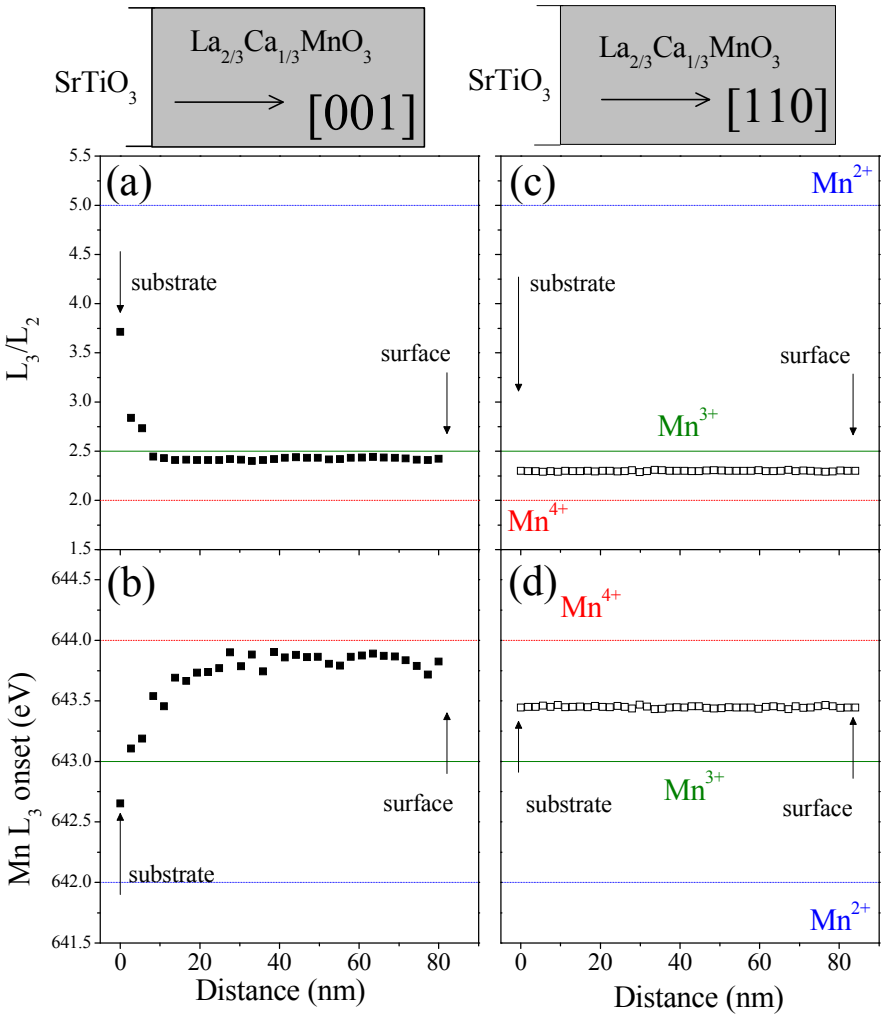

Figure 4.19. [(a) and (c)] Mn L_3/ Mn L_2 relative intensity and [(b) and (d)] Mn L_3 peak onset extracted from Mn 2p edges acquired in 85 nm films with [(a) and (b)] (001) and [(c) and (d)] (110) orientation. L_3/L_2 ratio and Mn L_3 energy references depending on the Mn oxidation states (4+, 3+ and 2+) are extracted from Ref. [13]. Top panel: schematic views of the sense of the EELS measurements.

In summary, conclusive evidences of anomalous cation distribution and inhomogeneous Mn oxidation state is found through (001) film whereas (110) film is chemically homogeneous, with $Mn^{3.3+}$ oxidation state. The link of both chemical and electronic effects signals that (110) film represent the ideal $La_{2/3}Ca_{1/3}MnO_3$ film whereas the (001) one presents inhomogeneous distribution of cations as well as different Mn electronic phases.

4.3.3 XPS and XAS experimental results: chemical segregation

XPS experimental results

X-ray photoelectron spectra were obtained from (001) and (110) samples of 17 and 50 nm thickness, listed in Table 4.11, at room temperature. The X-ray photoelectron spectra shown in this section were recorded by Dr. J.-P. Espinós at the Instituto de Ciencia de Materiales de Sevilla using an ESCALAB 210 spectrometer as described in Ch2.

Table 4.11. List of samples used for XPS experiments.

Sample	Substrate	Sample	Substrate	Nominal thickness (nm)
050329A	STO(001)	180304BB	STO(110)	17
050304A	STO(001)	050304B	STO(110)	17
060704A	STO(001)	060404B	STO(110)	50

A first comment has to be addressed to the probing depth of these experiments, (typically ~ 2 nm), which will determine the surface sensitivity. Therefore, it allows the investigation of possible surface segregation; in any case, it needs to be taken into account that surface contamination can mask the actual measured composition. Nevertheless, the surface contamination signal, mainly carbon (C 1*s* core), does not overlap with film peaks, and the measured chemical composition is truly not-affected by this contamination.

XPS measurements have been performed in as-grown couples of (001) and (110) films as well as in the very same samples after a soft Ar^+ sputtering of their surface. With these simple experiments, the composition of the bare surface of these films is known besides their bulk composition. It has to be noted that the sputtering process can make amorphous some of the exposed film, and, more remarkable, it can

preferentially etch some of the atoms. These effects are not forgotten on the analysis as they can modify the actual composition of the sputtered films.

To overview the composition of the bare surface of films, wide range energy spectra have been recorded from all samples, and we present in Figure 4.20 as an example the corresponding spectra for the 50 nm (001) and (110) films. The expected core levels (La $3d_{5/2}$, Mn 2p, Ca 2p and O 1s) are identified, as indicated on the figure. A significant C 1s core level, appearing at a binding energy of ~ 286 eV, is a signature of the detection of some carbon contamination, which is partly linked to the O 1s core spectrum.

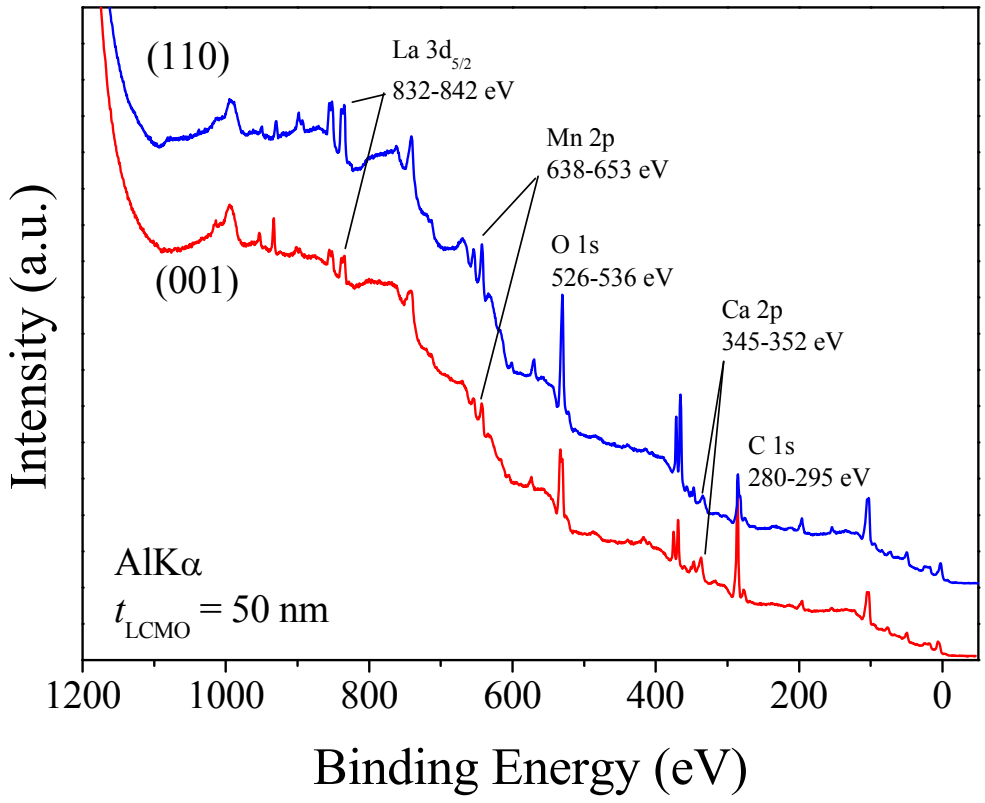

Figure 4.20. XPS spectra from as-grown 50 nm LCMO surfaces. Spectra were recorded at room temperature using a non-monochromatic AlKα source. Core energies that afterwards are explored in detailed are marked on the graph. (110) spectrum has been shifted upwards to avoid the overlapping with the (001) spectrum.

Detailed spectra at the energy range of some core levels were obtained at an energy step for each scan of 0.1 eV. In Figure 4.21 the spectra recorded from the C 1s core level for the as-grown surface (squares) of the 17 nm films are shown. As already observed in the general spectra of 50 nm films (Figure 4.20), carbon contamination is

present in the surface of as-grown films. In order to diminish this surface contamination, we etched the surface with an Ar^+ beam (ions accelerated at 2 kV, incidence angle of 60 deg, and attack of 3.5 min). We include in Figure 4.21 the resulting spectra after this treatment was performed (triangles). A relevant reduction of the carbon contamination is observed from the reduced intensity of the C 1s core level comparing the etched (triangles) and as-grown (squares) specra. We notice the existence of a low intensity peak appearing at ~ 288.5 eV in the as-grown spectra (squares), which can be linked to the existence of carbonates in the surface. In the Ar^+ etched surface spectra, this peak still exists, although much weaker. In general, the Ar^+ etching allows reducing importantly the overall carbon contamination, including the carbonates.

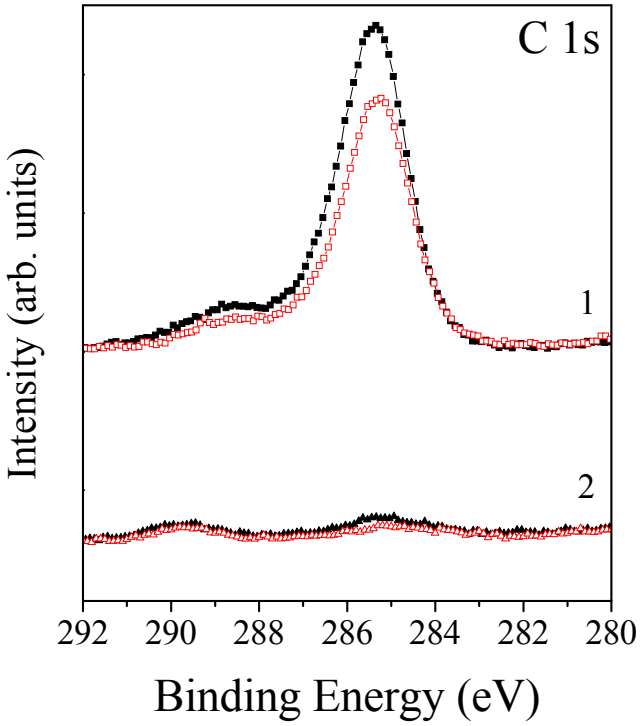

Figure 4.21. C 1s X-ray photoelectron emission spectra for 17 nm (001) and (110) films for the sample surface: (1) in the as-grown, and (2) after Ar^+ etching at 2 kV during 3.5 min (60 deg incidence). Close symbols correspond to (001) films and open symbols to (110) films. Normalization was performed using the La $3d_{5/2}$ line.

Turning to the study of the core level of other ions, in Figure 4.22 we present the La $3d_{5/2}$ (a), Mn 2p (b) and Ca 2p (c) spectra obtained from the 17 nm (001) and (110) films. We include the data recorded on the as-grown surfaces (squares) and after the Ar^+ etching (triangles), being the (001) film data the close symbols and the (110) film data the open symbols.

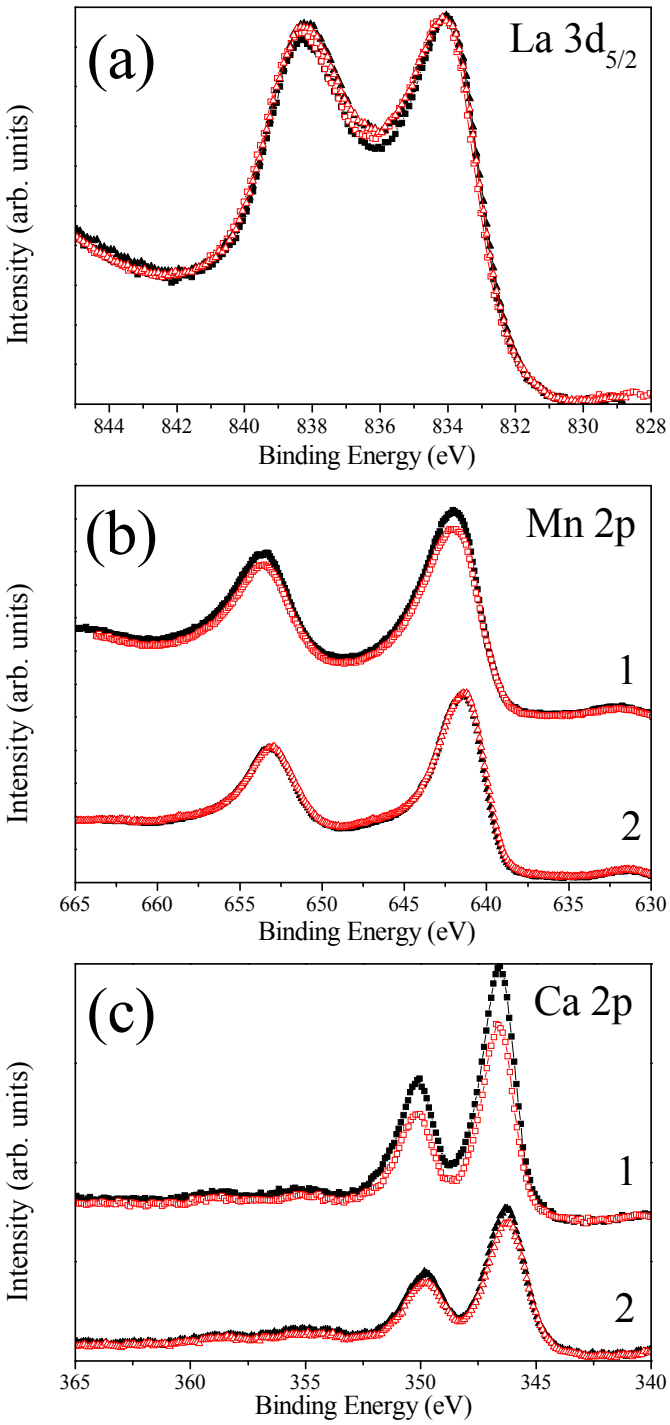

Figure 4.22. (a) La $3d_{5/2}$, (b) Mn 2p and (c) Ca 2p X-ray photoelectron emission spectra for 17 nm (001) and (110) films: (1) as-grown surface, and (2) after Ar^+ etching at 2 kV during 3.5 min (60 deg incidence). Close symbols correspond to (001) films and open symbols to (110) films. Normalization was performed using the La $3d_{5/2}$ line.

We start the analysis with the La $3d_{5/2}$ (a) spectra. For the (001) and (110) samples, the data from the La $3d_{5/2}$ spectra (Figure 4.22a) are almost coincident, and since we expect low changes in the electronic environment of the La^{3+} ions, we used the energy position of the La $3d_{5/2}$ peak as an internal energy reference in all the spectra. Therefore, in the analysis of Mn 2p and Ca 2p spectra, we consider La $3d_{5/2}$ as the energy and intensity reference for all surfaces. Within these considerations, the Mn 2p spectra (Figure 4.22b) of the as-grown surfaces indicate that the (001) and (110) surfaces are slightly different, observing higher signal for the (001) surface than for the (110) one. Upon Ar^+ etching, the Mn 2p signal of the (001) surface decreases, approaching the corresponding signal of the (110) surface. In fact, the similarity of the Mn 2p signals of the (110) as-grown and etched surfaces discards the possibility of a preferential attack of the Ar^+ ions. Turning to the inspection of Ca 2p core level (Figure 4.22c), the intensity of the spectra from the (001) film is in all cases larger than that of the spectra from the (110) film. Thus, the Ca content (measured respect to the La one) is larger in the (001) surfaces than in the (110) ones. The Ar^+ etching produces a decrease in the Ca 2p intensity from both (001) and (110) surfaces, thus a preferential attack of the Ca ions cannot be excluded. Within this scope, a relative Ca enrichment of the (001) surface is expected when compared to the (110) one. Similar results were found in the 50 nm films (Figure 4.20) and in another pair of 17 nm films.

An evaluation of the composition ratios [Ca]/[La], [Mn]/[La], [Mn]/[Ca], and [Mn]/([Ca]+[La]) has been performed in order to get a quantitative estimation of the surface composition, in addition to determine the possible occurrence of a surface chemical segregation. The evaluation method takes into account the relative sensitivity factors and the area of the photoemission peaks. The evaluated ratios, as well as the nominal ones, are summarized in Table 4.12.

Exploring the data in Table 4.12, when comparing ratios of (001) and (110) surfaces after the Ar^+ etching, both samples present a similar composition, matching reasonably well with the nominal values. In contrast, the surface composition of all as-grown samples differs from the nominal value. The most remarkable departure is observed in the (001) surface. The Ca content at the roughly first 2 nm of the film, as previously noted from direct observation of XPS spectra of Figure 4.22c, is found to exceed in a ~ 70 % the stoichiometric value (Table 4.12). In contrast, in the (110) surface, the Ca excess is only of ~ 30 %. In fact, the complex XPS quantification allows a reliable comparison between each pair of samples, although these results

partially lose their accuracy when studied independently. Indeed, since the layer removed by the Ar^+ etching is thinner than the probing depth, the observed differences account to a very superficial layer, and they are in magnitude higher than that quantified.

Table 4.12. Composition ratios (La, Ca, Mn) calculated from XPS measurements from the as-grown and Ar^+ etched surfaces of 17 nm (001) and (110) LCMO films.

	[Ca]/[La]	[Mn]/[La]	[Mn]/[Ca]	[Mn]/([La]+[Ca])
Nominal	0.50	1.50	3.00	1.00
(001) as-grown	0.85	1.66	1.95	0.90
(001) etched	0.50	1.57	3.11	1.04
(110) as-grown	0.65	1.53	2.34	0.93
(110) etched	0.47	1.55	3.31	1.06

In the case of LCMO (001) and similar (001) manganite films grown on $SrTiO_3$ substrates, some previous studies exist on the topic of phase segregation. The results presented here are in agreement with reported works of Simon et *al*. [7], Choi et *al*. [14], Bertacco et *al.* [15], and Maurice et *al.* [1]. In the case of Simon [7], the characterization by secondary ion mass spectrometry and energy electron loss spectroscopy (EELS) of strained LCMO films on STO (001) substrates claimed for a non-stoichiometric chemical composition and a Ca segregation at the surface. Evidence of Ca segregation in LCMO (001) epitaxial was also found from XPS measurements [14]. Similarly, Bertacco *et al.* [15] found the presence of a Sr rich layer in strained (001) $La_{2/3}Sr_{1/3}MnO_3$ thin films by means of XPS measurements. This observation of Sr rich layer at the surface of strained $La_{2/3}Sr_{1/3}MnO_3$ by EELS had been also documented by Maurice *et al.* [1]. The experimental data presented here agrees in signaling Ca enrichment at the surface of the (001) films, but more remarkably, this Ca segregation is seen to be less pronounced in (110) surfaces.

XAS experimental results

Using X-ray absorption spectroscopy the chemical and electronic state of the atoms at the surface of the films can be investigated. As it happened with XPS measurements, a different energy range of the absorbed X-ray source beam has been established to allow the accurate study of Mn 2p and O 1s edges, and thus the ionic

environment of these ions in the film surface. The samples were as-grown 9 nm (001) and (110) films (see Table 4.13), being studied by room temperature XAS.

Table 4.13. List of samples measured by XAS.

Sample	Substrate	Sample	Substrate	Nominal thickness (nm)
050929A1	STO(001)	050929B1	STO(110)	9

First, in Figure 4.23, the Mn 2p spectra of (001) (a) and (110) (b) 9 nm films are plotted. The XAS measurements correspond to transitions from the Mn 2p level to unoccupied Mn 3d states.

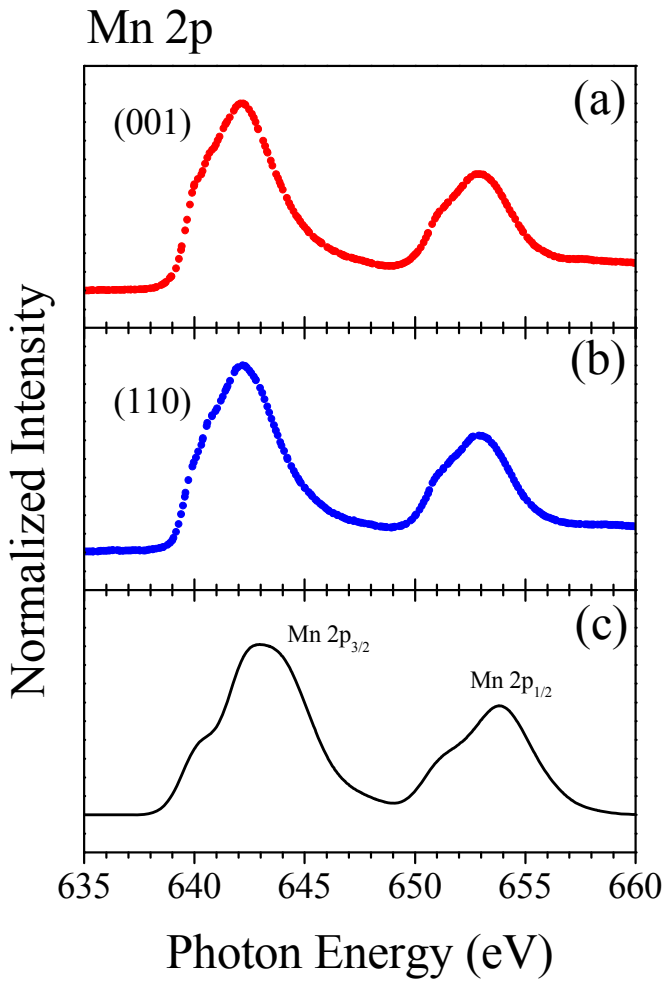

Figure 4.23. Mn 2p X-ray absorption spectra of 9 nm LCMO films of (a) (110) and (b) (001) orientation. (c) Atomic multiplet calculation shown for comparison.

The splitting into $2p_{3/2}$ and $2p_{1/2}$ components (peaks in Figure 4.23) is due to the spin-orbit interaction. The Mn 2p XAS spectra are dominated by atomic multiplet and crystal field effects. The shape of the multiplet is directly related to the Mn 3d occupancy and the ground state symmetry. The spectra can be calculated [16] by the projection of the atomic multiplet in octahedral symmetry (the actual arrangement of O neighbors surrounding Mn sites is an octahedron), as it is described in Ref. [17][18]. The resulting simulated spectrum is plotted in Figure 4.23c. The Mn 2p XAS spectra of $La_{2/3}Ca_{1/3}MnO_3$ can be calculated by appropriate combination (2/3:1/3) of the $2p^63d^n \rightarrow 2p^53d^{n+1}$ transitions in $LaMnO_3$ and $CaMnO_3$. The ground state of the Mn^{3+} ion was $t_{2g}(3)e_g(1)$ (^5E) with a crystal field of 10 Dq = 2.4 eV. The ground state of the Mn^{4+} ion was $t_{2g}(3)$ ($^4A_2$) with a crystal field of 10 Dq = 2.1 eV. The Mn 2p calculated spectrum agrees reasonably well with the experimental spectra taking into account the neglect of lower symmetry effects. This result shows that the Mn 3d – O 2p bonding is not affected by the substrate orientation. Indeed, it suggests that the MnO_6 octahedron is preserved as a series of building blocks in the films, at least within the limits of detection of XAS technique. It has to be stressed that the experimental XAS spectra of these films are similar to those of the related $La_{0.6(0.8)}Sr_{0.4(0.2)}MnO_3$ compound [18]. The shape of the multiplet is completely different when Mn^{2+} ions are present (see for example the Mn^{2+} in LCMO films in Ref. [20]), thus it can be ruled out their absence in these films. The different shape of $Mn^{3+/4+}$ and Mn^{2+} spectra can be observed inspecting Figure 4.24, where the experimental XAS spectra of $La_{1-x}Sr_xMnO_4$ samples (being x the doping level) (a) [18] clearly differ from the calculated spectra for Mn^{2+} ions (b) [19].

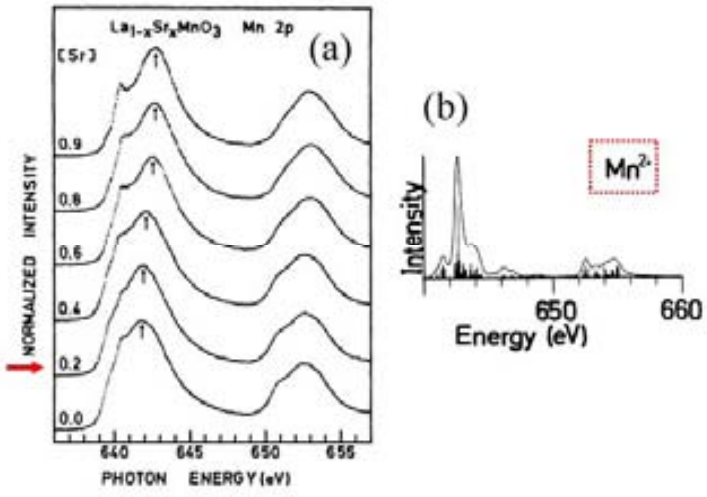

Figure 4.24. (a) Mn 2p XAS spectra obtained from $La_{1-x}Sr_xMnO_3$ samples with different Sr content (x), from Ref. [18]. (b) Calcultated XAS spectra of Mn^{2+} ions, after Ref. [19].

Figure 4.25 shows the O 1s XAS spectra of the same films studied previously. The spectra correspond to transitions from the O 1s level to unoccupied O 2p states.

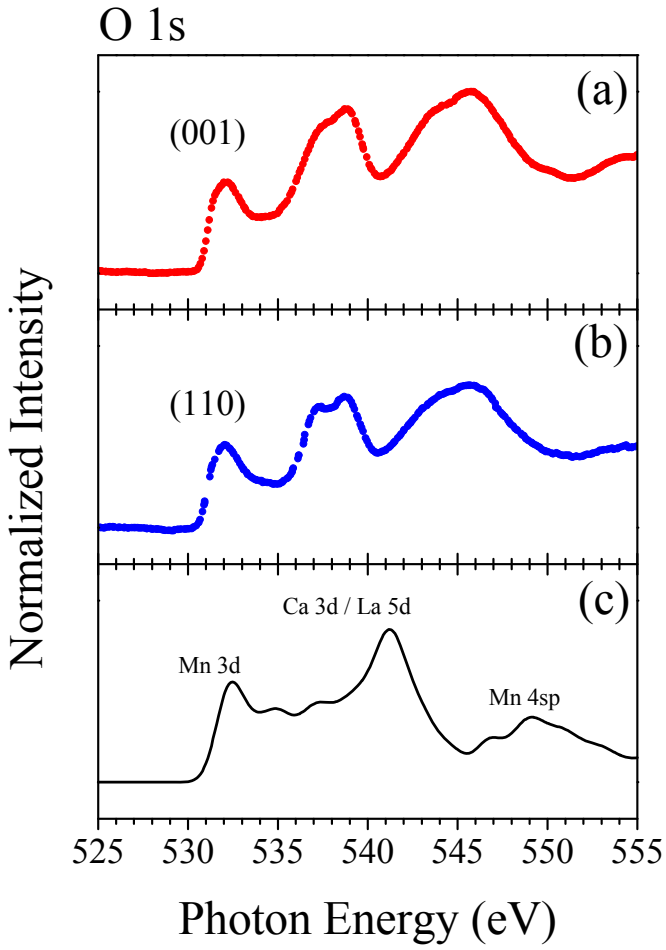

Figure 4.25. O 1s X-ray absorption spectra of 9 nm LCMO films with (a) (110) (b) and (001) orientation. (c) Atomic multiplet calculation shown for comparison.

The experimental oxygen spectra reflect, through hybridization, the different metal states in the conduction band. In particular, the structure at the threshold corresponds to O 2p character mixed with Mn 3d states. In Figure 4.25, the structure around 530–535 eV corresponds to the Mn 3d band region, the features about 540 eV are related to the Ca 3d / La 5d states, whereas the higher energy bumps can be attributed to the empty Mn 4sp bands. The overall shape of the spectra is similar to the O 1s XAS spectrum of the similar $La_{0.6(0.8)}Sr_{0.4(0.2)}MnO_3$ compound [18]. As in the case of Mn 2p absorption, the XAS spectra can be calculated (Figure 4.25c) using the O 2p partial density of unoccupied states [21] and the mixing of $LaMnO_3$ and $CaMnO_4$ contributions in a (2/3: 1/3) fraction. Remarkably, the O 1s spectra show differences in the Ca 3d - La 5d region, noticed at energies ~ 540 eV (Figure 4.25). This is probably

related to the different Ca-La termination in the (110) and (001) films, although differences in the Ca-La bonding at the LCMO/STO interface cannot be ruled out either.

Summarizing all this section on the study of the chemical and electronic phase separation on (001) and (110) LCMO films, NMR and EELS experiments have provided clear evidences of the occurrence of phase separation as well as a cationic redistribution in (001) films. Indeed, due to the absence of electronic phase separation measured by NMR experiments in (110) films, they are expected to present rougher ferromagnetism than (001) films. In agreement with NMR results, EELS experiments show that in (001) films Mn ions tend to have a reduced oxidized state near the substrate interface and a cationic redistribution with Ca segregation towards the surface. On the other hand, homogeneous electronic and cationic environment is measured in (110) films. Besides, from XPS and XAS surface measurements, compositional and ionic differences are observed in (001) and (110) films simultaneously grown. With these techniques, it has been seen that both (001) and (110) films and their surfaces are compositionally different. The fact that no sign of anomalous Mn^{2+} was found ensures that Mn-ionic state is not reduced after air exposure, although large surface composition change is found to be related to a Ca enrichment in (001) films.

References

[1] J. L. Maurice, F. Pailloux, A. Barthélémy, O. Durand, D. Imhoff, R. Lyonnet, A. Roher, and J. P. Contour, Philos. Mag. **83**, 3201 (2003)

[2] M. Bibes, Ll. Balcells, S. Valencia, J. Fontcuberta, M. Wojcik, E. Jedryka, and S. Nadolski, Phys. Rev. Lett. **87**, 67210 (2001) ; M. Bibes, S. Valencia, Ll. Balcells, B. Martínez, J. Fontcuberta, M. Wojcik, S. Nadolski, and E. Jedryka, Phys. Rev. B **66**, 134416 (2002)

[3] Y. Ogimoto, M. Nakamura, N. Takubo, H. Tamaru, M. Izumi, and K. Miyano, Phys. Rev. B **71**, 060403 (2005); K. Shibuya, T. Ohnishi, M. Lippmaa, M. Kawasaki, and H. Koinuma, Appl. Phys. Lett. **84**, 2142 (2004); C. U. Jung, H. Yamada, M. Kawasaki, and Y. Tokura, Appl. Phys. Lett. **84**, 2590 (2004)

[4] C. J. Lu, Z. L. Wang, C. Kwon, and Q. X. Jia, J. Appl. Phys. **88** 4032 (2000)

[5] O. I. Lebedev, G. Van Tendeloo, S. Amelinckx, B. Leibold, and H.U. Habermeier, Phys. Rev. B **58**, 8065 (1998)

[6] J. Brunen and J. Zegenhagen, Surf. Sci. **389**, 349 (1997); K. Szot and W. Speier, Phys. Rev. B **60**, 5909 (1999); K. Szot and W. Speier, Phys. Rev. B **60** 5909 (1999); F. Bottin, F. Finocchi, and C. Noguera, Surf. Sci. **574**, 65 (2005)

[7] J. Simon, T. Walther, W. Mader, J. Klein, D. Reisinger, L. Alff, and R. Gross, Appl. Phys. Lett. **84**, 3882 (2004)

[8] J. P. Renard and A. Anane, Mater. Sci. Eng. B **63**, 22 (1999)

[9] E. Jędryka, M. Wójcik, S. Nadolski, D. J. Kubinski, and H. Holloway, J. Magn. Magn. Mat. **165**, 292 (1997)

[10] G. Papavassiliou, M. Fardis, M. Belesi, T. G. Maris, G. Kallias, M. Pissas, D. Niarchos, C. Dimitropoulos, and J. Dolinsek, Phys. Rev. Lett. **84**, 761 (2000)

[11] T. Walther, Ultramicroscopy **96**, 401 (2003)

[12] S. Estradé, J. Arbiol, F. Peiró, Ll. Abad, V. Laukhin, Ll. Balcells, and B. Martínez, Appl. Phys. Lett. **91**, 252503 (2007)

[13] H. Kurata and C. Colliex, Phys. Rev. B **48**, 2102 (1993); Z. L. Wang, J. Bentley, N. D. Evans, Micron **31**, 355 (2000); Z. L. Wang, J. S. Yin and Y. D. Jiang, Micron **31**, 571 (2000)

[14] J. Choi, J. Zhang, S.-H. Liou, P. A. Dowden, and E. W. Plummer, Phys. Rev. B **59**, 13453 (1999)

[15] R. Bertacco, J. P. Contour, A. Barthélemy, and J. Olivier, Surf. Science **511**, 366 (2002)

[16] M. Abbate, Private communication

[17] M. Abbate, F. M. F. de Groot, J. C. Fuggle, A. Fujimori, Y. Tokura, Y. Fujishima, O. Strebel, M. Domke, G. Kaindl, J. Van Elp, B. T. Thole, G. A. Sawatzky, M. Sacchi, and N. Tsuda, Phys. Rev. B **44**, 5419 (1991)

[18] M. Abbate, F. M. F. de Groot, J. C. Fuggle, A. Fujimori, O. Strebel, F. López, M. Domke, G. Kaindl, G. A. Sawatzky, M. Takano, Y. Takeda, H. Eisaki, and S. Uchida, Phys. Rev. B **46**, 4511 (1992)

[19] F. M. F. de Groot, J. C. Fuggle, B. T. Thole, and G. A. Sawatzky, Phys. Rev. B **42**, 5459 (1990)

[20] S. Valencia, A. Gaupp, W. Gudat, Ll. Abad, Ll. Balcells, A. Cavallaro, B. Martínez, and F. J. Palomares, Phys. Rev. B **73**, 104402 (2006)

[21] F. M. F. de Groot, J. Faber, J. J. M. Michiels, M. T. Czyzyk, M. Abbate, and J. C. Fuggle, Phys. Rev. B **48**, 2074 (1993); M. Abbate, R. Potze, G. A. Sawatzky, and A. Fujimori, Phys. Rev. B **49**, 7210 (1994)

5 Magnetic properties and magnetotransport

In this chapter, the magnetic properties of LCMO films measured by SQUID magnetometry will be firstly presented. It will be shown that magnetization saturation (M_S) and Curie temperature (T_C) of LCMO films grown on (001) and (110) STO substrates are profoundly sensitive to substrate orientation. An analysis of the possible sources of this dissimilar response has been carried out. In particular, the possible correlation of film strain state and T_C using the magnetoelastic model [1] has been investigated. We signal that within this model the high depression of magnetic properties occurring in most strained films, (001) LCMO ones in this case, cannot be explained, and other sources of magnetic depression should be found. Knowing the well established tendency of manganite films to present dead layers and electronic phase separation, we use the compositional analysis of these (001) and (110) films (Ch4) and the mechanical and electronic characteristics of (001) and (110) planes (Ch1) to present a scenario that may explain the observed effects on the magnetic and electronic properties depending on the plane of growth.

Substrate selection not only modifies the M_S and T_C of the films but also the magnetic anisotropy. More precisely, magnetic anisotropy is changed within the film plane. We studied the magnetic anisotropy of (001) and (110) LCMO films, firstly evaluating it by magnetometry. Our results indicate that the in-plane magnetic anisotropy is in both cases stress-controlled. In a more general approach, we present

clear evidences of the strong relevancy of the intrinsic elastic properties of the manganite films to define the in-plane magnetic anisotropy of manganite films.

To end the chapter, we show the magnetotransport measurements carried out in (001) and (110) LCMO films. We signal the existence of a metal to insulator transition appearing at temperatures close to the T_C of the films. We worked also with lithographed LCMO electrodes, with paths and contacts that allowed the measurement of the longitudinal and transverse voltage generated by the injected current. With these lithographed samples, the injected current direction was controlled by the track and thus it has been possible to tune the relative position of the applied magnetic field and the current by rotating the sample in the external field. The angular dependence of the longitudinal resistance [anisotropic magnetoresistance (AMR)] and of the transverse resistance [planar Hall effect (PHE)] were investigated. The AMR amplitude was observed to be highly sensitive to the plane of growth and to the current direction. We argue that these results may be induced by the different scattering events happening in the (001) and (110) planes. The PHE experiments clearly indicated the magnetic anisotropy of the films influences the shape of the PHE curves, and in the case of (110) films it was possible to model the in-plane uniaxial magnetic anisotropy

5.1 Magnetometry

The magnetic properties of LCMO were studied by SQUID magnetometry. Relevant characteristics of the ferromagnetic transition and hysteresis loops at low temperature on (001) and (110) samples are carefully studied. We have observed that (001) films present depressed magnetic properties compared to those of (110) ones. Taking into account the existing theoretical approach to correlate the Curie temperature of manganite films to the elastic deformation of the unit cell, we have evaluated the possible relevance of the strain into the T_C of our films. From this analysis, we conclude that the applicability of this model is limited to the less strained films, (110) films in this case, and additional effects need to be considered to explain the high T_C reduction in the case of more strained films, which are the (001) ones.

Furthermore, from hysteresis loops measured with field applied along different direction, we have evaluated film magnetic anisotropy. For the in-plane anisotropy, both (001) and (110) films present a stress dependent magnetic anisotropy, being the easy axes defined by the more stressed direction. The symmetry of this magnetic anisotropy is quite different for (001) and (110) films: we observe a biaxial system for (001) films,

with easy [110] directions, and a uniaxial system for (110) films, with easy [001] directions. As expected for substrate-induced tensile strain and reduced dimensionality, out-of-plane direction is proved to be in both series of samples the hardest axis. The conclusions obtained from magnetometry measurements were confirmed by further ferromagnetic resonance (FMR) experiments carried in a pair of these (001) and (110) films.

The process to distinguish the different contributions to magnetic energy and how to extract the values of the magnetic anisotropy constants is shown. This detailed analysis demonstrates that the elastic properties of (001) and (110) films direct their magnetic anisotropy.

This section will be then structured in the following way:

1. Presentation of general results on the magnetic properties in (001) and (110) films of a wide range of thickness.

2. Analysis of the film Curie temperature on the framework of a magnetoelastic model that correlates the experimentally measured strain and T_C. Completing the analysis with chemical and electronic studies shown in Ch4, we present a scenario which allow understanding the observed magnetic and electronic properties (001) and (110) film.

3. Study of the magnetic anisotropy.

The LCMO samples used in this section and the corresponding thickness are listed in Table 5.1.

Table 5.1. List of LCMO samples used for this section.

Sample	Substrate	Sample	Substrate	Thickness (nm)
070704A	STO(001)	070704B	STO(110)	14
180304AA	STO(001)	180304BB	STO(110)	17
050929A3	STO(001)	050929B4	STO(110)	17
240204A	STO(001)	240204B	STO(110)	43
230204A	STO(001)	230204B	STO(110)	63
290504A	STO(001)	290504B	STO(110)	80
200204A	STO(001)	200204B	STO(110)	85
270504A	STO(001)	270504B	STO(110)	93
090704A	STO(001)	090704B	STO(110)	110
050406A	STO(001)	050406B	STO(110)	150

5.1.1 Experimental results

Magnetization dependence on temperature of (001) and (110) samples of different thickness (*t*) was studied applying the magnetic field of 5 kOe in the sample

plane. The magnetization dependence on the applied magnetic field, also with the magnetic field applied in the sample plane, was measured at 10 K.

First, the temperature dependence of the magnetization of each film of the series of simultaneously grown (001) and (110) films is presented in Figure 5.1. With these curves we can explore the film ferromagnetic transition. Some examples, corresponding to films of thickness $t = 17$ (squares), 43 (circles), 85 (up triangles), 110 (down triangles) and 150 nm (rhombi) are plotted in Figure 5.1, corresponding to (a) (001) films and to (b) (110) films.

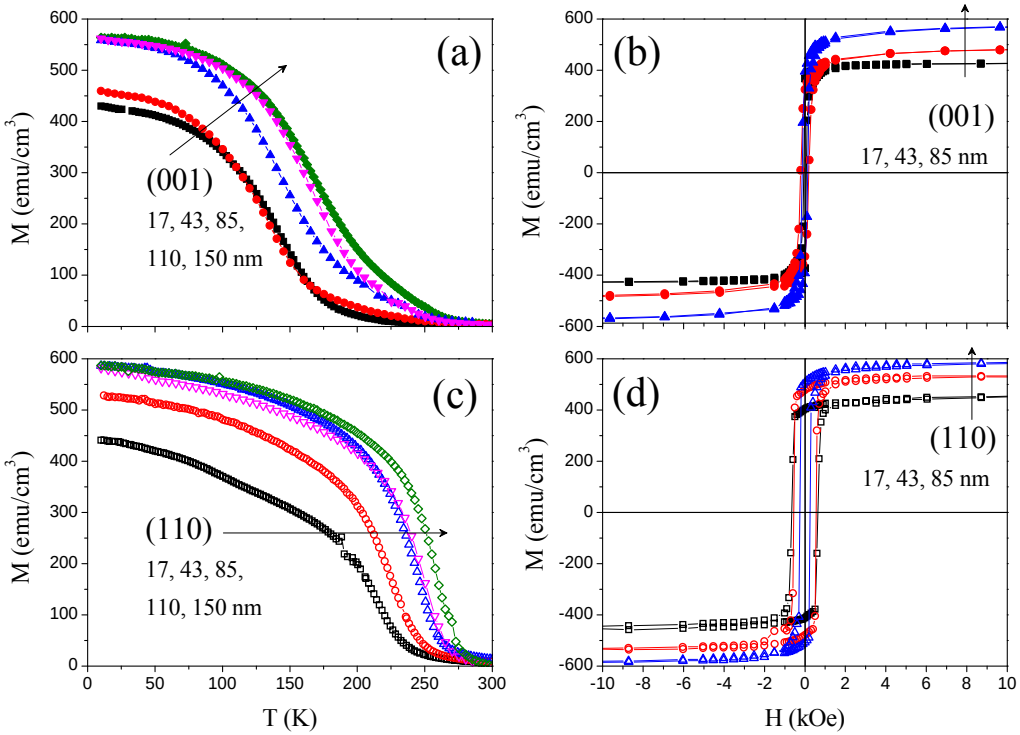

Figure 5.1. Magnetization *vs* temperature measured at 5 kOe of (a) (001) and (b) (110) films of thicknesses 43 nm (triangles) and 85 nm (circles). Field was applied in plane along the [100] direction for the (001) films and along [001] one for the (110) films. [(b) and (d)] Magnetization *vs* magnetic field loops measured at 10 K for the (001) and (110) 17, 43 and 85 nm films of [(a) and (c)], respectively.

An inspection of Figure 5.1a immediately reveals that the magnetization of the (001) films displays a decrease of the magnetization and a lowering of the temperature onset of ferromagnetic behavior (T_C) as t decreases. This trend has been reported earlier for (001) films of LCMO [2][3] and other $R_{1-x}A_xMnO_3$ manganites [4][5] grown on different substrates. The same trend is displayed by (110)LCMO films (Figure 5.1c). However, there are relevant differences: for the (110) films compared to the (001) ones,

the decay of T_C when reducing thickness is much less pronounced and the ferromagnetic transition occurs at higher temperature and the paramagnetic to ferromagnetic transition is sharper. These observations indicate that (110) films present improved magnetic properties. The deduction of the T_C from these measurements is done by taking the value of temperature at which a linear fit of the highly slope curve intersects M = 0. The extracted T_C values are included in Table 5.2, and for instance for the films with $t = 43$ nm, $T_C^{001} = 176$ K for the (001) film and $T_C^{110} = 252$ K for the (110) one. To monitor the different features of the ferromagnetic transition, in Figure 5.2a we present a series of derivatives of the magnetization dependence of temperature curves, weighted by the T_C of each film.

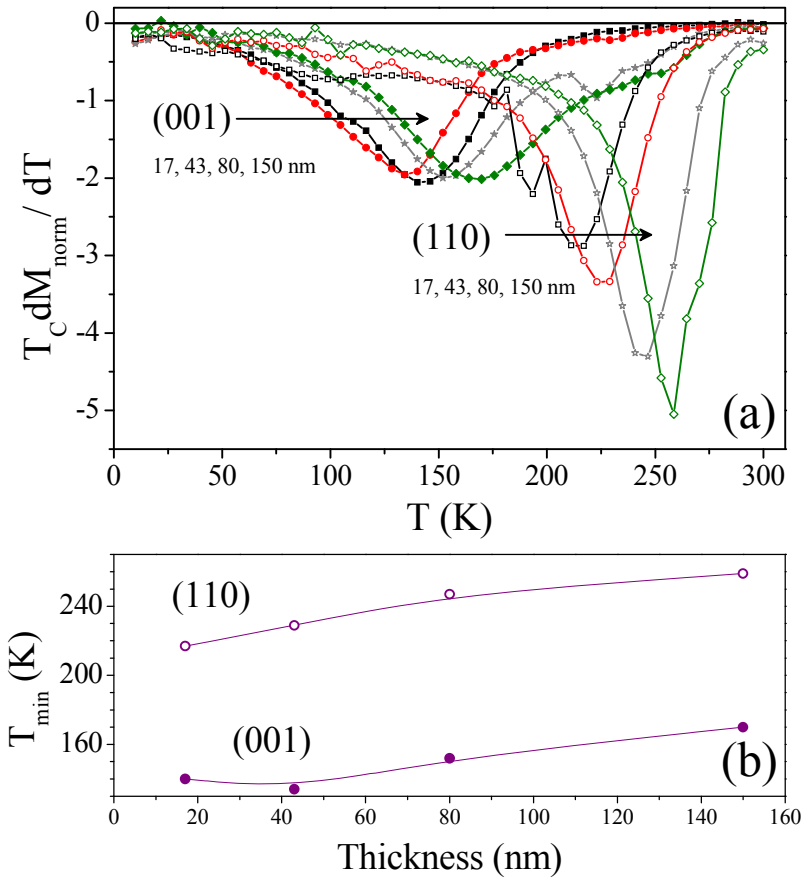

Figure 5.2. (a) Derivatives of the normalized magnetization (M_{norm}) for a series of films of $t = 17$ (squares), 43 (circles), 80 (stars), and 150 nm (rhombi) as a function of temperature, calculated from magnetization dependence on temperature curves; the derivatives are weighted by the correspondent film T_C [$T_C dM_{norm}/dT$]. Solid symbols correspond to (001) films and open symbols to (110) ones. (b) Thickness dependence of the minimum of $T_C dM_{norm}/dT$ curves (T_{min}) shown in (a).

The existence of a minimum in the curves depicted in Figure 5.2a is the signature of the ferromagnetic transition (negative slope in magnetization *s* temperature curves), and the abruptness of the transition can be characterized by the width of these derivatives curves. For a given thickness, the minimum position of the curves of (001) films differs from that of (110) ones, occurring at higher temperatures for the (110) films than for the (001) ones (approximately separated by $\Delta T \sim 80$ K). In Figure 5.2b we plot the position of the minimum of the temperature dependence of the derivative curves (T_{min}) as a function of film thickness. In all cases, (110) films present higher T_{min} values than (001) ones. Besides, from the curves shown in Figure 5.2a, the wider derivatives curves for the (001) films signal that the magnetic transition is progressive in these films; however, the (110) films present much narrower derivative peaks indicating abrupt magnetic transition.

Table 5.2. Experimental results on M_S obtained from 10 K hysteresis loops and T_C from magnetization *vs* temperature measured at 5 kOe (in both cases, magnetic fiel is applied in-plane) for the series of thickness explored. Percentages from the M_S and T_C maximum values for each sample are also shown.

Thickness (nm)	(001)				(110)			
	M_S (emu/cm^3)	$M_S/M_{S\,max}$ (%)	T_C (K)	$T_C/T_{C\,max}$ (%)	M_S (emu/cm^3)	$M_S/M_{S\,max}$ (%)	T_C (K)	$T_C/T_{C\,max}$ (%)
14					375	63.45	248	90.18
17	428	72.42	180	65.45	466	78.85	244	88.73
43	477	80.71	176	64.00	544	92.05	252	91.64
61	516	87.31	187	68.00	550	93.06	263	95.64
80	560	94.75	210	76.36	588	99.49	266	96.73
85	570	96.45	213	77.45	589	99.66	266	96.73
93	570	96.45	218	79.27	591	100.00	267	97.09
110	591	100.00	221	80.36	591	100.00	268	97.45
150	580	98.14	230	83.64	591	100.00	275	100.00

The low-temperature film magnetization as a function of magnetic field have been investigated, and we plot the experimental data from $t = 17$ nm (squares), 43 nm (circles), and 85 nm (up triangles) films of (001) and (110) orientation in Figure 5.1b and d, respectively. Lower saturation magnetization (M_S) values are observed for the (001) films compared to those for the (110) films from the analysis of the magnetic hysteresis loops shown in Figure 5.1b and d at high field (typically at 20 kOe). Being the $La_{2/3}Ca_{1/3}MnO_3$ bulk value 591 emu/cm^3, we signal the closer to bulk M_S values of

(110) films compared to those of (001) films, being for instance the M_S values for the t = 43 nm films M_S^{110} = 544 emu/cm^3 and M_S^{001} = 477 emu/cm^3.

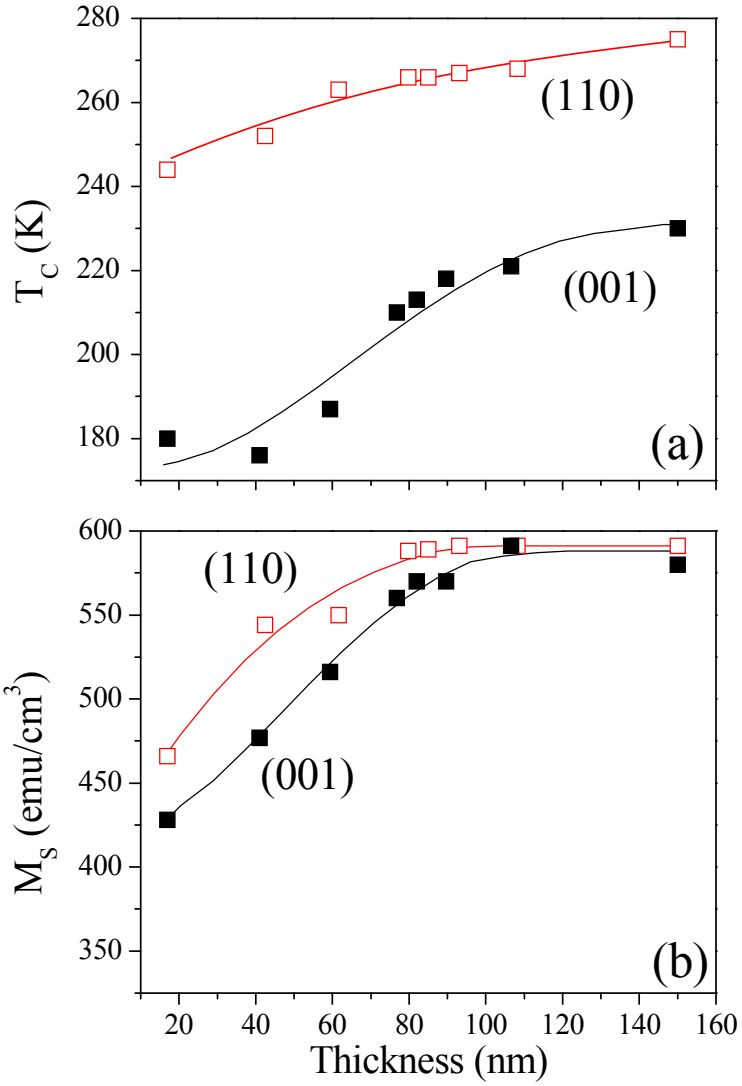

Figure 5.3. (a) Curie temperature and (b) saturation magnetization values of films from 17 nm to 150 nm thick. These values have been calculated from curves obtained in similar experimental conditions as those of curves shown in Figure 5.1.

The differences in T_C and M_S were *a priori* unexpected since both films were grown simultaneously on substrates having the same lattice mismatch with LCMO. However, as it has been shown in Ch4, (001) and (110) films are in different strain states. This point will be discussed later. In Table 5.2 we present a summary of all the collected values of T_C and M_S of (001) and (110) films, as well as the ratio from the

corresponding maximum measured values of M_S and T_C, which corresponds to those of the 150 nm (110) film.

We recall that the bulk values of $La_{2/3}Ca_{1/3}MnO_3$ are $T_C \sim 270$ K and $M_S = 591$ emu/cm^3. The observed trend signals that (110) film magnetic properties are better than those of (001) ones for the whole range of explored thickness. A clear image of this behavior is given in Figure 5.3, where the T_C and M_S dependence on thickness for films with both orientations are shown. It has to be noted that M_S values are influenced by a non-avoidable experimental error, as they depend on the thickness and area of each film. On the contrary, T_C is determined more accurately since the same experimental conditions are set for the magnetization *vs* temperature measurements and similar procedure have been used to determine the T_C. Remarkable differences of the T_C values are observed for instance comparing the $t = 43$ and 63 nm (001) and (110) films (up to 28 %).

In summary, the magnetic properties of LCMO films, and in concrete the saturation magnetization (M_S) and Curie temperature (T_C) are explored in (001) and (110) films from a wide range of thickness. Closer to bulk values are obtained in (110) samples, whereas depressed M_S and T_C as well as a gradual ferromagnetic transition is observed in (001) samples.

5.1.2 Magnetoelastic model applied to LCMO films

Now we recall the structural characterization of the films (presented in Ch4) to analyze the observed depletion of the (001) film properties compared to those of (110) ones. First, we summarize in short the reported scenarios as the causes of the depletion of magnetic properties of (001) films compared to those of the bulk.

The commonly found depression of T_C values in thin films [2][6][7] has been proposed by Millis [1] to be a consequence of the epitaxial strain of the lattice. Although some recent works [8] suggest that elastic strain could not be the only explanation, the model of Millis is still commonly accepted as a general rule.

Early suggested by Millis *et al.* [1], film strain induced by the epitaxial growth has two distinguishable consequences:

1. Similarly to what has been experimentally observed in bulk materials [9][10], a uniform compression (dilatation) of the manganite unit cell

would lead to a broadening (narrowing) of the conduction band, a reinforcement (weakening) of the Mn^{3+}-Mn^{4+} electron transfer and a weakening (reinforcement) of the electron-phonon coupling thus leading to an increase (decrease) of T_C.

2. A biaxial distortion strengths the Jahn-Teller distortion and produces a subsequent increase of the splitting of the e_g electron bands, eventually reinforcing a tendency to charge localization.

As a consequence of these facts, the dependence of T_C on substrate-induced strain can be written as [1]:

$$T_C(\varepsilon) = T_C(\varepsilon = 0)(1 - \alpha\varepsilon_B - \frac{1}{2}\beta\varepsilon_{bi}^{\,2}) \qquad [5.1]$$

where ε_B is the bulk strain and ε_{bi} is the biaxial strain.

The expressions of ε_B and ε_{bi} as a function of the strain values for two orthogonal in-plane directions, ε_{11} and ε_{22}, and for out-of-plane direction, ε_{33}, are:

$$\varepsilon_B = \frac{1}{3}(\varepsilon_{11} + \varepsilon_{22} + \varepsilon_{33}) \qquad [5.2]$$

$$\begin{aligned} \varepsilon_{bi} &= \sqrt{\left(\varepsilon_{bi}^{in}\right)^2 + \left(\varepsilon_{bi}^{out}\right)^2}, \\ \varepsilon_{bi}^{in} &= \frac{1}{2}(\varepsilon_{11} - \varepsilon_{22}), \\ \varepsilon_{bi}^{out} &= \frac{1}{4}(2\varepsilon_{33} - \varepsilon_{11} - \varepsilon_{22}) \end{aligned} \qquad [5.3]$$

where the strain values ε_{ij} ($i = j$, $1 \le i \le 3$) are calculated using the experimentally determined interplanar distances (Ch4: Figure 4.11 and Table 4.6) and the corresponding bulk value along the studied [*hkl*] directions, and the expression $\varepsilon_{ij} = (d^{film}_{hkl} - d^{bulk}_{hkl}) / d^{bulk}_{hkl}$ being [ij] ≡ [*hkl*]. In eq. 5.1, $\alpha = (1/T_C)\, dT_C/d\varepsilon_B$ is related to the unit-cell volume variations under strain ($\Delta V/V = 3\,\varepsilon_B$) and β accounts for the Jahn-Teller energy splitting.

It follows from the eq. 5.1 that whereas the biaxial distortion always leads to a reduction of T_C, this is not the case for the bulk contribution, which can be either positive or negative depending on the sign of $\Delta V/V$ under strain. Experimentally it has been found that in almost all the cases the T_C of films grown on single crystalline substrates is lower than its corresponding bulk value, irrespectively on the sign of the in-plain strain.

Assuming an elastic unit-cell deformation, the out-of-plane strain (ε_{33}) is related to the in-plane strain (ε_{11}, ε_{22}) by the elastic constants of the lattice, and differs from

them depending on the particular orientation of the substrate. For a cubic substrate and a (001) plane, $\varepsilon_{33} = \nu /(1-\nu) (\varepsilon_{11} + \varepsilon_{22})$ where ν is the Poisson ratio given by $\nu = c_{11} / (c_{11} + c_{12})$ being c_{11} and c_{12} the appropriate elastic constants [11]. When $\nu = 1/2$, the unit cell volume is preserved under strain, otherwise it changes.

In Ch4 (Figure 4.11) two different tendencies of the unit-cell volume of (001) and (110) films were shown. Recalling these data, most relevant observations are:

(a) Both (001) and (110) films present higher volume value than that of bulk LCMO unit cell.

(b) For $t > 20$ nm, (001) LCMO films are more strained than the (110) LCMO ones, being the corresponding (001) unit cell volume larger than that of (110) films: $V_{uc}^{001} > V_{uc}^{110}$. Thus, unit cell volume is not preserved, and it also changes under strain, thus we can discard the possibility that a constant Poisson ratio is applicable for the LCMO films.

Before presenting the dependencies of ε_{bi} on thickness, we need to comment on the measured anisotropic in-plane relaxation of interplanar distances in (110) films which contrast with the almost non-relaxed (001) films. In fact, (110) lattice relaxes faster along the [1-10] direction than along the [001] direction, and although the lattice mismatch (f) is identical for (001) and (110) planes of LCMO and STO, in-plane strains ε_{11} and ε_{22} are different since they are not only determined by the mismatch but also by the anisotropic elastic constants. The different atomic sequence along [001] and [1-10] directions anticipates different Young moduli ($Y_{001} \neq Y_{1-10}$) and thus structural relaxation must be in-plane anisotropic. In next section we will present the influence of these different elastic properties on the magnetic anisotropy of (001) and (110) films.

Now, turning to the investigation of how the strain influences the T_C of (001) and (110) films, we need to complement the already shown magnetic properties of films of 14 to 150 nm thickness, presented in Table 5.2 and Figure 5.3, with the strain values obtained from the structural characterization. The summary of the bulk strain (ε_B) and biaxial strain components [ε_{bi}(in) and ε_{bi}(out)] calculated using eq. 5.2 and eq. 5.3 is presented in Table 5.3. We plot the in-plane ε_{11} and ε_{22} and out-of-plane ε_{33} strain coefficients of (001) and (110) films, evaluated as the difference between interplanar distances for film and corresponding values for bulk samples. Table 5.3 shows the thickness dependences of the bulk (ε_B) and biaxial strains (ε_{bi}), calculated using eq. 5.2 and eq. 5.3. To clearly observe the evolution of strain values with film thickness, we

plot together in Figure 5.4 the strain parameters ε_{11}, ε_{22} and ε_{33} and the bulk (ε_B) and biaxial strains (ε_{bi}).

Table 5.3. Calculated strain coefficients for (001) and (110) films used for the magnetoelastic model fit. They correspond to: bulk strain ε_B, in-plane biaxial strain [ε_{bi}(in)], out-of-plane biaxial strain [ε_{bi}(out)] and total biaxial strain ε_{bi}^2.

Thickness (nm)	(001)			(110)		
	ε_B (%)	ε_{bi}(in) (%)	ε_{bi}(out) (%)	ε_B (%)	ε_{bi}(in) (%)	ε_{bi}(out) (%)
14	0.393	0	-1.176	0.396	-0.076	-0.942
17	0.344	0	-1.250	0.360	-0.123	-0.849
43	0.317	0	-1.290	0.216	-0.238	-0.702
63	0.317	0	-1.290	0.244	-0.139	-0.618
80	0.312	0	-1.298	0.241	-0.136	-0.511
85	0.328	0	-1.274	0.227	-0.142	-0.487
90	0.333	0	-1.266	0.236	-0.129	-0.454
110	0.339	0	-1.258	0.213	-0.086	-0.477
150	0.315	0	-1.216	0.037	-0.081	-0.067

To observe the influence of unit cell strain on T_C, we recall eq. 5.1. In this expression, there is a term related to unit cell compression (dilatation) given by $\alpha\varepsilon_B(t)$. For a film under a (thickness dependent) bulk strain $\varepsilon_B(t)$, the resulting stress is $\sigma_B \approx K\varepsilon_B(t)$, K being the bulk modulus elasticity [$K = (1/3)(c_{11} + 2c_{12})$]. Elastic constants of $La_{0.67}Ca_{0.33}MnO_3$ were experimentally determined by So *et al.* [12], being c_{11} = 350 GPa and c_{44} = 150 GPa. Using as reference the $SrTiO_3$ perovskite [13], it has been calculated the experimental ratio $(c_{12}/c_{11})_{STO} = 0.322$ and thus, applying this ratio to LCMO film elastic constants, c_{12} is $c_{12} = (c_{12}/c_{11})_{STO}\, c_{11}$ = 113 GPa. These elastic constants lead to K = 192 GPa, and the resulting bulk stress on thinner films, $\varepsilon_B \approx 0.4$ % (Table 5.3, ,Figure 5.4), amounts $\sigma_B \approx 1$ GPa. The change of the unit cell volume associated to this compression should produce a change of T_C comparable to what has been measured in experiments under hydrostatic pressure in LCMO crystals. From experiments performed on polycrystalline LCMO samples, $dT_C/dP \approx 0.9$ K/kbar [10]. Thus, substituting the dT_C/dP and K value, we obtain $\alpha = (1/T_C)\, dT_C/d\varepsilon_B = K\,(1/T_C)\, dT_C/dP \approx 6.4$. From experimental data in Figure 5.4b, the maximal ε_B occurring in the thinner films ($\varepsilon_B = 0.4$ %) will induce a reduction of only $|\Delta T_C| \approx 3$ %. This low decrease on T_C cannot be the only cause for the

experimentally measured T_C reduction of up to a 35 %, already shown in Table 5.2. Thus, bulk strain is not enough to account for the observed thickness dependence of T_C.

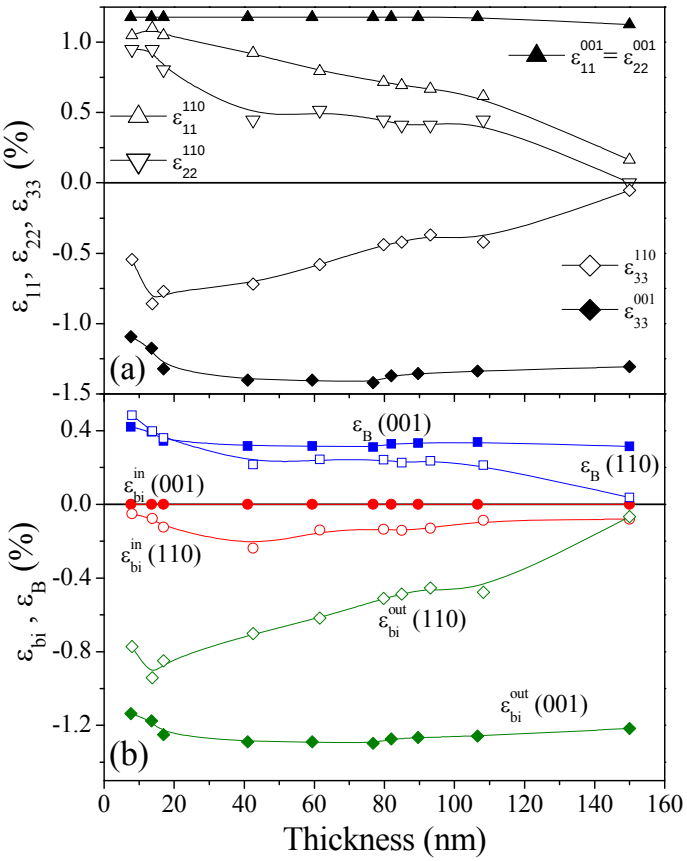

Figure 5.4. (a) Evaluated strains ε_{11}, ε_{22} and ε_{33} as a function of thickness for the (001) and (110) films. They correspond for (001) (solid symbols) to crystallographic directions in (001) films are $\varepsilon_{11} = \varepsilon_{100} = \varepsilon_{010}$ (up triangles) and $\varepsilon_{33} = \varepsilon_{001}$ (rhombi) and in (110) films are $\varepsilon_{11} = \varepsilon_{001}$ (up triangles), $\varepsilon_{22} = \varepsilon_{1\text{-}10}$ (down triangles) and $\varepsilon_{33} = \varepsilon_{110}$ (rhombi).(b) For (001) (solid symbols) and (110) films (open symbols) they are displayed the bulk strain ε_B (squares) and in-plane (circles) and out-of plane biaxial strain (rhombi) as a function of film thickness.

The biaxial strain effect on $T_C(t)$ is presented in Figure 5.5, where T_C(150nm) is the Curie temperature of the 150 nm film and ε^2_{bi} accounts for the total biaxial strain evaluated using eq. 5.3 for each film. Data appear concentrated around two strain regions, reflecting the fact that (110) films (circles) are under a much smaller biaxial strain than (001) ones (squares). Inspection of data in Figure 5.5 signals that for (110) films $T_C(t)$ / T_C(150nm) is roughly linear on ε^2_{bi} as predicted by eq. 5.1, thus suggesting that for (110) films elastic strain effects could be at the origin of the suppression of T_C of (110) strained films. However, the data for most strained (001) films dramatically

differ from the linear behavior. In fact, data in Figure 5.5 indicate that the T_C of (001) films changes without a significant variation of biaxial strain. In order to illustrate that the biaxial strain dependence of $T_C(t) / T_C(150nm)$ is not greatly affected by the presence of the bulk strain contribution, in Figure 5.5 we include the experimental data once the bulk strain contribution is corrected ($T_C(t) / T_C(150nm) + \alpha\varepsilon_B$) (open symbols).

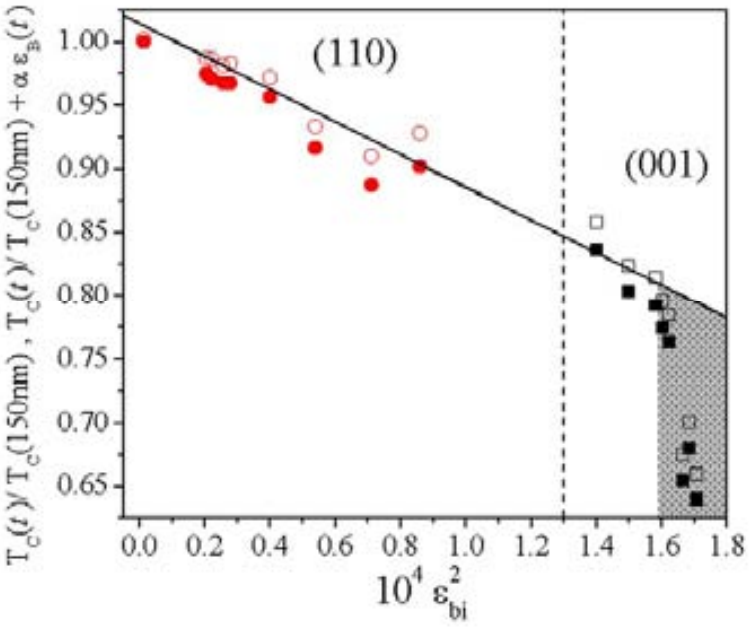

Figure 5.5. Dependence of the Curie temperature $T_C(t) / T_C(150nm)$ (closed symbols) on the square of the biaxial strain (ε^2_{bi}). Open symbols correspond to the $T_C(t) / T_C(150\ nm)$ after correction of the bulk strain contribution [$T_C(t) / T_C(150\ nm) + \alpha\cdot\varepsilon_B(t)$].

From this analysis of the T_C of (001) and (110) films within the magnetoelastic model, we conclude that the strong dependence of T_C on thickness observed in the thinner ($t < 85$ nm) (001) films is not dominated by the elastic strain deformation of the manganite lattice. However, one can notice that the linear dependence of the $T_C(t) / T_C(150nm)$ on ε^2_{bi} for (110) films can be extrapolated to higher strain region (solid line in Figure 5.5). The extrapolated curve overlaps with experimental data for the less strained (001) films. A linear fit analysis of these data allows calculating β, which accounts for the JT splitting. In these extrapolation, the resulting value is $\beta = 2.3\cdot10^3$ (with a 5% error). This result is coherent with reported β values for different manganite films [8], being all of the same order of magnitude that the one presented here ($\sim1\cdot10^3$).

In summary, the observed two strain regime in the $T_C(\varepsilon^2_{bi})$ indicates that two different mechanisms control the T_C value:

(1) The elastic strain-induced deformation of the lattice and subsequent reduction of the hopping probability between 3d-e_g orbitals, as predicted by the model of Millis *et al*. [1], dominate the $T_C(t)$ dependence of the films with biaxial strain of $\varepsilon^2_{bi} < 1.6\ 10^{-2}$.

(2) A non-elastic mechanism, related to the occurrence of other effects, is more relevant for more strained films, typically the (001) ones.

To build a macroscopic framework that may account for the experimental evidences of depressed T_C and M_S in (001) films compared to those of (110) films, we have analyzed our NMR, EELS and XPS results presented in Ch4 and we have considered the electronic and chemical information of these films that they revealed.

Discussion on the electronic and chemical effects in LCMO films grown on (001) and (110) STO substrates

Further keys to understand the role of the different orientation on the electronic and magnetic properties of (001) and (110) films are based on the experimental evidences found by NMR, EELS and XPS. We recall that not only the T_C of (001) films suffer a much relevant decrease that cannot be understood within the magnetoelastic model, but also the overall magnetization of these films, and more precisely M_S is found to be highly depressed (Figure 5.3, Table 5.2).

Our experimental results on the electronic and chemical effects on (001) and (110) films can be summarized as follows:

(a) Electronic phase separation has been clearly found to happen in the more strained (001) films, as extracted from NMR experiments:

(1) Localized $Mn^{4+}(Mn^{3+})$ state is a clear indication of the presence of phase separated ferromagnetic insulator regions on (001) films.

(2) A smaller fraction of ferromagnetic Mn^{m+} ions is found in (001) films compared to that in (110) films.

(b) XPS experiments have revealed a relative surface enrichment by divalent alkaline Ca^{2+} in (001) films respect to (110) ones.

(c) From EELS experiments, in (001) films is found that the electronic state of Mn is not homogeneous through the film, finding Mn^{3+} ions next to the film-substrate interface and Mn^{4+} ions next to the surface, whereas homogeneous mixed valent $Mn^{3+/4+}$ state is found all through (110) films.

To understand the possible origins of the observed phase separation and their relation to strain, we separate our discussion into two different scenarios: (1) The coexistence of phases with orbital order, and subsequent electronic charge localization, with phases with orbital disorder. (2) Chemical segregation.

(1) Coexistence of orbital ordered and disordered phases: About the relationship between strain and orbital ordering in manganite thin films, it has been reported that biaxial strain can trigger different orbital ordering such as antiferromagnetic A-type or antiferromagnetic C-type depending on the sign (tensile or compressive) of the strain [14]. In Figure 5.6a we show schematic views of these orbital ordered states [A-type in (ii) and C-type in (iii)] compared to that of the ferromagnetic state [F-type, (i)]. For the A-type magnetic order, the basal planes are ferromagnetic, and for the C-type one, the ferromagnertism is kept along the c-axis.

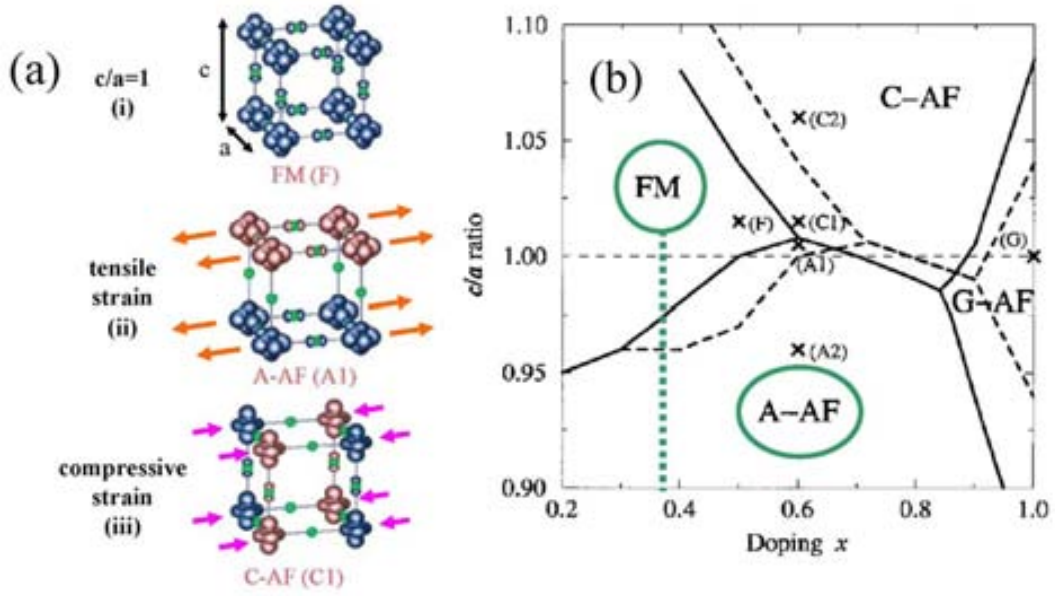

Figure 5.6. (a) Calculated charge density distribution, indicating the magnetic orderings depending on the unit cell deformation, being a and c the in-plane and out-of-plane parameters, respectively: (i) ferromagnetic F-type (c/a = 1), (ii) antiferromagnetic A-type (c/a < 1), with ferromagnetism within the planes, (iii) antiferromagnetic C-type (c/a > 1), with ferromagnetism within the c-axis. (b) Phase diagram of $La_{1-x}Sr_xMnO_3$ showing the magnetic ordering as a function of the Sr doping x and of the unit cell c/a ratio. [(a) and (b)] are extracted from Ref. [15].

From Z. Fang *et al.* [15], tensile in-plane strain on a (001) film stabilizes the x^2-y^2 orbital levels while the subsequent out-of-plane compression pushes up the z^2 orbital level, thus favoring electron occupancy of the x^2-y^2 orbitals and eventually leading to A-type orbital ordering.

To sketch the scenario under discussion, in Figure 5.7 the relevant orbitals for (001) and (110) films are shown, as well as the expected energy splitting of the e_g orbitals under the tensile biaxial strain developed in the LCMO/STO system.

Within this scenario, we can see in Figure 5.7a the relevant energy splitting happening in (001) orbitals under biaxial strain, as proposed by Fang *et al.* [15], with electron occupancy of the x^2-y^2 levels.

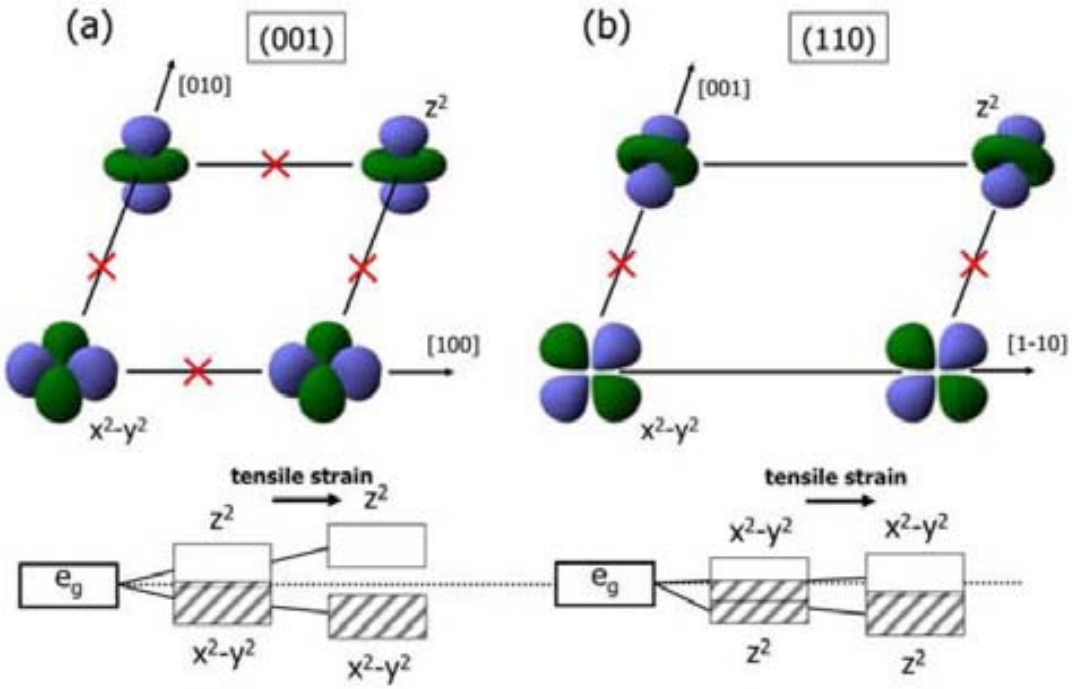

Figure 5.7. Sketch of the orbital arrangement (top panel) and energy levels (bottom panel) of e_g orbitals in tensile strained (001) (a) and (110) films (b). Mn-O bonds in the (001) case are elonganted along [100] and [010] directions and within the (001) plane, whereas in the (110) case Mn-O bonds along [1-10] direction are not contained in the (110) plane. For simplicity, at each Mn site it is shown only one of the e_g orbitals and oxygen sites have been represented by crosses.

The effect of the biaxial strain in the (110) film orbitals (Figure 5.7b) is much different. The (110) in-plane z^2 orbital level becomes stabilized by the tensile epitaxial strain. On the other hand, the x^2-y^2 orbitals are influenced by both the unit cell deformation within the (110) plane and along the out-of-plane direction since in the plane the orbitals are elongated along the [100] and [010] directions. We consider that under this strain map, which is of different sign being positive in-plane and negative out-of-plane, the x^2-y^2 orbitals should be not significantly lifted in energy. Therefore, the energy splitting between z^2 and x^2-y^2 orbitals in this case should be much smaller

than that occurring in the (001) films and thus the driving force towards antiferromagnetic orbital ordering should be reduced in (110) films. Consequently, the degenerated metallic and ferromagnetic orbital (F-type) ordering in (110) films should be more robust than in (001) films. This agrees with magnetization measurements and NMR and EELS experiments (Ch4). More explicitly, Fang *et al.* [15] showed that the tetragonal distortion of the $La_{1-x}Sr_xMnO_3$ lattice determines the magnetic ordering at a given x-doping. In Figure 5.6b we present the phase diagram of this manganite. For the $x \sim 0.3$ doping, the unit cell tetragonality, measured as the *c/a* ratio being *c* the parameter along the z^2 orbital and *a* the parameter within the basal plane (see scheme in Figure 5.6a) determines the occurrence of ferromagnetic or A-type magnetic orders.

To study the effect of the tetragonal deformation from the ideal ferromagnetic cubic environment, we include in Figure 5.8 the tetragonality τ (inset) and the variation of the tetragonality $\Delta\tau = |1-\tau|$ of the (001) (close symbols) and (110) (open symbols) LCMO unit cell as a function of thickness. We have calculated τ from structural data (Ch4, Figure 4.11) and using:

$$\tau^{001} = \frac{d_{001}}{d_{100}} \qquad [5.4]$$

$$\tau^{110} = \frac{d_{001}}{\sqrt{d_{1-10}^2 + d_{110}^2}} \qquad [5.5]$$

Eq. 5.4 was used for the (001) films and eq. 5.5 for the (110) ones. The film tetragonality values τ^{001} and τ^{110} shown in the inset of Figure 5.8 differ from the expected ideal cubic F-type environment $\tau = 1$ (dashed line). The deviation of τ^{001} and τ^{110} from the ideal FM value ($\Delta\tau = |1-\tau|$) is plotted against the film thickness in the main panel of Figure 5.8. Since for the (001) films larger values of $\Delta\tau$ are observed compared to those of (110) films, we suggest that the driving force towards the A-type ordering is stronger in the (001) films than in (110) ones.

The coexistence of A-type and F-type phases, stronger in the (001) films, implies that the (001) ones cannot be longer viewed as homogeneous but rather as a composite of A and F nanoclusters. The broader ferromagnetic transition observed for (001) films compared to that of (110) ones (Figure 5.1a and c) may illustrate this phase separation phenomenon.

So far, phase separation has been described and attributed to strain acting on the film. However, recently Brey [16] has shown that even in the absence of strain, at the

interface between an optimally doped (001) epitaxial manganite thin film and an insulator (for example, $SrTiO_3$), there is a charge depletion that weakens the ferromagnetic double exchange coupling and thus the interface layers are unstable against antiferromagnetic correlations.

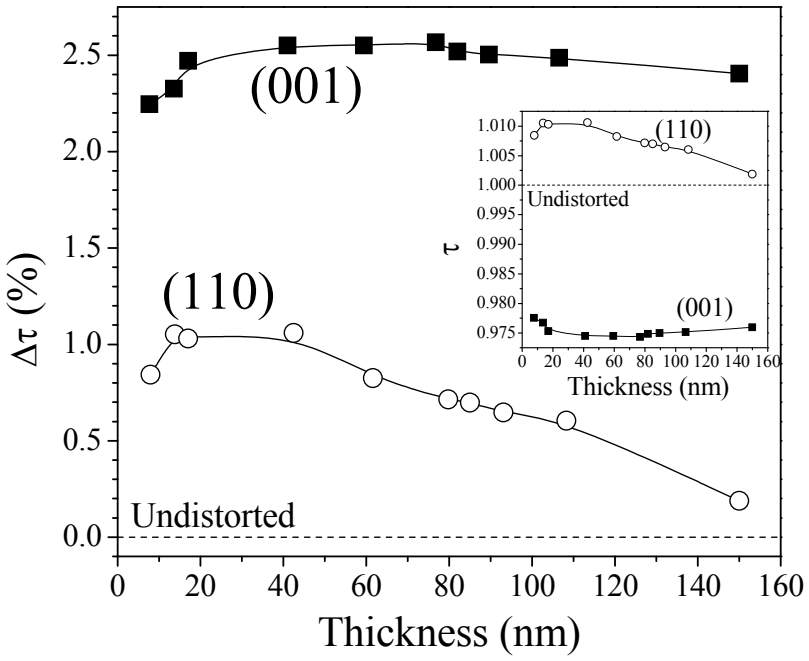

Figure 5.8. Main panel: Variation of the tetragonality (τ) of (001) (solid symbols) and (110) (open symbols) unit cell of LCMO films as a function of film thickness. Inset: Tetragonality of the same films. Dashed lines refer to the corresponding values for the undistorted unit cell.

As shown in Ch1, terminating planes in (001) STO can be TiO_2 and SrO, both being electrically neutral. In contrast, the $(R_{1-x}A_x)O$ and (MnO_2) layers of the upper growing manganite $R_{1-x}A_xMnO_3$ are charged: +(1-x) and –(1-x), respectively. Therefore, it is clear that due to the build-in potential at interfaces, charge redistribution within the manganite layer may occur, modifying their properties. In contrast, (110) STO free surfaces (SrTiO and O_2), are not neutral but charged: +4 and -4, respectively. However, in this case epitaxial stacking of a $R_{1-x}A_xMnO_3$ oxide on the (110) STO substrate would not lead to any polarity difference as the growing layers ($R_{1-x}A_xMnO$ and O_2) are also polar (+4 and -4) for any doping level. Thus, even in the absence of strain effects, one could also foresee that (110)LCMO films are less prone to display charge separation effects.

Therefore, both strain and electrostatic effects reinforce antiferromagnetic orbital ordering, reducing the total ferromagnetic response, and thus the discrimination between both effects is ambiguous. However, electrostatic effects are expected to be confined within few unit cells close to the interface [16] rather than ~ 5 -10 nm deep as indicated by the NMR and EELS data (Ch4). We thus suggest that the electronic phase separation in (001) films is not confined to the film/substrate interface and other sources different from electrostatic effects needs to be called.

(2) Chemical segregations: XPS experiments signal a relative surface enrichment by divalent alkaline Ca^{2+} in (001) films respect to (110) ones. Moreover, EELS measurements confirm the existence of Ca^{2+} segregation to the (001) surface, followed by the change in Mn electronic state, which does not occur in (110) films. As previously mentioned, some reports on Ca^{2+} substituted manganites [17][18] have shown that phase segregation can occur through the interchange of Ca^{2+} and La^{3+} sites, being found to cause a Ca^{2+}-enrichment of LCMO surfaces [17]. The decrease of Ca-contents in the bulk of $(La_{1-x}Ca_x)MnO_3$ film and/or eventually at the film/substrate interface leads to an expansion of the unit cell due to the larger ionic radius of La^{3+} (≈ 1.16 Å) compared to that of Ca^{2+} (≈ 1.12 Å). Therefore, we could expect that the elastic energy required to accommodate lattice mismatch (tensile in the present case) can be reduced by compositional changes. In the present case, enrichment of the La/Ca ratio deep into the film is foreseen. This process would lead to Ca^{2+} enrichment at the film surface in agreement with our XPS measurements. A similar process would also be operative in $La_{1-x}Sr_xMnO_3$ thin films on STO substrates, which are also under tensile strain. In fact, as reported by Maurice *et al*. [7] and Bertacco *et al*. [18], the surface of $La_{2/3}Sr_{1/3}MnO_3$ films on (001)STO were found to be Sr-rich. Simon *et al*. [17] reported a systematic EELS study of the interfaces in epitaxial films of $La_{2/3}Ca_{1/3}MnO_3$ and $La_{2/3}Ba_{1/3}MnO_3$ on (001) STO substrates, finding that the film-substrate interface is alkaline depleted in the case of films which are under tensile strain.

One could thus speculate that a driving force for chemical phase separation is the reduction of the elastic energy imposed by the heteroepitaxial growth. As, in average, the films have the appropriate hole doping ($x = 1/3$) for optimal ferromagnetic properties, the strain-induced compositional changes can only produce a depression of them, eventually creating non-ferromagnetic regions.

Before concluding, it is worth to comment on the remarkable observation that the unit cell parameters of thinner (001) and (110) films (Ch4: Figure 4.11)

anomalously increase when film thickness reduces below $t \sim 20$ nm. In low thickness LCMO films, de Andrés *et al*. [19] reported different crystal symmetry. Y. L. Qin *et al.* [20] also showed that thinner LCMO films on STO had a tetragonal symmetry instead of the orthorhombic observed in thicker ones. Our HRTEM images do not allow us to confirm that the same change of symmetry occurs in our thinner films, although the fact that a similar expansion of the unit cell was observed by de Andrés *et al.* [19] suggests that this symmetry change can be the cause. However, as the thinner (001) and (110) films present very different strain effects and T_C's, the change of symmetry can not be directly related to the magnetic properties of the ferromagnetic phase. We do not exclude that other defects can also promote the chemical or electronic inhomogeneities. Indeed, it has been previously shown that some other more trivial effects, such as the atomic quality of the surfaces of the underlying well-matching substrates $(Sr_2AlTaO_6)_{1-x}(LaAlO_3)_x$ for (001) LCMO grown onto them, has a significant roll onto the strength of the substrate-induced phase separation [18]. However, the systematic variations of all structural and magnetic properties with thickness reported here in the LCMO/STO system indicate that those effects are not relevant in the present case.

To conclude this discussion on the applicability of magnetoelastic model to (001) and (110) films grown on STO substrates we observe that systematically higher T_C and M_S of (110) films compared to those of (001) ones turned out to be caused by the different elastic constants. Thus, (110) films relax earlier than (001) ones and (110) films display a progressively reduced biaxial strain. The analysis of the dependence of the T_C on the biaxial strain has revealed that the elastic deformation of the manganite lattice can describe the response of the less strained films –(110) ones- whereas other effects should be invoked to account for the properties of the most strained films–(001) ones. The existence of phase separation, likely triggered by orbital ordering, may account for both the lowering of T_C and the higher concentration of non-ferromagnetic and non-metallic regions in the (001) films than in (110) ones. Our discussion on the possible sources of the depressed properties signals that both strain and charge depletion effects associated to polarity discontinuities at interfaces may reinforce antiferromagnetic orbital ordering. In the cases under study, different tetragonal deformations of the Mn octahedra are found for the (001) and (110) film unit cells. We suggest that the strain effects related to the tetragonal distortion of (001) and (110) unit cells determine film properties. Thus, for the less distorted (110) films, film properties,

and in particular the T_C's, can be understood in the framework of an elastic deformation of the unit cell. On the other hand, the more distorted (001) films cannot be described within the same model. Other effects, as chemical segregation, namely Ca-enrichment of the free surface of most strained films, are claimed to be possible mechanism of releasing elastic energy at the cost of depressing their magnetic properties. In any event, it is clear that (110) films and (110) interfaces of manganite epitaxial films are magnetically more robust.

5.1.3 Magnetic anisotropy

The magnetic anisotropy of manganite thin films has been widely studied by different groups for the identification of hard or easy axis magnetization and for its influence in domain wall arrangement, conductivity and optical properties [21][22]. The research, mainly in Ca and Sr-doped manganite films, has been focused in understanding the magnetic anisotropy of (001)-oriented films [25][26][27][28][29]. Special interest has been addressed to the role of substrate-induced strain on the magnetic anisotropy, and some of the cited articles compare films grown on different substrates. Nevertheless, there has not been achieved a conclusive answer to which the dominating source is.

To understand the phenomena underlying magnetic anisotropy of thin films, it is necessary to recall its sources. In fact, magnetic anisotropy is determined by the balance of intrinsic magnetocrystalline anisotropy, and magnetoelastic and magnetostatic energies. The former is usually considered to be less relevant than the later, as in manganites the orbital momentum of 3d Mn ions is quenched by the crystal field. In thin films, the substrate-induced lattice distortions and shape effects are thus most commonly directing the magnetic anisotropy. Manganite films are commonly grown on (001)-oriented cubic substrates that induce a tetragonal distortion of the unit cell depending on the lattice mismatch between the manganite and the substrate. The deformation of the unit cell causes a change of the Mn-Mn distances, and consequently the ferromagnetic properties of the material may change, including the magnetic anisotropy. Manganite films grown under tensile strain depict easy magnetic (001) plane and those grown under compressive strain, easy magnetic [001] axis [23]. In manganites, the magnetization lays preferentially along the elongated dimensions, signaled by the measured positive magnetostriction λ of these materials.

Magnetic anisotropy of LCMO films grown on (001) $SrTiO_3$ (STO) substrates, being tensile strained (nominal mismatch of ~ 1 %), has been studied by different groups [24][25], finding somehow contradictory results. Whereas for Nath *et al.* [24] the in-plane magnetization of (001) LCMO films has its easy axis along the [110] directions, O'Donnell *et al.* [25] conclude that the films are biaxial with the easy axis along [100] axes. Although both groups attributed the magnetic anisotropy to the substrate-induced strain, they do not agree on the easy axes identification. Reports on magnetic anisotropy of $La_{2/3}Sr_{1/3}MnO_3$ (LSMO) films grown on (001) STO substrates face similar difficulties [26][27]. Whereas Berndt *et al*. [26] find in-plane [100] easy axes and relate them to be strain-induced, Steenbeck and Hiergeist [27] signal that the [110] easy axes arise from intrinsic magnetocrystalline anisotropy. We notice that for LSMO films on STO the lattice mismatch is much lower (~ 0.3 %) and thus the strain of LSMO epitaxial films is much lower than that of LCMO ones. Furthermore, in these works, strain values (ε) are most commonly evaluated from the measurement of the out-of-plane unit cell parameter and supposing that in-plane parameters can be deduced using a fixed Poisson ratio. Concerning the elastic constants of the film unit cell, Young moduli of the manganite unit cell are obtained *ad hoc* from measurements carried on single crystals [30] or from other perovskites [31].

Aiming to disclose the source of low-temperature magnetic anisotropy in manganite films, we address this issue by first determining the thickness-dependent strain effects on our LCMO films simultaneously grown on (110) and (001) STO substrates. The magnetic anisotropy of a series of films of thicknesses between 17 and 85 nm has been studied, mainly by means of magnetic hysteresis loops, measured in a SQUID magnetometer, with the magnetic field applied either in-plane or out-of-plane. Also, ferromagnetic resonance technique (FMR) has been used to confirm the observed magnetic anisotropy. The detailed structural characterization (Ch4) allows us determining the unit cell parameters of (110) and (001) films of different thickness. Starting with (110) films, we prove that the magnetoelastic anisotropy arising from the different stress along the two in-plane orthogonal directions [001] and [1-10], which is driven by the different substrate-induced strain, dominates (110) film magnetic anisotropy. Learning from (110) film analysis the relevance of magnetoelastic effects, we apply the same methodology to the study of the magnetic anisotropy of (001) films. Substrate symmetry dictates a biaxial in-plain response, but remarkably enough, the easy axis is [110]. We suggest that these results spread out from the already observed

differences on the relative weight of substrate-induced strain anisotropy and intrinsic elastic properties (Young moduli) in (110) and (001) and films. Whereas the former dominates the in-plane magnetic anisotropy in (110) LCMO films, the later determines that of (001) LCMO ones.

(110) films: thickness dependent magnetoelastic energy

We will start studying the strain state of (110) films as a function of thickness. The strain values were calculated from the structural parameters (Ch4, Figure 4.11 and Table 4.6) as previously described in this chapter. The dependence of these strain values as a function of film thickness is shown in Figure 5.4a. As we work here only with (110) films, we will directly refer to the [*hkl*] direction associated to the inspected directions (in-plane ε_{001} and $\varepsilon_{1\text{-}10}$ strains and out-of-plane ε_{110}).

A summary of the in-plane strain values along the two orthogonal directions [001] and [1-10] is found in Table 5.4.

Table 5.4. Strain values (ε_{hkl}) of (110) films and corresponding magnetization saturation values (M_S) measured at 10 K.

Thickness (nm)	ε_{001} (%)	$\varepsilon_{1\text{-}10}$ (%)	ε_{110} (%)	M_S (emu/cm^3)
17	0.971	0.726	-0.849	466
43	0.843	0.367	-0.797	544
80	0.640	0.367	-0.517	588
85	0.615	0.332	-0.499	589

An inspection of the ε_{001} and $\varepsilon_{1\text{-}10}$ values in Table 5.4 indicates that for any given thickness (t) the strain in the (110) plane is anisotropic since $\varepsilon_{001} \neq \varepsilon_{1\text{-}10}$. Moreover, when looking at the thickness dependency of these strain values, we observe an evolution from higher to lower values, which is a signature of unit cell relaxation when increasing film thickness. Interestingly enough, when comparing strain values from films of different thickness (for instance, t_1 =17 nm and t_2 = 43 nm) it turns out that the relative change of strain is different along [001] and [1-10] directions [$(\varepsilon_{001}(t_1)\text{-}\varepsilon_{001}(t_2))/\varepsilon_{001}(t_1)$ = 12 % whereas $(\varepsilon_{1\text{-}10}(t_1)\text{-}\varepsilon_{1\text{-}10}(t_2))/\varepsilon_{1\text{-}10}(t_1)$ = 45 %]. On the other hand, the out-of-plane lattice parameter is compressed for all samples and thus the sign of [110] strain ε_{110} is negative (Table 5.4).

From the data shown in Figure 5.9, a clear image of the magnetic anisotropy of the (110) films can be obtained.

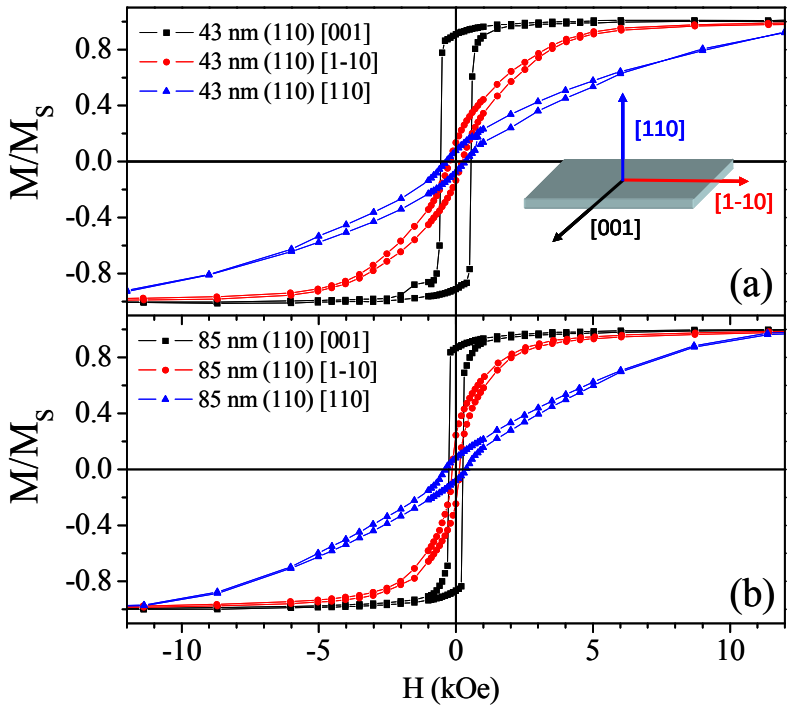

Figure 5.9. Normalized magnetization *vs* magnetic field loops measured at 10 K for (a) the 43 nm (110) film and (b) the 85 nm (110) films. Applied magnetic directions are in-plane [001] (squares) and [1-10] (circles) ones and out-of-plane [110] (triangles) one.

In Figure 5.9, the magnetic hysteresis loops of 43 nm (a) and 85 nm (b) thick films measured with the magnetic field applied parallel to in-plane [001] and [1-10] and along the out-of-plane [110] directions are included. High fields are necessary to saturate the films along the out-of-plane [110] direction, being this direction is a hard magnetic axis. Along the out-of-plane direction, the magnetic anisotropy is determined by the contraction of the unit cell parameter ($\varepsilon_{110} < 0$) that leads to a hard axis, and film shape effects [caused by the shorter out-of-plane dimension (film thickness)] are added to make this direction magnetically harder. As a result, the magnetization vector lies within in the (110) plane and the (110) plane is the easy magnetic plane. With the applied magnetic field along the in-plane [001] and [1-10] directions, for both films a square loop is recorded when magnetic field is applied parallel to [001] direction (squares) and a linear magnetization dependence on field when field is applied parallel to [1-10] direction (circles). These observations signal a uniaxial hard magnetic axis along [1-10] direction and an easy magnetic one along [001] direction. Indeed, the

comparison of magnetization loops of films of different thicknesses (Figure 5.9, t = 43 and 85 nm), we note that the hardness of the hard axis loops and the coercitivity of the easy axis loops are reduced values when increasing thickness.

To confirm the magnetic anisotropy observed by magnetometry, we performed ferromagnetic resonance (FMR) experiments on the 43 nm (110) film. These experiments were performed and analyzed by A. Brandlmaier and Dr. S. T. B. Goennenwein at the Walther-Meißner-Institut. In the FMR setup, we apply a static field that we can vary in position. We refer the in-plane θ and Θ angles to the [1-10] direction, where θ indicates the applied magnetic field position and Θ the magnetization vector position. The out-of-plane angles ϕ and Φ indicate the position of the applied magnetic field and magnetization vector, respectively, and they are referred to the [110] direction. A sketch of the angular relationship to the crystal axes is shown in Figure 5.10.

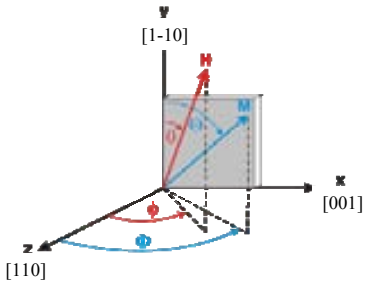

Figure 5.10. Sketch of the angular arrangement in the FMR experiment in the (110) film.

In Figure 5.11a and c we present the FMR spectra obtained for two different field-sample configurations: rotating the field out of the sample plane (θ is fixed and we vary ϕ, so–called out-of-plane configuration) or rotating the field within the sample plane (ϕ = 90 deg and we vary θ, so-called in-plane configuration). The FMR absorption along each direction appears as a peak-dip structure. The series of spectra have been shifted arbitrarily for clarity. We focus first in the analysis of FMR spectra obtained in the out-of-plane angular configuration (Figure 5.11a). For the range of applied magnetic field in this experiment (up to 10 kOe), the peak dip structures are only obtained when the magnetic field is applied parallel to the sample plane. In this case, the in-plane resonance has been measured along the in-plane [1-10] direction, and it is possible to apply the necessary field to achieve the resonance, so-called resonance field H_{res}. The flat spectra obtained for applied magnetic field parallel to the out-of-plane [110] direction signal that [110] direction is a hard magnetic axis. A clear image of the (110)

out-of-plane magnetic anisotropy is seen in Figure 5.11a, where the resonant field is plotted *vs* theθ angle. Along the [110] out-of-plane direction, it is not possible to achieve the necessary H_{res} to saturate the sample within the range of possible applied magnetic field.

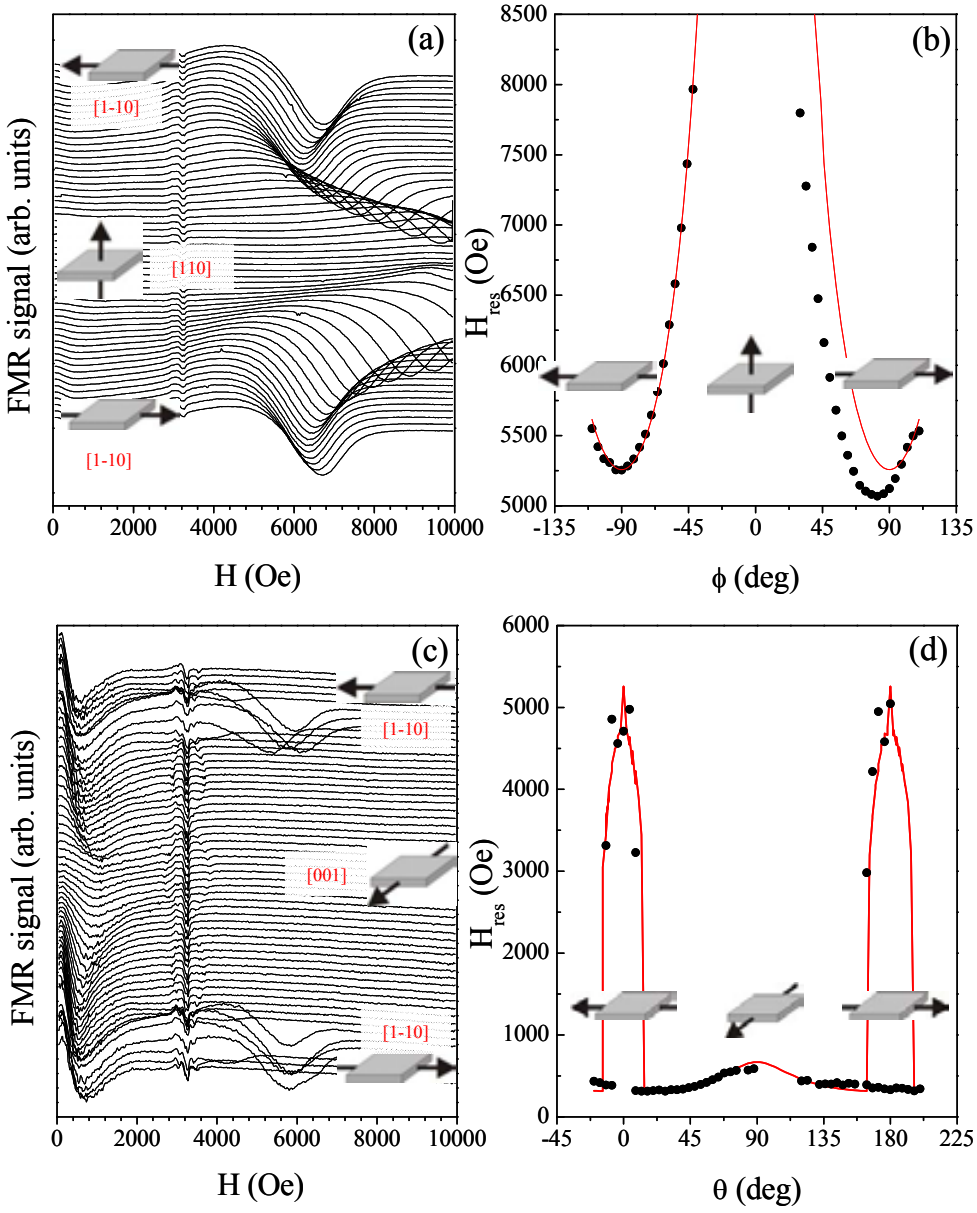

Figure 5.11. FMR measurements on 43 nm (110) film. Angular reference θ=0 is placed parallel to [1-10] direction. [(a) and (c)]: FMR spectra recorded with applied magnetic field varying (a) from in-plane [1-10] direction towards out-of-plane [110] direction and (c) in-plane of the sample, from [1-10] direction towards [001] one and back. [(b) and (d)]: Resonance field H_{res} for the different applied magnetic field orientation, being (b) for out-of-plane configuration and (d) for the in-plane configuration.

Now turning to the in-plane configuration, we notice that the FMR spectra shown in Figure 5.11c present peak-dip structures at different in-plane positions. Referred the in-plane angular position to the [1-10] direction, we observe an evolution of the resonances while changing the applied magnetic field from being parallel to [1-10] direction towards [001] one. As also shown in Figure 5.11d, the necessary H_{res} along [1-10] direction, is much higher than along [001] direction. From the dependence of H_{res} on the applied direction we deduce that a hard magnetic axis is found along [1-10] direction.

In order to extract the relevant magnetic parameters from the FMR data, the angular dependence of the resonant field H_{res} has been calculated by using the expression of the free energy (F_{tot}) of the system:

$$F^{110} = F^{110}_{Zeeman} + F^{110}_{cub} + F^{\mathbf{[1\text{-}10]}}_{\mathbf{u}} + F^{\mathbf{[110]}}_{\mathbf{u,eff}} \qquad [5.6]$$

$$F^{110}_{cub} = \tfrac{1}{4} K_{\mathbf{c1}}\left[\mathbf{sin}^2(2\Theta) + \mathbf{sin}^4\,\Theta\,\mathbf{sin}^2(2\Phi)\right] \qquad [5.7]$$

$$F^{[1-10]}_{u} = K^{\mathbf{me}}_{\mathbf{u}}\,\mathbf{sin}^2\,\Theta\,\mathbf{sin}^2\,\Phi \qquad [5.8]$$

$$F^{\mathbf{[110]}}_{\mathbf{u,eff}} = K^{[110]}_{u,eff}\,\mathbf{sin}^2\,\Theta\,\mathbf{cos}^2\,\Phi \qquad [5.9]$$

Magnetostastic energy ($F^{110}{}_{Zeeman}$) is a constant value added to the total free energy. $F^{110}{}_{cub}$ accounts for the magnetocristallyne anisotropy energy term and $F^{[1\text{-}10]}{}_{me}$ refers to the magnetoelastic energy, taking as angular origin the in-plane [1-10] direction. The uniaxial out-of-plane anisotropy $F^{[110]}{}_{u,eff}$ includes the contribution from the shape effect and a possible magnetoelastic source applicable to the [110] direction. As both anisotropy present the same angular dependence, we can reduce them to one expression, obtaining a constant $K^{[110]}{}_{u,eff}$ that unifies both contributions.

In the analysis of FMR data, the fitting procedure is based in the minimization of the free energy (F^{110}) for the given angles and for each configuration. The parameters that can be fitted are the magnetic anisotropy constants: $K^{110}{}_{c1}$ (magnetocrystalline), $K^{me}{}_{u}$ (magnetoelastic) and $K^{110}{}_{u,eff}$ (effective uniaxial out-of-plane). The minimization of F^{110} is subjected to equilibrium conditions for the saturated magnetization vector, described by:

$$\frac{\partial}{\partial \Phi} F^{110}\Big|_{\Phi=\Phi_0} = \frac{\partial}{\partial \Theta} F^{110}\Big|_{\Theta=\Theta_0} = 0 \qquad [5.10]$$

The simulation curves of Figure 5.11b and d (solid lines) have been calculated from eqs. 5.6-5.9 and 5.10, and using experimental value of saturation magnetization M_S = 544 emu/cm^3. Best simulations are those included in Figure 5.11b and d and the

correspond fitting values of magnetic anisotropy constants are: for the magnetocrystalline one $K_{c1} = -6.53 \cdot 10^5$ erg/cm^3, for the magnetoelastic one $K^{me}_u = 8.81 \cdot 10^5$ erg/cm^3 and for the effective uniaxial out-of-plane one $K^{110}_{u,eff} = 2.45 \cdot 10^6$ erg/cm^3.

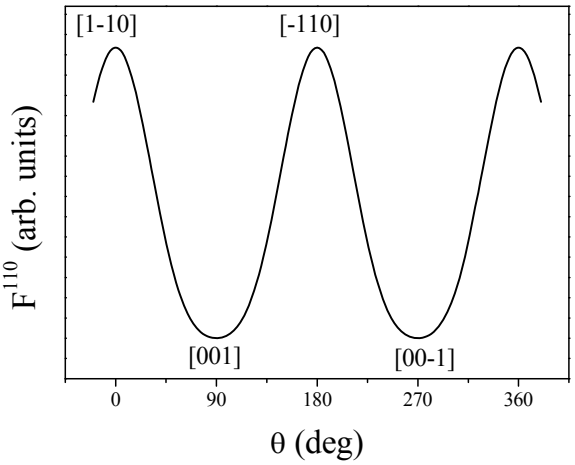

Figure 5.12. For the 43 nm (110) film, simulation of the total free energy F^{110} within the sample plane and in the absence of external magnetic field. The parameters used have been those extracted from simulations in Figure 5.11. Easy axis corresponds to [001] direction and hard axis to [1-10] direction.

Using the values extracted from the best simulations, we study in detail the magnetic anisotropy of within the (110) plane. We have simulated the angular dependence of F^{110} in the absence of magnetic field. The resulting curves are plotted in Figure 5.12. As already obtained from hysteresis loops ones (Figure 5.9), higher F^{110} occurs for magnetization parallel to the [1-10] direction, which indicates that this direction is a hard magnetic axis, and lower F^{110} values are found to happen for magnetization parallel to [001] direction, being an easy magnetic axis. Thus, uniaxial in-plane magnetic anisotropy in (110) films is confirmed.

In order to disclose the sources of the observed in-plane magnetic anisotropy we have extracted the magnetic anisotropy energies (E^{hyst}_{hkl}) from the measured hysteresis loops and compared them to the expected magnetoelastic energies (E^{me}_{hkl}) for these films. To obtain E^{hyst}_{hkl} we have calculated the work along the [hkl] direction done by the magnetic field (H_{hkl}) when the magnetization vector M changes from its saturation (M_S) to its remnant value (M_{rem}):

$$E_{hkl}^{hyst} = -\int_{M_S}^{M_{rem}} H_{hkl}\,dM = H_{\mathbf{max}}M_S + \int_{H_{\mathbf{max}}}^{0} M_{hkl}\,dH \qquad [5.11]$$

with H_{max} as the maximum field applied in the measurement. The resulting values are summarized in Table 5.4 and shown in Figure 5.13. As expected from the hardness of [1-10] loops, for a given thickness, the magnetic energy $E^{hyst}_{1\text{-}10}$ is larger than E^{hyst}_{001}. The in-plane uniaxial magnetic anisotropy of these films, characterized by a uniaxial magnetic anisotropy constant (K^{hyst}_{u}), is then calculated using the energy difference from the obtained values along these directions: $K_u = E^{hyst}_{1\text{-}10} - E^{hyst}_{001}$. The progressive decrease of K^{hkl}_{u} upon increasing thickness signals that the lattice relaxation accompanies the magnetic anisotropy.

The evaluation of magnetoelastic energy E^{me}_{hkl} has been performed using [32b]:

$$E_{001}^{me} = -\frac{3}{2}\lambda_{001}\sigma_{001} \qquad [5.12]$$

$$E_{1\text{-}10}^{me} = -\frac{3}{4}\lambda_{1\text{-}10}\sigma_{1\text{-}10} - \frac{3}{4}\lambda_{111}\sigma_{1\text{-}10} \qquad [5.13]$$

where λ_{001} and $\lambda_{1\text{-}10}$ account for the magnetostriction along [001] and [1-10] directions, respectively. As shown by eqs. 5.12 and 5.13, the E^{me}_{hkl} contributions depend on the epitaxial stress σ, defined in a general form by the Young modulus Y of the material and the strain ε: $\sigma = Y \cdot \varepsilon$. Along the different in-plane [*hkl*] directions, both the Young modulus and the strain ε may change, and thus we consequently evaluate the stress σ_{hkl} as: $\sigma_{hkl} = Y_{hkl} \cdot \varepsilon_{hkl}$, being [*hkl*] in the (110) films the in-plane [001] and [1-10]. In the case under study (LCMO/STO system) the in-plane strain is positive ($\varepsilon > 0$) for both in-plane directions, and thus the stress is also a positive magnitude ($\sigma > 0$). All the products of σ and ε are positive, and following eqs. 5.12 and 5.13 the final magnetoelastic energy sign will be determined by the magnetostriction λ. As λ is positive for manganites [23][33], the lower magnetoelastic energy (being $E^{me}_{hkl} < 0$, it means the higher absolute value of E^{me}_{hkl}) is expected to be found when magnetization is parallel to lengthened directions. For the evaluation of E^{me}_{hkl}, we use the magnetostriction value from thin LCMO films [33] ($\lambda_{001} = 5.5 \cdot 10^{-5}$), and we assume $\lambda_{1\text{-}10} = \lambda_{001} = \lambda_{111}$. The stress σ_{hkl} is evaluated using the strain values ε_{hkl} from Table 5.4 and the corresponding Young moduli (Y_{hkl}) which have been calculated using expressions from Ref. [34] and with the experimental values of Ref. [35], as explained

in detail in this chapter. Final values of Young moduli are $Y_{001} = 396$ GPa and $Y_{1\text{-}10} = 414$ GPa The resulting E^{me}_{hkl} values are shown in Table 5.5 and in Figure 5.13.

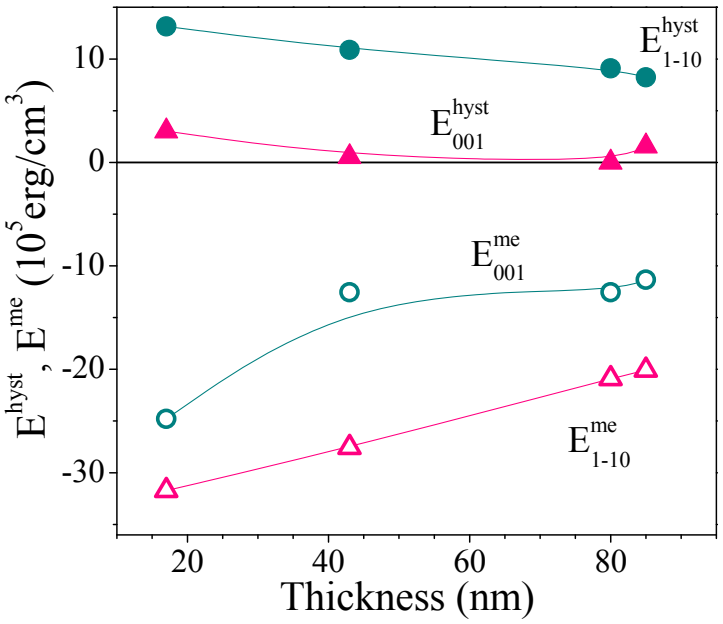

Figure 5.13. Experimental E^{hyst} values (solid symbols) along [1-10] (circles) or [001] (triangles) directions and calculated E^{me} values (open symbols) for [1-10] (circles) and [001] (triangles) directions as a function of film thickness.

Inspecting Figure 5.13, we notice that the pure experimental energies E^{hyst}_{hkl} and the evaluated magnetoelastic energies E^{me}_{hkl} are thickness dependence, as expected as the saturation magnetization M_S, the shape of the hysteresis loops and the strain values depend on the film thickness. The magnitude of the uniaxial in-plane magnetoelastic anisotropy has been determined by calculating its corresponding constant (K^{me}_u) from $K^{me}_u = E^{me}_{1\text{-}10} - E^{me}_{001}$ for each film. Comparing the K^{me}_u values, for instance the corresponding values for the 43 nm and 85 nm films are $K^{me}_u(43\text{ nm}) > K^{me}_u(85\text{ nm})$, being for the 43 nm film $K^{me}_u(43\text{ nm}) = 10.35 \cdot 10^5$ erg/cm^3. Comparing the dependence of K^{hyst}_u and K^{me}_u on film thickness (Table 5.5) we observe a similar evolution of both anisotropy constants. We note that all K^{hyst}_u and K^{me}_u values are of the same order of magnitude ($\sim 10^6$ erg/cm^3) and they are much stronger for the more strained thinner films. Although the anisotropy constant values obtained from the FMR measurements are not strictly comparable to those extracted from the hysteresis loops, we observe that the magnetoelastic constant is of the same order ($\sim 10^6$ erg/cm^3). These two sets experiments, magnetometry and FMR experiments, are characterized by working in

different time scales, with the former working with a quasi-static magnetization vector compared to the latter, which works a very short time scale. Thus, we suggest that due to this different methodological approach, the absolute value K^{me}_{u} cannot be directly compared between both methods.

Table 5.5. For (110) films of different thickness, evaluated in-plane magnetoelastic energies (E^{me}_{hkl}), magnetoelastic energy constant (K^{me}_{u}), measured in-plane magnetic anisotropy energies (E^{hyst}_{hkl}) and uniaxial magnetic anisotropy constant (K^{hyst}_{u}) are also shown.

Thickness (nm)	E^{me}_{001} (10^5 erg/cm^3)	$E^{me}_{1\text{-}10}$ (10^5 erg/cm^3)	K^{me}_{u} (10^5 erg/cm^3)	E^{hyst}_{001} (10^5 erg/cm^3)	$E^{hyst}_{1\text{-}10}$ (10^5 erg/cm^3)	K^{hyst}_{u} (10^5 erg/cm^3)
17	-31.72	-24.78	6.93	3.03	13.14	10.11
43	-27.55	-12.55	15.00	0.53	10.88	10.35
80	-20.91	-12.55	8.36	0.01	9.10	9.09
85	-20.08	-11.33	8.75	1.57	8.23	6.65

Up to this point, only magnetoelastic effects have been analyzed and no comment has been directed to the possible contribution of magnetocrystalline energy. We remark two important general points: (i) we notice that the magnetocrystalline anisotropy is independent of film thickness, (ii) magnetoelastic energy, linked to strain state of these films, depends on film thickness. Observing the evolution of the magnetic anisotropy on thickness (Figure 5.13), we conclude that the magnetoelastic energy dominates the magnetic anisotropy of (110) LCMO films.

(001) films: constant magnetoelastic energy

Using the structural characterization of the series of (001) films studied in this section (unit cell parameters shown in Figure 4.11 in Ch4), we present a summary of the film strain values ε_{hkl} (being [*hkl*] the crystallographic direction) in Table 5.6. In the (001) case, the in-plane unit cell parameters of the films and the substrate completely match, and no evolution as a function of thickness is observed (see Figure 5.4). Moreover, the strain along [100] and [110] in-plane directions is equal ($\varepsilon_{100} = \varepsilon_{110}$), meaning that the biaxial tensile strain drives the unit cell to be isotropically deformed in the (001) plane. The out-of-plane lattice parameter is compressed for all samples, and thus the sign of strain along [001] direction is negative ($\varepsilon_{001} < 0$) as it happens with the corresponding out-of-plane strain value of (110) films (Table 5.4).

Table 5.6. Strain values (ε_{hkl}) of (001) films and corresponding magnetization saturation values (M_S) measured at 10 K.

Thickness (nm)	$\varepsilon_{100}=\varepsilon_{010}$ (%)	ε_{001} (%)	M_S (emu/cm^3)
17	1.099	-1.399	428
43	1.099	-1.480	477
80	1.099	-1.496	560
85	1.099	-1.447	570

Magnetic hysteresis loops of 43 and 85 nm (001) films are plotted in Figure 5.14. Magnetic field was applied along in-plane [100] and [110] directions and along out-of-plane [001] one. Out-of-plane hysteresis loops (triangles) present a clear linear dependence on the applied field and thus [001] direction can be considered as a magnetic hard axis. As in the case of (110) films, shape effect and the fact that along the out-of-plane direction $\varepsilon_{110} < 0$ affect the magnetic anisotropy of (001) films, making the magnetization vector to rest within the (001) plane. The existence of a hard [001] axis signals the appearance of a uniaxial out-of-plane anisotropy with easy (001) plane.

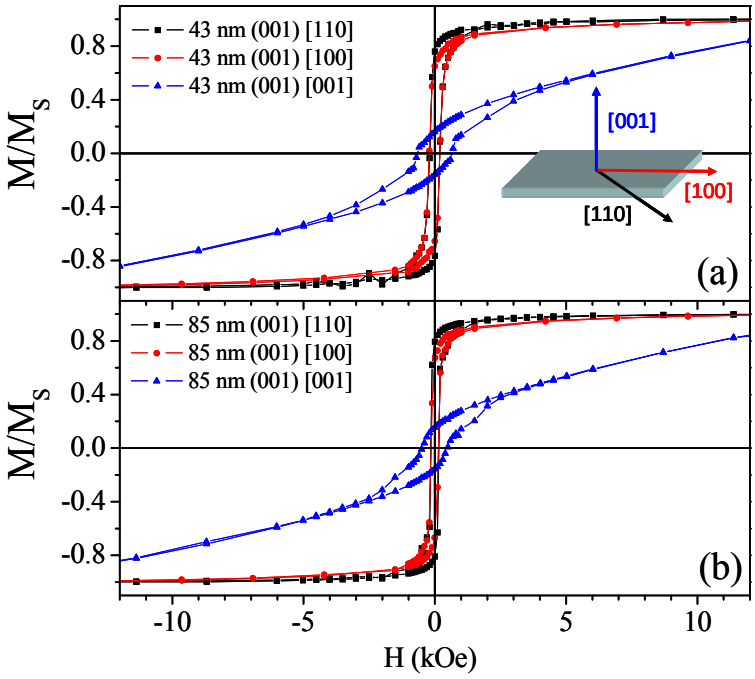

Figure 5.14. Normalized magnetization *vs* magnetic field loops measured at 10 K for (a) the 43 nm (001) film (b) and 85 nm (001) films. Applied magnetic directions are in-plane [110] (squares) and [100] (circles) ones and out-of-plane [100] (triangles) one. Inset: Sketch of the crystallographic directions with respect to film plane.

Focusing in the (001) in-plane hysteresis loops in Figure 5.14, we observe that the shape of loops along [110] (squares) and [100] (circles) directions is different. The remnant magnetization (M_{rem}) is larger along [110] than along [100] one. Furthermore, looking at the high field values, along [100] direction the saturation is achieved at a higher field than for [110] direction. To clarify the angular separation of the easy axes and thus determine the symmetry of the in-plane anisotropy, magnetization *vs* field curves have been measured with the applied field parallel to different directions. In Figure 5.15, the normalized curves for two 17 nm (001) films show easy [110] (up triangles) and [1-10] (squares) axes and hard [100] (circles) and [010] (down triangles), being the remnant magnetization along hard axis a 25 % lower than along the easy axes lower. Thus, four-fold magnetic anisotropy in the (001) plane is deduced, and also these experiments confirm that the observed magnetic anisotropy is intrinsic to the film rather than due to substrate-induced morphologic effects, as reported by Mattews *et al.* [36]. We conclude that in (001) films, [100] directions are clearly hard axes whereas those parallel to [110] directions are easy axes.

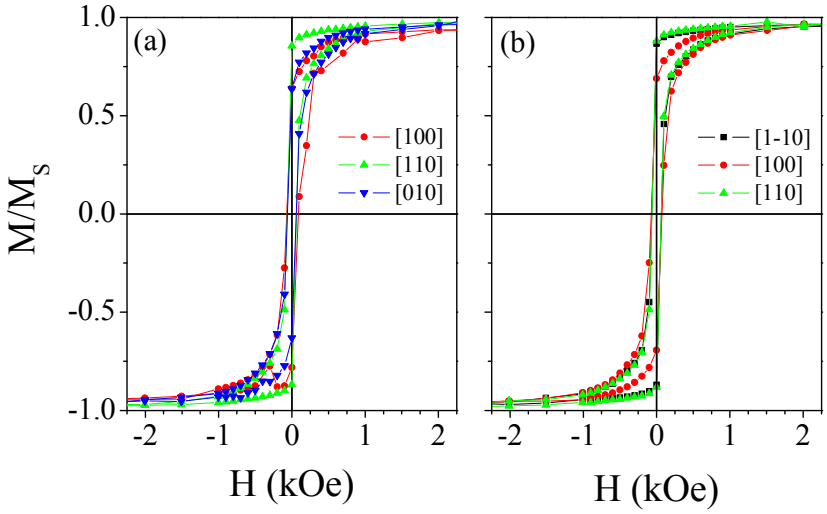

Figure 5.15. Normalized magnetization *vs* magnetic field loops measured at 10 K from two 17 nm (001) films (a) 050929A4 and (b) 050929A3. Magnetic field was applied in-plane of the samples and parallel to different directions separated by 45 deg: [1-10] (squares), [100] (circles), [110] (up triangles) and [010] (down triangles).

The magnetic anisotropy of (001) films has also been investigated by FMR experiments. A sketch of the angular relationship to the crystal axes in the (001) film is shown in Figure 5.16. shows the recorded FMR spectra of the 43 nm (001) sample. Out-

of-plane angles ϕ and Φ are referred to [001] direction, indicating the position of the applied magnetic field and magnetization vector, respectively.

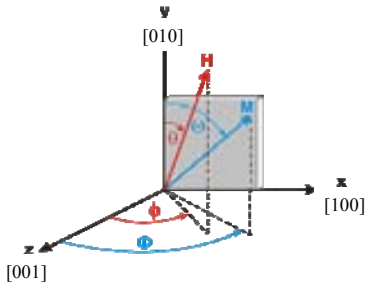

Figure 5.16. Sketch of the angular arrangement for the FMR measurement in the (001) film.

For clarity, the FMR spectra obtained for different applied field positions are arbitrarily shifted along the y-axis. In Figure 5.17 we include the data from the out-of-plane (a and b) and in-plane (c and d) configurations. Inspecting first the out-of-plane angular configuration spectra (Figure 5.17a), similarly to the (110) case, the range of applied magnetic field is not enough to saturate the sample when field is parallel to the out-of-plane direction, in this case [001] one. The only peak-dip structure, with a measurable value of resonance field H_{res}, observed appears when magnetic field is applied parallel to the plane, which under the used experimental conditions is the [010] direction. In Figure 5.17b, the dependence of H_{res} on the out-of-plane angle signals the divergence occurring near the [001] direction, which signals that [001] direction is a hard magnetic axis in the (001) sample.

Studying the in-plane configuration spectra (Figure 5.17c), we observe relevant differences with respect to the previously analyzed (110) ones (Figure 5.11c). In the (001) case, necessary H_{res} are lower than those of the (110) case. Moreover, the peak-dip structures present two main values of H_{res}, being the H_{res} value higher along [010] direction than along [110] direction. Figure 5.17d summarizes the dependence of H_{res} on the applied direction obtained from these FMR experiments.

To simulate the FMR data the total free energy F^{001} expressions are used but being adapted for the (001) plane and the corresponding expressions are:

$$F^{001} = F^{001}_{Zeeman} + F^{001}_{cub} + F^{[010]}_{u} + F^{[001]}_{u,eff} \qquad [5.14]$$

$$F^{010}_{cub} = \tfrac{1}{4} K_{c1} \left[\sin^2(2\Theta) + \sin^4\Theta \sin^2(2\Phi) \right] \qquad [5.15]$$

$$F^{[010]}_{u} = K^{me}_{u} \sin^2\Theta \sin^2\Phi \qquad [5.16]$$

$$F^{[001]}_{u,eff} = K^{[001]}_{u,eff} \sin^2\Theta \cos^2\Phi \qquad [5.17]$$

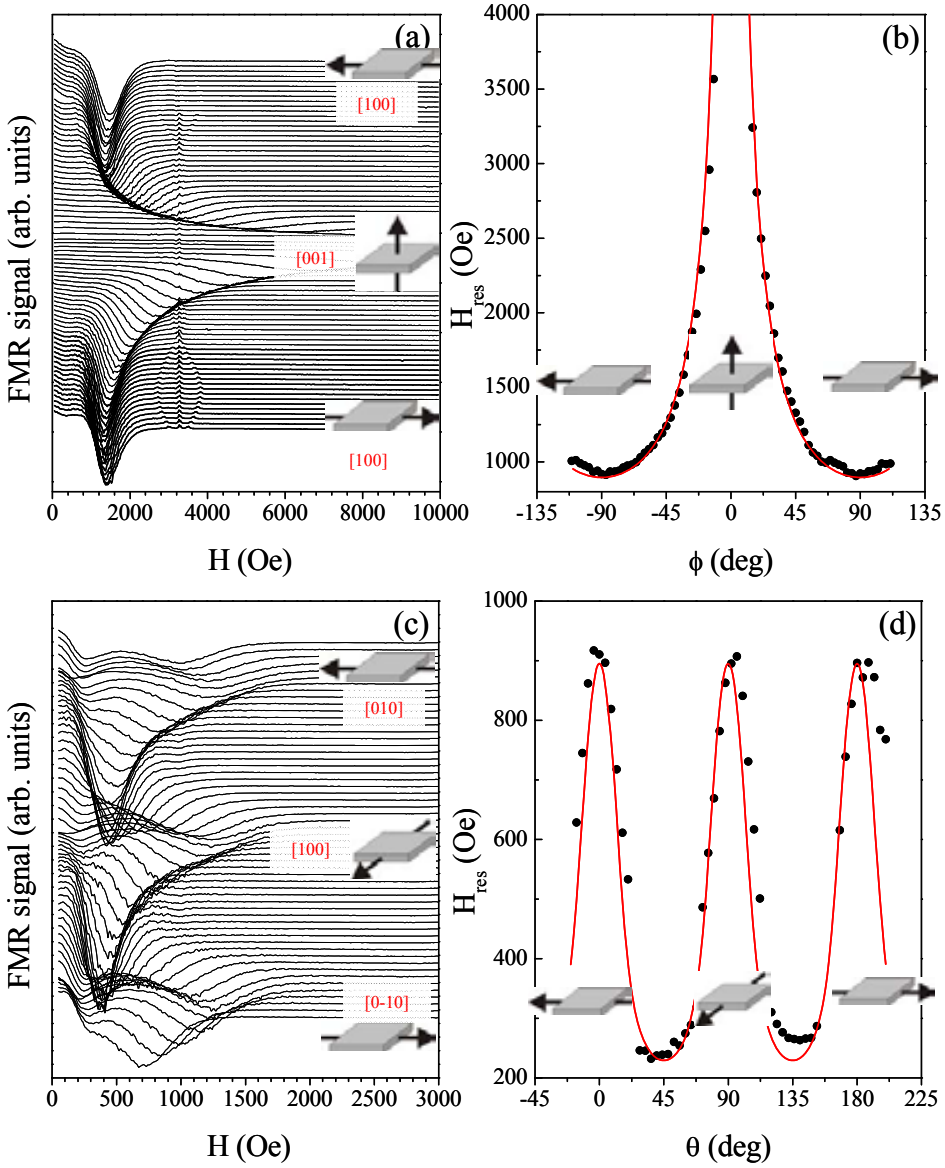

Figure 5.17. FMR measurements on 43 nm (001) film. Angular reference θ=0 is placed parallel to [010] direction. [(a) and (c)]: FMR spectra recorded with applied magnetic field varying (a) from in-plane [010] direction towards out-of-plane [001] direction and (c) in-plane of the sample, from [010] direction towards [110] one. [(b) and (d)]: Resonance field H_{res} for the different applied magnetic field orientation, being (b) for out-of-plane configuration and (d) for the in-plane configuration.

The simulation minimizes F^{001} following the equilibrium conditions of eq. 5.8. The terms in eqs. 5.14-5,17 have similar meanings than those on eqs. 5.6-5.9. The final simulation curves for both the out-of-plane and in-plane configuration are shown together with the acquired data in Figure 5.17b and d (solid lines). For these simulations, as the saturation magnetization value was $M_S = 477$ emu/cm^3. On the

fittings, cubic magnetocrystalline anisotropy expression (eq. 5.15) was used together with the uniaxial magnetoelastic term along the [010] direction (eq. 5.16). The chosen of [010] direction as a reference direction for the in-plane anisotropy was completely arbitrary. The final anisotropy constants deduced from best simulations indicates a negative biaxial constant $K^{001}_{c1} = -0.88 \cdot 10^5$ erg/cm^3 and the out-of-plane uniaxial anisotropy dominated by an effective constant of $K^{001}_{u,eff} = 4.58 \cdot 10^6$ erg/cm^3.

To illustrate the (001) in-plane magnetic anisotropy, we plot the angular dependence of F^{001} in the absence of applied magnetic field in Figure 5.18. We observe four-fold magnetic anisotropy, with easy axis along [110] direction and hard axis along [100] direction, in agreement with hysteresis loops measurements (Figure 5.14).

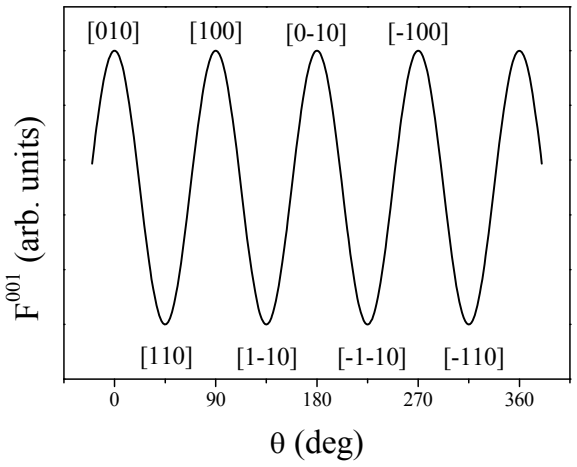

Figure 5.18. For the 43 nm (001) film, simulation of the total free energy F^{001} within the sample plane and in the absence of external magnetic field. The parameters used have been those extracted from simulations in Figure 5.17. Easy axes correspond to [110] and similar directions and hard axes to [100] and similar directions.

The deduction of in-plane magnetic anisotropy constants from hysteresis loops of (001) films has been performed using the same procedure described above used for (110) films. The experimental magnetic anisotropy energies are extracted from hysteresis loops with magnetic field applied along [110] and [100] directions, so-called E^{hyst}_{110} and E^{hyst}_{100}. The corresponding values are included in Table 5.7. For any given thickness, the magnetic anisotropy energy along the easy [110] axis is lower than along hard [100] axis. Within the (001) plane, the separation between these directions is 45 deg and to evaluate the magnetic anisotropy constant of these samples we used the expression for biaxial magnetic anisotropy related to [100] direction [32a]:

$K^{001}{}_1 = 4(E^{hyst}{}_{110} - E^{hyst}{}_{100})$. Except for the thinner 17 nm sample, the resulting $K^{001}{}_1$ values are approximately constant and of the order of 10^5 erg/cm^3, and comparing two different thickness results, the relative difference between $K^{001}{}_1$ constants is much weaker than for the (110) case.

For the evaluation of the magnetoelastic energy $E^{me}{}_{hkl}$, since equivalent crystallographic directions are found within (001) and (110) planes, we have used eqs. 5.10 and 5.11 but substituting (110) in-plane directions for the corresponding (001) in-plane ones: [100] replacing [001] and [110] replacing [1-10]. Similar changes have been performed for magnetostriction (λ_{100} for λ_{001}) and Young moduli (Y_{100} for Y_{001} and Y_{110} for $Y_{1\text{-}10}$) notation. Studying the strain values of the (001) plane, we notice that tensile strain ($\varepsilon > 0$) is developed along [110] and [100] directions (Table 5.6). However, the intrinsic elastic properties along these directions are different: $Y_{100} = 396$ GPa and $Y_{110} = 414$ GPa ($Y_{110} > Y_{100}$). The corresponding stress is for any given thickness higher along [110] than along [100] direction: $\sigma_{110} > \sigma_{100}$. Therefore, we conclude that the stress is dominated by this subtle difference in Young moduli, as virtually equal strain happens along [110] and [100] directions. The magnetoelastic effects therefore, favors the magnetization towards the [110] axis. The anisotropy constant expression is in analogy to (110) case $K^{me}{}_u = E^{me}{}_{110} - E^{me}{}_{100}$, and the corresponding values are shown in Table 5.7.

Table 5.7. For (001) films of different thickness, evaluated in-plane magnetoelastic energies ($E^{me}{}_{hkl}$), magnetoelastic energy constant ($K^{me}{}_1$), measured in-plane magnetic anisotropy energies ($E^{hyst}{}_{hkl}$) and uniaxial magnetic anisotropy constant ($K^{hyst}{}_1$) are also shown.

Thickness (nm)	$E^{me}{}_{100}$ (10^5 erg/cm^3)	$E^{me}{}_{110}$ (10^5 erg/cm^3)	$K^{me}{}_1$ (10^5 erg/cm^3)	$E^{hyst}{}_{100}$ (10^5 erg/cm^3)	$E^{hyst}{}_{110}$ (10^5 erg/cm^3)	$K^{hyst}{}_1$ (10^5 erg/cm^3)
17	-35.90	-37.53	-1.63	0.84	0.51	-1.34
43	-35.90	-37.53	-1.63	3.43	2.32	-4.44
80	-35.90	-37.53	-1.63	3.63	2.55	-4.32
85	-35.90	-37.53	-1.63	2.19	1.07	-4.48

Analyzing the results on (001) films, interestingly enough $K^{hyst}{}_u$ values follow the low thickness-dependency resembled by the out-of-plane strain ε_{001} (Table 5.6). Inspecting the absolute values of $K^{hyst}{}_1$ and $K^{me}{}_1$, similar magnetic anisotropy constants are evaluated using the hsyteresis loops or the magnetoelastic considerations. For instance, for the 43 nm film, these constants are $K^{hyst}{}_1(43\text{ nm}) = -4.44 \cdot 10^5$ erg/cm^3 and

K^{me}_1(43 nm) = -1.63·10^5 erg/cm^3. More importantly, we find clear evidences on the magnetic anisotropy origin of (001) films, with easy [110] axis and hard [100] axis. The FMR experiments and simulations signal the same trend observed in the hysteresis loops. The in-plane biaxial anisotropy constant deduced from FMR experiments is considerably lower than that obtained from hysteresis loops measurements, but both are of the same order of magnitude (~ -10^5 erg/cm^3), but as in the case of the (110) film we ascribe this effect to the different detention method.

Discussion on the origin of in-plane magnetic anisotropy in the LCMO/STO system

We have demonstrate the strong influence of the elastic deformation of the unit cell on the magnetic anisotropy of LCMO films grown on STO substrates of either (110) or (001) orientation. In short, for (110) films the more intense magnetoelastic energy along [001] direction induces an in-plane uniaxial anisotropy with hard [1-10] axis and easy [001] one, whereas for (001) films the stronger higher Young modulus along [110] axes promotes them to be easy magnetic axes.

Exploring the possible relevance of magnetocrystalline anisotropy, single crystal references of La-manganites, highlight the low value [37] or even the absence [38] of magnetocrystalline anisotropy. Perekalina *et al.*[37] studied the magnetic properties of orthorhombic $La_{1-x}Sr_xMnO_3$ single crystals with rhombohedral distortion (with symmetry along [001] axis) and found a magnetic easy axis along [001] direction and magnetic isotropy within the [001] plane. For Searle and Wang [38], $La_{1-x}Pb_xMnO_3$ single crystals did not show any magnetic anisotropy.

Turning to the studies focused on (001) manganite films, the most claimed cause of the in-plane magnetic anisotropy is the substrate-induced strain [24][25][26]. On the other hand, Steenbeck and Hiergiest [27] argued that its main source is the magnetocrystalline anisotropy. Analyzing our results on LCMO films grown on (110) and (001) STO substrates, the direct correlation between elastic properties and in-plane magnetic anisotropy for the (110) case helps to understand the magnetic anisotropy sources in (001) films. Magnetoelastic contributions to magnetic anisotropy of (110) films indicate that the unit cell deformation is the main cause of the appearing easy and hard axes. Thus, it is clear that single crystals do not develop any magnetic anisotropy when growth under no external force which may induce anisotropy [38], or maybe only a low one because of crystal distortions [37]. Interestingly, any unit cell deformation (magnetoelastic effects) as the one caused by the thin film epitaxial growth will

compete with the intrinsic magnetic isotropy of these manganites. We observe that the four-fold symmetry obtained for (001) LCMO and LSMO films grown on STO substrates [24][27] show easy [110] magnetic axis, with anisotropy constant slightly dependent on film thickness. The common characteristic of these films is that they present a unit cell deformation, not only of the in-plane lattice parameters but also of the out-of-plane one. Our experimental measurement of the in-plane magnetic anisotropy of (001) films agree with [24][27] in finding easy magnetic [110] axis. Also, from the strain values shown in Table 5.6, a slight dependency on film thickness of the calculated anisotropy constant K^{hyst}_1 needs to be related with unit cell deformation. Although in-plane lattice parameters are those of the cubic substrate (tetragonal unit cell), we detect a change in the out-of-plane lattice parameter of 17 nm film. Similar effects can be observed comparing ε_{001} and evaluated K^{hyst}_1 for all thicknesses. As any change on the unit cell can alter magnetic anisotropy, we conclude that the biaxial magnetic anisotropy of (001) films is caused by the epitaxial strain (ε_{hkl}) linked to the intrinsic manganite elastic properties (Y_{hkl}), being the intensity of this anisotropy related to the unit cell deformation.

To illustrate the thickness dependency of the resulting magnetic anisotropy constants for our (110) and (001) LCMO films, we plot in Figure 5.19a the values of K^{hyst}_u from (110) films and those of K^{hyst}_1 from (001) ones. We notice that (001) film values (close symbols) follow an almost thickness-independent curve if we do not include the thinner 17 nm sample, whereas (110) ones (open symbols) clearly evolves towards lower values with increasing thickness. Simulations of the corresponding magnetic anisotropy are shown in Figure 5.19b for (110) films and Figure 5.19c for (001) ones. Normalizing to the higher anisotropy constant of 43 nm (110) film (Table 5.4), we can clearly see in Figure 5.19b the two-fold in-plane magnetic anisotropy measured for (110) films and in Figure 5.19c the four-fold one observed in (001) films. A reduction on the y-scale on Figure 5.19c by three times compared to Figure 5.19b allows observing the small thickness dependence of the magnetic anisotropy of (001) films. It is remarkable that Figure 5.19 includes only experimental data and their corresponding simulated curves, and the evolution of the magnetic anisotropy constants and their simulations recall their elastic origin, as they are a simple image of the in-plane stress distribution.

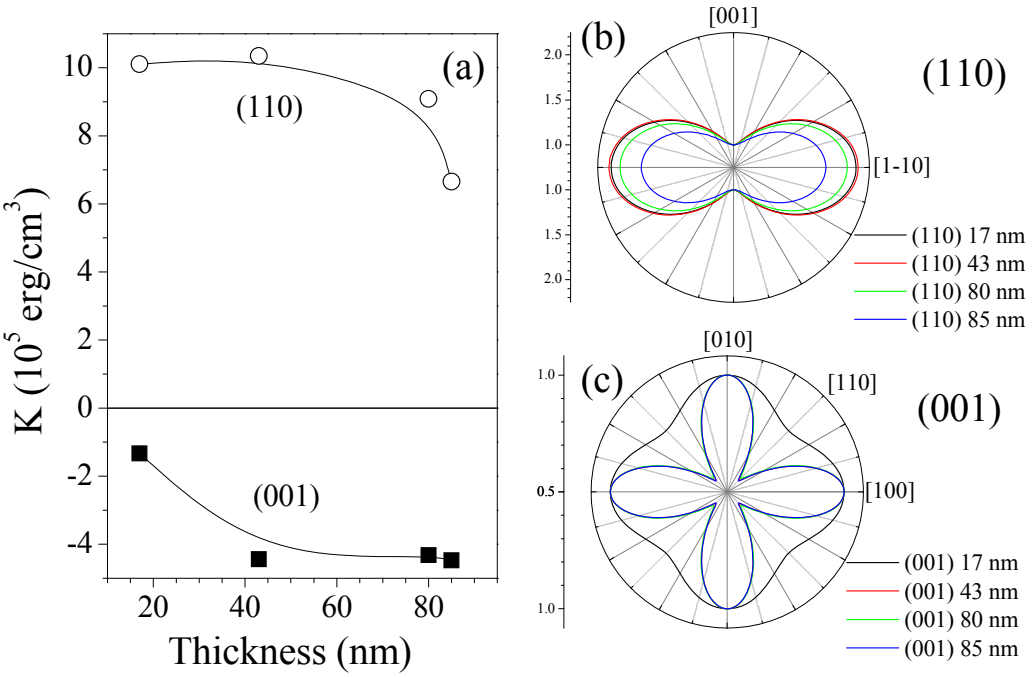

Figure 5.19. (a) Magnetic anisotropy constants evaluated from magnetic hysteresis loops of (110) and (001) films as a function of film thickness. For (110) films, $K = K^{hyst}_u$ (uniaxial magnetic anisotropy) and for (001) films $K = K^{hyst}_1$ (biaxial magnetic anisotropy). (b) Polar plot of simulated K^{hyst}_u as a function of the angular position of the magnetization for (110) samples. (c) Polar plot of simulated K^{hyst}_1 as a function of the angular position of the magnetization for (001) samples. Y-scale of (c) is 1/3 of y-scale of (b).

To summarize this topic, we have studied the magnetic anisotropy origin of manganite films using LCMO films grown on (110) and (001) STO substrates. The easy plane magnetic anisotropy is observed in both (110) and (001) case. Focusing in the in-plane magnetic anisotropy of these films, we have observed that the different structural properties of in-plane [001] and [1-10] directions within the (110) plane drives the manganite unit cell to deform anisotropically, and the most stressed [001] direction becomes easy magnetic axis and [1-10] one turns to be a hard magnetic axis. The progressive relaxation of the lattice parameters of (110) films upon increasing thickness ensures the elastic origin of (110) film uniaxial magnetic anisotropy. For the (001) case, in-plane biaxial magnetic anisotropy with easy [110] axis is related to the higher stress along [110] direction. Moreover, biaxial magnetic anisotropy of (001) films follows the much smaller thickness dependence unit cell deformation of (001) films. Our parallel analysis on the structural and magnetic properties of (110) and (001) LCMO films have

been useful to prove that elastic deformation of film unit cell dominates the in-plane magnetic anisotropy of manganite thin films.

5.2 Magnetotransport

The transport properties of thin manganite films are known to be highly influenced by the ferromagnetic order in the films. Some of these transport phenomena and their main features are:

1. The appearance of the insulator to metal transition at a temperature close to that of the paramagnetic to ferromagnetic transition. The strong coupling to the lattice of the conducting e_g electrons, which are also at the origin of the double-exchange ferromagnetism, is at the origin of this effect.

2. Higher values of resistivity are measured in films presenting electronically separated phases due to either the larger scattering of the carriers in an inhomogeneous material or the more insulating character of some of these regions.

Other interesting transport phenomenon of manganite films arises from the fact that upon changing the angular position of the magnetic field with respect to the injected current, the longitudinal and the transverse resistance can depend on the crystallographic direction of the current injection. The magnetotransport responses are thus influenced by the magnetic anisotropy of the films.

Motivated by the different magnetic properties of (001) and (110) LCMO films, we have investigated the effect of the orientation and also of the film thickness in the transition temperature from insulator to metal (T_{IM}) and in the resistivity values of these films. We have studied the angular dependence of the magnetoresistance at a given applied magnetic field in these films, focusing in the dependence on the plane of growth and of the direction of the injected current. Different transport effects will be presented, including for the longitudinal or transverse voltage measurement on the LCMO lithographed films. For (110) LCMO films, an appropriate modelling of the magnetization vector rotation has been developed and applied by Dr. David Hrabovský, being finally used to unambiguously determine the in-plane magnetic anisotropy of the films, and also to extract the uniaxial anisotropy constant.

We have organized the section as follows:

1. Considerations on the methodology and lithography.

2. Resistivity and metal to insulator transition in (001) and (110) films of different thickness. Resistivity of lithographed samples.

3 Introduction to the transport effects: anisotropic magnetoresistance (AMR) and planar Hall effect (PHE).

4. Experimental AMR results: Sign and magnitude of AMR as a function of film orientation and of the direction of current injection.

5. Experimental PHE results: Influence of the magnetic anisotropy on the transverse resistance. For (110) films, appearance of a switching effect. The (110) data is fitted following a magnetotransport model that accounts for the magnetic anisotropy of the film.

We include in Table 5.8 the list of the LCMO films used in this section, their thickness and, for the lithographed samples, the width and length of the tracks.

Table 5.8. List of LCMO samples used for magnetotransport measurements. For the lithographed samples, the track width is indicated and the length of the track was 1.5 mm in all cases.

Lithography	Track width (μm)	Sample	Substrate	Sample	Substrate	Nominal thickness (nm)
No		240204A	STO(001)	240204B	STO(110)	43
		200204A	STO(001)	200204B	STO(110)	85
Yes	22	130904A	STO(001)	160904B	STO(110)	17
	65			130904B	STO(110)	20
	75			050406B	STO(110)	150

5.2.1 Methodology and lithography

The magnetotransport properties of LCMO films were studied using a commercial system (PPMS) by 4-wire measuring. We used two types of sample holder, schematized in Figure 5.20. A normal resistivity holder (Figure 5.20a) was used for the resistivity measurements, being possible to apply the magnetic field out-of-plane of the samples. The angular dependence of the resistivity was measured with rotator holder depicted in Figure 5.20b. A plastic cube pasted to the holder served to fix the sample perpendicular to the holder plane, and thus allowing the rotation of the magnetic field within the sample plane. Both holders include two or three channels for the application of current and measurement of voltage, as depicted in Figure 5.20. For the resistivity measurements the contacts were equally distributed along the longer dimension of the film. For the angular measurements, it was necessary to pattern the films. We will show later the lithographically defined pattern. A step motor allows rotating the sample 360 deg from a given reference origin. During rotation measurement, the temperature was

stable and the resistance values are typically recorded at steps of 3 deg, pausing at each angular position. In all cases, the injected current intensity was tuned to optimize the range of measured voltage depending of the sample resistance.

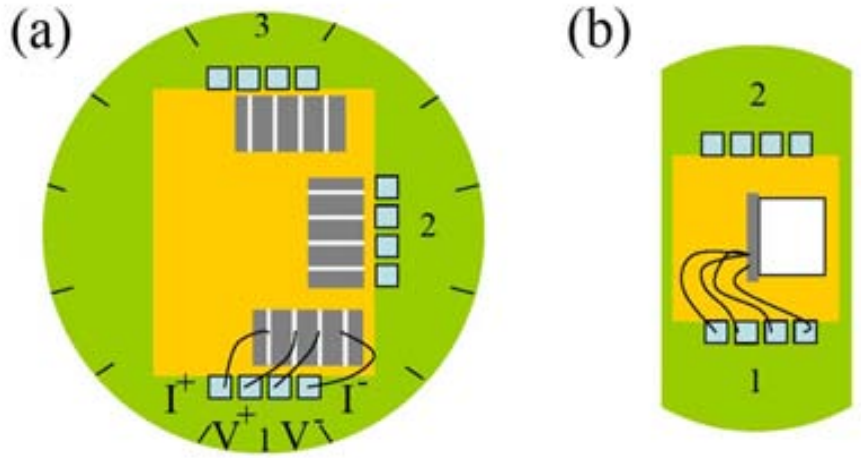

Figure 5.20. Sketch of the top view of sample holders of the PPMS: (a) common resistivity holder, with 3 channels for 4-wire measuring, and (b) rotator holder with 2 channels for 4-wire measuring. In (a), contacts are done with graphite paste onto the sample surface and connected as indicated. In (b), sample is mounted onto a fixed cube of plastic to place the sample perpendicular to the plane of the rotator holder.

In order to investigate on longitudinal and transverse resistivities along different in-plane directions, (001) and (110) LCMO films were lithographed using the mask shown in Figure 5.21a. The defined mask provides two different orthogonal paths for the current to flow. For two in-plane orthogonal directions [A] and [B], the proper alignment of one track to either [A] or [B] axes lets the injected current to flow through one of these crystallographic axes. This pad configuration is very useful for exploring the in-plane [001] and [1-10] directions in (110) samples, whereas for (001) samples [100] and [010] equivalent directions can be studied but also the [110] direction situated at 45 deg from the vertical and horizontal pads. We used the longer diagonal pads to evaluate the longitudinal resistance (AMR) by properly contacting onto them. For the vertical track in Figure 5.21a, longitudinal measurements are performed with the current flowing from 1 and 2 spots and with voltage contacts onto 3 and 4 spots. In the case of measuring transverse resistance, the voltage contacts are 5 and 6. Similar configuration can be performed along horizontal line. Samples were patterned using photolithography. A sample mounted in the sample holder is shown in Figure 5.21b, with electric contacts prepared for transverse voltage measurements. After lithography process, typical track

width was found to be 70 μm, with a length of 1.5 mm. Using the PPMS, transport experiments were performed at a low frequency (10 Hz) AC current and at a controlled temperature (from 5 K to 300 K) and applied magnetic field (up to 90 kOe). Typical value of applied current for longitudinal measurements was 20 μA and for transverse ones 0.1 μA. The magnetic field is applied in-plane and sample can be rotated in a 360 deg range in forward and backwards sweeps (3 deg/step).

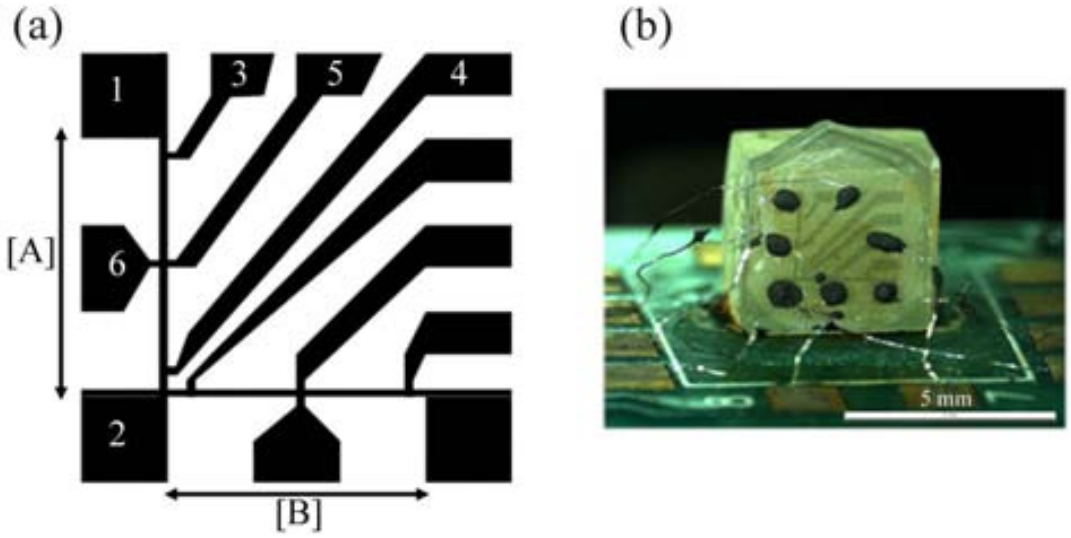

Figure 5.21. (a) Design of the photolithographic mask used for patterning. For this case, tracks are 70-80 μm wide. Samples have been patterned with the crystallographic axes parallel to the tracks as signalled by the arrows. Contacts for [A] bridge are: applied current $I^+(1) \rightarrow I^-(2)$; longitudinal measurement (AMR) $V^+(3) \rightarrow V^-(4)$; transverse measurement (PHE) $V^+(5) \rightarrow V^-(6)$. Sample is grounded by a contact placed on 2. For [B] bridge the contacts can be similarly connected. (b) Photograph of a lithographed (110) 20 nm film onto the sample holder and connected to perform PHE experiments.

Resistivity measurements on (001) and (110) films (43 and 85 nm thick) with applied field out-of-plane of the sample were done using the holder shown in Figure 5.20a. The shape of the films is rectangular (2.5x5) mm^2, allowing to define macroscopic contacts on their surface.

AMR and PHE experiments were developed in lithographed films of different thickness and orientation, changing the width of the lithographed track. We have measured a couple of 20 nm (001) and (110) films with tracks of 70 μm width, and others (110) films of 18 nm thickness with narrow 20 μm wide tracks and of 150 nm thickness with 75 μm wide tracks.

5.2.2 Resistivity and insulator to metal transition in (001) and (110) films

Resistivity values have been calculated using the measured resistance and knowing the corresponding values of the current section (*A*) and length (*l*). Samples are rectangular shaped, and we assumed that parallel current lines develop along the long dimension (*l*), and taking the suitable expression:

$$\rho_{xx} = \frac{A}{l} R_{xx} \qquad [5.18]$$

being R_{xx} the measured longitudinal resistance.

Zero field resistivity dependence on temperature of 43 and 85 nm (001) and (110) films is shown in Figure 5.22. The current injection were aligned to the [100] direction for the (001) films and along the [001] direction for the (110) films. We recorded the resistance from 300 K down to 5 K and from 5 K up to 300 K. Zero field resistivity maximum in experimental curves provides information about the transition from insulator-to-metal (IM), a phenomenum occurring in manganite thin films at a temperature close to the magnetic ordering one (T_C) [2][51]. From these ρ(T) curves, two main features are noticed:

(a) The temperature of the maxima of the curves from (001) films is lower at all thicknesses compared to that of (110) films, and these values are also thickness dependent, with lower values for the 43 nm films than for the 85 nm ones.

(b) The resistivity of these samples at any temperature is always higher for the (001) films than for the (110) ones, and also depends on the thickness of the films, being higher for 43 nm films than for 85 nm ones.

For these samples, we can compare the T_{IM} values with the T_C ones, obtained from magnetometry measurements (shown in Figure 5.3). The T_{IM} and T_C values are summarizes in Table 5.9. These values are clearly close one to the other for any given film. In all cases, T_{IM} is slightly lower than the corresponding T_C one, which is ascribed to the fact that the magnetization curves are recorded under magnetic field (5 kOe) and thus the ferromagnetic transition is shifted towards higher temperature. Interestingly, for both thicknesses we observe not only a higher temperature transition for the (110) films [$T^{110}_{IM} > T^{001}_{IM}$] but also the shape of the transition depends on the orientation of the films. In Figure 5.22, a wider IM-transition is observed for the (001) films, which possibly hints the existence of separated electronic phases through the film (also found

by NMR experiments, analyzed in Ch4), enhanced in the thinner 43 nm film. Moreover, the thermal hysteresis of the ρ(T) curves in Figure 5.22 may be related to these electronic inhomogeneities much pronounced in this thin 43 nm film.

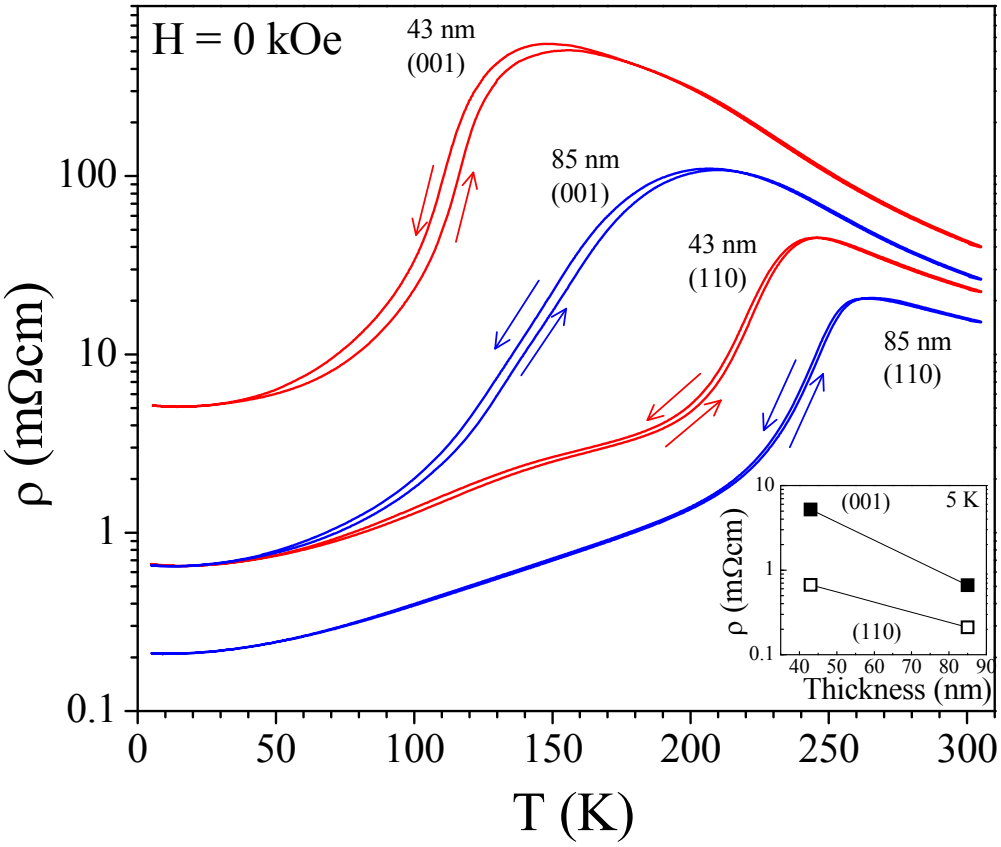

Figure 5.22. Zero field resistivity *vs* temperature of (001) and (110) films of 43 and 85 nm thickness. The sense of the temperature loops is also indicated, current was injected along [100] direction in (001) samples and along [001] direction for (110) samples. Inset: Resistivity values as a function of film thickness from the (001) (close symbols) and (110) (open symbols) samples extracted from the resistivity curves, at 5 K.

The resistivity values, especially those at low temperature, are an indication of the electronic homogeneity of the films. Analyzing the curves in Figure 5.22, we notice that lower ρ values correspond to the (110) films at any temperature. The corresponding ρ values are included in Table 5.9. From the thickness dependence of these values (inset of Figure 5.22), with higher ρ for thinner films, more evidences are found of the electronic inhomogeneities of (001) films contrasting with the electronically homogeneous (110) films.

Table 5.9. Resistivity (ρ) at 5 K of 43 and 85 nm (001) and (110) films, extacted from zero field ρ(T) curves. The metal to insulator [T(IM)] and ferromagnetic transition (TC) temperatures are also included.

Thickness (nm)	(001)			(110)		
	ρ (5K) (mΩcm)	T(IM) (K)	TC (K)	ρ (5K) (mΩcm)	T(IM) (K)	TC (K)
43	5.19	150	176	0.67	245	252
85	0.66	206	213	0.21	264	266

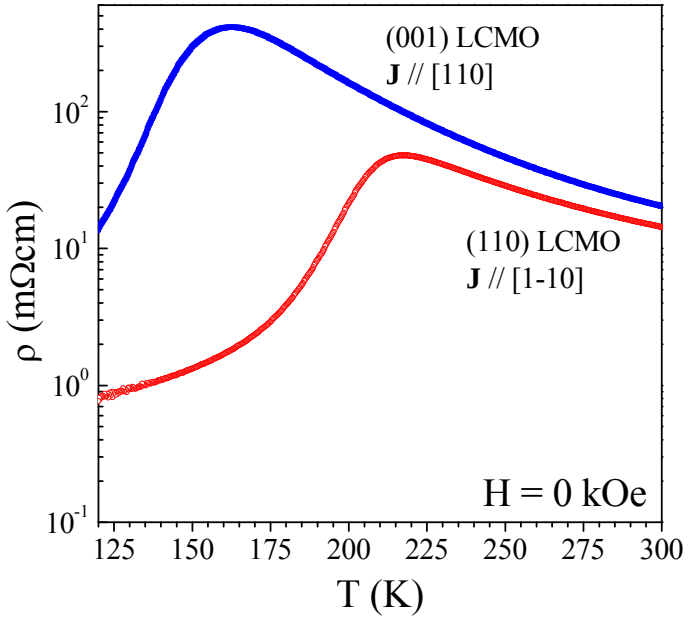

Figure 5.23. Zero field resistivity of 20 nm lithographed films, for **J** applied along [110] direction in the (001) one (solid symbols) and for **J** applied along [1-10] direction in a the (110) one (open symbols).

For the lithographed films, the main difference with the non-lithographed ones is that the current path is confined to the track dimensions. We show as an example the zero field ρ(T) curves of the 20 nm (001) and (110) lithographed films, with the injected current along the [110] and [1-10] directions for the (001) and (110) films, respectively. A similar analysis of the curves has been done in order to evaluate the quality of the samples after the lithographic process. The MI transition is observed for the (001) film at $T^{001}_{IM}[110] \sim 165$ K and for the (110) film for $T^{110}_{IM}[1\text{-}10] \sim 220$ K, being sharper for the (110) film than for the (001) one. The resistivity of the (001) film is higher than

that of the (110) one, as happened for each pair of 43 and 85 nm films of (001) and (110) orientation.

5.2.3 Introduction to anisotropic magnetoresistance (AMR) and planar Hall effect (PHE) in manganite films

In ferromagnetic materials, it is an experimental observation that for a given current flow direction **J**, the measured longitudinal resistivity ρ_{xx} depends on the relative orientation of their magnetizatization **M** with respect to the applied magnetic field **H**. This effect is the so-called anisotropic magnetoresistance (AMR) and it has been found to have a direct origin on the spin-orbit coupling and spin anisotropy [39].The amplitude of AMR effect is more commonly defined as:

$$\frac{\Delta\rho_{xx}}{\rho_{av}} = \frac{\rho_{//} - \rho_{\perp}}{\frac{1}{3}\rho_{//} + \frac{2}{3}\rho_{\perp}} \qquad [5.19]$$

where $\rho_{//}$ is the measured resistivity when **M** is parallel to **J** and $\rho_{\perp}$ corresponds to that one measured when **M** is perpendicular to **J**.

In ferromagnetic metals, as the 3d-metal alloys, the magnitude of AMR depends on the magnetization of the sample, decreasing its magnitude as the magnetization drops [40][41]. In most cases, as in Ni-Fe or Ni-Co alloys, it is measured that $\rho_{//} > \rho_{\perp}$, and thus AMR > 0 [40][41]. Although the dependence of AMR on magnetization is not simple, the spin order of these 3d-metals has been correlated to the observed changes in the resistivity. Microscopically, the scattering in these ferromagnetic metals depends on the spin-orientation and population of the 3d-bands. As the scattering events depends on the magnetic order of the material, any anisotropy on the spin (magnetization) can be associated also to the transport phenomena, and in particular to measurements of the resistance rotating the magnetization vector.

Concerning manganites, typical values of AMR are within few percent at low temperature, gradually increasing when approaching the Curie temperature (T_C) [42][43][44][45][46]. The AMR sign in manganites contrasts to the corresponding one found in conventional metallic ferromagnets: whereas in manganite films, typically with injected current along the [100] direction within the (001) plane, $\rho_{//} < \rho_{\perp}$ and AMR < 0 [42][43][44][45].

In addition to the AMR effect, the spin-orbit coupling also produces what is called the planar Hall effect (PHE), that is the appearance of a transverse voltage ρ_{xy} in

response to a longitudinal current flow even in the absence of an applied magnetic field [47]. It occurs when **M** and **J** are neither parallel nor perpendicular, but forming an angle φ. We describe the AMR and PHE in terms of in-plane components only. Assuming that the current flow is $\mathbf{J} = J_x\hat{\mathbf{i}}$ in the x-y plane, it can be shown that an electric field appears with longitudinal and transverse components given by [41]:

$$E_{xx} = \rho_{\perp} J_x + (\rho_{//} - \rho_{\perp}) J_x \cos^2\varphi \qquad [5.20]$$

$$E_{xy} = (\rho_{//} - \rho_{\perp}) J_x \sin\varphi\cos\varphi \qquad [5.21]$$

respectively, allowing to determine $\rho_{xx}(\varphi)$ (AMR) and $\rho_{xy}(\varphi)$ (PHE). Besides, the application of an external magnetic field modifies the magnetic domain structure and the orientation of **M**, and thus it should produce distinguishable changes on the transverse voltage as well as on the longitudinal one. A clear image of electric field components is presented in Figure 5.24.

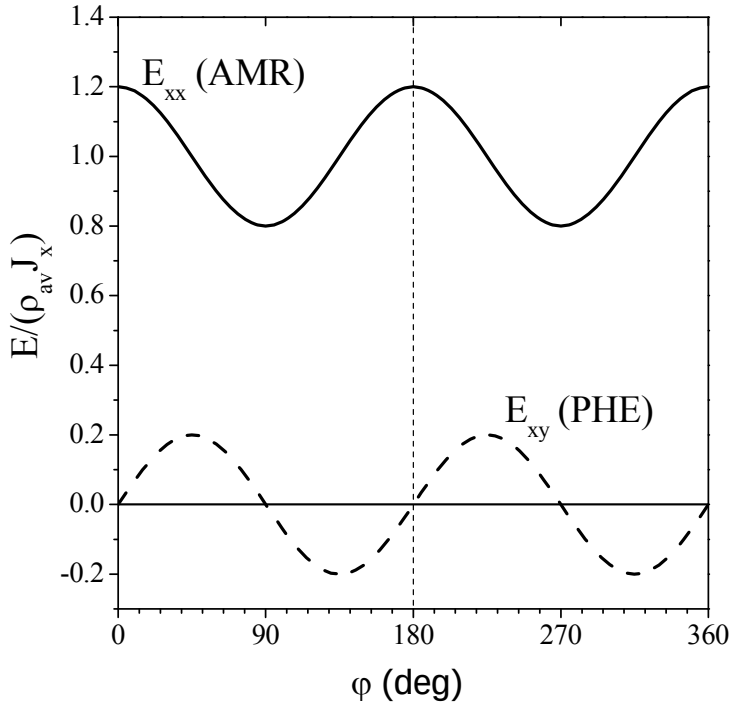

Figure 5.24. Evaluated electric field components associated to anisotropic magnetoresistance E_{xx}(AMR) and planar Hall effect E_{xy}(PHE). As an example, numerical values are $\rho_{//} = 3$ mΩcm and $\rho_{\perp} = 2$ mΩcm. ρ_{av} corresponds to the averaged value of resistivities ($\rho_{av} = (\rho_{//} + \rho_{\perp})/2$).

From eqs. 5.17 and 5.18 and using the simulations of E_{xx} and E_{xy} displayed in Figure 5.24, we notice two facts:

1. While the parity of E_{xx}(AMR) (even) and E_{xy}(PHE) (odd) functions is opposed, the amplitude of the oscillating component is the same.

2. A perpendicular to the current component $\rho_{\perp}J_x$ causes the E_{xx}(AMR) electric field component to rise its oscillation towards higher mean values, whereas the E_{xy}(PHE) component oscillates around zero.

From this comparative analysis of AMR and PHE, a higher sensitivity to resistivity changes is expected for transverse voltage measurement. Indeed, planar Hall effect has been used to investigate the magnetic domain structure in some ferromagnets to obtain the magnetic anisotropy [48]. In the particular case of manganites, PHE measurements have been reported for $La_{0.67}Ca_{0.33}MnO_3$ [49] and $La_{0.84}Sr_{0.16}MnO_3$ [50] thin films grown on the (001) plane of cubic substrates, although no attempts to derive magnetic anisotropy related parameters have been reported.

5.2.4 Experimental results of AMR and PHE in (001) and (110) films

The investigation turns to study of the influence of the relative position of magnetization and the current flow on magnetotransport properties (AMR, PHE). From the results shown in Figure 5.23, we decided to work at temperatures below the transition but sufficiently closer to it to obtain large AMR and PHE amplitudes. We chose 140 K and 180 K for the (001) and (110) films. To perform these magnetotransport measurements, we externally control the relative position of the applied magnetic field **H** and the current flow. The sketch in Figure 5.25a presents the current flows **J** and the relative orientation of the magnetization **M** (φ) and magnetic field **H** (θ).

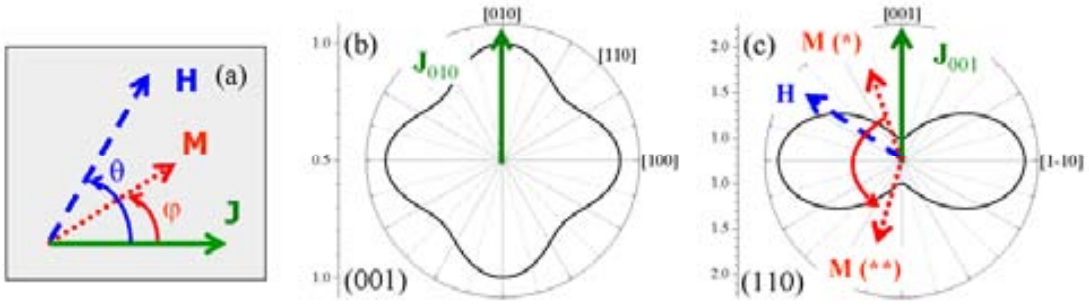

Figure 5.25. (a) Sketch of the defined angles with respect to the applied magnetic field **H** and sample magnetization **M**. The in-plane angles θ (for **H**) and φ (for **M**) are defined as the angles between **H** or **M** with respect to the current flow **J**. [(b) and (c)] Polar plots of the in-plane magnetic anisotropy energy as obtained from magnetometry measurements in 17 nm (b) (001) and (c) (110) film. In (c) we have superimposed to the energy plot a sketch of the magnetization switching around the [1-10] magnetic hard axis.

AMR in (001) films. Dependence of the AMR amplitude on the current direction

In Figure 5.26 we present the angular dependence of the longitudinal resistance (AMR) of the 20 nm (001) film for the current injected along the [*hkl*] direction. The AMR amplitude has been evaluated as $\Gamma^{hkl}=(R_{xx}(\theta)-R_{xx}(\theta = 0)/R_{xx}(\theta = 0)$, where θ is the angle between the applied magnetic field and the current as depicted in Figure 5.25. The current was injected either along the [100] direction (a) or along the [110] direction (b). In this high field measurements (10 kOe to 20 kOe of applied magnetic field), the sample magnetization is saturated, as it is deduced from the magnetization loops (not shown here) obtained at this temperature (140-180 K).

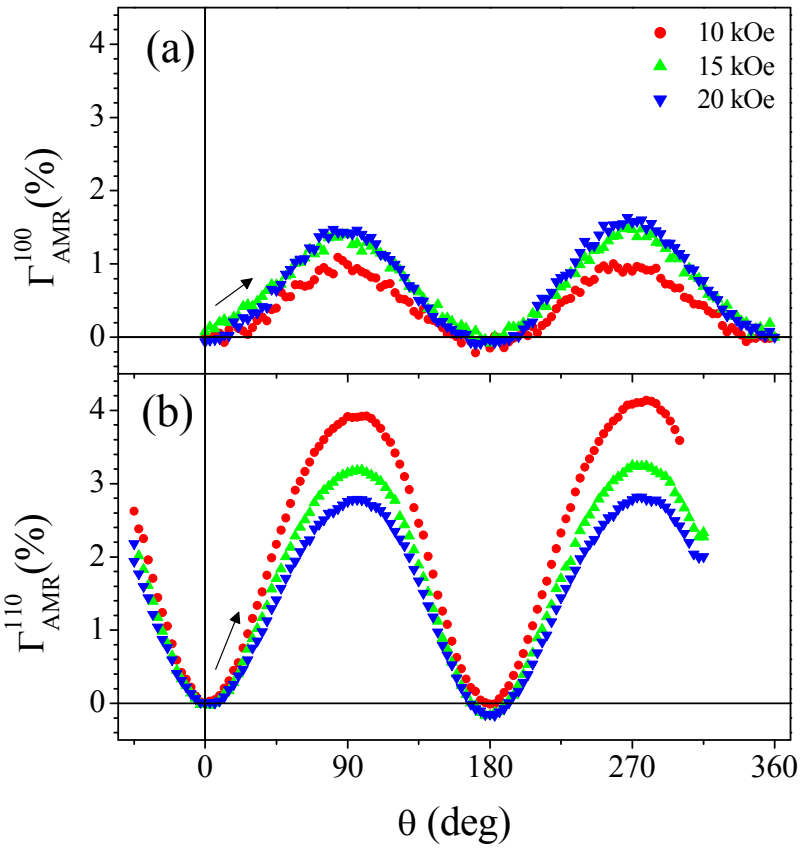

Figure 5.26. AMR amplitude at 10 kOe (circles), 15 kOe (up triangles) and at 20 kOe (down triangles) of the 20 nm (001) film with the current injected along (a) [100] and (b) [110] directions. Measurements in (a) were performed at 180 K and those in (b) at 140 K.

Inspecting the angular dependence of the AMR data for current along [100] (Figure 5.26a) and [110] (Figure 5.26b) directions, we observe that for both cases the Γ^{hkl} value is higher when the magnetic field is perpendicular than when it is parallel to the current flow direction [$R_{xx}(\theta = 90$ deg) > $R_{xx}(\theta = 0$ deg)]. Following eq. 17, the

amplitude of the AMR [AMR ~ $R_{xx}(\theta = 0\ deg) - R_{xx}(\theta = 90\ deg)$] is negative within the (001) plane, as previously seen in Ref. [42][43][44][45]. The angular dependence of AMR follows the expected $\cos^2(\theta)$ function, with an amplitude that is notably higher for the current injected along the [110] direction than along the [100]: $\Gamma^{110} > \Gamma^{100}$. Moreover, we notice that the amplitude and the shape are slightly sensitive to the intensity of the applied magnetic field, being much relevant for the case of current along the [110] direction. For the current along [110] direction, we observe a deviation from the $\cos^2(\theta)$ shape when the applied magnetic field is perpendicular to the track length at 90 and 270 deg (in Figure 5.26b). We attribute the slight field dependence and the unexpected shape of the AMR data, especially of those from the [110] direction, to the the shape of lithographic tracks of the film: as shown in Figure 5.21, the [110] tracks are wider and do not have a constant width which may induce some magnetic domain distribution that influences in the rotation of the overall magnetization.

Upon decreasing the magnetic field, the longitudinal resistance of the film increases and the angular dependence measurement becomes more noisy. As shown in Figure 5.27a (and b) for 0.70 kOe of applied field , an oscillation of ~10 kΩ (~20 kΩ) is measured around a background resistance value of ~3.07 MΩ (~325 kΩ). We recall that the tracks along [100] and [110] directions have different width and the contacts were situated at longer distances for the [100] direction that for the [110] one, thus affecting the background resistance value. Under different magnetic field and at these temperatures (close to the T_{IM} of the sample, T_{IM} = 165 K), the longitudinal resistance strongly depends on the field, as deduced comparing the background resistance of high field 20 kOe measurements, with a background value for the [100] direction ([110] diection) of ~1.53 MΩ (~550 kΩ) and the low field 700 Oe ones ~3.07 MΩ (~325 kΩ). We signal that even at this low 700 Oe applied field, the main features identified in the high field curves (Figure 5.26) with AMR following the $\cos^2(\theta)$ shape with an AMR of negative sign are still observed. We note that the deviation from the $\cos^2(\theta)$ in the [110] case (Figure 5.27b) is a reproducible effect, probably related to the magnetic anisotropy induced by the track shape, more visible at this low field.

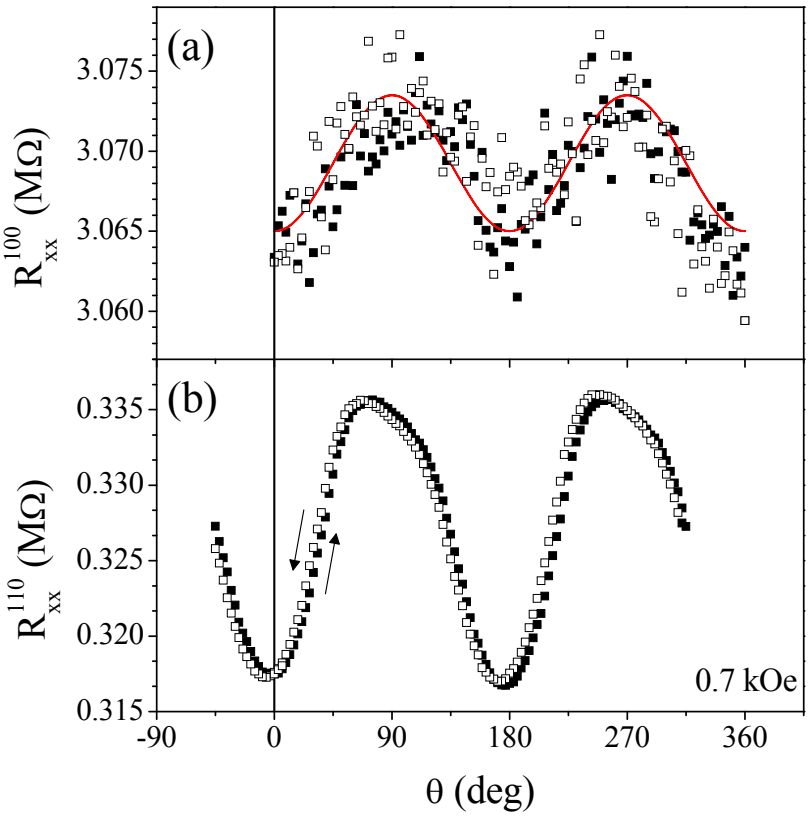

Figure 5.27. AMR amplitude of the 20 nm (001) film with an applied magnetic field of 0.7 kOe, with the current injected along (a) the [100] and (b) the [110] directions. Close and open symbols indicate the forwards and backwards measurements, respectively. In (a), a $\cos^2(\theta)$ fitting is included (line). Measurements were performed at 180 K.

AMR in (110) films. Dependence of the amplitude of the AMR on current direction and temperature

High field AMR curves recorded on the 18 nm (110) film (with narrow tracks) at 180 K are shown in Figure 5.28. At this interval of magnetic fields (10 to 20 kOe) film magnetization is saturated and rotates coherently with the field. Angular dependence of the AMR has been calculated as for the (001) case, using: $\Gamma^{hkl}=(R_{xx}(\theta) - R_{xx}(\theta = 0)/R_{xx}(\theta = 0)$. In this case, the two in-plane directions are [001] (Figure 5.28a) and [1-10] (Figure 5.28b). Studying the evolution of the AMR data starting from the situation where current and magnetization are parallel [$R_{xx}(\theta = 0)$], we notice that whereas Γ^{001} evolves towards larger values for $\theta > 0$, $\Gamma^{1\text{-}10}$ decreases for $\theta > 0$, as indicated by the arrows in Figure 5.28. Comparing the parallel and perpendicular configurations for each current direction, it is remarkable that whereas higher

perpendicular resistance is obtained for the [001] case, lower perpendicular resistance is observed for the [1-10] case. Therefore, for the [001] direction, $AMR^{001} < 0$, and for the [1-10] direction, $AMR^{1-10} > 0$. On the other hand, the AMR data follows the $\cos^2(\theta)$ dependence and the AMR amplitude is not relevantly affected by the change in the intensity of the magnetic field. However, the absolute value of the AMR amplitude is seen to depend on the injected current direction, and at this temperature the comparison of the AMR for each direction is $|\Gamma^{001}| > \Gamma^{1-10}$. Similar results have been obtained from the measurement of 20 nm (110) film, being the AMR sign different ($AMR^{001} < 0$ and $AMR^{1-10} > 0$) and its absolute values present the same dependence on the current direction ($|\Gamma^{001}| > \Gamma^{1-10}$).

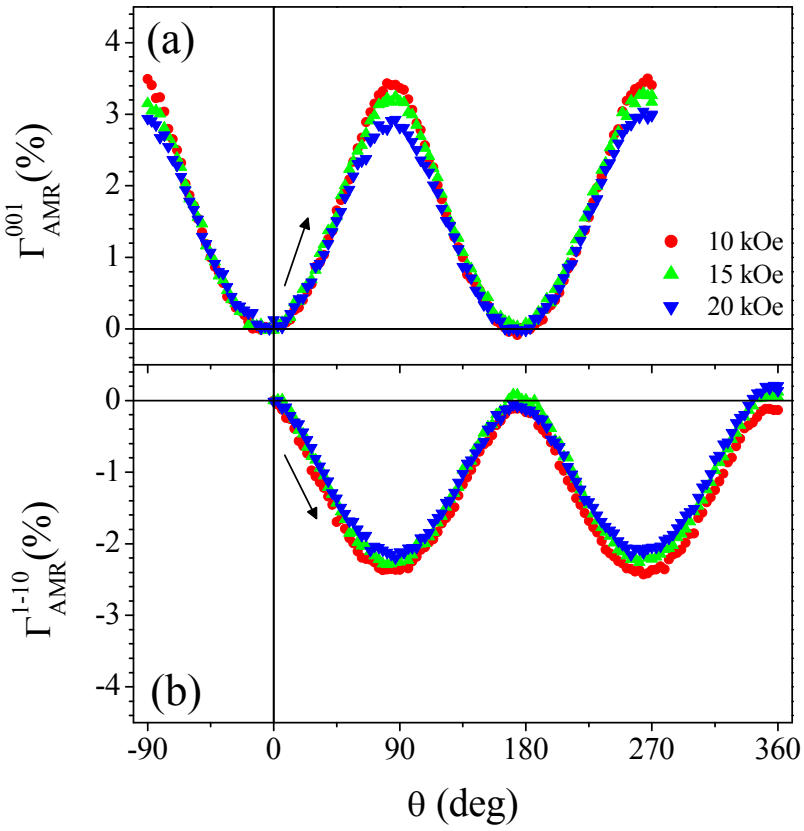

Figure 5.28. AMR amplitude at 10 kOe (circles), 15 kOe (up triangles) and at 20 kOe (down triangles) of the 18 nm (110) film (narrow tracks) with the current injected along (a) the [001] and (b) the [1-10] directions. Measurements in were performed at 180 K.

Aiming to understand the change of sign of the AMR amplitude and its thermal evolution, we have also studied a thick 150 nm (110) film. In order to investigate the thermal dependence of the AMR, we have performed resistivty *vs* temperature experiments cooling the sample with the applied magnetic field parallel to the [001]

direction (perpendicular to the [1-10] one) or parallel to the [1-10] one (perpendicular to the [001] one). As an example, in the main panel Figure 5.29 the zero field and 20 kOe field cooling curves for the current along [1-10] direction are shown. In the inset of Figure 5.29 a zoom of the 245 to 280 K temperature range with the resistivity curves of both [001] and [1-10] tracks in the parallel (thick lines) and perpendicular (thin lines) configurations are shown. For current injected along the [001] direction, we find a perpendicular resistivity higher than the parallel $\rho_{\perp} > \rho_{//}$ and thus AMR < 0 and for current along the [1-10] direction, the results is the opposite in sign $\rho_{\perp} < \rho_{//}$ and thus AMR > 0. These results in are in agreement with those obtained from AMR curves of the 18-20 nm (110) films.

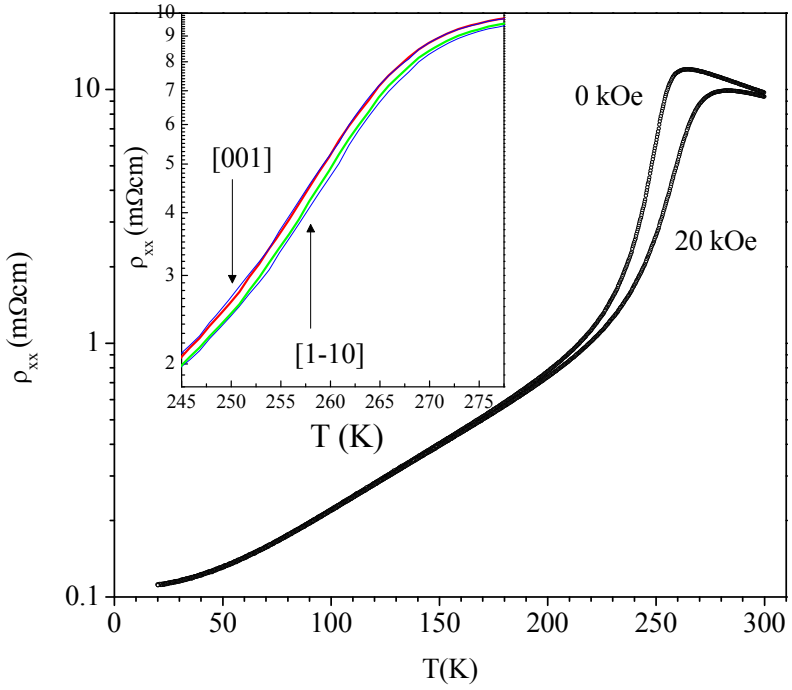

Figure 5.29. Resistivity *vs* temperature of the 150 nm (110) film at zero field and with applied magnetic field of 20 kOe for the injected current along [1-10] direction. In the inset, a zoom on the ρ(T) curves measured at 20 kOe for injected current along [1-10] and [001] direction and with the magnetic field applied parallel (thick lines) or perpendicular (thin lines) to the current flow.

We can further evaluate the AMR from these 20 kOe curves, computing the normalized difference between parallel and perpendicular states as $AMR = (\rho_{//}-\rho_{\perp}) / \rho_{av}$, with $\rho_{av} = (\rho_{//}-\rho_{\perp})/2$, as a function of the temperature for the current injected along [001] and [1-10] directions. The obtained AMR dependences are plotted in Figure 5.30.

Remarkably, the positive and negative AMR sign for [1-10] and [001] current injection, respectively, is extended to all the temperature range. Coming from the low temperature data, with low absolute values of AMR of |AMR| < 1 % at T = 200 K, the |AMR| value increases for both current directions achieving a maximum close to 250 K for the [001] direction and to 265 K for the [1-10] direction. This high increase in the |AMR| up to $|AMR^{001}| \sim 2.5$ % and $|AMR^{1\text{-}10}| \sim 3.5$ % occurs at a temperature very close to the ferromagnetic transition of this film.

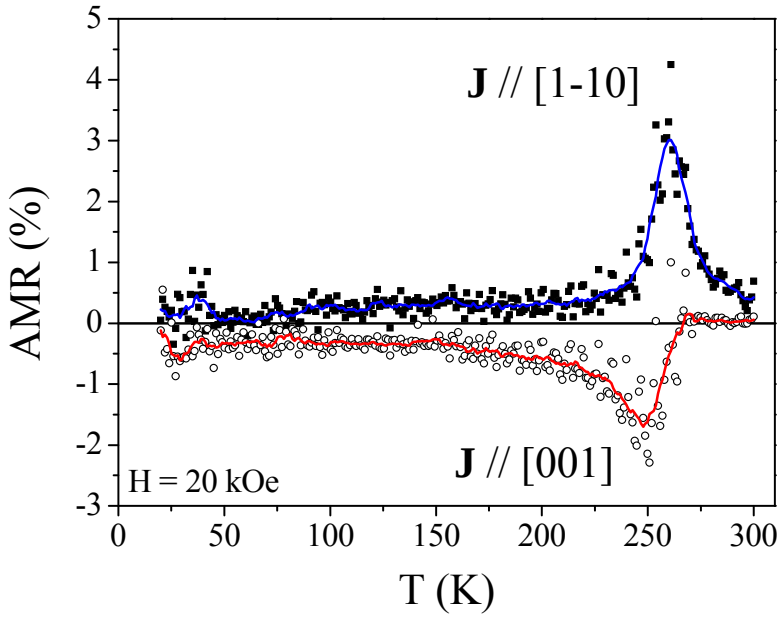

Figure 5.30. AMR as a function of the temperature for the 150 nm (110) film. Values extracted from the correponding ρ(T) curves recorded at 20 kOe (inset of Figure 5.29).

Therefore, we have confirmed that the sign of the AMR depends on the current directions.

Aiming to explore the AMR at low field, in Figure 5.31 we plot the longitudinal resistance measured at 180 K of the 18 nm (110) film (narrow tracks) at 0.7 kOe and 1.0 kOe. As expected, the angular dependence of the AMR is no longer $\cos^2(\theta)$: the data around 0 deg for the [001] direction (Figure 5.31a) and around 90 deg for the [1-10] direction (Figure 5.31b) are flat, having the minimum of resistance a wider area around them. On the other hand, around 90 deg for the [001] direction (Figure 5.31a) and around 0 deg for the [1-10] direction (Figure 5.31b) the data present a peaky shape, and comparing forwards (close symbols) and backwards (open symbols) data, the maximum of resistance is shifted towards higher and lower angles, respectively. Interestingly,

from magnetometry measurements we have identified the hard and easy magnetization axis in the (110) films, and in these AMR curves the minima appear for both injected current directions when the magnetization vector should be at along the [001] direction ($\theta = 0$ in Figure 5.31a and $\theta = 90$ deg in Figure 5.31b), which is in fact the easy magnetization direction. The peaky resistance data are recorded around the hard [1-10] axis magnetization, and comparing the 1 kOe (triangles) and 0.7 kOe (circles) data in Figure 5.31, we notice that upon decreasing the magnetic field the angular shift becomes broader. Nevertheless, lowering the magnetic field directly increases the longitudinal resistance, and the oscillation becomes more difficult to observe (Figure 5.31).

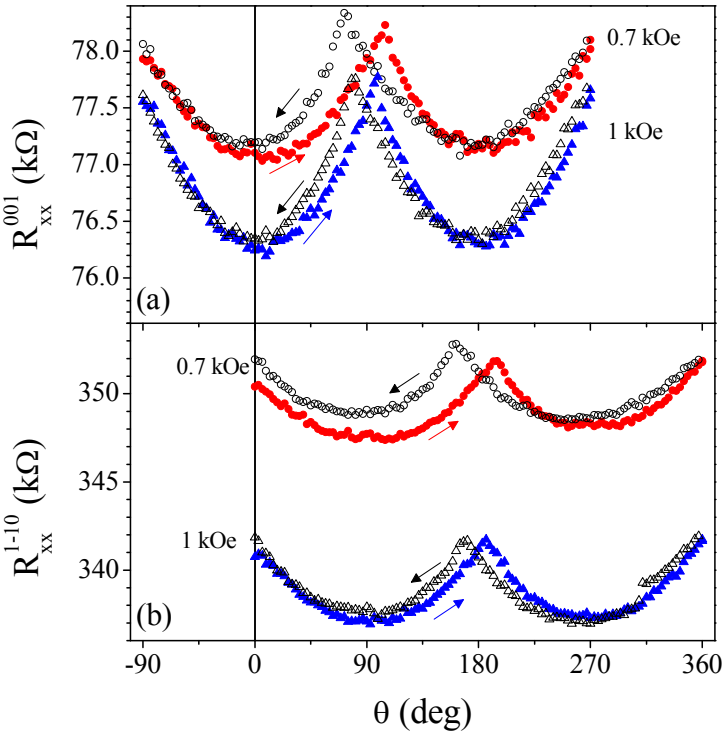

Figure 5.31. AMR curves measured on the 18 nm (110) film (narrow tracks) for the injected current along (a) the [001] and (b) the [1-10] direction, recorded with applied field of 0.07 kOe and 0.10 kOe, as indicated. Forwards and backwards data correspond to close and open symbols, respectively.

Summary of AMR results on (001) and (110) films

We have measured the AMR value of (001) and (110) films for injected current along different crystallographic directions and working at high and low magnetic fied. The AMR amplitude has been observed to depend on the current direction in the

(001) film, with $|\Gamma^{110}| > |\Gamma^{100}|$ but to keep the sign for both directions: $AMR^{100}(001)$, $AMR^{110}(001) < 0$. For (110) films, the AMR is negative or positive depending on the current direction, being $AMR^{001}(110) < 0$ and $AMR^{1-10}(110) > 0$, and the amplitude is dependent on the current direction: $|\Gamma^{1-10}| < |\Gamma^{001}|$ and reveals that in (110) films the [001] direction is a magnetic easy axis. We have explored the AMR in temperature, and the results confirm these previous conclusions and also they signal the development of a maximum of |AMR| close to the ferromagnetic transition. Besides, the angular dependence of the AMR data, especially remarkable at low field in the (110) films, indicate the influence of the magnetic anisotropy of the films in the magnetotransport data.

PHE in (001) films.

PHE measurements have been performed for the injected current along [100] and [010 directions. Due to the mask design (Figure 5.21) it has not been possible to measure the PHE of [110] direction.

The PHE of the 20 nm (001) film has been measured at low and high field, at 180 K. In Figure 5.32 the normalized PHE curves at 20 kOe (a) and 0.4 (down triangles), 0.7 (up triangles) and 1 kOe (circles) are shown. Comparing PHE measurements to the AMR ones (Figure 5.27), we note in the PHE ones the absence of a background contribution to the oscillation. As it is seen in Figure 5.32, the $\sin(\theta)\cos(\theta)$ shape predicted for the angular dependence of the PHE (eq. 5.21) is observed at all fields. The amplitude of the PHE is also indicating the corresponding AMR sign. The PHE data decreases around $\theta = 0$ when $\theta > 0$, and thus the AMR is expected to be negative, as it has been proved in above [in Figure 5.26, $AMR^{100}(001) \sim -\Gamma^{100}(001)$ and $AMR^{110}(001) \sim -\Gamma^{110}(001)$]. The forwards (close symbols) and backwards (open symbols) data almost coincide, and only a low deviation of the experimental curves compared to the reference $\sin(\theta)\cos(\theta)$ is observed in the $\theta = 45$ deg (and equivalent) angular position in the low field data (Figure 5.32b). Comparing the data (symbols) around $\theta = 45$ deg and the fit to the PHE $\sin(\theta)\cos(\theta)$ dependence (line), we observe that the experimental values present a distribution in θ at these angles. Around $\theta = 90$ deg, the experimental values also deviate from the expected curve, but in this case the data changes in θ more abruptly. Interestingly, from magnetomerty we have identified the easy axis magnetization to be located along the [110] direction, which

corresponds to the angular position θ = 45 deg. We ascribe to the biaxial magnetic anisotropy of the (001) film the slight observed deviations from the sin(θ)cos(θ) dependence.

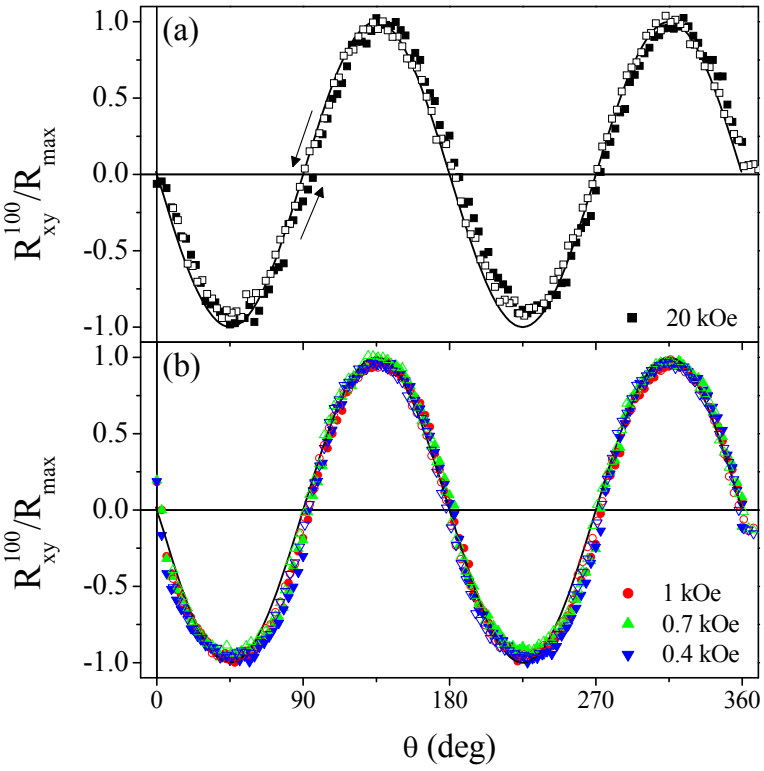

Figure 5.32. Normalized PHE curves from the 20 nm (001) film at (a) 20 kOe and (b) at 1 kOe (circles), 0.7 kOe (up triangles) and 0.4 kOe (down triangles). Close and open symbols correspond to forwards and backwards data.

PHE in (110) films. Evaluation of in-plane magnetic anisotropy.

The PHE experiments on the 20 nm (110) film obtained at 180 K and applying high fields (10 o 20 kOe) are shown in Figure 5.33. At this high field, the magnetization is expected to rotate with the field coherently. Comparing in this figure the expected sin(θ)cos(θ) function (lines) of the PHE and the experimental data, the sin(θ)cos(θ) shape is clearly conserved at all fields and for both injected current along (a) [001] and (b) [1-10] directions. The amplitude of the PHE, negative for the [001] case and positive for the [1-10] case, agrees with the data found from the AMR measurements previously analyzed. Nevertheless, a slight deviation from the sin(θ)cos(θ) function is observed,

causing a shift of the maxima-minima position although conserving the overall width of the data around these points.

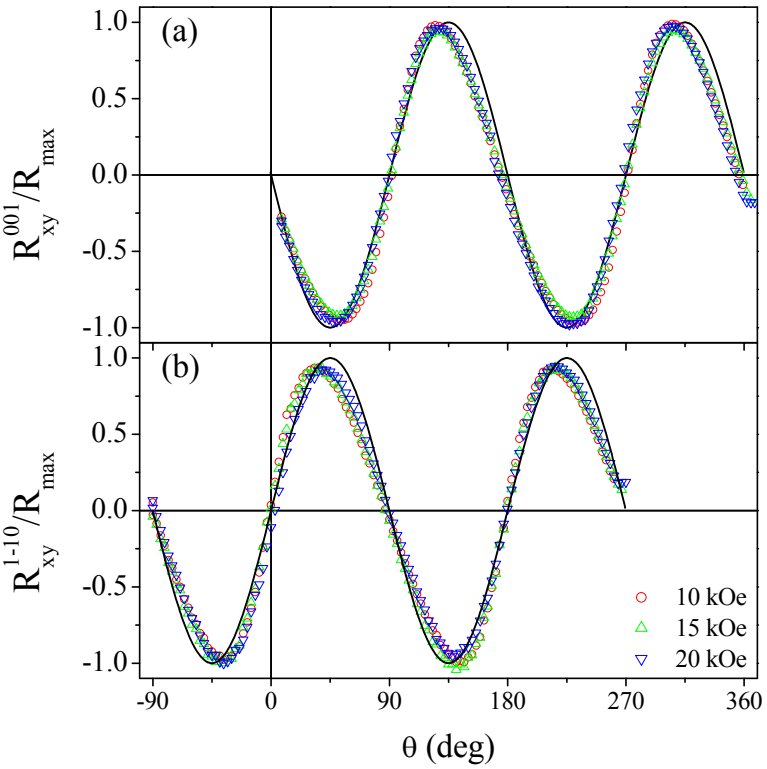

Figure 5.33. Normalized PHE data (symbols) from the 20 nm (110) film with the injected current along (a) the [001] and (b) the [1-10] directions, being the applied fields 10 kOe (circles), 15 kOe (up triangles) and 20 kOe (down triangles). In (a) and (b), lines correspond to sin(θ)cos(θ) fittings for the experimental data. Experimental data correspond to backwards loop.

Recalling that within the (110) plane a uniaxial magnetic anisotropy exist, we turn now to investigate the low field dependence, similarly to what we have done with the AMR measurements. In Figure 5.34 we plot the normalized PHE curves measured on the 20 nm (110) film at 180 K at an applied field of 0.6 (symbols) and 0.7 kOe (lines). We observe that the shape of the PHE has undergone major changes and largely deviates deviation from the sin(θ)cos(θ) dependence. The figure recalls the existence of a minimum for the injected current along the [001] direction around θ = 0 and sharp steps of the resistance at θ = 90 deg. These positions correspond to the hard [1-10] axis, and the sign of the PHE amplitude agrees with AMR results and negative AMR is deduced for [001] direction and positive AMR for [1-10] one. Upon lowering the magnetic field, there is a promotion of this switching effect causing greater angular

shifts, as seen in Figure 5.34 from the increase in the angular positions of the forwards and backwards minima-maxima for 0.6 kOe.

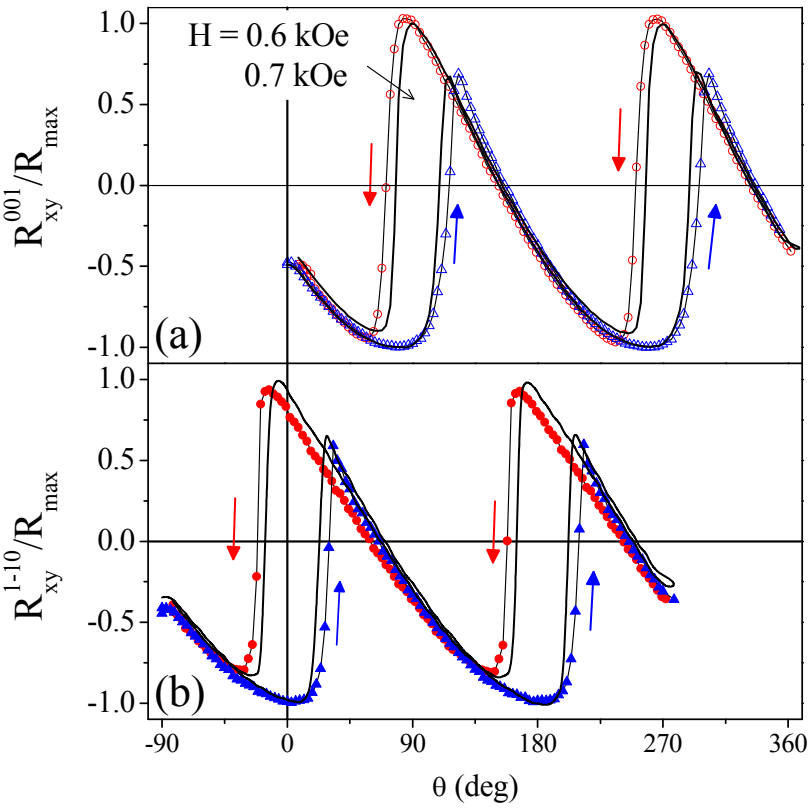

Figure 5.34. Normalized planar Hall effect from the 20 nm (110) film at 180 K and at applied fields of 0.7 kOe (lines) and 0.6 kOe (symbols) for injected current parallel (a) to [001] and (b) to [1-10]. Forwards data correspond to triangles and backwards data to circles. All sweeps present reproducible switching effects.

The switching effects observed in the 18-20 nm (110) thin films have been also studied in a thicker 150 nm one. In Figure 5.35 the normalized PHE curves measured from the 150 nm (110) film at 140 K and 180 K at an applied magnetic field of 0.7 kOe present an altered sin(θ)cos(θ) shape overlapped by the switching effects happening for the current along [001] direction at θ = 90 deg and θ = 180 deg. We notice that the switching effect in Figure 5.35 presents a different curvature than that observed in thinner films (Figure 5.34). This curvature change arises from the expected decrease of the magnetic anisotropy in the thick (110) film (see this previous section on (110) film magnetic anisotropy as a function of thickness, Figure 5.19), which is more relaxed than the ~ 20 nm ones, (Ch4, Figure 4.11). The increase of switching sharpness at 140 K

temperature compared to that of 180 K can be understood within the framework of the thermal dependence of the magnetic anisotropy, which becomes stronger at lower temperatures.

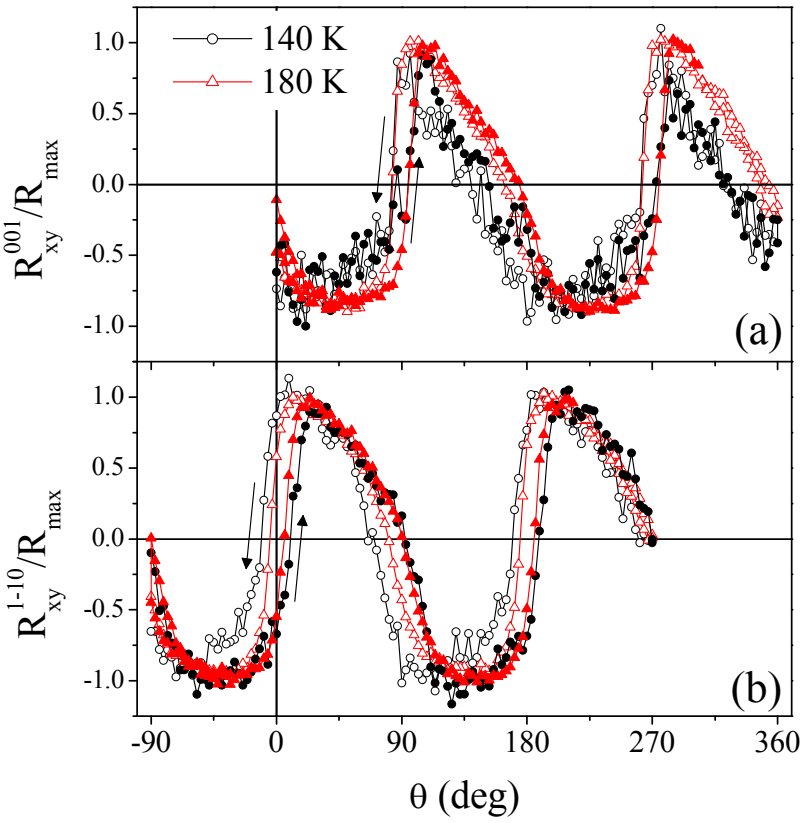

Figure 5.35. Normalized PHE of 150 nm (110) film for injected current along (a) [001] and (b) [1-10] directions at an applied field of 0.7 kOe and at different temperatures: 140 K (circles) and 180 K (triangles). Forwards and backwards data correspond to close and open symbols, respectively.

Summary on PHE results in (001) and (110) films

The PHE experiments on (001) and (110) films allows obtaining the sign of the AMR for the current injected along different directions, but it is especially sensitive to the magnetic anisotropy of the film. We have identified the in-plane magnetic anisotropy of (001) and (110) films, being the former a biaxial system with easy (110) axes and the latter a uniaxial system with [001] easy and [1-10] hard axes. The switching effect in (110) films is observed to be stable in field and temperature, and it is a persistent phenomenon even in relaxed films.

Model: combination of AMR and PHE experiments to obtain the magnetic anisotropy of (110) films.

With the aim of understanding the magnetic anisotropy of (110) films from the magnetotransport measurements, and combining both AMR and PHE experiments, we have developed a model to fit the magnetotransport data and evaluate the magnetic anisotropy. This model has been created and developed by Dr. D. Hrabovský and applied to the 20 nm (110) film data acquired at 180 K at low and high field for current along [001] direction.

The used AMR and PHE measurements are depicted in Figure 5.36 (a and b, respectively). Solid lines connect simulated data points and they would be later explained. A quick inspection of the shape of the AMR and PHE curves signals the agreement of the experimental data and eqs. 5.17 and 5.18. No hysteresis is observed suggesting that the applied magnetic field overcomes any anisotropy and saturates the sample. However, a closer inspection reveals that the AMR (Figure 5.36a) that the maxima are sharper than it would be expected for a pure $\cos^2(\theta)$ dependence. The discrepancy is even more visible in the PHE data (Figure 5.36b), where the minima are shifted from the 45 deg and 225 deg position as it would be expected for $\sin(\theta)\cos(\theta)$. Both effects have the same origin: although the applied magnetic field (20 kOe) is high enough to saturate the sample magnetization along the hard axis (situated along the in-plane [1-10] direction as shown within this chapter in the previous section on magnetic anisotropy) it is not strong enough to keep the magnetization exactly in the direction of magnetic field at any θ value, and thus the angles referred to the magnetic field θ and to magnetization vector φ differ slightly.

If the magnetic field is further reduced, the discrepancies between the behavior predicted by eqs. 5.17 and 5.18 and the experimental data should be more apparent. With this objective, we explored the effect of a low applied field. In Figure 5.37 AMR and PHE data measured at 700 Oe are shown. The inspection of the AMR(θ) data (Figure 5.37a) close to the origin ($\theta \approx 0$ deg) reveals a shape similar to $\cos^2(\varphi)$ as observed at higher field (Figure 5.36a). When the applied magnetic field approaches being perpendicular to the current ($\theta \approx 90$ deg), the AMR value is somewhat smaller than what would be expected from the pure $\cos^2(\varphi)$ behavior, thus implying that $\varphi < \theta$, that is, that the magnetization vector lies behind the magnetic field, reaching its maximum at $\theta \approx 115$ deg; and afterwards it decays rapidly. An observable sharp jump in

PHE curve (Figure 5.37b) occurring at the same angular position ($\theta \approx 115$ deg) is another signature of this switch on magnetization.

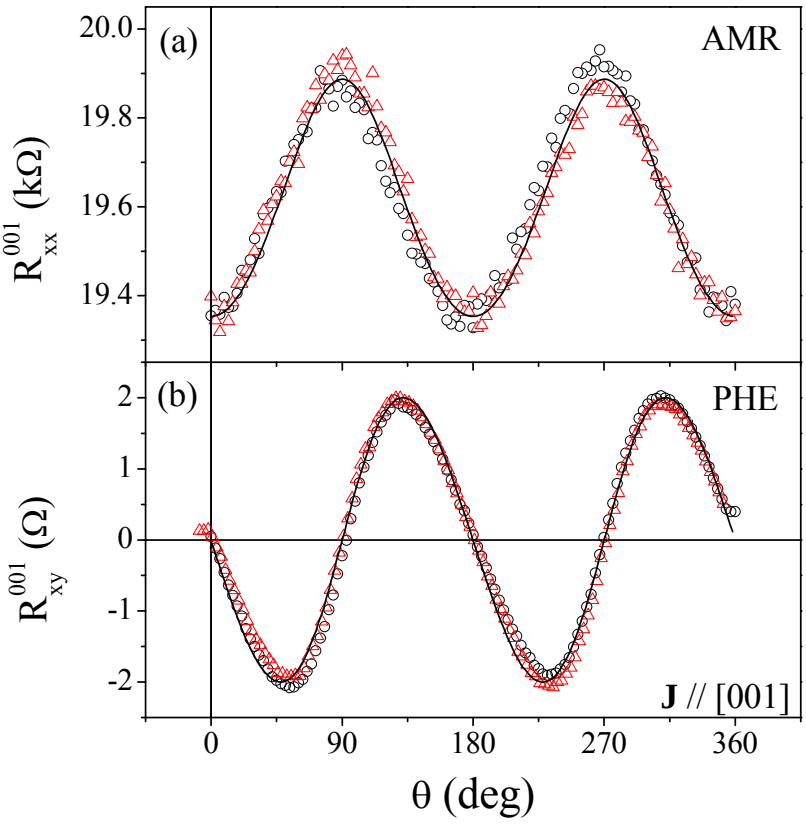

Figure 5.36. Anisotropic magnetoresistance (a) and planar Hall effect (b) as a function of θ at T = 180 K and H = 20 kOe for injected current parallel to [001] direction. Symbols (triangles for forwards and circles for backwards measurements) are experimental data; lines are simulated curves as described in text.

Taking into account that PHE is an odd function of magnetization direction (as already shown in Figure 5.24, with a 180 deg period oscillating around zero), the sharp jump is interpreted with the aid of Figure 5.25c. A switching of the magnetization **M** appears from $\varphi < 90$ deg -in Figure 5.25c it corresponds to **M** at the position defined by (*)- to the symmetrical position at $\varphi > 90$ deg -in Figure 5.25c, it corresponds to **M** at the position defied by (**). This means that the magnetization rotates coherently until magnetic field is not enough to overcome magnetic anisotropy and then, suddenly, it reverses its direction into a new energy minimum. The polar plot of the uniaxial magnetic anisotropy energy within the (110) plane is intrinsic to (110) films, as shown from the magnetic anisotropy studies previously analyzed. Minima of magnetic

anisotropy energy appear along the [001] direction, parallel to $\mathbf{J}_{001}$. These data confirm that the hard magnetic axis is at 90 deg from the [001] direction, that is along the [1-10] axis.

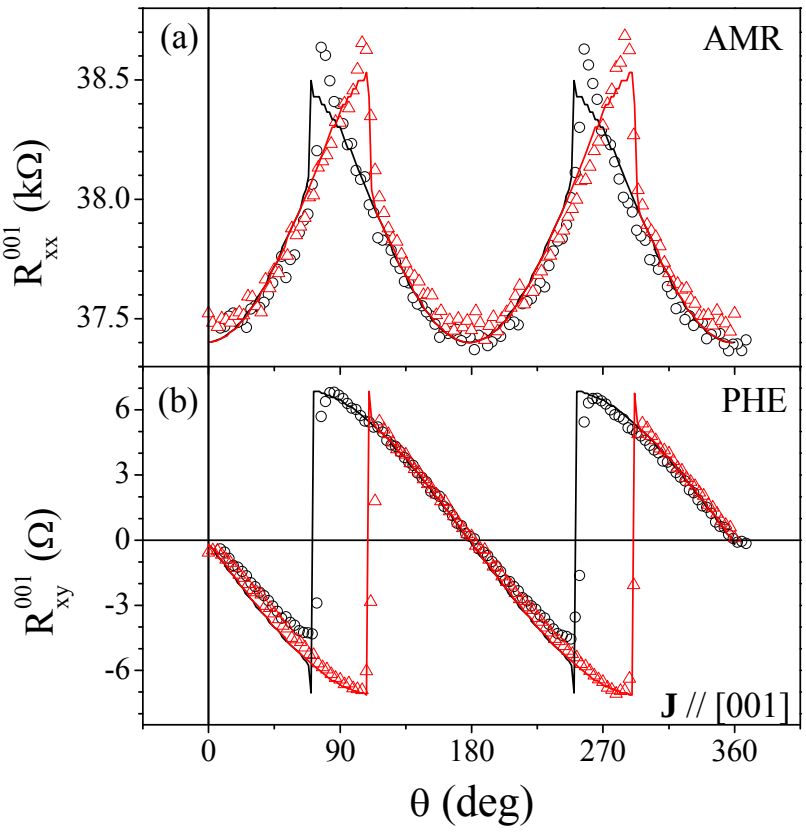

Figure 5.37. Anisotropic magnetoresistance (a) and planar Hall effect (b) as a function of θ at T = 180 K and H = 700 Oe for injected current parallel to [001] direction. Symbols (triangles for forward and circles for backwards measurements) are experimental data, lines are simulated data as described in text.

In order to analyze quantitatively the data and to confirm the above picture, a numerical calculation of the angular dependence of AMR and PHE given by eqs. 5.17 and 5.18 are performed. For this purpose, it is necessary to determine the angular position of the magnetization (φ) at any position of the applied magnetic field (θ). To find the φ(θ) function, the calculation consists in minimizing the total magnetic energy of the system for a given in-plane magnetic field direction. A modified version of the classical expression for Stoner-Wohlfarth total magnetic energy [52] has been used, writing the total energy in the following expression:

$$E = HM_S\cos(\theta-\varphi)+K_u\sin^2(\varphi)+H_CM_S\cos(\varphi_n-\varphi_{n-1}) \qquad [5.22]$$

The first term is the Zeeman magnetic energy and it depends on the relative positions of magnetization and magnetic field; the second term represents the uniaxial magnetic anisotropy with K_u constant; and the third one is a hysteretic term that introduces the dependence of the energy on the previous magnetization position. The minimization of eq. 5.20 allows obtaining the $\varphi(\theta)$ expression for a given set of M_S, H_C, H and K_u values, and with the subsequent use of eqs. 5.17 and 5.18 we can determine AMR(θ) and PHE(θ). Calculations are repeated for various K_u and H_C values until agreement with experimental data is obtained.

Initial parameters for simulation have been extracted from magnetometry measurements at 180 K: $M_S = 300$ emu/cm^3, $K_u \sim 0.25\ 10^6$ erg/cm^3 and $H_C = 200$ Oe, The calculated loops are displayed as solid and dashed lines in Figure 5.36 and Figure 5.37. The values of uniaxial anisotropy and coercive field have been slightly tuned in order to obtain best fit of a total of four loops (two forwards and two backwards). The corresponding final values are: $K_u = 0.3 \cdot 10^6$erg/cm^3 and $H_C = 250$ Oe, which do not differ appreciably from the values extracted from the analysis of SQUID measurements. Moreover, it can be appreciated in Figure 5.36 and Figure 5.37 that the agreement between the experimental and calculated data is excellent. This implies that AMR and PHE experimental data is accurately described by the model. Besides, it can be concluded that the system exhibits a pure uniaxial magnetic anisotropy with hard axis along [1-10] direction and easy axis along [001] direction.

5.2.5 Conclusions on AMR in (001) and (110) films

As proposed by Smit [53] and later by Van Elst [54], the spin-orbit interaction (H_{SO}) is at the origin of the AMR. The expression of H_{SO} as a function of the atomic spin (**S**) and orbital (**L**) momentum operators is:

$$H_{SO} = \lambda\left[L_Z S_Z + \frac{1}{2}\left(L_+ S_- + L_- S_+\right)\right] \qquad [5.23]$$

where λ is the spin-orbit coupling constant and the magnetization is assumed to be parallel to z-direction. Acting on the d bands of the 3d metals, H_{SO} promotes that part of the d majority spin band d↑ (or d minority spin band d↓) band mixes with the d↓ (or d↑) band influenced by the L_+S_- (or L_+S_-) operator. The magnetization vector provides a preferential axis for H_{SO} through the polarization term L_zS_z, the d states are not mixed isotropically. The theory of this effect was further developed by Berger [55], Jaoul *et al.*

[56] and Campbell and Fert [39] and the scenario includes the application of the two-current model, which assumes that two conduction channels exist, one channel with the electrons of the majority (↑) spin band and another channel with the electrons of the minority (↓) spin band. The resistivity (ρ) in the ferromagnetic state is determined from the resistivity of this majority (ρ↑) and minority (ρ↓) spin bands and from the resistivity caused by the spin-flip scattering (ρ↑↓) [39]:

$$\rho = \frac{\rho_\uparrow \rho_\downarrow + \rho_{\uparrow\downarrow}\left(\rho_\uparrow + \rho_\downarrow\right)}{\rho_\uparrow + \rho_\downarrow + 4\rho_{\uparrow\downarrow}} \qquad [5.24]$$

The definition of the AMR is:

$$\frac{\Delta\rho}{\rho} = \frac{\rho_{//} - \rho_\perp}{\rho_{av}} \qquad [5.25]$$

where $\rho_{//}$ and $\rho_\perp$ account for the resistivity measured with the magnetization parallel or perpendicular to the current flow direction, respectively, and ρ_{av} for the appropriate average of parallel and perpendicular resistivities. Using $\Delta\rho_\uparrow$ and $\Delta\rho_\downarrow$ as the changes in the resistivity of the majority and minority spin bands between the longitudinal and transverse configuration, we can derive from eqs. 5.24 the AMR expression as:

$$\frac{\Delta\rho}{\rho} = \frac{\rho_\uparrow \Delta\rho_\downarrow + \rho_\downarrow \Delta\rho_\uparrow + \rho_{\uparrow\downarrow}\left(\Delta\rho_\uparrow + \Delta\rho_\downarrow\right)}{\rho_\uparrow \rho_\downarrow + \rho_{\uparrow\downarrow}\left(\rho_\uparrow + \rho_\downarrow\right)} - \frac{\Delta\rho_\uparrow + \Delta\rho_\downarrow}{\rho_\uparrow + \rho_\downarrow + 4\rho_{\uparrow\downarrow}} \qquad [5.26]$$

From the analysis of Malozemoff [57] applied to the AMR of Ni alloys, the changes in the resistivity $\Delta\rho_\uparrow$ and $\Delta\rho_\downarrow$ can be expressed as a function of the resistivities of each channel as:

$$\Delta\rho_\uparrow = \gamma_{\uparrow\uparrow}\rho_\uparrow + \gamma_{\uparrow\downarrow}\rho_\downarrow \qquad [5.27]$$

$$\Delta\rho_\downarrow = \gamma_{\downarrow\downarrow}\rho_\downarrow + \gamma_{\downarrow\uparrow}\rho_\uparrow \qquad [5.28]$$

being $\gamma_{\uparrow\uparrow}$, $\gamma_{\downarrow\downarrow}$ and $\gamma_{\uparrow\downarrow}$ constant values related to the spin-orbit coupling. Referring to Ni alloys with unoccupied d↑ band, that is, with no virtual bound states at the spin ↑ Fermi surface, $\Delta\rho_\uparrow$ and $\Delta\rho_\downarrow$ can be rewritten in terms only of the resistivity of the occupied d↓ band as $\rho_\downarrow >> \rho_\uparrow$. In these conditions, as shown in Refs. [56][57], eqs. 5.27 and 5.28 lead to $\Delta\rho_\uparrow = \gamma\rho_\downarrow$ and $\Delta\rho_\downarrow = -\gamma\rho_\downarrow$, and neglecting the spin-flit term $\rho_{\uparrow\downarrow}$ in eq. 5.24, AMR is thus given by:

$$\frac{\Delta\rho}{\rho} = \gamma\left(\alpha - 1\right) \qquad [5.29]$$

where γ is a constant related to the spin-orbit coupling constant λ and to the exchange energy splitting H_{ex} in the form of $\gamma = (\lambda/H_{ex})^2$and α is the ratio of majority and minority spin resistivities $\alpha = \rho\downarrow/\rho\uparrow$.

We note that this model is developed for 3d metals alloys, as NiFe, and the conducting carriers are electrons from the s-band. The scattering events are ideally generated through the interaction of an electron with a characteristic s-wavefunction and an potential generated by the impurities [57]. The case of manganites presents some relevant differences: the conducting electrons come from the 3d-band of Mn, characterized by their corresponding 3d-wavefunction, and the scattering events cannot be described within an isotropic potential approach since the interacting orbitals are not isotopic (3d-orbitals).

As a first approach to the understanding of the AMR effect in manganites, we have applied the model developed by Malozemoff [57], which was developed for 3d-metals with the current injected along the [100] direction. For manganites, fully spin polarization of the conduction band can be observed at low temperature by spectroscopic measurement [58]. First, we consider the model at low temperature (ferromagnetic phase), where the energy separation between the majority and minority spin bands (exchange energy splitting H_{ex}) are experimentally measured and in $La_{0.7}Ca_{0.3}MnO_3$ films is $H_{ex} = 3.3$ eV [59]. Due to the symmetry of the potential generated by the oxygen octahedron, between the t_{2g} and e_g orbitals an energy splitting develops, so-called crystal field splitting (Δ_{CF}), being measured for $La_{2/3}Ca_{1/3}MnO_3$ films as $\Delta_{CF} = 1.92$ eV. Besides, in the manganites the Jahn-Teller distortion becomes relevant at temperatures close to the ferromagnetic transition temperature (T_C). The energy splitting caused by the Jahn-Teller affects all the 3d-band, but more relevantly promotes the stabilization of the e_g conduction electrons as the e_g levels are splitted by $\Delta_{JT} = 0.5$ eV [60]. For the application of this model, the spin-orbit constant λ is also necessary; for the Mn^{3+} ions, $\lambda = 0.05$ eV [61]. A scheme of the involved energy on the Mn3+ ions is shown in Figure 5.38.

Working in the ferromagnetic phase, sizeable fully spin polarization of the conduction bands occurs, and conducting electrons can find available states only in the majority spin band. Thus, we can simplify the two band model to a one band model: since no states are available in the minority band, $\rho\downarrow \sim \infty$ infinite and applying this

condition to eq. 5.24, resistivity depends only on majority and spin-flip terms $\rho = \rho_{\uparrow} + \rho_{\uparrow\downarrow}$, and applying this result in eqs. 5.26-28, the final AMR expression is [62]:

$$\frac{\Delta\rho}{\rho} = \gamma_{\uparrow\uparrow} = \frac{3\lambda^2}{4}\left[\frac{1}{\Delta_{CF}^2} - \frac{1}{\left(H_{ex} - \Delta_{CF}\right)^2}\right] \qquad [5.30]$$

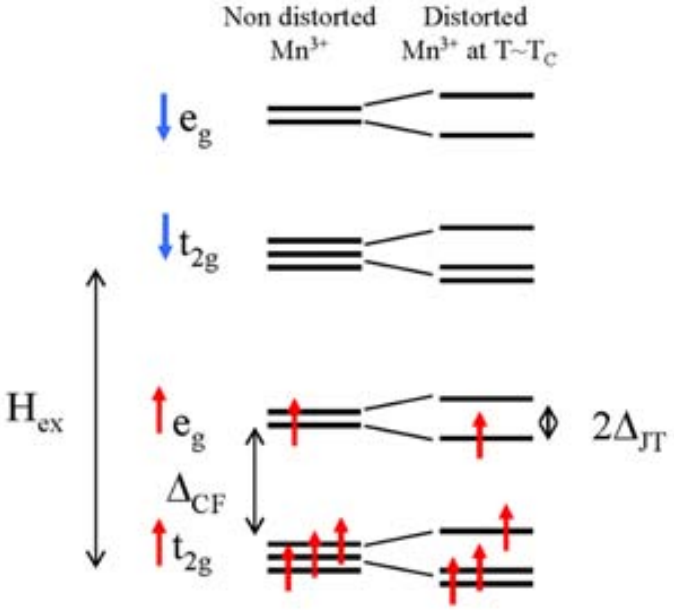

Figure 5.38. Schematic view of 3d the orbital energy in Mn3+ ions, beng Hex the exchange energy splitting, Δ_{CF} the crstal field energy, and $2\Delta_{JT}$ the Jahn-Teller energy splitting.

Using eq. 30 and the energy values shown previously, we can estimate for LCMO films the expected sign and amplitude of the AMR, being AMR = -0.05 %. This value agrees in sign with the AMR results presented here for (001) films and also for current injected along [100] and [110] directions ($AMR^{100}(001) < 0$, and $AMR^{110}(001) < 0$). Reported studies on the AMR of manganite films also signal the negative AMR within the (001) plane [62]. However, the amplitude of the effect is much lower than the experimental values: $AMR^{100}(001) \sim$ -1.5 % and $AMR^{110}(001) \sim$ -3.0 % (Figure 5.26a and b, respectively), and values reported in Ref. [62]. Besides, it has been experimentally measured in manganite films a peak in the temperature dependence of the AMR close to T_C [44][62][63] which cannot be described by the model used here.

Aiming to reproduce the experimental AMR peak, we have continued applying the one channel conduction model but we have considered that the energies (H_{ex}, Δ_{CF}, Δ_{JT}) of our system may change. We have created three different scenarios, trying to

mimic the AMR curve with temperature following different energy diagrams. These three scenarios are:

1. Considering that the crystal field Δ_{CF} can change close to T_C due to the Jahn-Teller distortion. The value of Δ_{CF} is expected to be virtually reduced since the 3d-orbitals split. We have generated this variation of Δ_{CF} by a Gaussian function:

$$\Delta_{CF}(T) = \Delta_{CF}(T=0) - A\exp\left[-2\ln(4)\frac{(T-T_C)^2}{w^2}\right] \qquad [5.31]$$

where w is the full width at half maximum of the transition (extension in temperature of the Jahn-Teller distortion) and A is the energy amplitude of the effect (defined as the Jahn-Teller energy Δ_{JT}). The other energy values are kept constant.

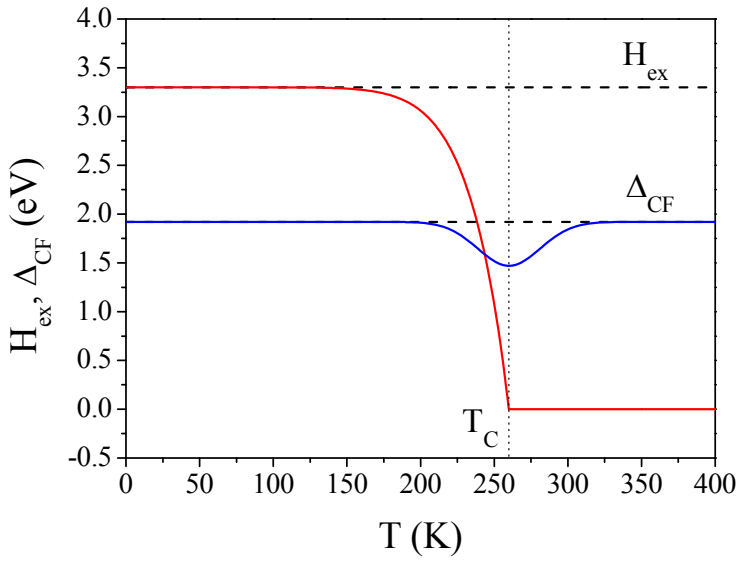

Figure 5.39. Exchange energy splitting H_{ex} and cristal field energy Δ_{CF} as a function of temperature (solid lines), with the reference values are indicated by dashed lines. Dotted line signals the T_C.

2. Considering that the exchange energy H_{ex} depends on the temperature. The argument is based on the fact that above T_C the spin of the electrons can fluctuate at a timescales shorter than those of the transport or spectroscopic measurements (see Ref. [58] and [59]). Thus, we can consider a temperature dependent H_{ex}, thus a mixing of the majority and minority spin bands, leading to above T_C to $H_{ex} = 0$. H_{ex} is thus expected to be temperature dependent [64], we have assumed it to evolve as a function of the magnetization:

$$H_{ex}(T) = H_{ex}(T=0)\left[1-\left(\frac{T}{T_C}\right)^n\right] \cdot \quad T \le T_C$$
$$H_{ex}(T) = 0 \qquad\qquad T > T_C \qquad [5.32]$$

To approximate the $H_{ex}(T)$ function to the square of the magnetization dependence on temperature, as suggested by Ref. [64], we have chosen n = 10. The other energy values are kept constant.

3. Taking into account the points1 and 2, we create a third scenario combining both Δ_{CF} and H_{ex}variable energies.

The results of the different simulations are shown in Figure 5.40. Considering the Δ_{CF} energy variation causes a peak in the AMR, as seen in Figure 5.40a, but it would not reproduce the experimental minimum but a maximum. Moreover, other experimental feature of the AMR measurement, that is, the disappearance of the AMR at $T > T_C$ cannot be obtained with this approach. On the other hand, the AMR for varying H_{ex} (Figure 5.40b) or the combination of H_{ex} and Δ_{CF} (Figure 5.40c) clearly depict the experimental facts: a negative value of AMR at low temperature, a minimum of the AMR at temperatures close to the T_C and a trend to AMR = 0 at $T > T_C$.

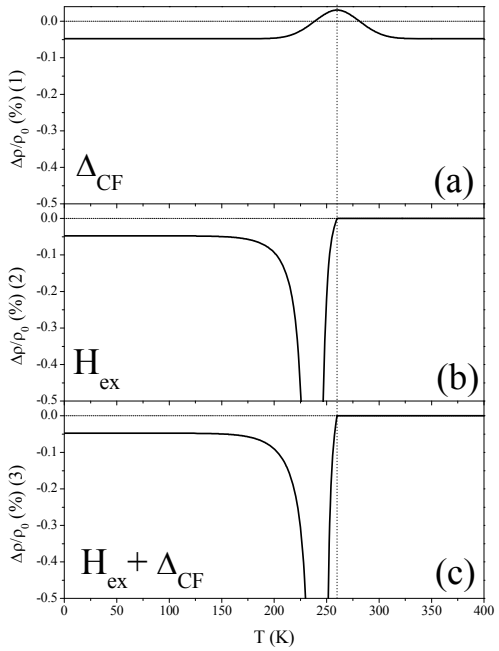

Figure 5.40. Simulated temperature dependence of the AMR considering (a) Δ_{CF} changes due to Jahn-Teller distortion near T_C, (b) H_{ex} depends on the magnetization of the sample, and (c) both Δ_{CF} and H_{ex} change. Dotted line indicate the simulated T_C.

From the given hypothesis and the resulting simulations, we deduce that the better approach to solve the AMR dependence on temperature includes considering the exchange energy splitting H_{ex} to depend in temperature. The difference when adding the crystal field Δ_{CF} can be deduced from Figure 5.41: the occurrence of the minimum in the AMR temperature dependence is expected to occur at higher temperature if the crystal field has a relevant role.

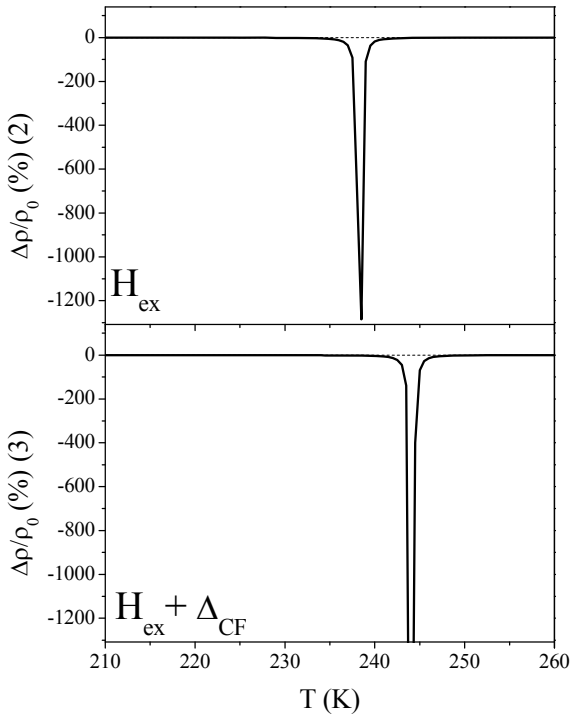

Figure 5.41. Simulated temperature dependence of the AMR considering (a) H_{ex} depends on the magnetization of the sample, and (b) both Δ_{CF} and H_{ex} change.

Analyzing these simulations in the framework of the presented data on (001) and (110) films and on the reported data [44][62][63], the AMR sign in (001) films can be explained with the presented one channel mode. Nevertheless, the expected AMR amplitude differs from the experimental one, being the expected value ~ -0.05 % and the experimental one ~ -2-3 %.. On the other hand, adding to the model considerations on the temperature dependence of the energies involved in the system can reproduce the experimental peak measured near T_C. These results can also explain the AMR observed in (110) films, but only for the current injected along the [001] direction (see Figure 5.30, where $AMR^{001}(110) < 0$ but $AMR^{1\text{-}10}(110) > 0$). We need to recall that the model is developed constructing the spin-orbit matrix with the 3d-wavefunctions and afterwards supposing that the current is injected along [100] direction. An accurate

recalculation of the energy terms arising from the crystal field and exchange energy splitting may be necessary to fully understand the AMR sign within the (110) plane, and in particular for the current injected along [1-10] direction.

References

[1] A. J. Millis, T. Darling, and A. Migliori, J. Appl. Phys. **83**, 1588 (1998); K. H. Ahn and A. J. Millis, Phys. Rev. B **64**, 115103 (2001)

[2] M. Ziese, H. C. Semmelhack, and K. H. Han, Phys. Rev. B **68**, 134444 (2003)

[3] M. Bibes, LL. Balcells, S. València, J. Fontcuberta, M. Wojcik, E. Jedryka, and S. Nadolski, Phys. Rev. Lett. **87**, 67210 (2001); M. Bibes, S. València, Ll. Balcells, B. Martínez, J. Fontcuberta, M. Wojcik, S. Nadolski, and E. Jedryka, Phys. Rev. B **66,** 134416 (2002)

[4] J. O'Donnell, M. Onellion, M. S. Rzchowski, J. N. Eckstein, and I. Bozovic, Phys. Rev. B **54**, R6841 (1996); Y. Suzuki, H. Y. Hwang, S-W. Cheong, and R. B. van Dover, Appl. Phys. Lett. **71**, 140 (1997); M. Izumi, Y. Konishi, T. Nishihara, S. Hayashi, M. Shinohara, M. Kawasaki, and Y. Tokura, Appl. Phys. Lett. **73**, 2497 (1998); K. A. Thomas, P. S. I. P. N. de Silva, L. F. Cohen, A. Hossain, M. Rajeswari, T. Venkatesan, R. Hiskes, and J. L. MacManus-Driscoll, J. Appl. Phys. **84**, 3939 (1998); R. A. Rao, D. Lavric, T. K. Nath, C. B. Eom, L. Wu, and F. Tsui, J. Appl. Phys. **85**, 4794 (1999); W. Prellier, A. Biswas, M. Rajeswari, T. Venkatesan, and R. L. Greene, Appl. Phys. Lett. **75**, 397 (1999); X. W. Wu, M. S. Rzchowski, H. S. Wang, and QiLi, Phys. Rev. B **61**, 501 (2000); G. Campillo, A. Berger, J. Osorio, J. E. Pearson, S. D. Bader, E. Baca, and P. Prieto, J. Magn. Magn. Mater. **237**, 61 (2001); M. Paranjape, A. K. Raychaudhuri, N. D. Mathur, and M. G. Blamire, Phys. Rev. B **67**, 214415 (2003)

[5] J. Z. Sun, D. W. Abraham, R. A. Rao, and C. B. Eom, Appl. Phys. Lett. **74**, 3017 (1999)

[6] G. Harzheim, J. Schubert, L. Beckers, W. Zander, D. Meertens, C. Osthöver, Ch. Buchal, Mater.Sci. Eng. B **56**, 147 (1998); R. B. Praus, G. M. Gross, F. S. Razabi, and H.U. Habermeier, J. Magn. Magn. Mater. **211**, 41 (2000); Y. Lu, C. Höfener, B. Wiedenhorst, J. B. Philipp, F. Herbstritt, A. Marx, L. Alff, and R. Gross, Phys. Rev. B **62**, 15806 (2000); M. Paranjape, A. K. Raychaudhuri, N. D. Mathur, and M. G. Blamire, Phys. Rev. B **67**, 214415 (2003)

[7] J. L. Maurice, F. Pailloux, A. Barthélémy, O. Durand, D. Imhoff, R.Lyonnet, A. Roher, and J. P. Contour, Philos. Mag. **83**, 3201 (2003)

[8] M. Angeloni, G. Balestrino, N. G: Boggio, P. G. Medaglia, P. Orgiani, and A. Tebano, J. Appl. Phys. **96**, 6387 (2004); J. Dvorak, Y. U. Ydzerda, S. B. Ogale,

S. Shinde, Tao Wu, T Venkatesan, R Godfrey, R. Ramesh, J. Appl. Phys. **97**, 10C102 (2005)

[9] H. Y. Hwang, T. T. M. Palstra, S.-W. Cheong, and B. Batlogg, Phys. Rev. B **52**, 15046 (1995); J. J. Neumeier, M. F. Hundley, J. D. Thompson, and R. H. Heffner, Phys. Rev. B **52**, R7006 (1995)

[10] V. Laukhin, J. Fontcuberta, J. L. García-Muñoz, and X. Obradors, Phys. Rev. B **56**, R10009 (1997)

[11] D. Sander, Rep. Prog. Phys. **62**, 809 (1999)

[12] Jin H. So, J. R. Gladden, Y. F. Hu, J. D. Maynard, and Qi Li, Phys. Rev. Lett. **90**, 036103 (2003)

[13] R. O. Bell and G. Rupprecht, Phys. Rev. **129**, 90 (1963)

[14] A. Tebano, C. Aruta, P. G. Medaglia, F. Tozzi, G. Balestrino, A. A. Sidorenko, G. Allodi, R. De Renzi, G. Ghiringhelli, C. Dallera, L. Braicovich, and N. B. Brookes, Phys. Rev. B **74**, 245116 (2006); C. Aruta, G. Ghiringhelli, A. Tebano, N. G. Boggio, N. B. Brookes, P. G. Medaglia, and G. Balestrino, Phys. Rev. B **73**, 235121 (2006); J. J. Kavich, M. P. Warusawithana, J. W. Freeland, P. Ryan, X. Zhai, R. H. Kodama, and J. N. Eckstein, Phys. Rev. B **76**, 014410 (2007)

[15] Z. Fang, I. V. Solovyev, and K. Terakura, Phys. Rev. Lett. **84**, 3169 (2000)

[16] L. Brey, Phys. Rev. B **75**, 104423 (2007)

[17] J. Simon, T. Walther, W. Mader, J. Klein, D. Reisinger, L. Alff, and R. Gross, Appl. Phys. Lett. **84**, 3882 (2004)

[18] R. Bertacco, J. P. Contour, A. Barthélémy, and J. Olivier, Surf. Sci. **511**, 366 (2002)

[19] A. de Andrés, J. Rubio, G. Castro, S. Taboada, J. L. Martínez and J. M. Colino, Appl. Phys. Lett. **83,** 713 (2003); J. Rubio-Zuazo, A. de Andrés, S. Taboada, C. Prieto, J. L. Martínez, and G. R. Castro, Physica B **357**, 159 (2005)

[20] Y. L. Qin, H. W. Zandbergen, Z. Q. Yang, and J. Aarts, Phil. Mag. **85**, 4465 (2005)

[21] W. Prellier, Ph. Lecoeur and B. Mercey, J. Phys.: Condens. Matter **13,** R915 (2001)

[22] A-M. Haghiri-Gosnet and J-P Renard, J. Phys. D: Appl. Phys. **36**, R127 (2003); K. Dörr, J. Phys. D: Appl. Phys. **39,** R125 (2006)

[23] J. H. Song, J.-H. Park, J.-Y. Kim, B.-G. Park, Y. H. Jeong, H.-J. Noh, S.-J. Oh, H.-J. Lin, and C. T. Chen, Phys. Rev. B **72**, 060405 (2005)

[24] T. K. Nath, R. A. Rao, D. LAvric, C. B. Eom, L. Wu, and F. Tsui, Appl. Phys. Lett. **74**, 1615 (1999)

[25] J. O'Donnell, M. S. Rzchowski, J. N. Eckstein, and I. Bozovic, Appl. Phys. Lett. **72**, 1775 (1998)

[26] L. M. Berndt, V. Barbarin, and Y. Suzuki, Appl. Phys. Lett. **77**, 2903 (2000)

[27] K. Steenbeck and R. Hiergeist, Appl. Phys. Lett. **75**, 1778 (1999)

[28] K. Steenbeck, T. Habisreuther, C. Dubordieu, and J. P. Sénateur, Appl. Phys. Lett. **80**, 3361 (2003)

[29] M. Ziese, Phys. Stat. Sol. (b) **242**, No. 13 R116 (2005)

[30] T. W. Darling, A. Migliori, E. G. Moshopoulou, S. A. Trugman, J. J. Neumeier, J. L. Sarrao, A. R. Bishop, and J. D. Thompson, Phys. Rev. B **57**, 5093 (1998)

[31] *American Institute of Physics Handbook*, edited by D. E. Gray (McGraw–Hill), New York, 1972, p. 3–126

[32] B. D. Cullity, *Introduction to Magnetic Materials* (Addison–Wesley cop. Reading, MA, 1972): (a) p. 211; (b) p. 270

[33] Linear magnetostriction examples of some La-manganite films can be found in M. Ziese, H. C. Semmelack, and P. Busch, J. Magn. Magn. Mat. **246**, 327 (2002)

[34] W. D. Nix, Metall. Trans. A **20**, 2217 (1989)

[35] $c_{11} = 350$ GPa and $c_{44} = 150$ GPa are extracted from experimental measurements on $La_{0.67}Ca_{0.33}MnO_3$ films grown on (001)STO reported by Jin H. So, J. R. Gladden, Y. F. Hu, J. D. Maynard, and Qi Li, Phys. Rev. Lett. **90**, 036103 (2003). To calculate c_{12}, it was used the experimental ratio of $SrTiO_3$ $(c_{12}/c_{11})_{STO} = 0.322$ reported by R. O. Bell and G. Rupprecht, Phys. Rev. **129**, 90 (1963): $c_{12} = (c_{12}/c_{11})_{STO}\, c_{11} = 113$ GPa.

[36] M. Matthews, F. M. Postma, J. C. Lodder, R. Jansen, G. Rijnders, and D. H. Blank, Appl. Phys. Lett. **87**, 242507 (2005)

[37] T. M. Perekalina, I. E. Lipinski, V. A. Timofeeva, and S. A. Cherkezyan, Sov. Phys. Solid State **32**, 3146 (1990)

[38] C. W. Searle and S. T. Wang, Can. J. Phys. **47**, 2703 (1969)

[39] I. A. Campbell, and A. Fert, Ferromagnetic Materials, Vol. 3, E.P. Wohlfarth, North-Holland, 1982, p 747

[40] R. M. Bozorth, Phys. Rev. **70**, 923 (1946)

[41] T. R. McGuire, and R. I. Potter, IEEE Trans. Magn. **11**, 1018 (1975)

[42] M. Ziese, and S. P. Sena, J. Phys. Condens. Matter **10**, 2727 (1998)

[43] V. S. Amaral, A.A.C.S. Lourenço, J. P. Araújo, P. M. Pereira, J. B. Sousa, P. B. Tavares, J. M. Vieira, E. Alves, M. F. da Silva, and J. C. Soares, J. Appl. Phys. **87** 5570 (2000)

[44] M. Bibes, O. Gorbenko, B. Martínez, A. Kaul, and J. Fontcuberta. J. Magn. Magn. Mater. **211**, 47 (2000)

[45] J. O'Donnell, M. Onellion, M. S. Rzchowski, J. N. Eckstein, and I. Bozovic, Phys. Rev. B **54**, R6841 (1996)

[46] M. Bibes, V. Laukhin, S. Valencia, B. Martínez, J. Fontcuberta, O. Yu Gorbenko, A. R. Kaul, and J. L. Martínez, J. Phys. Condens. Matter **17**, 2733 (2005)

[47] C. Goldberg, and R. E. Davis, Phys. Rev. **94**, 1121 (1954)

[48] F.Y. Ogrin, S. L. Lee, and Y. G. Ogrin, J. Magn. Magn. Mater. **219**, 331 (2000)

[49] C. Mitze, C. Osthöver, F. Voges, U. Hasenkox, R. Waser, and R. R. Arons, Solid State Commun. **109**, 189 (1999)

[50] Y. Bason, L. Klein, J.-B. Yau, X. Hong, and C. H. Ahn, Appl. Phys. Lett. **84**, 2593 (2004)

[51] M. Bibes, Ll. Balcells, S. Valencia, S. Sena, B. Martínez, J. Fontcuberta, S. Nadolski, M. Wojcik, and E. Jedryka, J. Appl. Phys. **89**, 6686 (2001)

[52] E. P. Wohlfarth and E. C. Stoner, Philos. Trans. R. Soc. **A240**, 599 (1948)

[53] J. Smit, Physica **16**, 612 (1951)

[54] H. C. Van Elst, Physica **25**, 708 (1959)

[55] L. Berger, Physica **30**, 1141 (1964)

[56] O. Jaoul, I. A. Campbell, and A. Fert, J. Magn. Magn. Mat. **5**, 23 (1977)

[57] A. P. Malozemoff, Phys. Rev. B **34**, 1853 (1986)

[58] J.-H. Park, E. Vescovo, H.-J. Kim, C. Kwon, R. Ramesh, and T. Venkatesan, Nature **392**, 794 (1998)

[59] J. Y. T. Wei, N.-C. Yeh, R. P. Vasquez, and A. Gupta, J. Appl. Phys. **83**, 7366 (1998)

[60] A. J. Millis, P. B. Littlewood, and B. I. Shraiman, Phys. Rev. Lett. **74**, 5144 (1995); J. Y. T. Wei, N.-C. Yeh, and R. P. Vasquez, Phys. Rev. Lett. **79**, 5150 (1997)

[61] J. S. Griffith, *The theory of transition metal ions* (Cambridge University Press, Cambridge, 1964), pg. 437; E. Francisco and L. Pueyo, Phys. Rev. A **36**, 1978 (1987)

[62] M. Ziese and S. P. Sena, J. Phys.: Cond. Matter **10**, 2727 (1998); M. Ziese, Phys. Rev. B **62**, 1044 (2000)

[63] J. N. Eckstein, I. Bozovic, J. O'Donnell, M. Onellion, and M. S. Rzchowski, Appl. Phys. Lett. **69**, 1312 (1996); M. Bibes, O. Gorbenko, B. Martínez, A. Kaul, and J. Fontcuberta, J. Magn. Magn. Mater. **211**, 47 (2000); I. C. Infante, V. Laukhin, F. Sánchez, J. Fontcuberta, O. Melnikov, O. Yu Gorbenko, and A. R. Kaul, J. Appl. Phys. **99**, 08C502 (2006)

[64] P.A. Stampe, H. P. Kunkel, Z. Wang, and G. Williams, Phys. Rev. B **52**, 335 (1995)

6 $SrTiO_3/La_{2/3}Ca_{1/3}MnO_3$ bilayers for MTJs

In this chapter, the microstructure of $SrTiO_3$ (STO) layers deposited on LCMO films onto (001) and (110) STO substrates and their properties will be shown. The interest in these heterostructures arises from their capability of being used in magnetic tunnel junctions (MTJs). .With this purpose, different topics concerning the STO/LCMO heterostructures are presented in this chapter:

1. Description of the bilayer growth and analysis of their microstructure by X-ray diffraction reciprocal space maps (RSMs) and by high resolution transmission electron microscopy (HRTEM).

2. Study of the magnetic and electronic properties (001) and (110) single LCMO electrodes and STO capped LCMO electrodes (bilayers) by magnetometry and nuclear magnetic resonance (NMR). The electronic and chemical properties of the STO/LCMO interfaces have been investigated by X-ray photoemission experiments (XPS). The results will be discussed in the framework of the relevance of the interface phenomena arising at oxide interfaces on the functional properties of the used heterostructures.

3. Surface morphology and resistance maps have been measured on the STO/LCMO bilayers by conducting atomic force microscopy (C-AFM) technique. Careful analysis of the data allowed extracting the barrier height values.

4. The fabrication of MTJs has been achieved by two different lithographic techniques. Preliminary measurements on these MTJs will be shown, probing that

tunnel magnetoresistance have been achieved using STO/LCMO(001) and (110) bilayers.

6.1 Growth and microstructure characterization

In this section, the results of the characterization of the samples listed in Table 6.1, are presented and analyzed.

Table 6.1. Samples referred in this section and the corresponding LCMO and thickness STO together with the growth temperature during LCMO deposition.

Sample	Substrate	LCMO thickness (nm)	T_d (LCMO) (C)	STO thickness (nm)
060908STO	$NGO(001)_C$			20
051011A	STO(001)	21.3	800	15
051010B	STO(110)	21.5	800	27
080118A1	STO(001)	39	800	5
070119B1	STO(110)	39	750	5

6.1.1 Control of $SrTiO_3$ growth: rate calibration

STO/LCMO bilayers were grown in a single process and simultaneously on (001) and (110) STO substrates. The bilayers were fabricated by rf magnetron sputtering, in the same chamber used to deposit the single LCMO films and described in Ch2. Before fabricating the bilayers, single STO layers were grown to calibrate the STO growth deposition rate. For this purpose, $NdGaO_3$ (NGO), an orthorhombic perovskite that can be easily indexed as pseudobic, was selected as substrate instead of STO single crystals, in order to make possible XRD and XRR characterization. The NGO substrate orientation has been chosen as $(001)_c$, in pseudocubic indexation. In the pseudocubic aproximatimation, the lattice parameter is $a_{NGO} = 3.861$ Å, which is close to that of STO. The STO thin film is expected to grow epitaxially on NGO $(001)_c$, being the lattice mismatch - 1.2 %. In Figure 6.1a, the zoom of a θ-2θ scan on STO/NGO (001) shows that the out-of-plane parameter of the STO unit cell is larger than that of the NGO substrate ($2\theta_{STO} < 2\theta_{NGO}$). In complete θ-2θ scan (not shown), only substrate and STO (00*l*) reflections were seen. The evaluation of the out-of-plane parameter is performed as previously described for LCMO films (Ch4), and the value is found to be $c_{STO} = 3.953$ Å, which is higher than the bulk value ($a_{STO} = 3.905$ Å) and in agreement with the expected out-of-plane expansion due to the tensile stress imposed by the substrate. In Figure 6.1b it is shown a XRR measurement of a STO film, deposited

during 100 min, on the NGO $(001)_c$ substrate. From the minima (and maxima) positions, the thickness is determined to be of 20 nm, and thus the growth rate of STO under the used experimental conditions is estimated to be 0.2 nm/min.

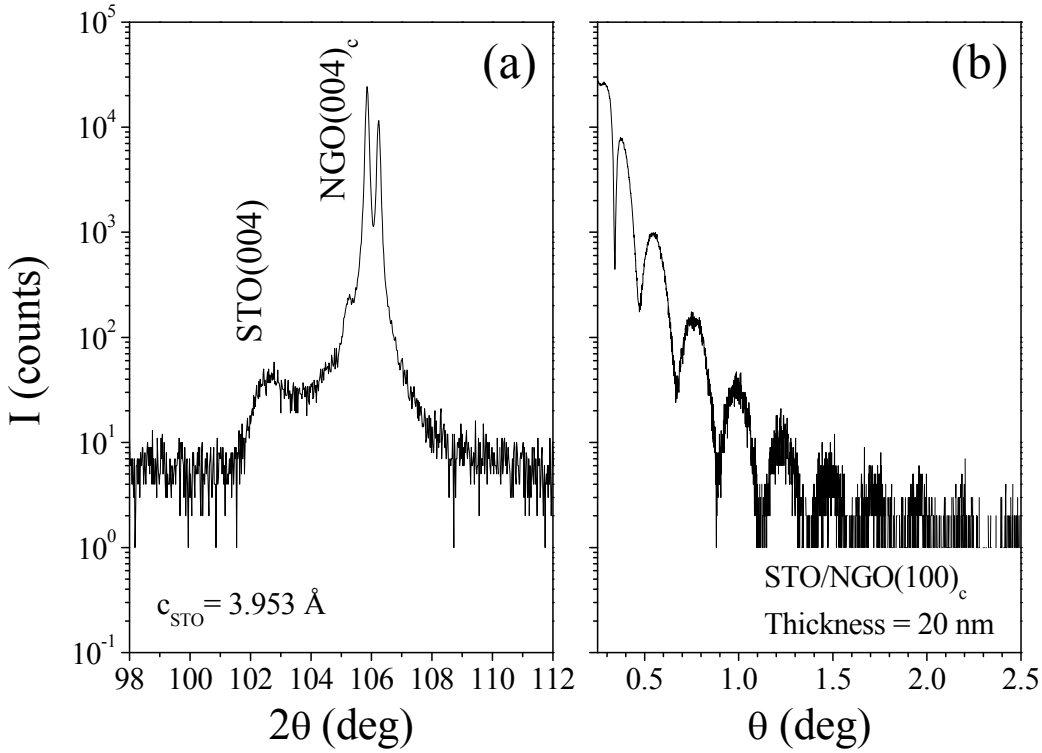

Figure 6.1. (a) Zoom of the θ-2θ scan performed on the very same film. STO c axis is found to be expanded, as expected since the film is under compressive epitaxial stress. (b) XRR measurement on a STO/NGO $(100)_c$ sample. From the calculated thickness (20 nm) and deposition time (100 min), growth rate is found to be 0.2 nm/min.

Turning now to bilayer preparation, STO layers with thickness (*t*) from 0.85 to 5 nm were prepared. Also, thicker STO layers of ~ 14-27 nm were grown on LCMO electrodes for HRTEM experiments. The substrate temperature during the STO deposition was fixed to 800 C and the deposition pressure and ratio of Ar/O was the same as those of LCMO layers (Ch2). STO thickness was controlled by the deposition time according to the calibrated growth rate.

6.1.2 Microstructure by RSMs and HRTEM

Reciprocal space maps (RSMs): no influence of STO capping layers on LCMO strain state

The unit cell parameters of LCMO (001) and (110) electrodes with and without STO capping have been determined using RSMs. In Figure 6.2 only reflections from (103) reflection for the (001) oriented samples and from (130) reflection for the (110) oriented samples are shown.

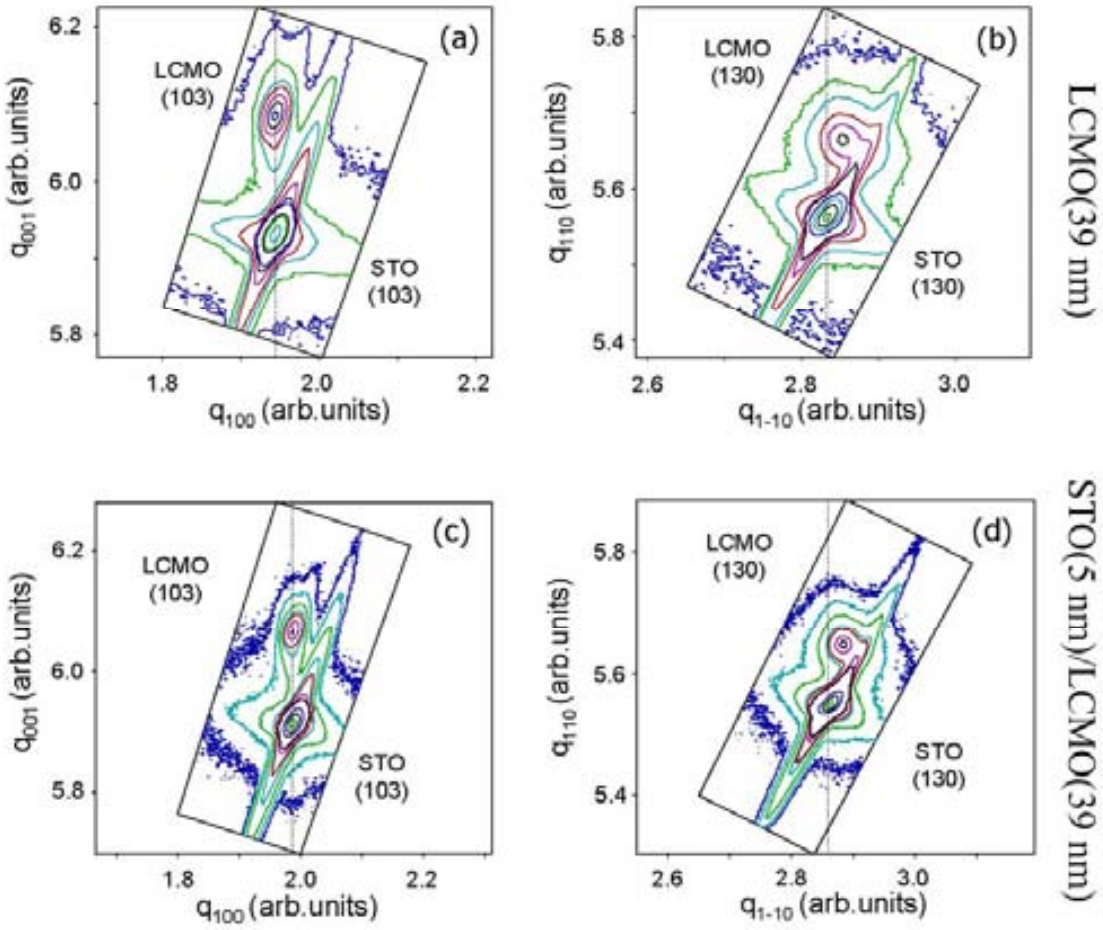

Figure 6.2. RSMs from [(a) and (c)] STO (103) and LCMO (103) reflection from (a) a single layer of 39 nm of LCMO (001) and (c) a STO(5 nm)/LCMO(39 nm) (001) bilayer. RSMs from [(b) and (d)] STO (130) and LCMO (130) reflections from (b) a single layer of 39 nm of LCMO (110) and (d) a STO(5 nm)/LCMO(39 nm) (110) bilayer. Each line is a guide for the eye, signaling the vertical alignment of STO and LCMO peaks.

Inspecting RSMs from (103) reflection of (001) samples (Figure 6.2a and c), we clearly observe similar results to those obtained previously in (001) films (Ch4). As observed in Figure 6.2a, the in-plane component q_{100} of the LCMO reflection and that of the STO reflection are vertically aligned, meaning that the film is fully strained. The

analysis of RSM corresponding to the (001) bilayer (Figure 6.2c), the strained state of the STO capped LCMO is very similar to that of single LCMO layer (Figure 6.2a). In fact, STO substrate and LCMO reflections in the (001) bilayer RSM are almost aligned. The values of the unit cell parameters of the (001) LCMO unit cell in the single film and bilayer are summarized in Table 6.2. Only a very small variation of the in-plane and out-of-plane parameters is measured, but from its magnitude (~ 0.1 %) it can be included within the experimental limits of the X-ray diffraction setup (error ~ 0.5 %).

Table 6.2. Unit cell parameters of 39 nm LCMO electrode with and without STO capping layer. Values are extracted from RSMs of (103) reflection for the (001) samples and of (130) and (222) reflections for the (110) samples.

	(001)			(110)	
	$d_{100}=d_{010}$ (Å)	d_{001} (Å)	$d_{1\text{-}10}$ (Å)	d_{001} (Å)	d_{110} (Å)
LCMO(39nm)	3.905	3.806	3.879	3.900	3.837
STO(5nm)/LCMO(39nm)	3.903	3.807	3.876	3.896	3.836
$(d^{bilayer}_{hkl}- d^{film}_{hkl})/d^{film}_{hkl}$ (%)	-0.05	0.03	-0.05	-0.10	-0.03

Concerning the results on (110) samples, the RSMs acquired from (130) reflection are shown in Figure 6.2b and d. In this case, the in-plane direction is [1-10] one. As presented in Ch4 (Figure 4.8), for the thickness of the (110) LCMO electrode studied here (t = 39 nm), LCMO unit cell grown on (110) STO is partially relaxed, and thus the in-plane component $q_{1\text{-}10}$ is not completely aligned with that of the STO substrate (Figure 6.2b). A similar unit cell deformation as in the case of the single LCMO layer is found for the STO capped LCMO electrode. A summary of the corresponding (110) LCMO unit cell parameters is shown in Table 6.2. As in the (001) case, the variations of the LCMO unit cell parameters with and without capping are within the limits of the technique, thus the same strain state is observed for the (110) LCMO unit cell before and after STO capping.

We conclude that the STO capping of up to 5 nm on LCMO layers grown on (001) and (110) STO substrates does not change the corresponding strain state of the LCMO unit cell upon the limits of detection of the used RSMs.

HRTEM images: microstructure and interfaces

Using thicker STO capping layers, we have studied the microstructure and the interfaces in STO/LCMO//STO (001) and (110) bilayers. TEM sample preparation as well as the HRTEM images and corresponding analysis were performed by S. Estradé and they are part of her PhD thesis.

Results on a STO/LCMO//STO(001) bilayer are presented in Figure 6.3. The cross section HRTEM images were acquired along the [100] zone axis. The bilayer is formed by a LCMO bottom layer of 21.3 nm covered by a STO layer 14.6 nm. In Figure 6.3a, the STO layer/LCMO electrode interface is seen, whereas in Figure 6.3b it is LCMO electrode/STO (001) substrate one which is shown. Both interfaces are sharp and coherent. Within the resolution of the image, no defects are detected. Fast Fourier transforms (FFTs) from STO (Figure 6.3i) and LCMO (Figure 6.3ii) layers and that from STO (001) substrate (Figure 6.3iii) confirm the cube-on-cube epitaxial relationships between both layers and the substrate STO(001[100])/LCMO(001)[100]//STO(001)[100].

The HRTEM images corresponding to a STO/LCMO//STO(110) bilayer are presented in Figure 6.4. The images were acquired along the [1-10] zone axis. The bilayer is formed by a LCMO bottom electrode of 21.5 nm covered by a STO layer 27 nm. Interfaces are seen in Figure 6.4a (STO layer/LCMO electrode) and in Figure 6.4b (LCMO electrode/STO (110) substrate). As in the case of the (001) bilayer, the interfaces in (110) one are abrupt and coherent, and defects are not observed in the films. FFT's from STO (Figure 6.4i) and LCMO (Figure 6.4ii) layers and from STO (110) substrate (Figure 6.4iii), provided the confirmation of cube-on-cube epitaxial growth in this heterostructure: STO(110)[1-10]/LCMO(110) [1-10]//STO(110) [1-10].

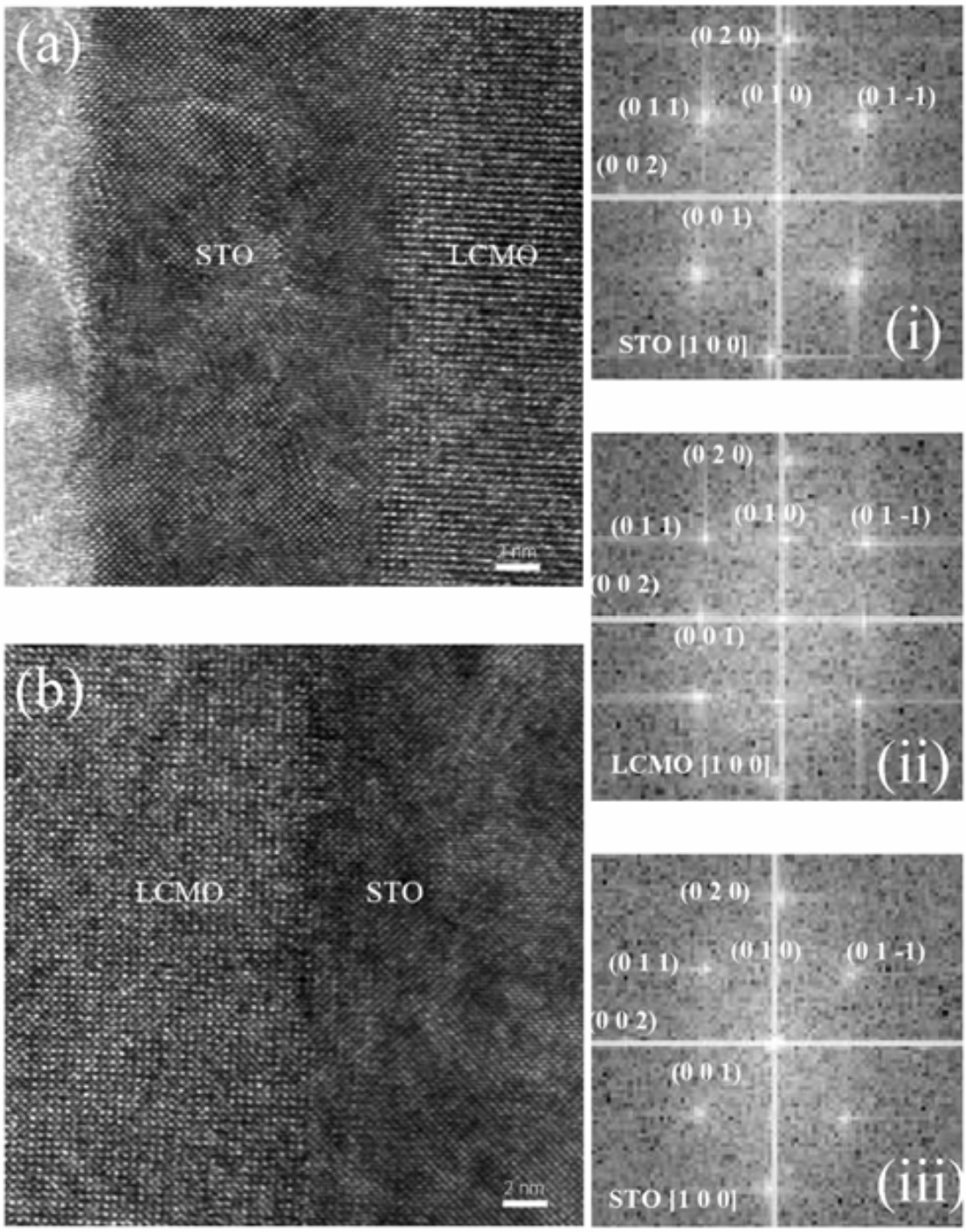

Figure 6.3. Cross section HRTEM images from a STO/LCMO/STO(001) bilayer along the [100] zone axis. Details (a) on the STO film/LCMO interface and (b) on the LCMO/STO(001) substrate interface. Corresponding FFTs calculated from (i) STO layer, (ii) LCMO film and (iii) STO (001) substrate are shown.

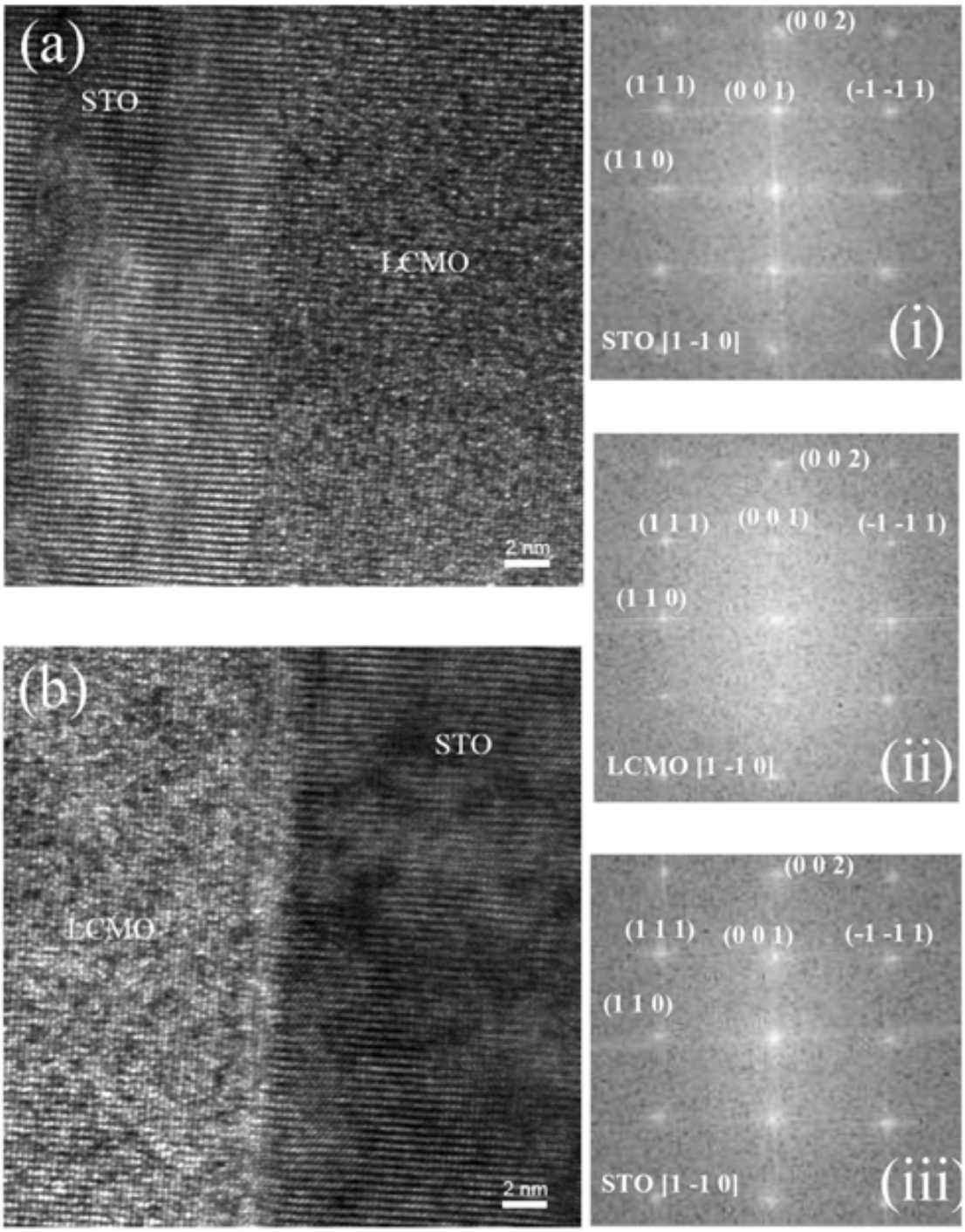

Figure 6.4. Cross section HRTEM images from a STO/LCMO/STO(110) bilayer along the [1-10] zone axis. Details (a) on the STO film/LCMO interface and (b) on the LCMO/STO(110) substrate interface. At the right, corresponding FFTs calculated from (i) STO layer, (ii) LCMO film and (iii) STO (110) substrate.

In conclusion, the inspection of the HRTEM images by cross section of (001) and (110) STO/LCMO bilayers indicates that the microstructure of these heterostructures do not present defects and their interfaces are highly abrupt.

6.2 Influence of STO capping in the magnetic and electronic properties of LCMO electrodes

With the aim of studying the influence of insulating capping layers on (001) and (110) oriented manganite electrodes, we have characterized the magnetic and electronic properties of LCMO electrodes with and without STO capping layers. To perform this study, single LCMO electrodes and STO/LCMO bilayers have been grown, fixing the thickness of the underneath LCMO electrode to 39 nm. Bilayer samples have been grown with different STO thickness, and we have compared their properties to those of single LCMO electrodes. The samples used (electrodes and bilayers) are listed in Table 6.3, and we also indicate the substrate temperature for the LCMO deposition and the corresponding thickness of the LCMO and STO layers.

Table 6.3. List of electrodes and bilayers used in this section. For each substrate and STO thickness, two samples were grown simultaneously, as indicated.

Samples	Substrate	LCMO thickness (nm)	T_d (LCMO) (C)	STO thickness (nm)
070110A1 & A2	STO(001)	39	800	0
070109B1 & B2	STO(110)	39	750	0
070116A1 & A2	STO(001)	39	800	2
070115B1 & B2	STO(110)	39	750	2
070125A1 & A2	STO(001)	39	800	4
070117B1 & B2	STO(110)	39	750	4
070118A1 & A2	STO(001)	39	800	5
070119B1 & B2	STO(110)	39	750	5

From the characterization of this series of samples it follows that the magnetic properties of (001) and (110) capped electrodes are found to evolve differently when the STO capping layer thickness increases, revealing a gradual reduction of the saturation magnetization for the (001) ones. Electronic properties are studied combining ^{55}Mn nuclear magnetic resonance (NMR) and X-ray photoelectron spectroscopy (XPS). NMR experiments highlight that electronic phase separation in (001) electrodes is enhanced by the presence of the $SrTiO_3$ capping layer and XPS measurements show that the electronic state of interfacial Mn ions from (001) electrode is more sensitive to the capping layer. We present these results separately and afterwards we will discuss them in order to shed light into the nature of the differential effect of the STO capping layer depending on the sample orientation.

6.2.1 Magnetic properties: depressed magnetic properties in STO capped (001) LCMO electrodes

To investigate the magnetic properties of bare LCMO electrodes and STO capped ones, we have measured the magnetization dependence on field at low temperature and the temperature dependence of magnetization of these samples using SQUID magnetometry. In these experiments, the magnetic field was applied in the sample plane and along the same crystallographic direction for each series of samples, being for (001) samples along [100] direction and for (110) samples along [001] direction.

In Figure 6.5, the magnetization dependence on field measured at 10 K of bare electrodes and capped ones is shown. As expected from the previous analysis of the magnetic properties of (001) and (110) LCMO films (Ch5), higher values of magnetization are obtained for the bare (110) electrode than for the (001) one of the same thickness. Also, at a fixed STO thickness, this statement is valid for all pair of (001) and (110) capped electrodes. Turning to the data of (001) samples, comparing the bare electrode magnetization curve to those of capped electrodes (Figure 6.5a), we observe a trend to depressed magnetization upon increasing STO thickness in the (001) samples. On the other hand, (110) samples (Figure 6.5b) show a much weaker dependence of their magnetization on STO thickness. Investigating the high field region of these curves (around H ~ 20 kOe), we have extracted the saturation magnetization (M_S) of the samples and the results are summarized in.Table 6.4. Using as references the magnetization values of the bare LCMO electrodes, for each orientation it has been calculated the relative decrease of M_S as a function of the STO capping. Remarkably, a variation of a ~ 11 % of M_S is measured when comparing the (001) 5 nm STO capped electrode and the corresponding (001) one, whereas for the same couple of samples but grown of (110) orientation the M_S decrease reaches only a ~ 4 % value.

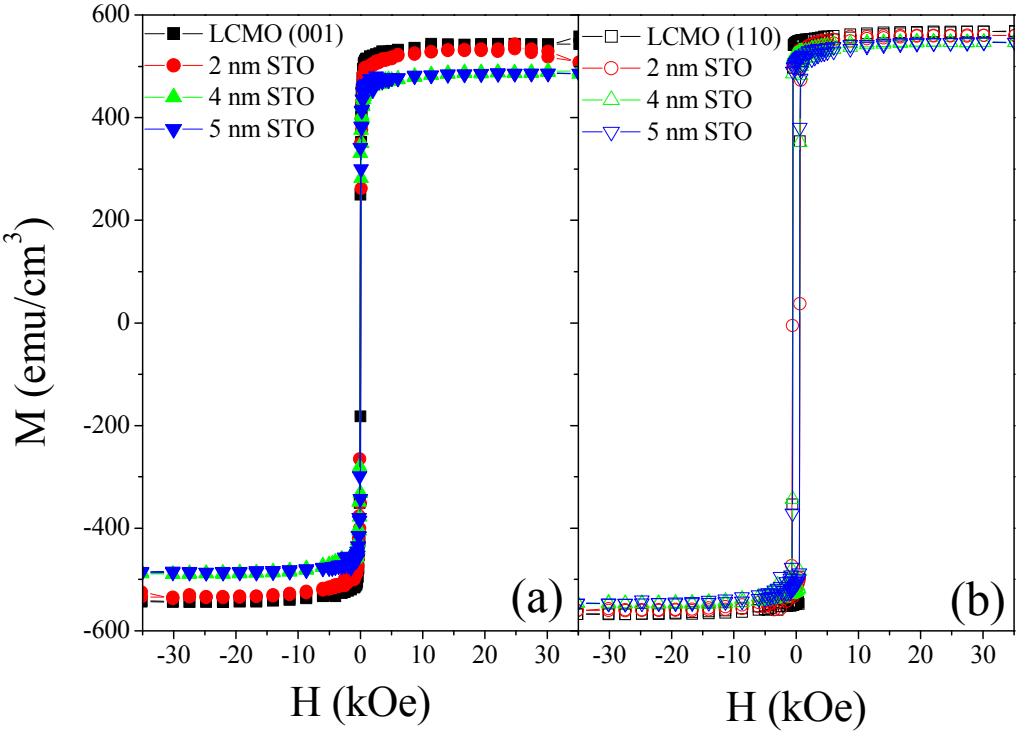

Figure 6.5. Magnetization *vs* field measurements carried out on bare LCMO electrodes (squares) and STO capped ones, with corresponding STO thickness of 2 nm, (circles), 4 nm (up triangles) and 5 nm (down triangles). The curves shown in (a) correspond to (001) samples and those in (b) to (110) samples.

Table 6.4. Saturation magnetization (M_S) of (001) and (110) samples as a function of the STO capping thickness. Bare LCMO electrodes correspond to 0 nm of STO thickness. Referred to the measured M_S of the (001) and (110) LCMO bare electrodes, the relative reduction of M_S for each capped electrode is also shown. The dead layer increase is calculated using the reduction of M_S and the LCMO thickness (39 nm).

STO thickness (nm)	(001)			(110)		
	M_S (emu/cm^3)	Reduction M_S (%)	Dead layer increase (nm)	M_S (emu/cm^3)	Reduction M_S (%)	Dead layer increase (nm)
0	543	0	0	570	0	0
2	530	2.39	0.93	560	1.75	0.68
4	489	9.94	3.88	548	3.86	1.51
5	484	10.87	4.24	546	4.21	1.64

The temperature dependence of magnetization of bare electrodes and STO capped ones is shown in Figure 6.6. For these measurements the applied magnetic field was 5 kOe. As it was deduced from magnetization dependence of field (Figure 6.5), the magnetization of (001) electrodes drops as the STO capping thickness increases (Figure

6.6a) whereas in the case of (110) electrodes the magnetization of capped electrodes is much less affected (Figure 6.6b). As expected from the results shown in Ch5, the ferromagnetic transition of the (001) bare electrode is much lower than that of the (110) one. The corresponding Curie temperature (T_C) values are $T_{C\ 001} \sim 180$ K and $T_{C\ 110} \sim 256$ K. More information about the ferromagnetism of the capped electrodes can be extracted from the shape of the magnetization curves. Inspecting the curves from the (001) capped electrodes (Figure 6.6a), we notice that the magnetic transition becomes slightly wider as the STO capping increases, which is a signature of the existence of poorly ferromagnetic or non-ferromagnetic Mn phases that decrease the ferromagnetic interactions at lower temperature. On the other hand, no relevant change on the abruptness of the transition is observed in the corresponding curves (110) capped electrodes (Figure 6.6b).

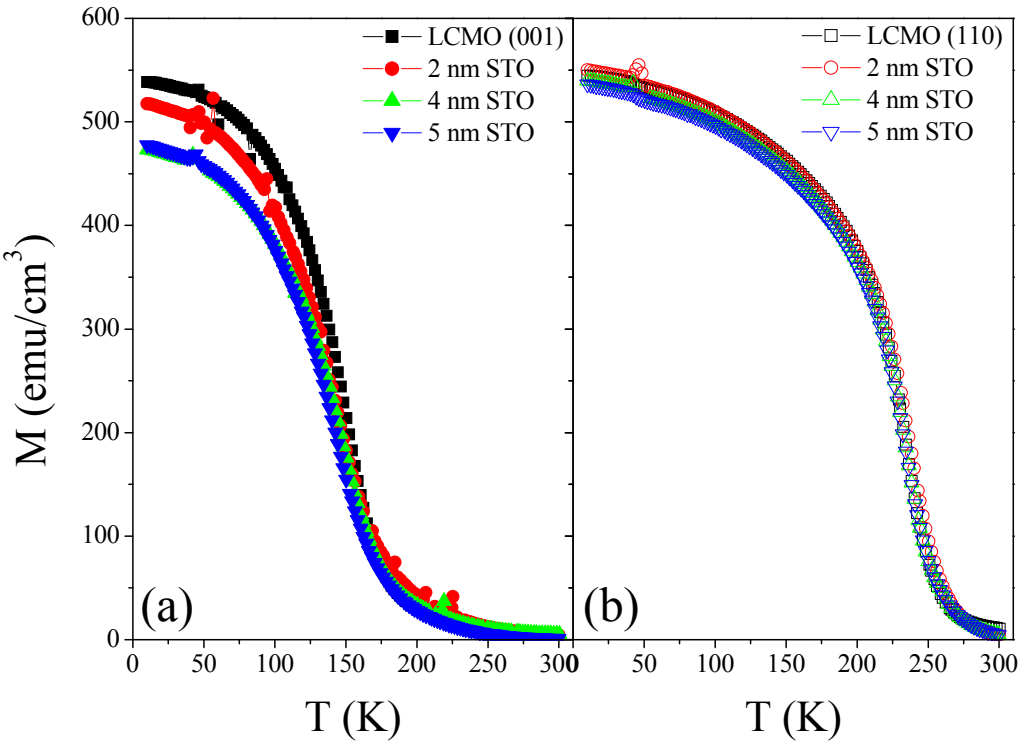

Figure 6.6. Temperature dependence of magnetization measured at 5 kOe on bare LCMO electrodes (squares) and STO capped ones, with corresponding STO thickness of 2 nm, (circles), 4 nm (up triangles) and 5 nm (down triangles). The curves shown in (a) correspond to (001) samples and those in (b) to (110) samples.

6.2.2 ^{55}Mn NMR experimental results: increase of electronic phase separation in STO capped (001) LCMO electrodes

The electronic state of Mn ions in bare and capped electrodes has been studied by ^{55}Mn NM. The experiments were carried out and analyzed by Dr. M. Wojcik at the Institute of Physics, Polish Academy of Sciences (Warszawa). Figure 6.7 presents the NMR spectra of the (001) [(a) and (c)] and the (110) [(b) and (d)] samples.

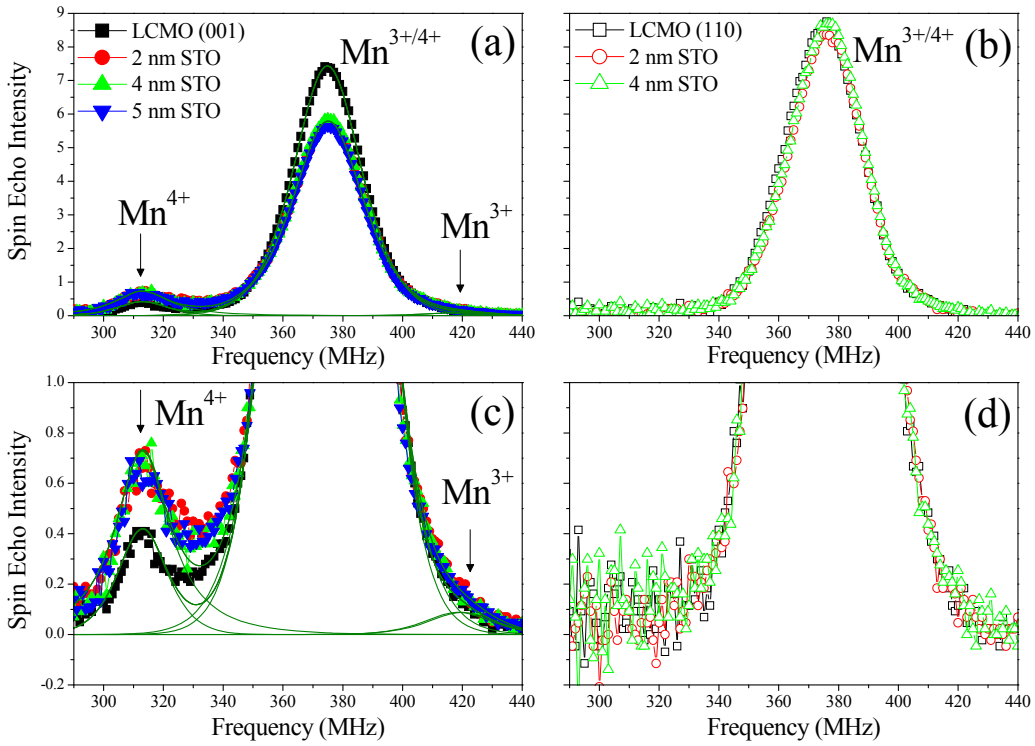

Figure 6.7. NMR spectra from [(a) and (c)] (001) and [(c) and (d)] (110) single LCMO electrodes and STO capped ones. The total NMR spectra are shown in [(a) and (b)] and low intensity region of the same spectra is zoomed in [(c) and (d)].

The dominating line corresponds to the mixed valent $Mn^{3+/4+}$ state, appearing at a frequency (ν) of $\nu \sim 375$ MHz. This $Mn^{3+/4+}$ state is related to the averaged ^{55}Mn hyperfine field created by electron-holes fast motion over manganese sites Mn^{4+}-Mn^{3+}, which is a linked to the existing double-exchange mechanism. Inspection of the (001) spectra (Figure 6.7a) reveals the presence of a broad peak at lower frequency ($\nu \sim 315$ MHz) and of smaller intensity, which is much clearly seen in the zoom shown in Figure 6.7c. This secondary line is attributed to the existence of localized ferromagnetic Mn^{4+} state and thus of electronic phase separation. As we have previously explained (NMR analysis in Ch4), electronic phase separation has been

repetitively found in (001) manganite films grown under different conditions [1][2]. Still studying the (001) spectra (Figure 6.7c), their slight asymmetry at high frequency ($\nu \sim 420$ MHz) signals the existence of another ferromagnetic state of Mn, which corresponds to localized Mn^{+3} one [3]. However, the intensity of this NMR resonance does not appreciably change by the presence of a capping layer which may be due to the very fast relaxation reported for Mn^{3+} state. On the other hand, the (110) spectra are clearly symmetric (Figure 6.7b and d), presenting only the $Mn^{3+/4+}$ line and therefore no electronic phase separation is expected in these (110) electrodes.

Table 6.5. Total intensity of the NMR spectra [I(total)] extracted from the NMR spectra obtained on the (001) and (110) samples, together with the intensities of the $Mn^{3+/4+}$ [I(Mn3+/4+)] and of the Mn^{4+} [I(Mn4+)] lines measured on the (001) samples. The calculated ratios of the Mn^{4+} and $Mn^{3+/4+}$ intensities of the NMR spectra of (001) samples are shown.

STO capping thickness (nm)	(001)					(110)	
	I(total) (arb. units)	I(Mn3+/4+) (arb. units)	Dif(Mn3+/4+) (%)	I(Mn4+) (arb. units)	Ratio(Mn4+) (%)	I(total) (arb. units)	Dif(Mn3+/4+) (%)
0	235.0	226.0	0	10.1	10.1	287.7	0
2	210.5	191.9	-15.09	18.6	18.6	285.5	-0.76
4	209.5	192.4	-14.89	17.1	17.1	273.8	-4.85
5	203.3	186.0	-17.72	17.3	17.3		

Investigating the (001) spectra (Figure 6.7a and c), capped electrodes show a clear decrease on the intensity of the dominant double-exchange $Mn^{3+/4+}$ line intensity as well as an increase of the Mn^{4+} one. We have performed Gaussian-Lorentzian fits of the $Mn^{3+/4+}$ and Mn^{4+} lines of the (001) samples, as well of the $Mn^{3+/4+}$of the (110) ones. The resulting fits are also included in Figure 6.7 (lines). From these fits, a quantification of the expected $Mn^{3+/4}$ and Mn^{4+} population in these samples can be extracted taking into account that the area of each resonant line is directly related to the amount of the corresponding phase present in the sample. The total intensity of the NMR spectra as well as the intensities of the $Mn^{3+/4+}$ and Mn^{4+} contributions to the NMR spectra for the (001) and (110) samples are summarized in Table 6.5. We include in Table 6.5 the difference between the $Mn^{3+/4+}$ intensity from each capped electrode and that of the corresponding electrode: $Dif(Mn^{3+/4+})=[I(Mn^{3+/4+})_{capped}-I(Mn^{3+/4+})_{bare}]/I(Mn^{3+/4+})_{bare}$. These values are also indicated in Table 6.5 and provide important information about the loss of the ferromagnetic and metallic $Mn^{3+/4+}$ ions in the capped electrodes. Upon

increasing STO thickness, in the (001) case the $Mn^{3+/4+}$ intensity is strongly affected, and for 5 nm of STO capping the reduction is of ~ 17 %. The (110) case is much different, with a $Mn^{3+/4+}$ intensity drop of only ~ 5 % for the electrode with STO capping thickness of 4 nm. Besides to this analysis of the $Mn^{3+/4+}$ intensity, we can evaluate the ratio of the Mn^{4+} to $Mn^{3+/4+}$ phases in all the (001) electrodes from the corresponding intensities of the Mn^{4+} and $Mn^{3+/4+}$ lines as a function of STO thickness: $Ratio(Mn^{4+})=I(Mn^{4+})/I(Mn^{3+/4+})$ %. The calculated values are included in Table 6.5. From the ~ 4 % of Mn^{4+} phase separation observed in the bare electrode, all capped electrodes suffer an increase of this separated phase towards a final ~ 8 %. On the other hand, as already observed from the investigation of the NMR spectra, higher values of $Mn^{3+/4+}$ line areas are obtained for the (110) samples, and only a small drop of the $Mn^{3+/4+}$ intensity upon increasing the STO capping thickness is detected.

The analysis of NMR spectra signals not only the occurrence of electronic phase separation in bare (001) electrodes, but also the increase of this phenomenon upon increasing the STO capping thickness. Indeed, the lowering on the $Mn^{3+/4+}$ ferromagnetic and metallic ions is also promoted by the STO capping in both (001) and (110) capped electrodes, but the effect is enhanced in the (001) samples. Thus, the STO capping is strongly promoting the electronic phase separation in (001) electrodes, whereas the electronically homogeneous (110) electrodes are much less affected by the capping.

6.2.3 XPS experimental results: study of the Mn electronic state near the STO/LCMO interface

To study the interface composition, we performed XPS experiments on bare electrodes and STO capped ones using the PHI 5500 Multitechnique System (Physical Electronics) as described in Ch2. The surface sensitivity of this technique has served to inspect the top layers of the LCMO electrodes in the bare electrodes but also those underneath the ultrathin STO capping layers. A sketch of the XPS experiments is shown in Figure 6.8d. Using the displayed configuration, we have access to the Mn ions using thin STO layers up around 4 nm. Focused in the study of the Mn core levels, we have extracted information about the electronic state of the Mn ions near the interface by acquiring X-ray photoemission spectra from Mn 3s and Mn 2p core levels.

Although in the explored manganites it is expected a strong hybridation between the Mn and O core levels, we can use a simple ionic picture to understand the interest in the Mn 3s core level. For core levels with orbital moment l = 0, so-called s core levels, after a photoelectron emission process takes place, the remaining electron of the s-core level strongly interacts with the outer unfilled shells. From the photoelectron emission process, one of the electrons of the s-shell leaves it and the one remaining is stringly coupled to the electrons of the open shells. The final state of the ion is not uniquely defined, and instead of achieving the relaxed state E_1, it can remains in an excited one E_2, being $E_2 > E_1$. The kinetic energy KE of an emitted photoelectron will be consequently affected by the difference between E_1 and E_2. Thus, if a photoelectron is emitted from an ion that finally relaxes or from another one that remains excited, the corresponding KE will be different and two peaks will appear in the photoelectron spectra. The lower binding energy (BE) peak will correspond to the photoelectrons from relaxed final states (higher KE) and the higher BE peak will correspond to those from the excited final states (lower KE).

For the case of 3d transition metals, the energetic difference (energy splitting) between the final states of the X-ray photoelectron emission spectra depends on two factors: the local spin of the initial state (ion before the photoelectron emission) and the magnitude of the overlapping of the 3s and 3d orbitals given by the corresponding Slater integral [G^2(3s,3d)]. The local spin of the initial state *S* is determined by the spin configuration of the open 3d shell ground state. Following with the analysis of the Mn 3s core level, for one electron of the Mn 3s with spin s = ½, it can be coupled either parallelly or antiparallelly to the outer Mn 3d shell. Mn^{3+} ground electronic state is $1s^2 2s^2 2p^6 3s^2 3p^6 3d^4$, and with the $3d^4$ electrons coupled parallelly among them (S = 2) and also to the electron of the 3s shell, final value of local spin of he initial state will be *S* = 5/2. Analogous calculus can be performed for a Mn^{4+} ion, with ground state $1s^2 2s^2 2p^6 3s^2 3p^6 3d^3$ (S = 3/2), and thus the parallel coupling of 3d electrons and the 3s one leads to *S* = 2. The calculated energy splitting (ΔE_{3s}) is proportional to the Slater integral [G^2(3s,3d)] and the local spin *S*, and following Van Vleck [4], it is predicted:

$$\Delta E_{3s} = (2S+1)\frac{G^2(3s,3d)}{5} \qquad [6.1]$$

The XPS measurements of 3d metal compounds show that the experimental ΔE_{3s} values double the predicted ones, indicating that other effects as the intrashell correlations (between 3p and 3d levels) [5] and charge transfer processes (between 3d

and 3s levels) [6] contribute to increase ΔE_{3s}. In any event, following the simple picture presented in eq. 6.1, the spin state and thus the valence of the local 3d ion determines the energy splitting ΔE_{3s}. Conversely, it is possible to determine the valence of the 3d ion from the observed splitting ΔE_{3s}. In manganites and other Mn oxides, Mn 3s core level has been previously studied by XPS, and it has been probed the usefulness of the study of the energy splitting on the Mn 3s core level to determine Mn valence or the corresponding S value [7][8][9][10].

The Mn 3s photoemission spectra are shown in Figure 6.8a. For any Mn 3s photoemission spectrum, the main peak corresponds to the high spin state and the satellite to the low spin state. The measured energy splitting values ΔE_{3s} are collected in Figure 6.8c. First, from the analysis of the Mn 3s spectra of the bare electrodes (Figure 6.8a, squares) we observe that for the given experimental XPS configuration no relevant differences are found in the free top layers of the (001) and (110) LCMO electrodes. Upon capping with STO layers (circles and triangles corresponding to 2 nm and 4 nm of STO capping, respectively), the Mn 3s photoemission spectrum intensity decreases, as expected from the limited mean free path of the photoelectrons emitted from the underneath Mn ions.

To inspect the evolution of the energy splitting of the LCMO electrodes when increasing STO capping thickness, a zoom of the Mn 3s satellites is shown in Figure 6.8b. From the bare electrodes to the 4 nm STO capped electrodes, we find a clear trend towards higher binding energies, and thus towards higher energy splitting, arising from both (001) and (110) STO/LCMO interfaces. We have fitted the experimental data using the software Multipak V6.0A provided by Physical Electronics. We have used Gaussian-Lorentzian and iterated-Shirley functions to fit each photoemission peak and the background, respectively. The final fits are shown in Figure 6.8a and b (lines). The relative position of the Mn 3s satellite (vertical lines in Figure 6.8b) can be extracted from these fittings. The increase of the STO capping thickness induces a shift of the satellite position towards higher binding energies. Remarkably, this effect is stronger in (001) capped electrodes (close symbols, dashed lines) than in (110) ones (open symbols, solid lines).

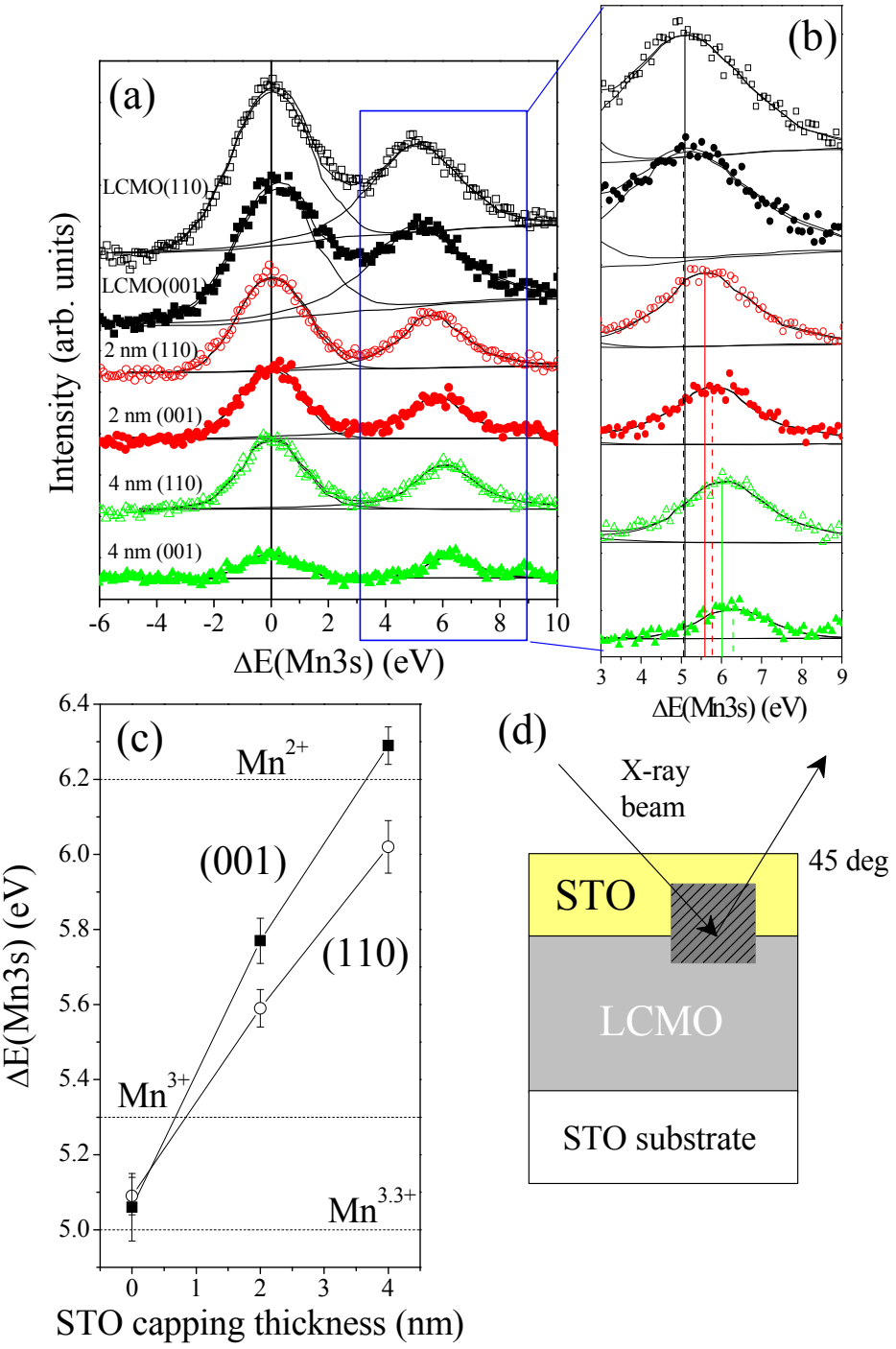

Figure 6.8. (a) Mn 3s X-ray photoelectron emission spectra of (001) (close symbols) and (110) (open symbols) LCMO electrodes without STO capping (squares) and with 2 nm (circles) and 4 nm (triangles) of STO capping. Lines are Gaussian–Lorentzian fits and iterated-Shirley background. (b) Zoom of the satellites of (a), vertical lines indicating the corresponding energy position. (c) Energy splitting of the Mn 3s spectra as a function of the STO capping thickness and sample orientation. (d) Sketch illustrating the XPS experiment.

The increase of the Mn 3s energy splitting is understood as a signature that reduced Mn ions are detected [7][8][9][10]. Thus, we proceed to evaluate the Mn valence as a function of the STO capping thickness and orientation from the energy position of the Mn 3s satellites. In Table 6.6 we summarize the experimental values of the binding energies of the Mn 3s peaks and the energy splitting. As already mentioned in the analysis of Figure 6.8a and b, higher energy splitting ΔE(Mn 3s) is measured upon the STO capping thickness increases for both (001) and (110) samples, being much relevant in the (001) case. Furthermore, the reduction of the Mn valence should imply the lowering of the binding energy of the main Mn 3s peak [E(Mn 3s)]. Data in Table 6.6 agrees with this argument, and the E(Mn 3s) values decrease as the STO capping thickness increases. In Figure 6.8c the Mn 3s energy splitting is plotted as a function of the STO capping thickness. The energy reference for the Mn^{2+}, Mn^{3+} and mixed-valent $Mn^{3.3+}$ ions are extracted from the linear fit to the experimental values included in Ref. [9]. From the Mn 3s energy splitting of bare electrodes, which corresponds formally to the ideal $Mn^{3.3+}$ ions, we detect Mn^{2+} ions as the STO capping thickness rises. This monotonic evolution of the Mn formal valence is caused by: (i) the diminished contribution to the collected spectra of the electrons emitted from deeper LCMO unit cells; and (ii) the formation of a thicker insulating STO layer with more rigid electronic bands, which may promote stronger electrostatics effects at the interface. We will discuss deeply on this topic in next section.

Table 6.6. Binding energies of Mn 3s core level corresponding to the main peak [E(Mn 3s)] and to the satellite [E(Mn 3s sat)]. The energy splitting [ΔE(Mn 3s)] is also shown. The error in ΔE(Mn 3s) has been calculated from the statistic error associated to the fits.

STO capping thickness (nm)	(001)			(110)		
	E(Mn 3s) (eV)	E(Mn 3s sat) (eV)	ΔE(Mn 3s) (eV)	E(Mn 3s) (eV)	E(Mn 3s sat) (eV)	ΔE(Mn 3s) (eV)
0	85.48	90.54	5.06±0.09	85.18	90.27	5.09±0.05
2	85.10	90.87	5.77±0.06	85.07	90.66	5.59±0.05
4	84.94	91.23	6.29±0.05	84.71	90.73	6.02±0.07

We turn now to the study of Mn 2p spectra. We recall first that, for core levels with non-zero orbital momentum l ($l \neq 0$), their corresponding electrons experiment a coupling of their orbital l and spin s momentum through the spin-orbit interaction. For a p core level, $l = 1$ and the available values of the total angular momentum j are splitted

into two: for parallel *l* and *s* momentums $j = 3/2$, and for antiparallel ones $j = ½$. The energy of the electrons is consequently affected by the *j* value, having lower binding energies the electrons characterized by a higher *j* value. In the XPS experiment, the photons can interact with these populations of electrons with different binding energy, and the effects are observed in the XPS spectra as the arising of two peaks separated by a characteristic energy (spin-orbit energy splitting).

Figure 6.9 shows the experimental Mn 2p photoemission spectra. We analyze first the main characteristics of spectra of the bare electrodes compared to those of 2 nm STO capped ones in Figure 6.9a. The binding energy in both (001) and (110) electrodes as well as the splitting is the same as that expected for an intermediate state $Mn^{3+/4+}$ [11], thus indicating that within the experimental conditions for detection (Figure 6.8d) similar Mn electronic states are expected in the last LCMO unit cells. In the case of the spectra from capped electrodes, we observe a shift of the core levels towards lower binding energy similarly to the experimental results on the Mn 3s main peaks (Table 6.6) as the STO capping thickness increases. The origin of the energy shift in the Mn 2p core level is attributed to a change in the overall charge on the Mn ion, with reduced Mn sites [12]. Moreover, in the (001) capped electrode (close circles) another contribution marked by an arrow appears at ~ 5 eV of the $Mn2p_{3/2}$ peak, likely to be a shake up peak related to the presence of reduced Mn ions (Mn^{2+}) [10]. On the other hand, the (110) capped electrode spectrum (open circles) does not present evidence of this secondary contribution, and a smaller energy shift in Mn 2p binding energy (-0.15 eV) is observed compared to (001) counterparts (-0.20 eV). In Figure 6.9b and c show the Mn 2p normalized spectra of the complete series of bare and capped electrodes with (001) and (110) orientation, respectively. The normalization allows observing more clearly the appearance of a shake-up satellite, much pronounced in the 4 nm STO capped electrodes. A qualitative evaluation of the spectra of (001) and (110) capped electrodes signals that the reduction happens in both cases, but the relative intensity of the shake-up satellite to that of the Mn $2p_{3/2}$ is higher in the (001) case. From these results, we conclude that the contribution of Mn^{2+} phases in these spectra is more relevant in the (001) capped electrodes and thus a more reduced interface is expected in the (110) capped electrodes.

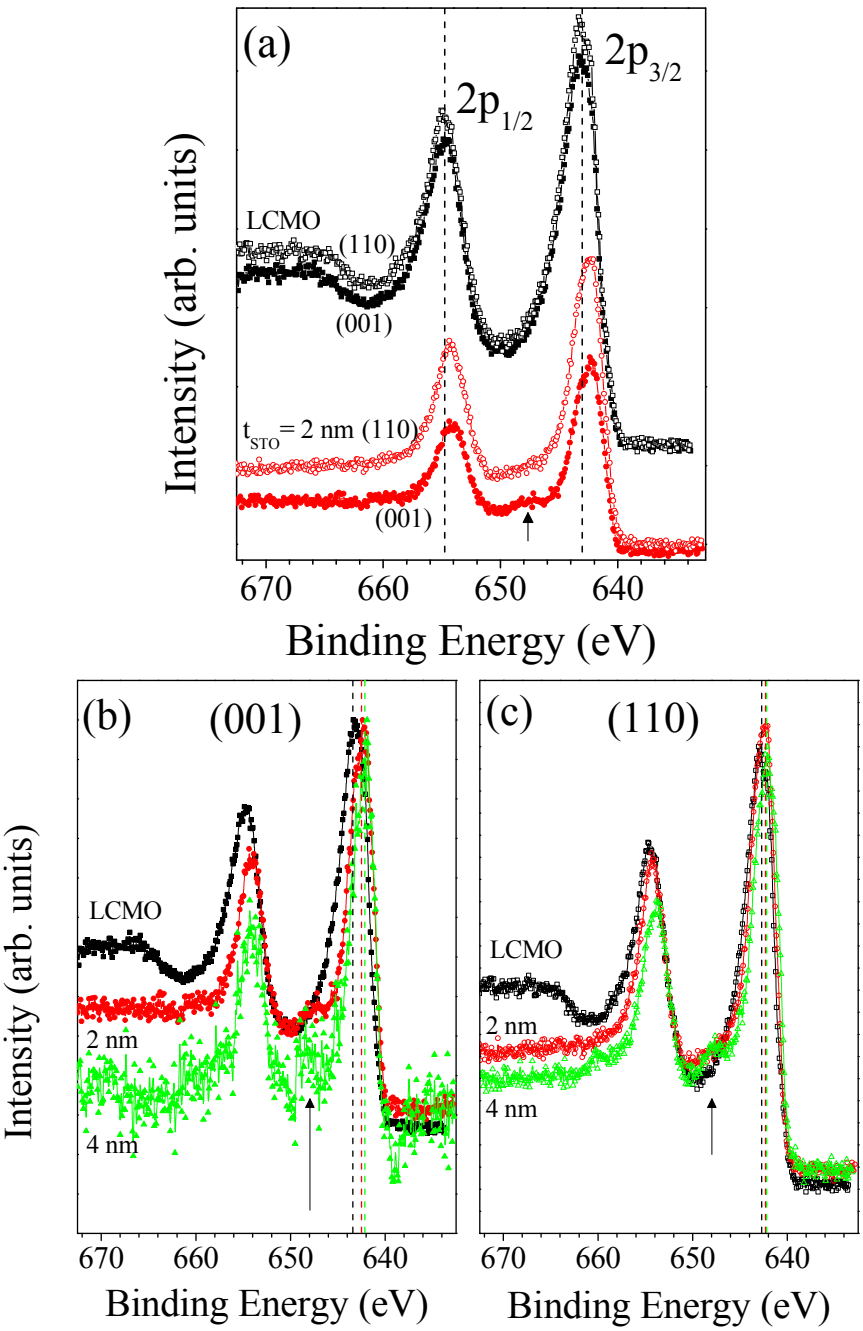

Figure 6.9. X-ray photoelectron emission spectra of Mn 2p core level of (001) (close symbols) and (110) (open symbols) LCMO electrodes without STO capping (squares) and with 2 nm (circles) and 4 nm (triangles) of STO capping. Vertical lines indicate the binding energy of Mn $2p_{3/2}$ peaks and arrows mark the Mn^{2+} satellite. In (a) the spectra are shifted in the y-axis. In [(b) and (c)] the spectra are normalized to the intensity of Mn $2p_{3/2}$.

Discussion

The physical phenomena arising at the interfaces between manganite and insulating layers in epitaxial heterostructures has received much attention since the functionality of future spintronics devices using these materials will strongly depend on them. Among the variety of heterostructures investigated, the most commonly ones have been those combining La-manganites and $SrTiO_3$ (STO) insulating layers. Grown either in superlattices [13][14] or in bilayer or trilayer heterostructures [15][16][17][18], in all cases the properties of the La-manganites layers present depressed magnetic and electronic properties, which increased upon thicker STO or thinner La-manganite layers are grown. The origin of this depression has been attributed to the loss of spin-polarization at the interface region, understood as the formation of clusters of separated phases either ferromagnetic (FM) or antiferromagnetic (AFM) [13][14], as the occurrence of charge transfer with hole doping from the adjacent STO layer towards the La-manganite one [15][17] or as the loss of the oxygen octahedron symmetry [16][18]. Theoretical studies of the magnetic surface states in La-manganites/STO interfaces [19][20] signal that the STO insulating layer enhances the carrier confinement in a two dimensional slab at the interface, which promotes the AFM coupling of the last La-manganite unit cells to the underneath FM film.

Our results on STO/LCMO (001) and (110) heterostructures indicate that upon STO capping the magnetic and electronic properties of LCMO layers get relevantly depressed in the (001) case. From the structural characterization of these bilayers (Figure 6.2), we have observed that the LCMO unit cell parameters are not affected by the presence of the STO capping layer, thus we can rule out any contribution of the strain to this depression. The different experimental evidences highlight the sensitivity of the (001) LCMO layer to the presence of the STO capping layer:

(1) The increase of the STO thickness layer promotes a clear depression of the saturation magnetization (M_S) in (001) samples (Table 6.4).

(2) From NMR experiments, the electronic phase separation existing in the bare LCMO (001) electrode increases (Table 6.5).

(3) The Mn ions at the interface are reduced (Table 6.6) towards Mn^{2+}.

On the other hand, few effects of the STO layer are observed in the magnetic and electronic properties of LCMO (110) layers. Although Mn^{2+} ions are detected in the (110) interfaces (Figure 6.9c), no electronic phase separation is measured by NMR

(Figure 6.7b and d) and the decrease in M_S is much lower than in the (001) case (Table 6.4).

The summary of the experimental results on STO/LCMO bilayers is shown in Figure 6.10. The induced non-FM layer values in Figure 6.10a have been calculated using the reduction ratio of M_S values in STO capped electrodes compared to those of bare electrodes (Table 6.4) and the nominal LCMO thickness (39 nm).

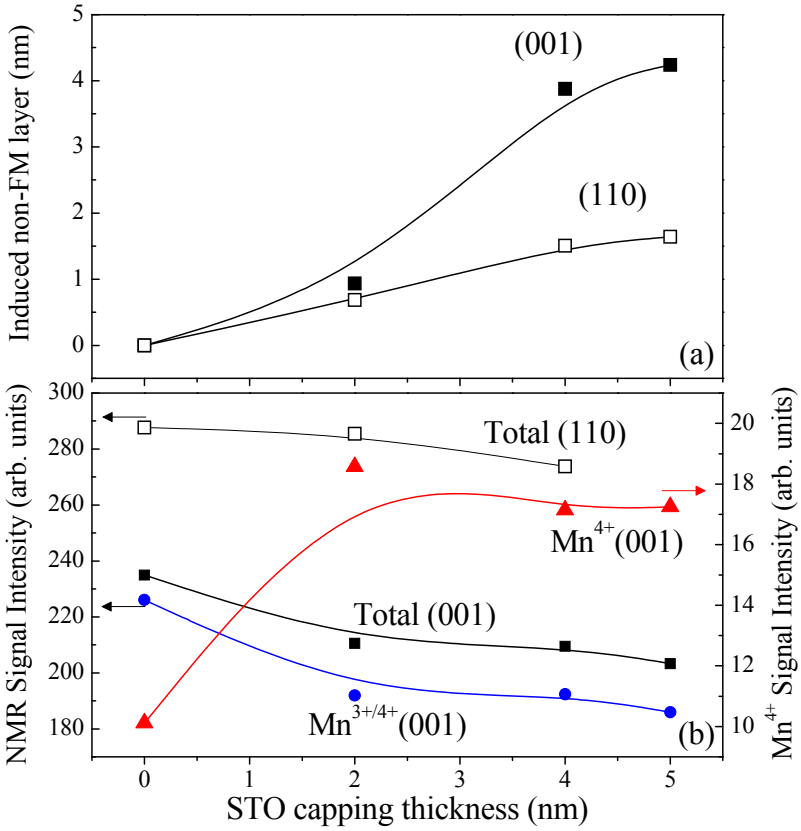

Figure 6.10. As a function of the STO capping thickness: (a) Induced non-FM layer in (001) (close symbols) and (110) (open symbols) STO capped electrodes, calculated from M_S values shown in Table 6.4; (b) Left axis: NMR signal intensity corresponding to the total spectra of (001) (close squares) and (110) (open squares) capped electrodes, together with the intensity of $Mn^{3+/4+}$ line in (001) samples (circles); Right axis: NMR Mn^{4+} signal intensity of the (001) capped electrodes (triangles).

With Figure 6.10 we can evaluate the correlation between magnetic and NMR measurements. Investigating first the dependence in STO thickness of the (110) results, we observe that a slight promotion of non-FM layer appears in (110) capped electrodes (open symbols, Figure 6.10a), which is correlated to a similar decrease in the NMR total signal (open symbols, Figure 6.10b). The nominal value of this non-FM layer is

~ 1.4 nm. However, we recall that no Mn^{4+} phases are detected in (110) capped electrodes by NMR, although at the interface Mn^{2+} ions are found by XPS. Turning to (001) samples, the induction of a non-FM layer is evident from Figure 6.10a, and up to ~ 4.2 nm of the LCMO (001) electrode becomes non-FM. NMR results (Figure 6.10b) show an increase in the Mn^{4+} phase (triangles) and an overall reduction of the total and the $Mn^{3+/4+}$ NMR intensity. Furthermore, Mn^{2+} ions were detected by XPS in these (001) capped electrodes, much significantly than in the (110) case.

The depletion of the magnetic properties of (001) La-manganite electrodes used in oxide heterostructures have been studied by many groups [13][14][15][16][17][18]. We monitor the difficulty to find conclusive remarks on the origin of these effects by analyzing some of the reported results of Koinuma's group [17][21]. In Figure 6.11 we present some of their results obtained using photoemission spectroscopy (PES) and angle-resolved PES (ARPES). In Ref. [17], they explored by PES (001) $La_{1-x}Sr_xMnO_3$ (LSMO) electrodes with doping level $x = 0.4$ and heterostructures with STO layers of different thickness (Figure 6.11a). They observed that upon the deposition of a STO layer of higher thickness, the peak at ~ 1 eV decreases in amplitude. Measuring also a LSMO film with higher doping ($x = 0.55$), they found the lowering of the ~ 1 eV peak amplitude compared to that of the $x = 0.4$ LSMO film. Their conclusions were to assign the ~ 1 eV peak to a decrease of the occupancy of the e_g levels of the Mn 3d band, which had lowered their population upon STO layer growth. On the other hand, in Ref. [21] the ARPES experiments performed on single films of (001) $La_{1-x}Sr_xMnO_3$ of varied doping ($0.1 \leq x \leq 0.4$) (Figure 6.11b) signaled the occurrence of a similar peak near the Fermi level ~ 1 eV for the same doping $x = 0.4$, but upon decreasing the doping, the peak amplitude decreased, contrary to what expected from the conclusions of Ref. [17]. In this case, the scenario proposed is that the strong electron-electron interaction of these manganites leads to a spectral weight transfer from the coherent component (peak at ~ 1 eV, related to the real occupancy of the Mn 3d band) to the incoherent component (related to the O 2p bands). Thus, we notice that for the STO/LSMO heterostructures the argument given in Ref. [17] that the STO layer can induce hole doping on the LSMO electrode needs to be revised from the results shown in Ref. [21].

The XPS study presented here is focused on Mn core levels (Mn 3s and Mn 2p), which allow a much straightforward interpretation of the physical origin of the spectra. Mn interface reduction has been also detected by electron energy loss spectroscopy

(EELS) by Maurice *et al.* [12] inspecting the interfaces of (001) $La_{0.7}Sr_{0.3}MnO_3/SrTiO_3/La_{0.7}Sr_{0.3}MnO_3$ trilayers. In this case, Mn 2p EELS spectra show a shift towards lower energies near the STO layer.

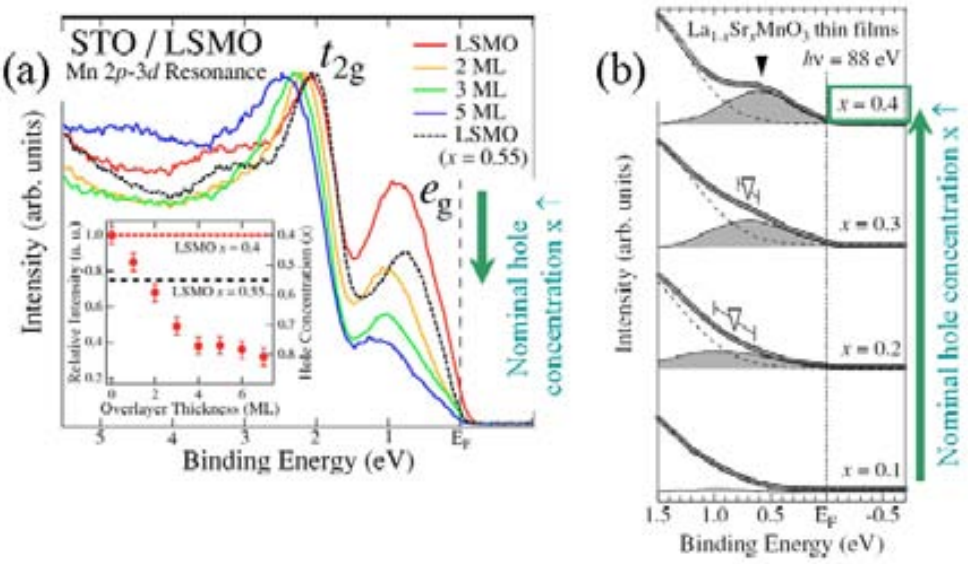

Figure 6.11. (a) Mn 3d PES spectra obtained from $La_{0.6}Sr_{0.4}MnO_3$ (LSMO) electrodes and STO/LSMO heterostructures, together with that from $La_{0.55}Sr_{0.45}MnO_3$ electrode; at the inset, the relative intensity of the eg states as a function of the STO layer thickness (from Ref. [17]). (b) ARPES of $La_{1-x}Sr_xMnO_3$ electrodes of varied doping level x (from Ref. [21]).

Our data signal the occurrence of a clear charge modification in the Mn ions at the (001) interfaces. Within the framework of the reported studies in La-manganite/STO interfaces, it has been observed that Mn reduction happens near the STO interface [12] although no explanation has been provided to this fact. On the other hand,, the common trend to consider AFM order at the interface linked to a interface hole doping still needs to be probed [17][21]. The analysis of our results indicates that a simultaneous drop of ferromagnetic itinerant $Mn^{3+/4+}$ phase and increase of the Mn^{4+} phase happens in (001) capped electrodes, as well as the formation of interface Mn^{2+} states. As reported by Alonso *et al*. [22], the Mn^{3+} disproportion in $La_{1-x}Ca_xMnO_3$ powders relieves the internal energy of the manganite in reducing conditions, and $2Mn^{3+/4+}$ ions may lead to Mn^{4+}-Mn^{2+} ions. This scenario can explain the increase of Mn^{4+} and appearance of Mn^{2+} states near the (001) interface. In any event, for the optimally doped LCMO electrodes any change on the doping (by holes or electrons) leads to a decrease in the magnetic properties and to an increase of the electronic phase separation. We have clearly observed that the (001) interfaces are highly sensitive compared to (110) ones, The fact that a charge discontinuity happens in the (001) STO/LCMO interface may

promote the charge redistribution, which is not the case of (110) interfaces. The reduction process at the STO/LCMO interface may be linked to the oxygen net, which is expected to have a different symmetry within the (001) and (110) planes, or it can be caused by the removal of interfacial oxygen due to oxygen gathering from the STO capping layer.

To summarize this topic, we have studied the magnetic and electronic properties of (001) and (110) STO capped LCMO electrodes. The STO capping layer favors the electronic phase separation of (001) electrodes, strongly reducing their saturation magnetization, whereas much lower influence is observed in (110) interfaces. The detection of Mn^{2+} ions at the (001) and (110) interface suggests that the oxygen content of the interface is influenced by the STO insulating layer. The distortion of the symmetry of the oxygen lattice in the (001) STO/LCMO interfaces can be at the origin of the depleted magnetic properties of these heterostructures, leading to a preferential loss of oxygen in the (001) interface. We suggest that this effect may be less relevant in the (110) interface We cannot rule out that other effects, as the charge discontinuity between (001) LCMO and STO perovskite planes, may enhance the charge redistribution, contributing to the Mn reduction and electronic phase separation.

6.3 Functional properties of STO/LCMO bilayers: study of the tunneling conduction by Conducting-AFM

Before the integration of epitaxial STO/LCMO bilayers into magnetic tunnel junctions (MTJs), it is mandatory to confirm that tunneling conduction is possible through the used bilayers. Furthermore, more relevant information can be obtained from the study of the tunneling parameters, and the knowledge of the barrier height energy in the insulator/electrode system may lead to deduce the future interval of the necessary voltage range for the device functionality.

Within this framework, we have studied the tunneling conduction in STO/LCMO bilayers grown on (001) and (110) STO substrates. The results shown here correspond to two series of bilayers, a first series with 19 nm LCMO electrodes and a second series with 70 nm LCMO electrodes. The thickness of STO barriers varies between 0.4 to 3.4 nm (~1 to 9 u.c.).

Prior to present the experimental data and their analysis, some comments about tunneling conduction through oxide heterostructures are necessary. Electric transport through a thin insulating layer is a characteristic feature of tunnel devices, such as magnetic tunnel junctions or spin filters. Besides structural and electronic wave-function symmetry matching [23][24] and barrier thickness (*t*), the conductance of a tunnel barrier is critically determined by the energies of its barrier heights (ϕ), which correspond to the energy difference between the Fermi level in the electrodes and the bottom of the conduction band in the insulator. This is the key parameter for the detailed understanding of the transport process across the MTJ and for optimal design and operation.

Epitaxial nanometric STO and MgO layers are being considered as tunnel barriers in spintronics devices. Most commonly, ϕ is determined from the analysis of the current-voltage I(V) characteristics of the junction, after multilayer growth and subsequent lithography processing, which may modify the junction properties. An I(V) curve of a MTJs averages the response over the junction area, losing information on local variations of conductance. Given the exponential dependence of current over barrier thickness, unknown local variations of barrier conductance could dominate transport properties of the junction leading to large error on the future analysis. Moreover, the I(V) curves differ subtly depending on voltage regime or, more precisely, on the eV/ϕ ratio which is, *a priori,* unknown. It turns out that the reliability of the ϕ values may be questionable. Some of these difficulties may be behind the significant scattering of reported values for ϕ (STO) in MTJs made using manganites as electrodes (50 meV [25], 0.5-0.7 eV [26], and 1.2 eV [27]) as well as for MgO (0.39 eV [23] and 2.4-3.6 eV [28]).

Conducting atomic force microscopy (C-AFM) allows obtaining maps with nanometric resolution of the topography and simultaneously of the electrical current when a voltage is applied between a bottom electrode and the conducting tip [29][31][32][33][34][35]. Besides, in principle, the homogeneity of thin insulating layers on electrodes can be investigated from these maps and from spectroscopic I(V) measurements. Indeed, C-AFM has been used to evaluate ϕ in magnetic tunnel junctions with Al_2O_3 as barrier. Local I(V) measurements [32][33][34] or histograms from current maps [35][36][37] were used for this purpose. Both methods rely on fitting, using a suitable model, a single measurement, either an I(V) curve or a current histogram from a

C-AFM image, to extract ϕ. We note however that the current flow is largely determined by the ill-defined contact area and the barrier thickness and their possible spatial fluctuations [38], thus leading to large error on determination of ϕ.

An original method to overcome these difficulties has been developed and now introduced. It is based on the accurate resistance mapping of nanometric barriers. Details on the C-AFM set-up are in Ch2 and in Ref. [37].We have measured the electric resistance under different conditions of bare LCMO electrodes and STO/LCMO bilayers grown on (001) and (110) STO. The results shown here are obtained from the samples listed in Table 6.7, and the corresponding layer thickness is also included.

Table 6.7. List of samples used for the C-AFM experiments. The thickness of the LCMO and STO layer is also indicated.

Sample	Substrate	Sample	Substrate	LCMO thickness (nm)	STO thickness (nm)
050929A3	STO(001)	050929B3	STO(110)	17	0
050713A	STO(001)	050713B	STO(110)	19	0.85
050705A	STO(001)	050705B	STO(110)	19	1.7
050707A	STO(001)	050707B	STO(110)	19	2.55
050706A	STO(001)	050706B	STO(110)	19	3.4
051125A	STO(001)			73	0
051129A	STO(001)			73	0.4
051128A	STO(001)			73	1.2
051126A	STO(001)			73	2.0

The section is organized as follows:

1. Explanation of the method.
2. Application of the procedure to (001) bilayers. Evaluation of the insulating properties of STO layers and considerations on the tunneling process to estimate the barrier height energy.
3. Application of the procedure to (110) bilayers.
4. Final results on the evaluation of the barrier height and on the applicability of the method.

6.3.1 C-AFM procedure

The procedure can be simply explained as follows: instead of analyzing local I(V) curves or conductance histograms from a single bilayer, the originality of the method relies on the use of C-AFM resistance maps of samples with different barrier thickness and using different bias conditions. From the maps, a mean resistance value has to be determined for each sample, making sure that the experimental conditions are

exactly the same in all cases. It requires that the applied force has to be exactly the same as well as similar ambient conditions. The process done is as follows:

(1) Scan of a reduced area of the sample using a force F1.

(2) Subsequently scan of a larger area which includes the previous one, with a force F2 (F2 < F1).

Typical scan sizes were (500x500) nm^2 for (1) and (3x3) μm^2 for (2). The same surface is then scanned again in a (500x500) nm^2, and a measurement is accepted to be correct if there are no significant changes of resistance in the region scanned twice. An example is shown in Figure 6.12. The rectangle marked on the (3x3) μm^2 images (Figure 6.12b) shows the previously (500x500) nm^2 scanned area (Figure 6.12a).

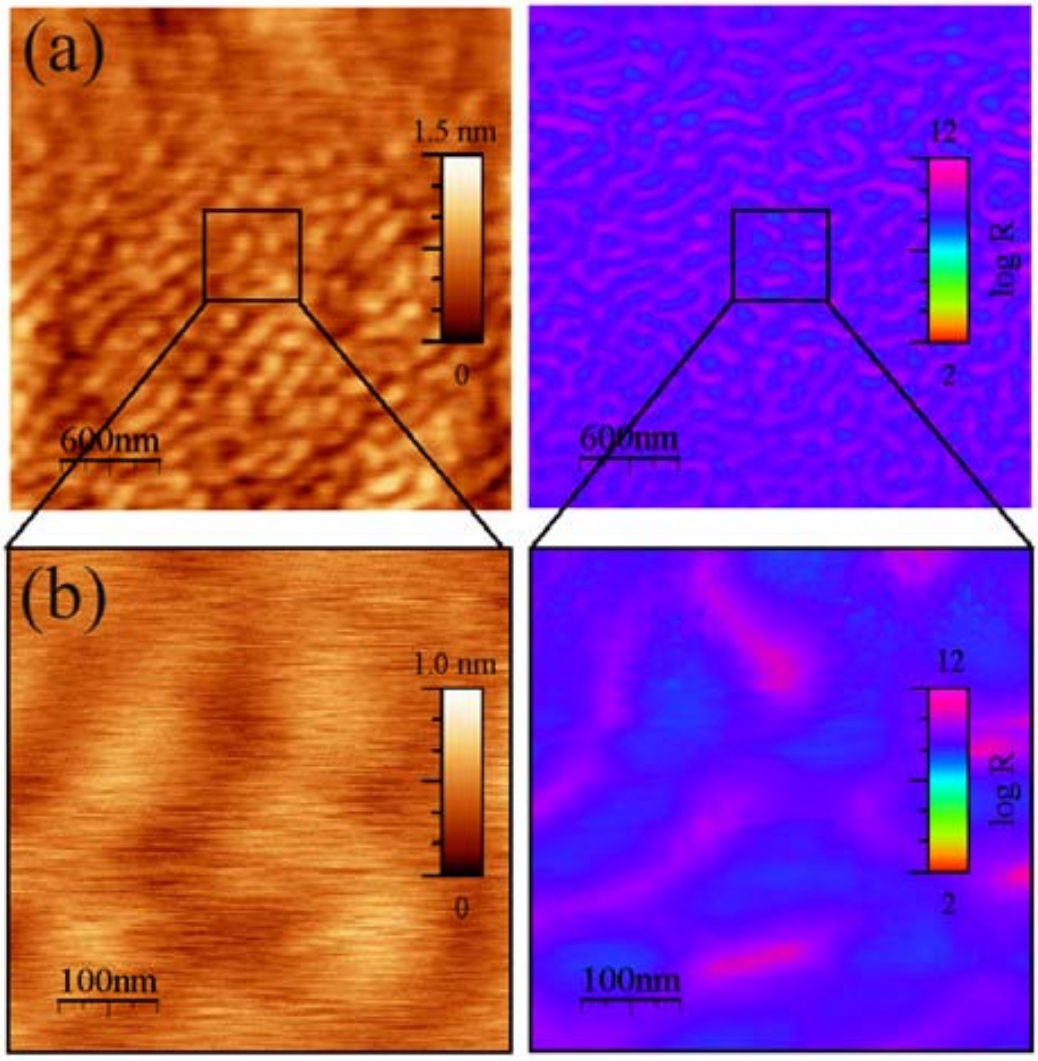

Figure 6.12. Topography (left) and resistance CAFM maps (right) corresponding to a (001) bilayer of t_{STO} = 2.0 nm and with the LCMO electrode of 73 nm. In panel (a), (3x3) μm^2 scans obtained after bottom panel (b) (500x500) nm^2 scans were performed. The rectangles on panel (a) mark the previously scanned area shown on panel (b). Scales are included in the right side of each image, and the resistance unit is Ω.

6.3.2 (001) bilayers

In Figure 6.13 the topographic and resistance maps corresponding to the (001) 19 nm LCMO electrode and to the (001) bilayers with thickness from t_{STO} = 0.85 to 3.40 nm are shown. The resistance maps were recorded with a bias of 2 V. The topographic images acquired simultaneously as well as measurements by tapping mode (not shown here) reveal very flat surfaces, with the presence of unit cell steps and two-dimensional islands, with a low roughness in all the samples below 0.5 nm (rms). Although the surface roughness is quite similar in all these samples, they show huge differences in the electrical resistance. This fact can be realized observing the corresponding histograms of the electrical resistance. In Figure 6.14, histograms from the bare electrode and from the bilayers with barrier thickness of 0.85, 1.70, 2.55 and 3.40 nm are shown. It is noted:

(1) Histograms can be discriminated one from another.

(2) Bilayer histograms are slightly broader than that of the electrode.

(3) Mean value resistance of the samples increases very rapidly, by 5 orders of magnitude, with a range of barrier thickness from 0 to 3.40 nm.

All these factors imply that the local variation of thickness in a given sample is below the interval in STO thickness between the prepared samples, which is of about 2 u.c. Explained with another words, histograms in Figure 6.14 show that the most probable resistance [maximum of the resistance histogram (R_m)] of each sample clearly shifts to higher resistance with t_{STO}, thus it can be used as a parameter to characterize the barrier. In the case of maps shown in Figure 6.13, acquired with a bias of 2 V, the resistances extracted from the corresponding histograms shown in Figure 6.14 are $1.4x10^6$, $3.2x10^7$, and $6.3x10^{10}$ Ω for t_{STO} = 0, 0.85 and 3.40 nm samples, respectively.

Similarly to maps in Figure 6.13, which were acquired with a bias of 2 V, other maps were acquired in the same samples with bias of 1 and 3 V. The extracted values of $R_m(t)$ from maps acquired at these three bias (1, 2 and 3 V) are shown in Figure 6.15a. The conductance through the barrier is increased by three orders of magnitude when increasing bias from 1 to 3 V. When plotting the resistance values it is found that their dependence on barrier thickness corresponds to an exponential increase, attesting the tunneling mechanism in the electrical transport. Different tunneling regimes can occur depending on the bias and the barrier thickness and energy height. Electric tunneling current obeys different dependences on the bias determined by a series of parameters of

the system, as it is the electron affinity and the thickness of the insulating barrier, as well as work functions of the used electrodes. Furthermore, the value of the bias, compared to ϕ/e, is a critical factor and thus, before analyzing the data of Figure 6.15a, it is useful to estimate the expected barrier height under the actual experimental conditions.

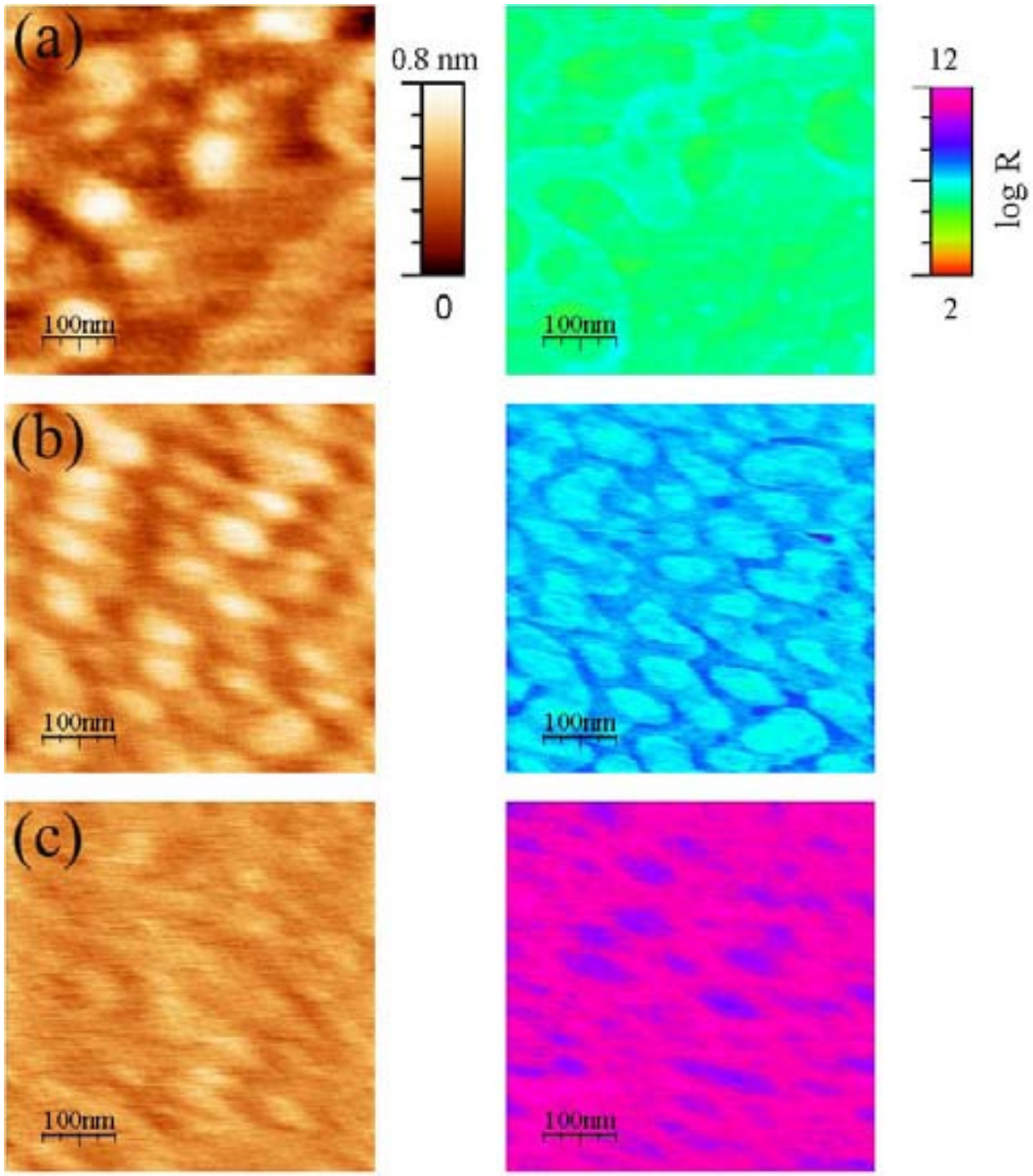

Figure 6.13. (500x500) nm^2 topographic (left) and electrical resistance maps (right) acquired with a bias of 2 V on (a) the (001) 19 nm LCMO electrode, and on (001) STO barriers (b) 0.85 nm and (c) 3.40 nm thick. Resistance maps are plotted in logarithmic scale that is shown at the right, being the resistance unit Ω.

A plot of the band structure of the AFM tip/STO barrier/LCMO electrode is shown in Figure 6.16. The sketch illustrates the case of a defect-free STO insulator and in absence of trapped charge (Schottky limit), and with the LCMO electrode positively

biased with $V > \phi_2/e$. The evaluation of the barrier height (ϕ_2) between LCMO and STO would follow the relation $\phi_2 \approx W_{LCMO} - \chi_{STO}$, being W_{LCMO} the work function of LCMO and χ_{STO} the electron affinity of STO. Since W_{LCMO} is ~ 4.8 eV [38] and χ_{STO} is ~ 3.9 eV [39], the barrier height is expected to be no larger than ~ 0.9 eV. Moreover, if interface states appear in the gap of STO [39] the barrier height could be decreased. Indeed, using the charge neutral level position for STO reported in Ref. [39], ϕ_2 is estimated to 0.75 eV. Additional barrier lowering can occur due to image charge effects [40][41].

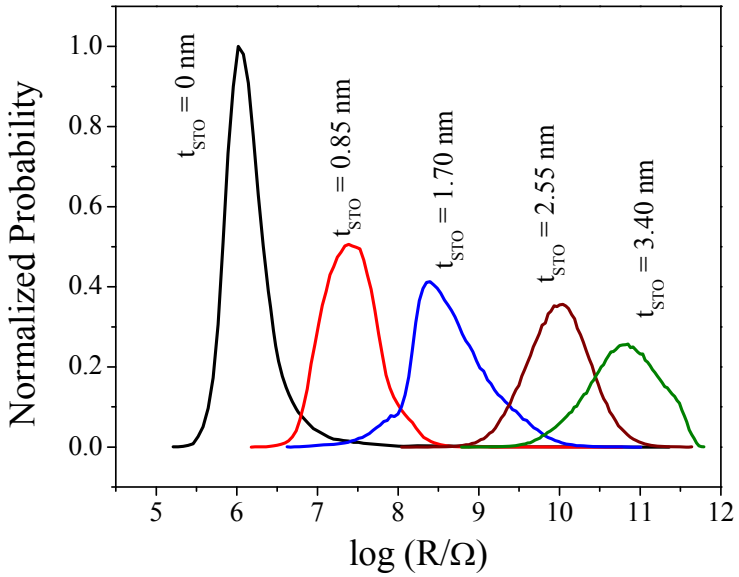

Figure 6.14. Histograms of resistance (at 2 V bias) corresponding to the (001) electrode (t_{STO} = 0 nm) and samples with t_{STO} of 0.85, 1.70, 2.55 and 3.40 nm

Now, turning to the interpretation of the tunneling process, when a bias $V > \phi_2/e$ is applied, the tunnel transport takes place through an effective barrier thinner than its nominal thickness. This regime of tunnel transport is called Fowler-Nordheim [41]. In the case assumed in the sketch shown in Figure 6.16, the electrons injected from the AFM tip to the LCMO electrode find a barrier of a height ϕ_1 that depends on the work function of the AFM tip and not on the work function of LCMO itself, and thus it can be different from ϕ_2.

Resistance maps were recorded at 1, 2 or 3 V bias, when the transport is expected to occur in the Fowler-Nordheim (FN) regime. In this limit, the dependence of I on V is given by [41]

$$I = \frac{2Ae^3}{8\pi h\beta^2 t^2 \phi_1} V^2 \exp\left(\frac{-8\pi\beta\sqrt{2m^*}\phi_1^{3/2}}{3he}\frac{1}{V}t\right) \quad [6.2]$$

where A is the contact area, β is the barrier shape correction factor, t is the barrier thickness, V is the bias voltage, and e, m*, h are the electron charge, effective mass of the electron, and Plank constant, respectively. Approximating the barrier shape to a rectangular one (β = 1),eq. 6.2 can be rewritten as

$$\ln\frac{I}{V^2} = \ln\left[\frac{2Ae^3}{8\pi ht^2\phi_1}\right] + Bt \quad [6.3]$$

with B given by

$$B = -\frac{8\pi\sqrt{2m^*}\phi_1^{3/2}}{3he}\frac{1}{V} \quad [6.4]$$

According to eq. 6.3, at a given bias voltage, ln (I/V^2) should exhibit a linear dependence in *t*, which in fact data in Figure 6.15b signal. Moreover, a careful inspection of the linear dependencies of the sets of ln (I/V^2) versus *t* clearly indicates a change in the slope (B), which gradually decreases when increasing voltage. In Figure 6.15c, B values determined from the three bias voltages of Figure 6.15b are plotted as a function of 1/V. From eq. 6.4, B *vs* (1/V) linear dependence is expected if FN regime is achieved. Thus, it is deduced from experimental data analysis of Figure 6.15c that the tunneling transport occurs in the FN regime. In addition, the slope provides a direct way to estimate $(2m^*)^{1/2}\phi_1^{3/2}$. From the B vs (1/V) slope, $\phi_1(m^*)^{1/3} \sim 0.41$ eV is determined. It is to be remarked that tunneling current depends on both m* and ϕ_1 as a product, and from these experiments an independent determination of both magnitudes is not possible. Nevertheless, an estimated value of ϕ_1 can be obtained taking into account that the effective mass in STO is $m^* \sim 6\, m_e$ [42]. Thus, the barrier height would be $\phi_1 \approx 0.23$ eV. About the value of m*, it has been emphasized by Scott [42] that while it is true that m* at the interfaces may differ from the band mass, it is not expected to be lower than the bulk value, and that it never can be treated as a fitting parameter in the analysis of tunneling data. However, m* in STO has been found to depend on carrier concentration, and thus accurate (local) values of m* are inaccessible. Assuming a limiting value $m^* \sim 1\, m_e$ [43] the upper bound estimation found for ϕ_1 is 0.41 eV. It is to be remarked that in the method used here to deduce the barrier height ϕ_1, the contact area does not contribute explicitly, in contrast with other methods described in the introduction of this section.

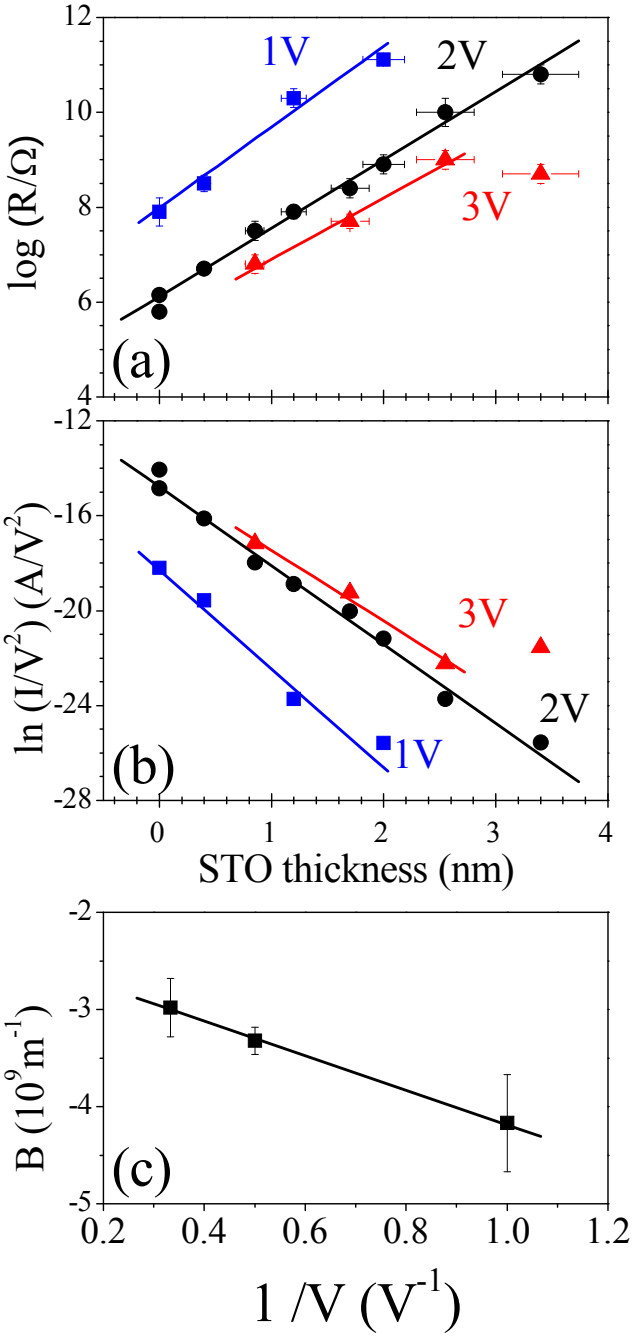

Figure 6.15. (a) Resistance of (001) samples as a function of the barrier thickness (*t*) for bias of 1, 2, and 3 V. (b) ln (I/V^2) plotted against *t* barrier thickness. (c) Factor B (slope of $\ln(I/V^2)= f(t)$) plotted against the reciprocal of the bias. Straight lines in the panels are linear fits (the value corresponding to the thicker barrier and a bias of 3 V was not included)

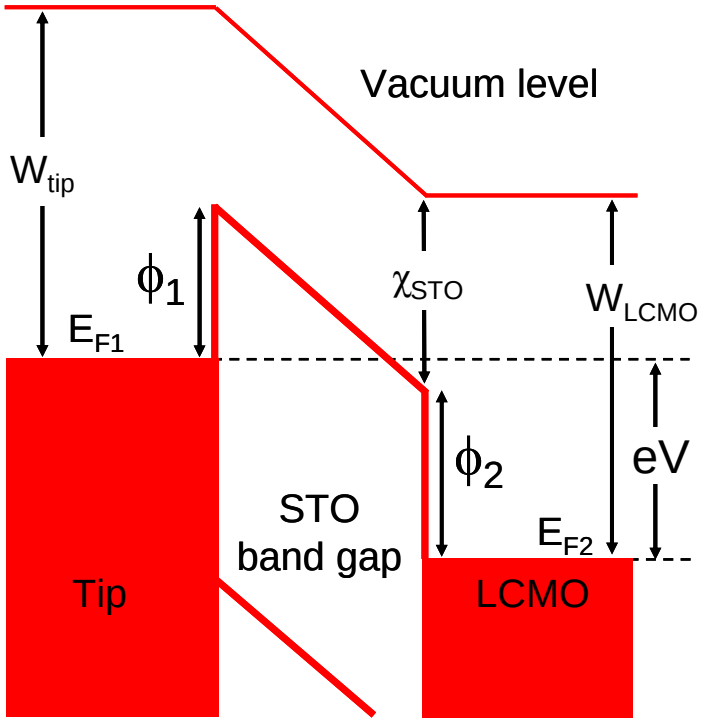

Figure 6.16. Sketch of the band structure (in the Schottky limit) of the AFM tip/STO barrier/LCMO electrode. STO electron affinity is represented by χ_{STO} and LCMO work function and AFM tip by W_{LCMO} and W_{tip}. The barrier heights are ϕ_1 and ϕ_2. It is shown the band structure being the LCMO electrode positively biased with $V > \phi_2/e$.

6.3.3 (110) bilayers

A similar characterization of the (110) bilayers has been carried out. In Figure 6.17 they are shown the simultaneously acquired topographic and resistance maps, recorded under an applied bias of 2 V, from the corresponding bare 19 nm LCMO (110) electrode and STO/LCMO (110) bilayers with barrier thickness of t_{STO} = 0.85, 1.70, and 3.40 nm. The coated tip used in CAFM measurement and the rougher surface of (110) samples contribute to lower the topographic image resolution; in spite of this, the most relevant morphologic features of film surfaces can still be observed. These features in topography are also observed in the resistance maps, due to local variations of the tip force or contact area. However, as it happened with (001) resistance maps, these topographic changes in resistance are much smaller than the average variation between STO barriers of different thicknesses.

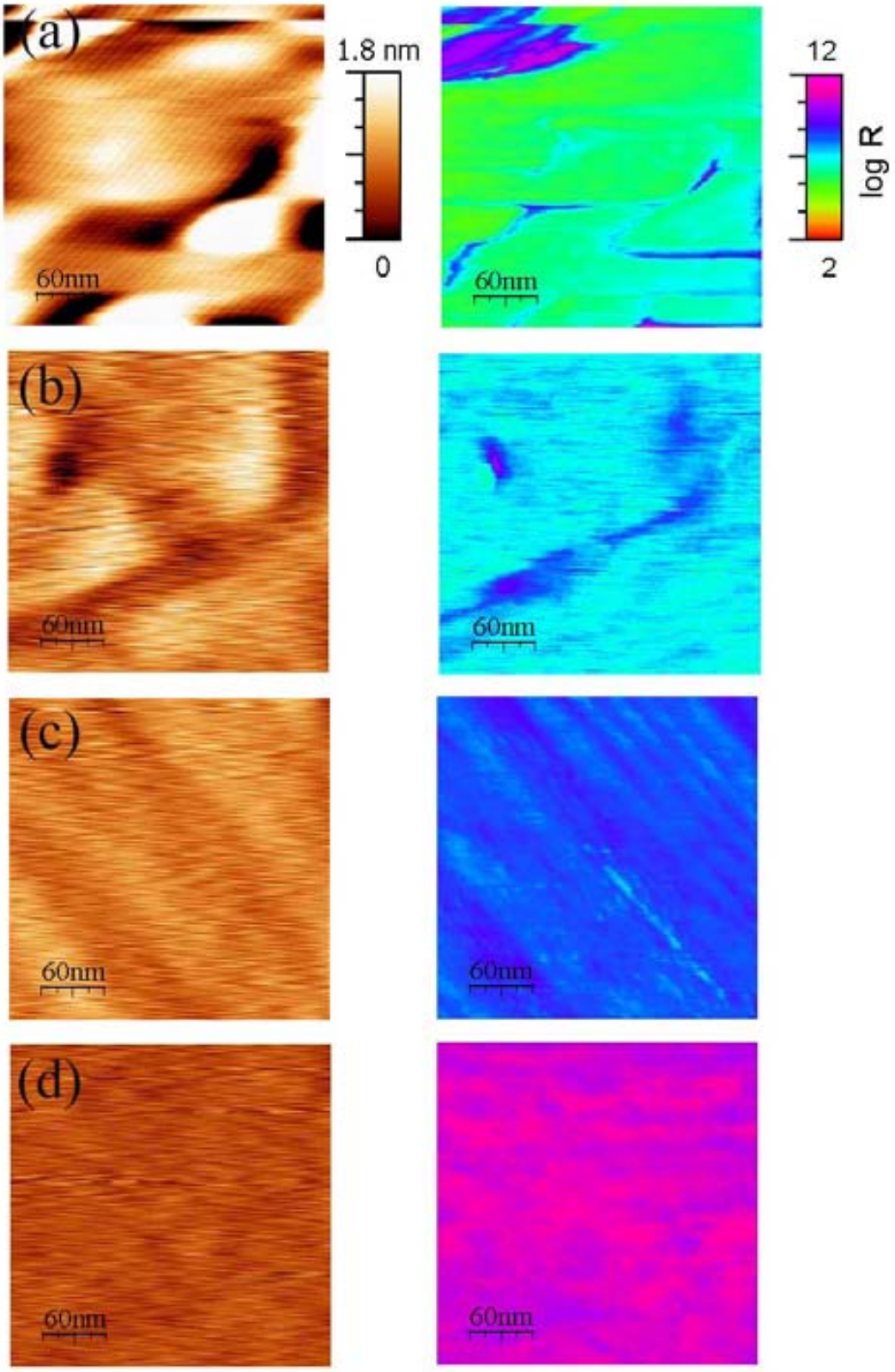

Figure 6.17. (300x300) nm^2 topographic images (left) and resistance maps (right) from (a) the 19 nm LCMO electrode, and from bilayers presenting different STO thickness: (b) 0.85 nm, (c) 1.70 nm, and (d) 3.40 nm. Resistance maps were obtained with a bias of 2 V and they are plotted in logarithmic scale, displayed at the right.

In Figure 6.18, histograms from resistance maps acquired with a bias of 2 V on the (110) electrode and (110) bilayers present similar characteristics as (001) ones. Even with an increase in thickness of nominally 2 u.c. (only 0.85 nm) from one to the next, their corresponding histograms are well separated and with a slight overlapping. Then, in the (110) bilayers too, it is possible to discriminate each histogram from one another, and it is seen that the resistance of the samples increases very rapidly, within the barrier thickness variation (from 0 to 3.40 nm). This suggests that the insulating STO layer is covering homogeneously the LCMO (110) electrode in the range of STO thickness studied, in agreement with the absence of pinholes confirmed by the topographic and resistance maps. The huge increase of the measured resistance with the thickness of the barrier is indicated by a local resistance of the order of 10^6 Ω in the bare electrode (resistance map in Figure 6.17a, histogram in Figure 6.18), increasing up to around 10^{11} Ω for the t = 3.40 nm barrier (resistance map in Figure 6.17d, histogram in Figure 6.18).

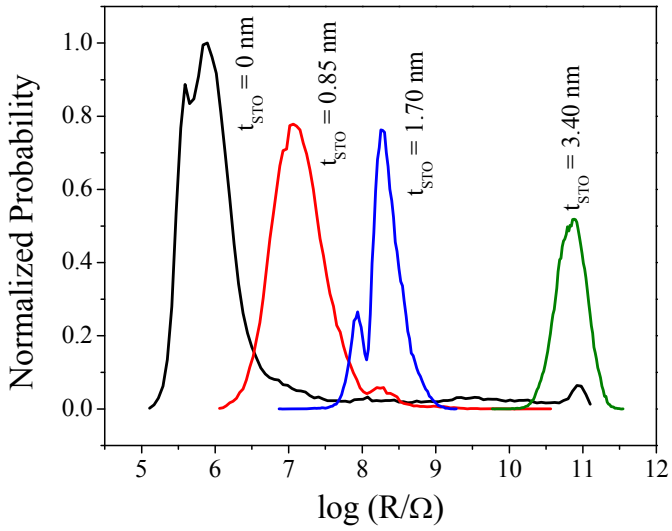

Figure 6.18. (a) Histograms of resistance for a 19 nm LCMO (110) electrode and STO/LCMO (110) bilayers (tSTO = 0.85, 1.70 and 3.40 nm) obtained with a bias of 2 V.

6.3.4 Barrier height in (001) and (110) bilayers. Conclusions on the applicability of the method

In Figure 6.19 (right axis) the corresponding R_m values (red triangles) versus film thickness are plotted. The exponential increase of resistance with STO thickness, signals that the conduction mechanism through the barrier corresponds in (110) samples

is a tunneling process. The estimation of the expected barrier height in the (001) bilayers is valid for the (110) ones too. Then, taking into account eq. 6.3, the values of ln (I/V^2) as a function of STO thickness are plotted in Figure 6.19 (left axis). The values ln (I/V^2) were calculated with the associated experimental values of R_m (Figure 6.19, right axis). The linear dependence of ln(I/V^2) on thickness is well visible, confirming the exponential dependence of (I/V^2) on barrier thickness. Differently that for (001) samples, the collected data for (110) ones did not include different bias voltage. However, a comparison with the corresponding data of ln (I/V^2) vs. *t* collected on (001) STO barriers on LCMO (001) electrodes can be done. In Figure 6.19 (left axis) they are plotted both data from 2 V resistance maps of (001) (close symbols) and (110) barriers (open symbols), which were simultaneously grown. The conductance through (001) and (110) STO barriers is very similar, thus suggesting a comparable energy barrier. Since the energy barrier between the AFM tip and a STO barrier on LCMO (001) has been found to be 0.2-0.4 eV, a similar height is expected in the case of the STO (110) barriers. This observation would imply that the band gaps in STO layers along [001] and [110] are similar. However, calculations of the electronic band structure in STO showed that the theoretical energy gaps along these directions are 1.82 eV and 1.49 eV, respectively [44].

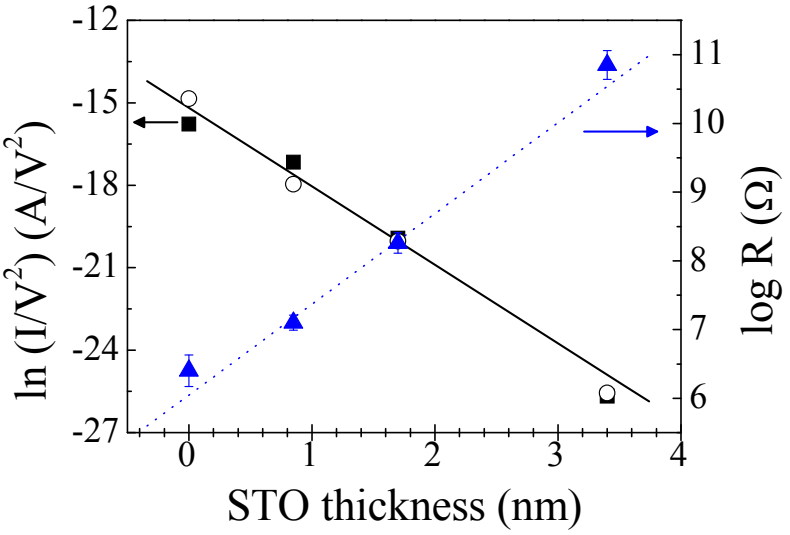

Figure 6.19. Right axis: Dependence of the maxima of the resistance in histograms of Figure 6.18 *vs t* (triangles) and linear fit to these data (dashed line). Left axis: ln (I/V^2) plotted against *t* barrier thickness for the series of (110) films measured at 2 V (open symbols) and corresponding linear fit (black solid line); results on LCMO (001) films and STO/LCMO(001) bilayers at the same polarization are also plotted (squares).

To conclude, the use of resistance maps obtained by CAFM has been found to be perfectly suitable to allow a functional characterization of STO tunnel barriers. The homogeneity with a nanometric resolution of the electrical resistance of barriers has been characterized, and resistance mapping under various bias of (001) samples with different barrier thickness has been used to investigate the transport mechanism. A new method has been developed to avoid the assumption of a value of the tip contact area as a necessary input. The method has allowed estimating the barrier height between the AFM tip and the STO layer to be 0.2-0.4 eV. Similar height has been determined for (110) bilayers. Therefore, the observation of tunnel transport through either (001) or (110) STO barriers demonstrates that MTJ's can be fabricated with these base STO/LCMO bilayers.

6.4 Experimental results on MTJs based on (001) and (110) STO/LCMO bilayers

6.4.1 MTJs fabricated by e-beam lithography

As described in Ch2, e-beam lithography has been used for the fabrication of magnetic tunnel junctions (MTJs) based on STO/LCMO bilayers. The bilayer is placed as the bottom electrode and Co is used as the top ferromagnetic electrode. Two different methods have been used for Co deposition, dc sputtering and evaporation, and for the definition of Co electrodes we have used a mask with a matrix of square holes, as depicted in detail in Ch2. In Table 6.8 we list the samples referred through this section, their corresponding layer thickness and deposition parameters.

Table 6.8. List of samples referred in this section. The corresponding thickness of the LCMO and STO layers and the nominal deposited Co thickness are indicated, together with the corresponding growth technique used for the Co deposition and the final use of the sample.

Sample	Substrate	LCMO thickness (nm)	STO thickness (nm)	Co thickness (nm)	Co deposition technique	
050404bilayerB	STO(110)	30	3.0	30	Sputtering	SQUID test
050401stolcmoB (stolcmo2)	STO(110)	30	2.4	30	Sputtering	Device
050714stolcmoA (stolcmo4)	STO(001)	19	1.7	10	Evaporation	Device

Before measuring the transport properties of the junctions, we checked the magnetic properties of the top Co electrode. It is important to remark the necessity of

verifying that the grown Co material is fully ferromagnetic, knowing that Co under the presence of a low content of oxygen can form CoO, which is an antiferromagnet. Magnetic measurements were carried out on samples with Co continuous electrode deposited either by dc sputtering (nominal Co thickness 30 nm) or by evaporation (nominal Co thickness 6 nm). As an example, we present in Figure 6.20 the results on the trilayer sample Co(30 nm)/STO(3.0 nm)/LCMO(30 nm)//STO(110). Knowing that the bottom electrode of LCMO(30 nm) have a Curie temperature around 250 K, the magnetic signal measured at 300 K arises only from the Co layer and in consequence we can evaluate the total ferromagnetic response of the Co layer from the Co thickness and sample area. The saturation magnetization deduced from Figure 6.20 is 1400 emu/cm^3, which is close to the pure ferromagnetic Co value 1426 emu/cm^3, indicating that the Co layer is ferromagnetic with a saturation value only a 2%.lower than that of pure Co.

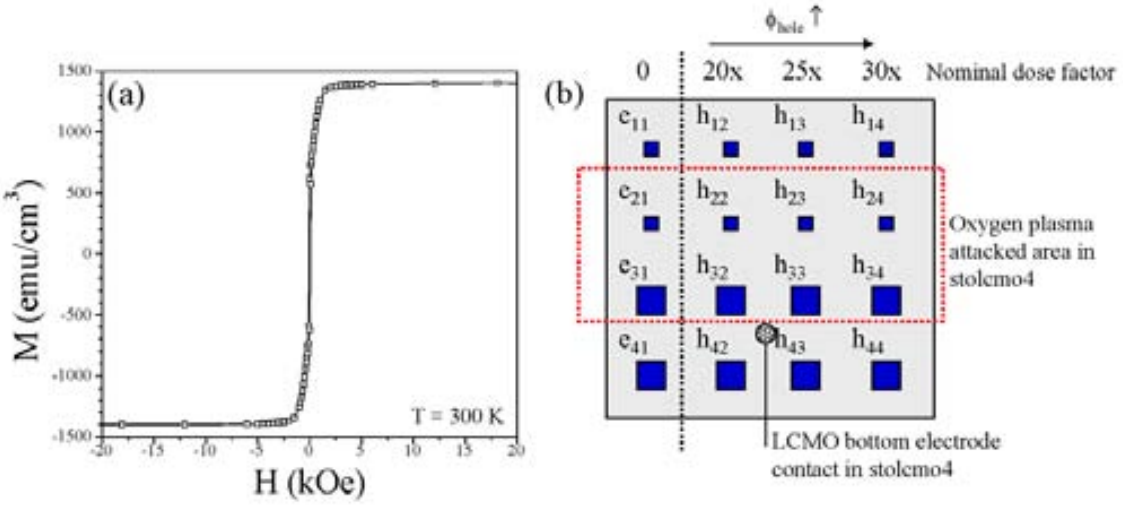

Figure 6.20. (a) Magnetization *vs* magnetic field measured at 300 K for a trilayer sample of Co(30 nm)/STO(3.0 nm)/LCMO(30 nm)//STO(110), being the Co layer deposited by dc sputtering. Magnetic field was applied in-plane. (b) Sketch of the matrix of Co top electrodes deposited onto (10x10) mm^2 samples. Co electrodes are referred as (e_{i1}) if they account only for the Co electrode and (h_{ij}) for Co electrodes deposited on e-beam litographed holes. The nominal dose factor for each hole and the evolution of the hole size (ϕ_{hole}) are indicated. Also, the area attacked by the oxygen plasma in sample stolcmo4 is marked.

Turning to the devices, the final junctions are based on the e-beam lithographed STO/LCMO samples. The e-beam lithography of these samples was performed using a scanning electron microscope, which was prepared to perform controlled electron irradiations onto the samples. On top of the STO/LCMO bilayers, we had previously deposited thick polymers layers (resists) that are sensitive to the electrons and thus we can define a matrix of irradiated areas which after a chemical treatment will define a

matrix of holes. More details on this process are included in Ch2. The holes on the resists allow the contact of the deposited Co electrode and the surface of the STO/LCMO bilayer. Using a metallic mask during the Co deposition, we have defined a matrix of (4x4) Co electrodes properly aligned to have the lithographed holes underneath them. In Figure 6.20b a schematic view of the defined Co electrodes on the final devices is shown. Two rows of top Co electrodes of 1 mm^2 and the other two rows with electrodes of 0.25 mm^2 are defined. One column was left to test the insulating properties of the resist and no lithographed holes were underneath. The notation used to label the Co electrodes is:

(a) $e_{i1,}$: Co electrodes deposited onto the resist only, being i the row number, with $1 \leq i \leq 4$.

(b) $h_{ij,}$: Co electrodes deposited onto e-beam lithographed holes, being i and j the row and column number, respectively, with $1 \leq i \leq 4$ and $2 \leq j \leq 4$.

The created matrix is expected to present resistance values that will depend on the nominal factor dose as well as on the oxygen attack and on the size of the top Co electrodes. Taking into account all these factors, and from Figure 6.20b the resistance for each element of this matrix is expected to vary as follows:

(a) e_{i1} ($1 \leq i \leq 4$): As the Co electrode is contacting only the resist, they are expected to be fully insulating.

(b) For a given i-row ($1 \leq i \leq 4$), for column numbers $2 \leq j \leq 4$: $R_{ij} > R_{i(j+1)}$

Also, if some contribution to the resistance comes from the electrical resistance of the resist (size of Co top electrode), then:

(c) Being distributed the (0.5x0.5) mm^2 and (1x1) mm^2Co electrodes into i = 1,2 and i = 3,4, respectively, for the column numbers $2 \leq j \leq 4$: R_{1j}, $R_{2j} > R_{3j}$, R_{4j}

If it is performed an oxygen plasma attack, these evaluations should be refined:

(b') For a fixed j-value ($2 \leq j \leq 4$): $R_{1j} > R_{2j}$ and $R_{3j} < R_{4j}$

We can finally add the contribution of Co electrode of different size (not clearly predictable):

(c') For a fixed j-value ($2 \leq j \leq 4$): $R_{1j} > R_{4j}$ and $R_{2j} > R_{3j}$

Prior to analyzing the actual experimental data, we can numerically estimate the resistance that we would ideally measure when connecting two top Co electrodes with lithographed structures on the bottom. In a circuit including two nanopillars of Co/STO/LCMO, different elements contribute to the measured resistance. In Table 6.9

the resistivity values from the different materials that can constitute elements of the circuit are summarized (Co, resist, LCMO). A sketch of the ideal circuit is shown in Figure 6.21. We have fixed the sample characteristics to be those of stolcmo4, with LCMO electrode thickness of t_{LCMO} = 19 nm~ 20 nm and STO barrier thickness of t_{STO} = 1.6 nm~ 2 nm, and we consider that the lateral size of the holes is that of the smallest one (nominal dose factor of 20x), which gives ϕ_{hole}~ 400 nm. Resist thickness (t_{resist}) is approximately 300 nm and top Co electrodes of (1x1) mm^2 area. For calculating the LCMO electrode resistance, the separation between the centers of two Co electrodes is 2 mm, and we take as the penetration depth of the current in the LCMO electrode a maximal value of ~ 0.1 mm.

From this sample and circuit parameters, we calculate the resistance values shown in Table 6.10. If the current passes only the two interconnected nanopillars, the expected resistance will include R(Co) and one R(LCMO) connected in series, leading to a final value of $R_1 \sim 10^6\ \Omega$. Connected in parallel to this resistance we find R_2 = R(resist), which is much higher than the previous one $R_{resist} \sim 10^{11}\ \Omega$, $R_2 >> R_1$. Thus, we predict that the injected current should flow through the nanopillars and not through the resist.

Table 6.9. Resistivity values (ρ) of the materials present in the stolcmo2 and stolcmo4 samples.

	Resistivity (ρ) (Ωcm)
Co (ρ_{Co})	10^{-6}
Resist (ρ_{resist})	10^{14}
20 nm LCMO film (ρ_{LCMO})	10^{-1}

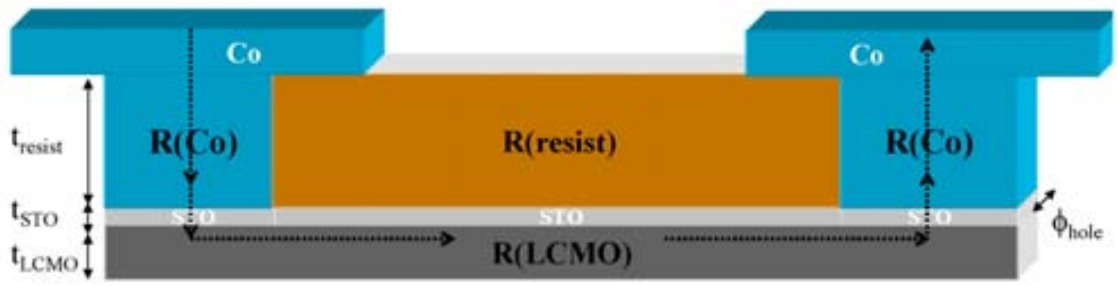

Figure 6.21. Sketch of the resistive elements on a circuit composed by two nanopillars on a STO/LCMO bilayer: for Co in the nanopillar R(Co), for the LCMO electrode R(LCMO) and for the resist R(resist) Arrows define the ideal current path for the transport measurement.

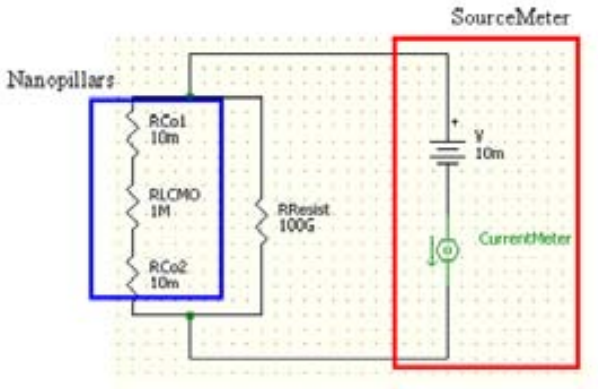

Figure 6.22. Schematic view of the equivalent circuit generated when connecting the SourceMeter, which includes the DC voltage source working with a maximum voltage of $|V_{max}|$=10mV and the current detector (CurrentMeter), to two nanopillars. The evaluated resistance of the LCMO, Co electrodes and resist are indicated by RLCMO, RCo1 and RCo2, and RResist, respectively. The corresponding resistance values are in Ω.

Table 6.10. Resistance values (R_x) of each element in the ideal circuit depicted shown in Figure 6.21 and Figure 6.22. The dimensions are the length [d] and the area [A] of the current path through the element. Resistivity ρ values are included in Table 6.9.

Path	Resistive element	Dimensions [d]=cm; [A]=cm^2	$R_x = \rho_X \frac{d_x}{A_x}$ (Ω)
Nanopillars	Co electrode	$d_{Co}=t_{Co}=3\cdot10^{-5}$ $A_{Co}=(4\cdot10^{-5}x4\cdot10^{-5})$	10^{-2}
	LCMO electrode	$d_{LCMO}=2\cdot10^{-1}$ $A_{LCMO}=(2\cdot10^{-6}x1\cdot10^{-2})$	10^{6}
Resist	Resist	$d_{resist}=t_{resist}=3\cdot10^{-5}$ $A_{resist}=(1\cdot10^{-1}x1\cdot10^{-1})$	10^{11}

We have performed transport measurement on stolcmo2 and stolcmo4 at 300 K in order to evaluate the junction resistance before further tests at low temperature and under magnetic field. Two types of transport setup have been used: Keithley SourceMeters and a tester, 2-wire and 4-wire measuring. A SourceMeter works as a voltage source and measure the whreas the tester provides a rougher estimation of the voltage (resistance) between two contacts by applying a current. The stolcmo2 and stolcmo4 samples have a configuration of holes and Co contacts as presented in Figure 6.21 with the only difference that in the case of stolcmo2 no oxygen plasma attack has been performed before the Co deposition. A sketch of the equivalent circuit formed by the SourceMeter and the sample elements is depicted in Figure 6.22.

First, we comment on the transport measurements of stolcmo2. In this case, we connected two nanopillars with Co top electrodes of the same size [(1x1) mm^2]. The chosen nanopillars have different diameter, since pillars with different nominal dose factor are chosen. The used pillars were h_{34}, h_{44} and h_{43}, having h_{34} and h_{44} a wider width (30x nominal dose factor) than h_{43} (25x nominal dose factor). Using the Keithley SourceMeter in 4-wires measuring, we applied a voltage and measured the current, thus finally obtaining I(V) curves. In Figure 6.23, the I(V) curves obtained from connecting h_{34}, h_{44} and h_{43} among them are shown. In both measurements we fixed one of the nanopillars to be h_{34}, and we studied the effect of the change in the nanopillar size adding to the circuit in one case the h_{44} nanopillar (squares-high dose) and in the other case the h_{43} nanopillar (circles-low dose). Since the nanopillar size will determine the current flow size, the resistance for the lower dose nanopillar h_{43} is expected to be higher than for the higher dose h_{44}. The I(V) cuves of Figure 6.23 present a clear linear behavior in the range of applied voltage. From the slope of the curves we determine in each case the equivalent resistance of the nanopillars. We notice that lower slope is observed for the h_{34}-h_{44} nanopillars than for the h_{34}-h_{43} ones, being theresistance values $R(h_{34}\text{-}h_{44}) = 0.28 \cdot 10^6 \Omega$ and $R(h_{34}\text{-}h_{43}) = 2.33 \cdot 10^6\ \Omega$. These results are of the same order of magnitude than the previous evaluated result on narrower pillars (20x dose factor), which was $\sim 10^6\ \Omega$. By 2-wires measuring with a tester we have found $R(h_{34}\text{-}h_{44}) = 0.4 \cdot 10^6\ \Omega$ and $R(h_{34}\text{-}h_{43}) = 1.9 \cdot 10^6\ \Omega$, which are similar results to those obtained the Keithley. Thus, from the good agreement between the expected values and the experimental ones, we conclude that at room temperature the measured resistance values arise from the designed nanopillars.

On stolcmo4, Figure 6.24 summarizes the transport measurements performed using two Keithley SourceMeters (K-2601 and K-2400 models). The reason to use two SourceMeter was to control the current offset, but the overall resistance values obtained from both equipments are much similar. For this sample, we have studied one nanopillar by scratching the sample surface and directly contacting with graphite paste the LCMO bottom electrode, as sketched in Figure 6.20b. Similar slopes of the I(V) curves are found using these two Keithley setups for h_{43} (Figure 6.24a) and h_{32} (Figure 6.24b), while h_{42} is found to be highly insulating and out of the measurable range (inset of Figure 6.24).

For simplicity, we start inspecting the data from the as-created hole h_{42} (dose factor 20x) (inset of Figure 6.24). A strong insulating behavior is observed. The I(V) curves of the as-created hole h_{43} (dose factor 25x) shown in Figure 6.24a gives a resistance value of $R_{43} \sim 0.1 \cdot 10^6\ \Omega$. The results on the oxygen plasma attacked h_{32} (20x dose factor) are shown in Figure 6.24b. Contrary to the results on the as-created h_{42} nanopillar, we are able to measure the resistance of the oxygen plasma attacked h_{32} one, being $R_{32} \sim 35 \cdot 10^6\ \Omega$. We ascribe the lowering in the nanopillar resistance of h_{32} compared to that of h_{42} to the possible change in the nanopillar size caused by the oxygen plasma attack.

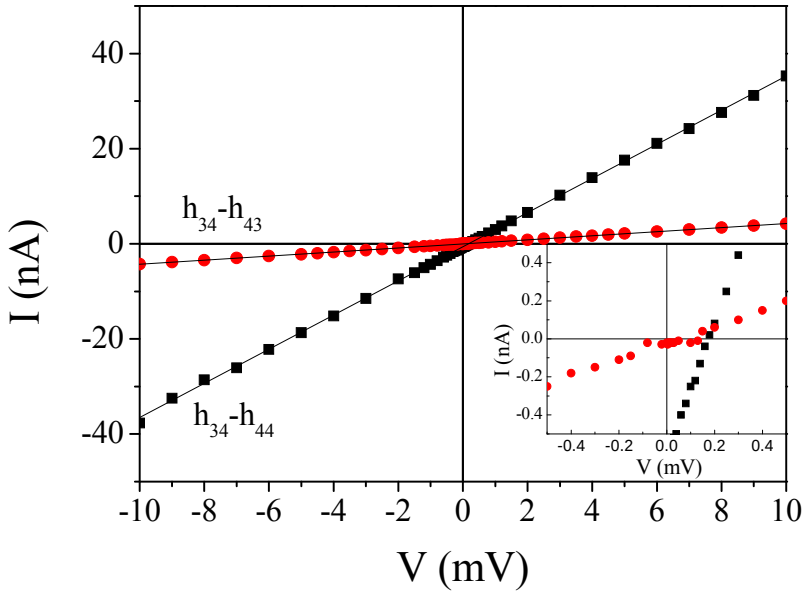

Figure 6.23. I(V) curves recorded in stolcmo2 sample, connecting the nanopillars h_{34}-h_{43} (circles) and h_{34}-h_{44} (squares) are shown. Inset: detail of the low voltage-current region.

From these transport measurement, we can extract some preliminary conclusions about the e-beam lithographic procedure and MTJs performance process. First, both Co contacts deposited by dc sputtering (stolcmo2) or evaporation (stolcmo4) are fully operative as useful electrodes. Although in our first measurements we found out-of-range resistive values of the nanopillars, after a slight scratch of the Co electrode and contacting with the graphite paste, the resistance value became measurable, meaning that on the topmost Co electrode surface some insulating layer (possibly CoO) is formed. This technical problem could be easily solved by *in-situ* capping the Co electrodes with a nonreactive metal (Au). In relation to the dose factor and the oxygen plasma attack, further experiments are necessary to confirm the observed double trend:

that the nanopillar conductance increase with the dose factor and with the oxygen attack. From these room temperature results, the transport properties of these samples are now ready to be tested at low temperature and under magnetic field.

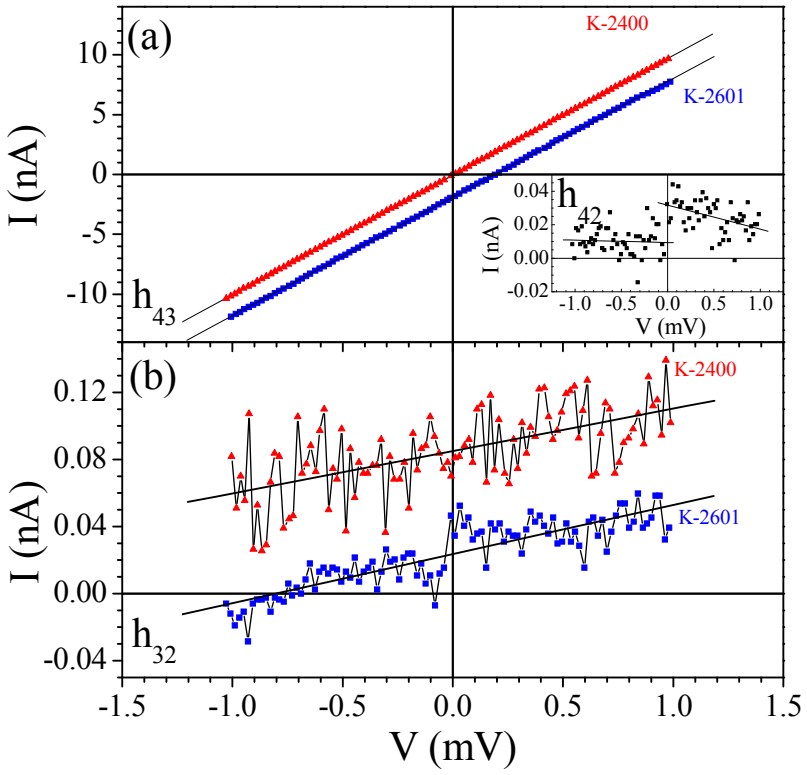

Figure 6.24. I(V) curves recorded in stolcmo4 sample, connecting the one nanopillars (a) h_{43} and (b) h_{32}, and in the inset h_{42}.In (a) and (b), results of measurements performed with K-2400 (triangles) and K-2601 (squares) are shown for comparison.

6.4.2 MTJs fabricated by nanoindentation

During the last years, nanoindentation using Conducting-AFM has been extensively applied for the fabrication of nanojunctions at the Unité Mixte de Physique CNRS-Thales (Orsay, France). The nanolithography technique is extensively explained in Ch2, and in short it involves the creation of a nanohole onto previously deposited resist. After the deposition of top ferromagnetic Co layer and a controlled oxidation into antiferromagnetic CoO, the sample is continuosly covered by a Au thick layer. Protecting the junction area with a local deposition of a resist, the top electrodes are defined etching the sample with an ion beam etching.

Nanojunctions have been patterned onto a series of STO/LCMO//STO bilayers with different STO thickness (2 and 4 nm) and fixed 25 nm LCMO electrode. For each STO thickness, we had one (110) and one (001) bilayer (four bilayers in total), and the nanolithography process was carried out in all them. The transport measurements were performed by contacting with Au wires the top Au electrode of each nanojunctions to a metallic sample holder pad, as shown in Figure 6.25a. The external pads of the holder will allow the transport measurement. Before the transport experiments, ground connections are done to the sample holder to avoid short-circuits.

The transport measurements were performed into a cryostat supplied by liquid He. The lowest temperature that the system can reach is close to ~ 2.6 K. The sample holder is placed between the poles of an electromagnet with a maximum magnetic field of 6000 Oe. For the measurements on the MTJs based on STO/LCMO bilayers the magnetic field was applied in-plane of the samples. The sample holder can be externally rotated in order to optimize the alignment between easy axis and applied magnetic field. The manipulation of the samples is performed using bracelets that connect the manipulator to the ground avoiding the possible breakdown of the junction through the manipulator. The electrical resistance was measured using a Keithley Electrometer and a computer station with home-made Lab-view programs are used to control the experimental parameters (magnetic field, applied voltage, detection range, acquisition time, etc) and acquire the data.

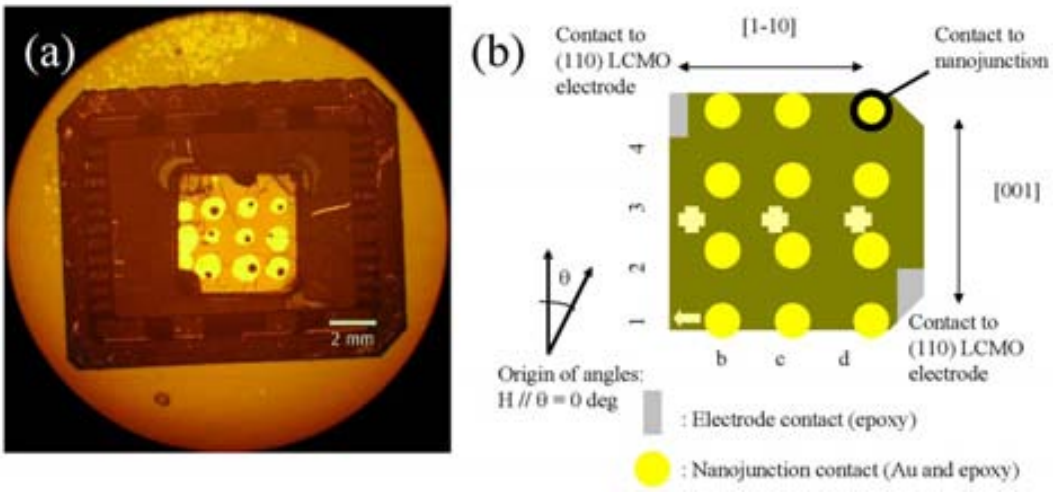

Figure 6.25. (a) Photograph of the sample holder used for the magnetotransport measurements, together with a processed sample showing the defined Au electrodes and the wiring from these electrodes towards the sample holder pads. (b) Sketch of the defined nanolithographed sample, with top Au electrodes (circles) onto a (110) bilayer (crystallographic directions are indicated). The references of the UV photolithography are still marked on the surface (arrow and crosses). The applied field is parallel to the set θ value. Further information is given in Ch2.

From the series of nanojunctions prepared (nine nanojunction per sample) only two junction on two different samples were probed to work. Sample description including the corresponding layer thickness is shown in Table 6.11.

Table 6.11. List of samples that presented TMR.

Sample	Substrate	LCMO thickness (nm)	STO thickness (nm)	Operative junctions
060920A	STO(110)	25	2	1 (broken)
060921B2	STO(110)	25	4	1

Unfortunately, the first sample showing tunnel magnetoresistance broke after one resistance *vs* field measurement was carried out. The underneath bilayer sample was STO(2 nm)/LCMO(25 nm)//STO(001) and the obtained curve is shown in Figure 6.26. The junction displayed insulating characteristics after the application of a moderate voltage (V_{dc} ~ 500 mV) and complete insulating behavior was afterwards measured. With the aim of discussing in detail a complete series of magnetotransport measurements, we turn to those obtained from nanojunctions performed on STO(4 nm)/LCMO(25 nm)//STO(110) bilayers.

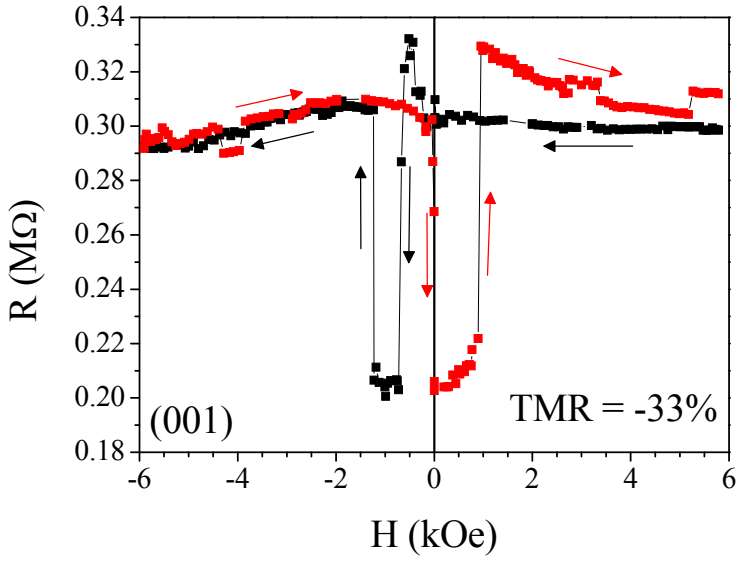

Figure 6.26. Resistance *vs* magnetic field measured at 4.2 K of a nanojunction on STO(2 nm)/LCMO(25 nm)//STO(001). Applied voltage was -10 mV. Magnetic field was applied parallel to the initial freezing magnetic field (θ = 0 deg).

In Figure 6.25b the scheme of the arrangement of contacts and crystal directions is shown. Changing the relative position of the applied magnetic field to the (110) sample, due to the uniaxial in-plane anisotropy of the (110) LCMO electrode, relevant effects in the tunneling process were expected.

In Figure 6.27 we show the transport properties at 4.2 K from a nanojunction of based on STO(4nm)/LCMO(25nm)//STO(110) bilayer. For the curve plotted in Figure 6.27, the applied bias voltage was V_{dc} = -10 mV. For this experiment, the sample was cooled down under maximum magnetic field of 6 kOe parallel to the [001] sample direction. This freezing field is used to fix the antiferromagnetic (AF) CoO layer magnetic anisotropy. The unidirectional pinning of this CoO layer will drive the underneath Co ferromagnetic layer to have a preferential magnetic configuration parallel to this AF layer. The final effect on the dependence of the junction resistance on the applied magnetic field will be the observation of two different coercive fields for positive or negative magnetic fields.

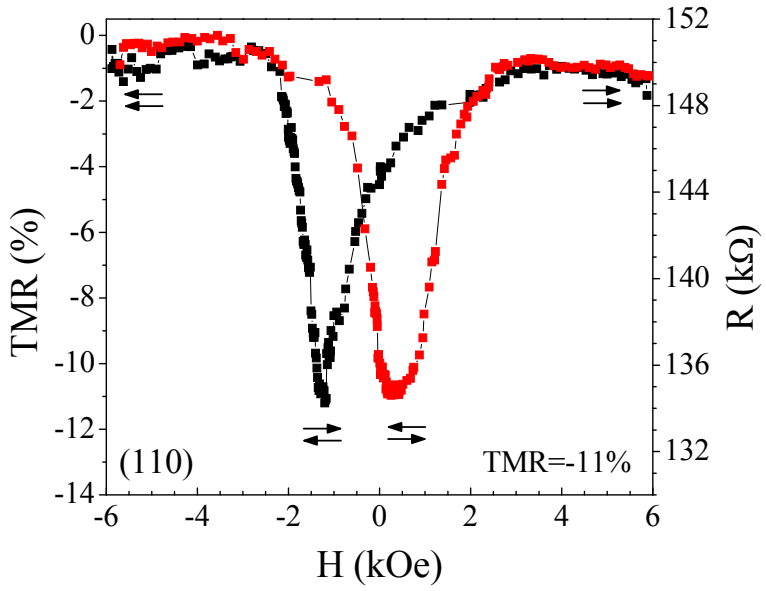

Figure 6.27. Resistance *vs* magnetic field measured at 4.2 K of a nanojunction on STO(4 nm)/LCMO(25 nm)//STO(110). Applied voltage was -10 mV. Magnetic field was applied parallel to the initial freezing magnetic field H_0, which was applied parallel to [001] direction (θ = 0 deg).

To describe the tunnel magnetoresistance (TMR) curve displayed in Figure 6.27, we start from the saturated state at positive magnetic field, where top Co and bottom LCMO electrodes have their magnetization vectors pointing in the same direction (parallel state, P). Lowering applied magnetic field, magnetization of Co electrode starts

rotating till it points towards negative magnetic field, whereas LCMO magnetization stays pointing towards positive field. At this antiparallel (AP) state, nanojunction resistance decreases, and a negative TMR [$TMR = (R_{AP}-R_P)/R_P$ %] appears. Negative sign on TMR was also observed by De Teresa *et al.*[45] in magnetic tunnel junctions using Co and $La_{2/3}Sr_{1/3}MnO_3$ (LSMO) electrodes, and it was ascribed to be caused by the electron tunneling between Co minority spin 3d band and LSMO majority spin band. Similar argument can be deduced from our experiments with Co and LCMO electrodes.

Following with the description of Figure 6.27, after both electrodes are saturated with negative field, junction resistance increases as electrodes are in a P state. In order to close the resistance loop, we further reduce the magnitude of the magnetic field and it can be seen that around zero magnetic field Co magnetization starts to reverse. Different TMR coercive fields are thus measured for negative and positive applied field, and it is correlated to the AF CoO pinning layer. After the AP state, final rotation of LCMO electrode happens at LCMO coercive field, and thus a high resistive parallel state is recovered at higher magnetic fields.

To monitor the influence of the CoO AFM layer in the TMR curve, we have rotated the sample tuning the angle θ (Figure 6.20b) and applied the magnetic field parallel to different in-plane directions. Being the sample cooled down with a freezing field (H_0) of 6 kOe applied parallel to [1-10] direction ($\theta = 90$ deg), we present in Figure 6.28 the TMR curves measured with field applied along [1-10] direction ($\theta = 90$ deg) (a), with field at $\theta = 45$ deg (b) and with field parallel to [001] direction ($\theta = 0$ deg) (c). We start analyzing the curves obtained with the magnetic field applied parallel to the initial freezing field (Figure 6.28a). Coming from the high field region, both the Co and LCMO electrodes are expected to have their magnetization parallelly aligned to the applied magnetic field. The measured junction resistance is constant in these conditions. Approaching the zero field region, the resistance gradually decreases. Once the magnetic field changes in sign, the drop in the resistance is enhanced. Nevertheless, this drop is not fully abrupt, since the curve in Figure 6.28a depicts small resistance steps. Upon the application of higher magnetic field (in absolute value), the resistance achieves a minimum value. At higher magnetic field ($H > 1.6$ kOe), the resistance returns to the high value measured at high field following small steps in resistance. The existence of these steps in resistance instead of abrupt ones may be

caused by changes in the relative alignment of the magnetization of Co and LCMO electrodes. If either the LCMO or the Co electrodes do not follow the applied magnetic field, magnetic domains with different orientation may appear. The effect on the tunnelling current is the consequently gradual evolution of the junction resistance.

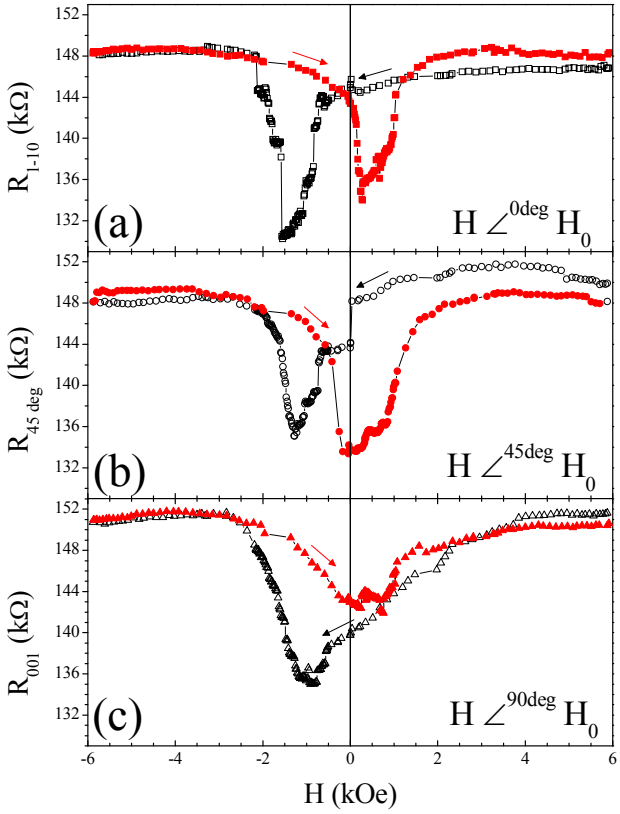

Figure 6.28. Resistance *vs* magnetic field measured at 4.2 K of a nanojunction on STO(4 nm)/LCMO(25 nm)//STO(110). Applied voltage was -10 mV. Magnetic field was applied (a) parallel to the initial freezing magnetic field H_0 along [1-10] direction H // H_0, (b) at 45 deg from H_0 ($\theta = 45$ deg), and (c) perpendicular to H_0 and along the [001] direction H ⊥ H_0. Open and close symbols indicate the positive to negative field half of the loop and the negative to positive half of loop, respectively.

In Figure 6.28b and c, the magnetic field is applied at 45 deg of [1-10] direction (b) and at 90 deg from it (parallel to [001] direction) (c). Similarly the curve presented in (Figure 6.28a), from the saturation value at high fields, the junction resistance evolves gradually to low values when decreasing the applied magnetic field (in absolute value). As the angle between the freezing field direction (in this case [1-10]) and the applied one increases, the shape of the resistance curve presents less abrupt steps. The uniaxial magnetic anisotropy of the bare LCMO electrode provide easy in-plane

magnetic axis for the [001] direction and hard one along [1-10] direction. From Figure 6.28a, we have obtained more abrupt steps for when the magnetizations of the CoO pinning layer and that of the LCMO electrode were parallelly aligned, although in this case the field was applied parallel to the hard axis of the LCMO electrode. Since no influence of the magnetic anisotropy of the LCMO layer is observed in the junction resistance, we suggest that inhomogeneous magnetization rotation happens at either the Co/STO or at the STO/LCMO, or at both. Besides, adding that the LCMO magnetization was observed to rotate coherently with the magnetic field (Ch5), it seems more plausible that incoherent magnetization rotation arises from the Co layer.

In Figure 6.29, we present the bias dependence of the tunneling current (main panel) and conductance (inset) across the same junction at 4.2 K cooled down at freezing field H_0 of 6 kOe parallel to [1-10] direction ($\theta = 90$ deg). In the present case shown in Figure 6.29, the relative orientation of each electrode is fixed and we measure the conductance of the junction into different magnetization configurations: (i) with parallel (P) magnetized electrodes, at 6 kOe, the conductance is low, and (ii) with anti-parallel (AP) magnetized electrodes, at -1.2 kOe, the conductance is high. Therefore, we confirm the observed negative TMR [$TMR = (I_P-I_{AP})/I_{AP} = (G_P-G_{AP})/G_{AP}$ %] with these current and conductance dependences on bias.

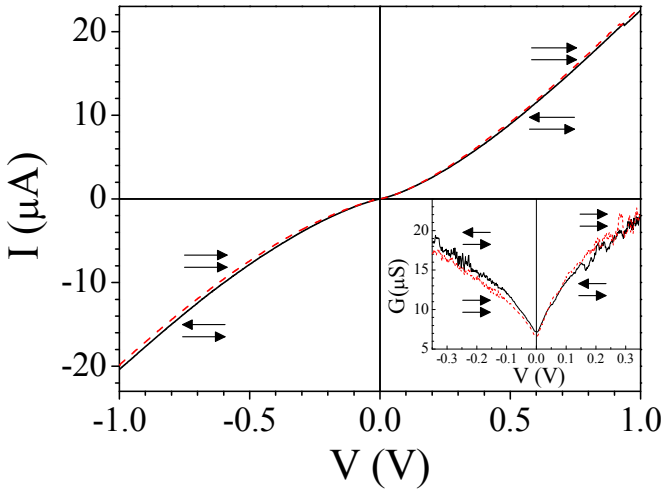

Figure 6.29. I(V) curves obtained at in-plane magnetic fiels of 6 kOe (P configuration) and -1.2 kOe (AP configuration). Inset: Conductivity calculated from the I(V) curves. In both cases, P (dashed line) and AP (solid line) configurations are indicated by arrows. Measurements were performed at 4.2 K after a freezing field of 6 kOe was applied along the [1-10] direction ($\theta = 90$ deg).

From the measured -11 % value of TMR, and assuming the Jullière model [$TMR = P_1P_2/(1-P_1P_2)$, being P_1 and P_2 the corresponding spin polarization of each electrode] [46] and taking as the spin polarization of Co $P_{Co} = –37$ % [47], we evaluate the spin polarization of LCMO electrodes as $P_{LCMO} = +14$ %. This value is surprisingly lower than the expected one for half-metallic ferromagnets, but it could be related to intrinsic problems such as symmetry matching between spin-dependent wave functions in Co electrodes and (110) STO barriers, although other non-intrinsic effects could also contribute.

An analysis of the bias dependence of the TMR curves provide relevant information on the functionality of the device, as well as direct insight in the structure of the density of states of LCMO and Co electrodes. First, the resistance *vs* field curves recorded at 4.2 K obtained from the previously studied junction under the freezing conditions of 6 kOe and $\theta = 90$ deg are shown in Figure 6.30.

The procedure to record the R(H) curves implies the application of the bias voltage starting from low magnitude values (± 10 mV) and increasing towards high absolute values (up to + 1 V and - 6 V). Inspection of the R(H) curves recorded at the low applied voltage of $V_{dc} = \pm 10$ mV (squares) signal the existence of the parallel (low resistance) and antiparallel (high resistance) states associated to the two different configurations of the magnetization of Co and LCMO electrodes. The junction conductance depends on the applied bias voltage sign and amplitude, already noted in Figure 6.23. Since the junction is based on different ferromagnetic electrodes (LCMO and Co) separated by the insulating STO layer, we expect that different barrier heights are formed in the LCMO/STO and STO/Co interfaces. Using the reported work function W from LCMO and Co electrodes, $W_{LCMO} = 4.8$ eV [38] and $W_{Co} = 5$ eV [48], and the electron affinity χ of STO, $\chi_{STO} = 3.9$ eV [39], we can build a simple energy diagram of the barrier height, shown in Figure 6.31. The different response to positive and negative bias can be predicted considering understood following the model presented by Brinkman *et al*. [49] on non-symmetric junctions. From Figure 6.30, the evolution of the TMR amplitude with applied voltage signals a decrease in the amplitude of the effect, disappearing at lower voltages (in absolute value) for positive bias ($V_{dc} = + 1$ V) than for negative values ($V_{dc} = - 6$ V).

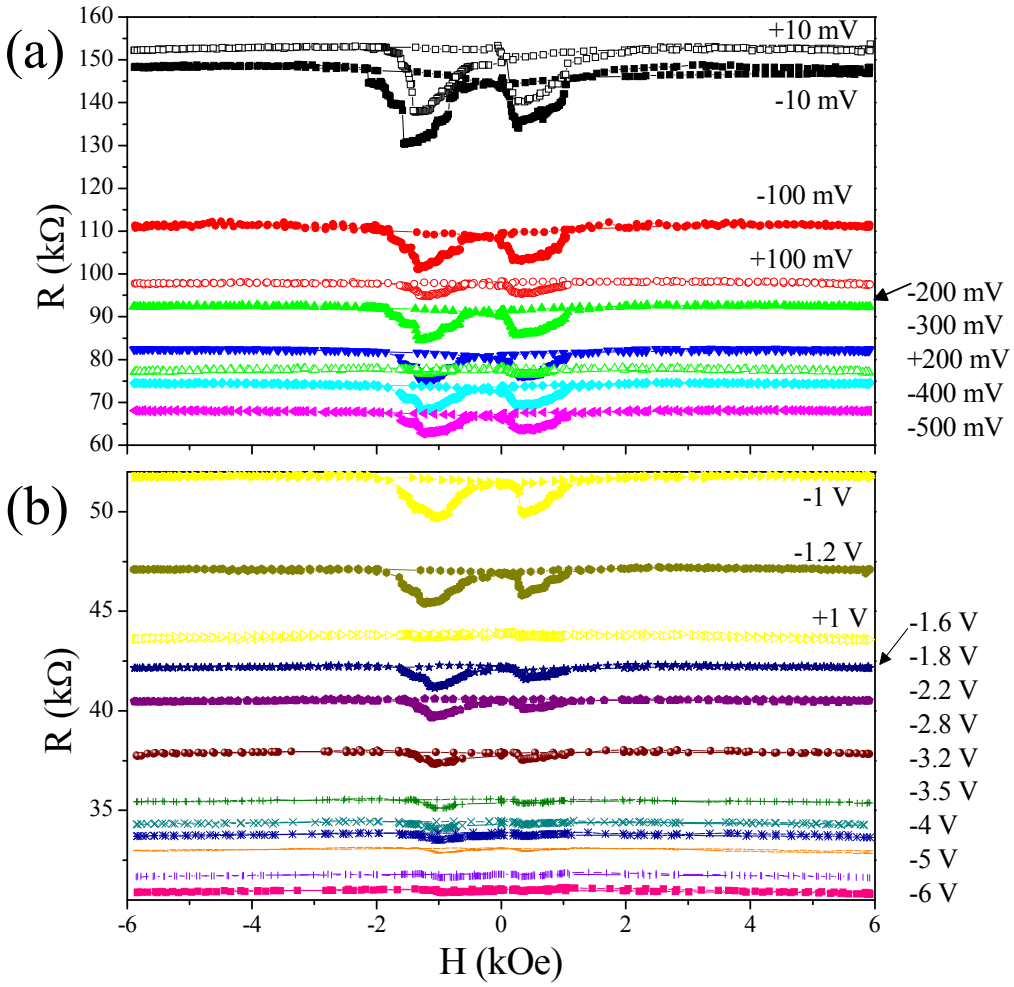

Figure 6.30. Resistance *vs* magnetic field measured at 4.2 K of a nanojunction on STO(4 nm)/LCMO(25 nm)//STO(110) at different applied voltages. Magnetic field was applied parallel to the initial freezing magnetic field H_0 ($\theta = 90$ deg) and thus H // [1-10] direction. Close and open symbols correspond to data recorded at negative and positive applied voltage, respectively. R(H) curves are separated into (a) and (b) depending on the mean resistance value of the junction at the correspondent applied voltage.

Following with the analysis of the bias dependence of TMR in this junction, the TMR values extracted from the R(H) curves in Figure 6.30 are plotted in Figure 6.32 as a function of the bias voltage. We observe a clear dissimilar behavior of the TMR ratio for positive and negative V_{dc}: TMR decreases very quickly for positive V_{dc} whereas it remains still measurable for large negative V_{dc}. Knowing that in these transport measurements LCMO electrode is positively biased, we deduce the direction sense of tunneling electrons in each case. For positive V_{dc}, Co 3d electrons tunnel towards available LCMO states and for negative V_{dc} Mn 3d electrons of LCMO electrode tunnel

towards Co 3d states. The reduction of TMR at $V_{dc} > 0$ is possibly caused by the balance of spin up and spin down electrons from the Co 3d bands [50], which lowers the spin polarization of the tunneling current and thus the TMR decreases. For $V_{dc} < 0$, LCMO electrons tunnel into Co bands. An inspection of the low bias region ($|V_{dc}| < 0.5$ V) is shown in the inset of Figure 6.32. Superimposed to TMR values obtained from TMR curves (symbols), it is seen the corresponding TMR bias dependence extracted from experimental I(V) curves measured at the parallel (I_P) and antiparallel (I_{AP}) states (line).

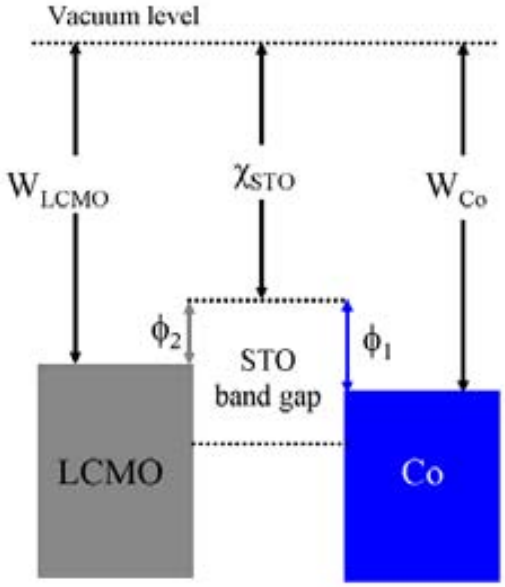

Figure 6.31. Sketch of the band structure (in the Schottky limit) of the LCMO/STO barrier/Co electrode. STO electron affinity is represented by χ_{STO} and LCMO work function and Co tip by W_{LCMO} and W_{tip}. The barrier heights are ϕ_1 and ϕ_2.

The TMR calculated from the I(V) (line in Figure 6.32) agrees with the bias dependence obtained from TMR curves (symbols). Close to $V_{dc} \sim 0$ V, higher |TMR| ratios are measured, which stand for the so-called a zero bias anomaly (ZBA). For the ZBA, its possible origins were presented by Bratkovsky [51] , being the most probable cause of this anomaly the spin wave excitations occurring at this low bias regime [52]. a Also in Figure 6.32, we notice a local plateau in the |TMR| ratio at $V_{dc} \sim -300$ mV that we may be ascribed to the density-of-states of the minority spin Co band around this energy below the Co Fermi level.

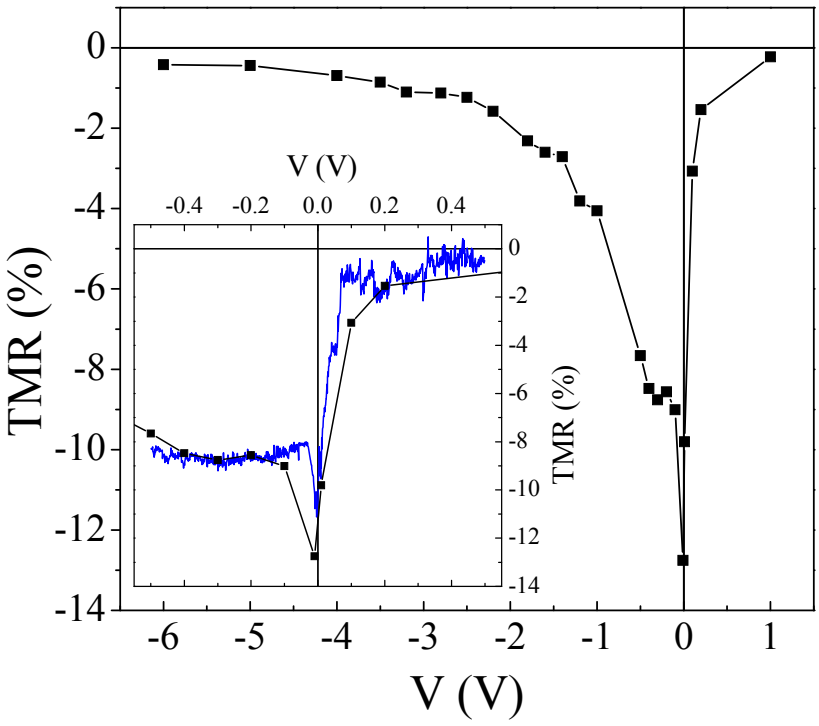

Figure 6.32. TMR ratio calculated from R(H) loops as a function of the applied V_{dc}, measured at 4.2 K on a nanojunction on the STO(4 nm)/LCMO(25 nm)//STO(110) bilayer. Zero bias anomaly is observed, associated to a negative TMR of 13 % at -1mV. Inset: low V_{dc} range of the same data (symbols), showing also the equivalent TMR ratio calculated from experimental I(V) curves (line) measured between -0.5 and +0.5 V.

The evolution of the observed TMR on temperature is shown in Figure 6.33 (symbols). At a fixed bias of V_{dc} = -10 mV, TMR curves are measured at the conditions where LCMO electrons tunnel into Co 3d band. Comparing these data to the experimental magnetization dependence on temperature of the bare LCMO electrode (line), we notice a decrease in the |TMR| ratio at lower temperatures that the ferromagnetic to paramagnetic transition of LCMO electrode (T_C ~ 245 K). Although the vanishing of TMR is clearly much relevant at low temperature (~ 125 K), we still measure a clear TMR signal for ~ 200 K. The thermally activation of spin scattering at defects, most probably located at the interface Co/STO interface which may be rougher due to the *ex-situ* deposition of Co top electrode, but also the intrinsic electronic asymmetry of Co/STO and STO/LCMO interfaces can be at the origin of the observed decrease of TMR with temperature.

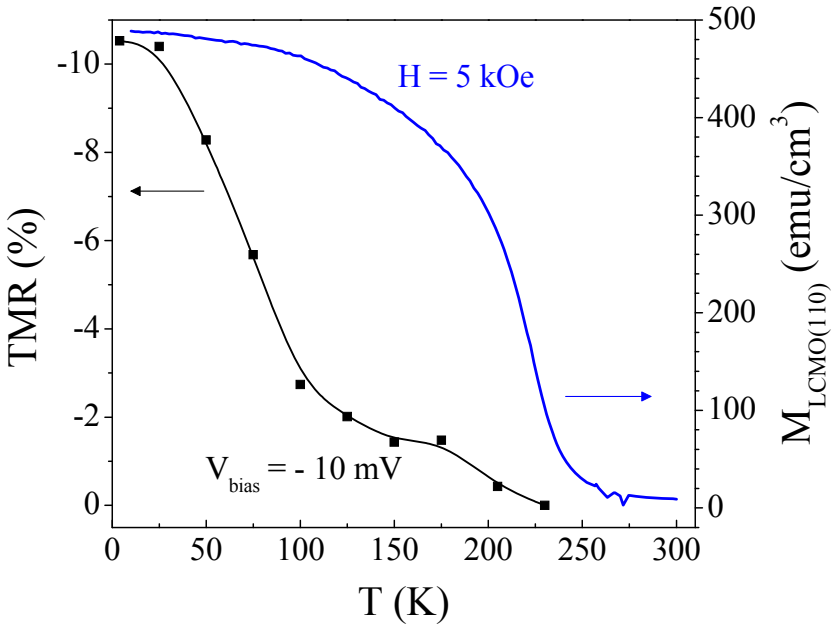

Figure 6.33. TMR ratio measured (symbols) at V_{dc} = -10 mV on a nanojunction on STO(4 nm)/LCMO(25 nm)//STO(110) bilayer and magnetization dependence on temperature (line) measured on bare LCMO(110) electrode at 5 kOe of in-plane magnetic field.

In summary, we have fabricated nanojunctions based on STO/LCMO//STO (001) and (110) bilayers by nanoindentation, with final Co top electrodes. Magnetotransport experiments indicate that in (001) and (110) nanojunctions noticeable TMR is measured at low temperature. However, the number of junctions successfully measured is very few, and further devices need to be fabricated. Nevertheless, from a (110) nanojunction we have obtained several clues about the relevance of the use of Co electrode as ferromagnetic top electrode, according to the asymmetric bias dependence of the TMR values. The TMR ratio vanishes at lower temperature than the T_C of bare LCMO(110) electrode, which may be caused by the loss spin polarization by interface roughness (more relevant in the Co/STO interface) or by the electronic asymmetry of Co and LCMO bands. From these first measurements on LCMO(110) based MTJs, symmetric devices, using both half metallic electrodes, might be necessary in order to fully exploit the high transition temperature of bare LCMO(110) electrodes and study the possible role of the LCMO/STO(110) interfaces on the final device functionality.

References

[1] M. Bibes, Ll. Balcells, S. Valencia, J. Fontcuberta, M. Wojcik, E. Jedryka, and S. Nadolski, Phys. Rev. Lett. **87,** 067210 (2001); M. Bibes, S. Valencia, Ll. Balcells, B. Martínez, J. Fontcuberta, M. Wojcik, S. Nadolski, and E. Jedryka, Phys. Rev. B **66**, 134416 (2002)

[2] A. A. Sidorenko, G. Allodi, R De Renzi, G. Ballestrino, and M. Angeloni, Phys. Rev. B **73**, 054406 (2006)

[3] J. P. Renard and A. Anane, Mater. Sci. Eng. B **63**, 22 (1999)

[4] J. H. Vleck, Phys. Rev. **45**, 405 (1934)

[5] P. S. Bagus, A. J. Freeman, and F. Sasaki, Phys. Rev. Lett. **30**, 850 (1973); E.-K. Viinikka, and Y. Öhrn, Phys. Rev. B **11**, 4168 (1975)

[6] K. Okada, A. Kotani, and B. T. Thole, J. Electron Spectrosc. Relat. Phenom. **58**, 325 (1992)

[7] L. Zhong Zhao and V. Young, J. Electron Spectrosc. Relat. Phenom. **34**, 45 (1984)

[8] T. Saitoh, A. E. Bocquet, T. Mizokawa, H. Namatame, A. Fujimori, M. Abbate, Y. Takeda, and M. Takano, Phys. Rev. B **51**, 13942 (1995)

[9] V. R. Galakhov, M. Demeter, S. Bartkowski, M. Neumann, N. A. Ovechkina, E. Z. Kurmaev, N. I. Lobachevskaya, Ya. M. Mukovskii, J. Mitchell, and D. L. Ederer, Phys. Rev. B **65**, 113102 (2002)

[10] E. Beyreuther, S. Grafstrom, L. M. Eng, C. Thiele, and K. Dörr, Phys. Rev. B **73**, 155425 (2006)

[11] M. Oku, K. Hirokawa, and S. Ikeda, J. Electron Spectectrosc. Relat. Phenom. **7**, 465 (1975)

[12] J.-L. Maurice, D. Imhoff, J.-P. Contour, and C. Colliex, Philos. Mag. **86**, 2127 (2006)

[13] K. Dörr, T. Walter, M.Sahana, K.-H. Müller, K. Nenkov, K. Brand, and L. Schultz, J. Appl. Phys. **89**, 6973 (2001); M.Sahana, T. Walter, K. Dörr, K.-H. Müller, D. Eckert, and K. Brand, J. Appl. Phys. **89**, 6834 (2001)

[14] M. Izumi, Y. Ogimoto, Y. Okimoto, T. Manako, P. Ahmet, K. Nakajima, T. Chikyow, M. Kawasaki, and Y. Tokura, Phys. Rev. B **64**, 964429 (2001)

[15] H. Yamada, M. Kawasaki, Y. Ogawa, and Y. Tokura, Appl. Phys. Lett. **81**, 4793 (2002)

[16] V. García, M. Bibes, A. Barthélémy, M. Bowen, E. Jacquet, J.-P-Contour, and A. Fert, Phys. Rev. B **69**, 052403 (2004)

[17] H. Kumigashira, A. Chikamatsu, R. Hashimoto, M. Oshima, T. Ohnishi, M. Lippmaa, H. Wadati, A. Fujimori, K. Ono, M. Kawasaki, and H. Koinuma, Appl. Phys. Lett. **88**, 192504 (2006)

[18] J. J. Kavich, M. P. Warusawithana, J. W. Freeland, P. Ryan, X. Zhai, R: H. Kodama, and J. N. Eckstein, Phys. Rev. B **76**, 014410 (2007); J. W. Freeland, J. J. Kavich, K. E. Gray, L. Ozyuzer, H. Zheng, J. F. Mitchell, M. P. Warusawithana, P. Ryan, X. Zhai, R: H. Kodama, and J. N. Eckstein, J. Phys.: Condens. Matter **19**, 315210 (2007)

[19] H. Zenia, G. A. Gehring, and W. M. Temmerman, New J. Phys. **9**, 105 (2007)

[20] L. Brey, Phys. Rev. B **75**, 104423 (2007)

[21] A. Chikamatsu, H. Wadati, H. Kumigashira, M. Oshima, A. Fujimori, M. Lippmaa, K. Ono, M. Kawasaki, and H. Koinuma, Phys. Rev. B **76**, 201103 (2007)

[22] J. M. Alonso, R. Cortés-Gil, L. Ruíz-González, J. M. González-Calbet, A. Hernando, M. Vallet-Regí, M. E. Dávila, and M. C. Asensio, Eur. J. Inorg. Chem. 3350 (2007)

[23] S. Yuasa, T. Nagahama, A. Fukushima, Y. Suzuki, and K. Ando, Nature Mat. **3**, 868 (2004)

[24] W.H. Butler, X.G. Zhang, T.C. Schulthess, and J.M. MacLaren, Phys. Rev. B **63**, 054416 (2001)

[25] M. Viret, M. Drouet, J. Nassar, J.P. Contour, C. Fermon, and A. Fert, Europhys. Lett. **39**, 545 (1997)

[26] J.Z. Sun, L. Krusin-Elbaum, P.R. Duncombe, A. Gupta, and R.B. Laibowitz, Appl. Phys. Lett. **70**, 1769 (1997)

[27] J.M. De Teresa, A. Barthélémy, A. Fert, J.P. Contour, R. Lyonnet, F. Montaigne, P. Seneor, and A. Vaurès, Phys. Rev. Lett. **82**, 4288 (1999)

[28] M. Klaua, D. Ullmann, J. Barthel, W. Wulfhekel, J. Kirschner, R. Urban, T. L. Monchesky, A. Enders, J. F. Cochran, and B. Heinrich, Phys. Rev. B **64**, 134411 (2001)

[29] M. Bibes, K. Bouzehouane, A. Barthélémy, M. Besse, S. Fusil, M. Bowen, P. Seneor, J. Carrey, V. Cros, A. Vaurès, J. P. Contour, and A. Fert, Appl. Phys. Lett. **83**, 2629 (2003)

[30] D. Xu, G. D. Watt, J. N. Harb, and R.C. Davis, Nanoletters **5**, 571 (2005)

[31] W. Wang, T. Lee, and M. A. Reed, Phys. Rev. B **68**, 035416 (2003)

[32] T. Dimopoulos, V. Da Costa, C. Tiusan, K. Ounadjela, and H.A.M. van den Berg, J. Appl. Phys. **89**, 7371 (2001)

[33] Y. Ando, H. Kameda, H. Kubota, and T. Miyazaki, J. Appl. Phys. **87**, 5206 (2000)

[34] E. Z. Luo, S.K. Wong, A.B. Pakhomov, J.B. Xu, I.H. Wilson, and C.Y. Wong, J. Appl. Phys. **90**, 5202 (2001)

[35] V. Da Costa, C. Tiusan, T. Dimopoulos, and K. Ounadjela, Phys. Rev. Lett. **85**, 876 (2000)

[36] V. Da Costa, Y. Henry, F. Bardou, M. Romero, and K. Ounadjela, Eur. Phys. J. B **13**, 297 (2000)

[37] F. Houzé, R. Meyer, O. Schneegans, and L. Boyer, Appl. Phys. Lett. **69**, 1975 (1996)

[38] D.W. Reagor, S.Y. Lee, Y. Li, and Q.X. Jia, J. Appl. Phys. **95**, 7971 (2004)

[39] J. Robertson, J. Vac. Sci. Technol. B **18,** 1785 (2000) (Using S = 0.3 and $\phi_{NDL} \approx 3.9$ eV)

[40] J.G. Simmons, J. Appl. Phys. **34**, 1963 (1963)

[41] J.G. Simmons, J. Phys. D: Appl. Phys. **4**, 613 (1971)

[42] J.F. Scott, Integrated Ferroelectrics **42**, 1 (2002)

[43] J.D. Baniecki, T. Shioga, K. Kurihara, and N. Kamehara, J. Appl. Phys. **94**, 6741 (2003)

[44] T. Tanaka, K. Matsunaga, Y. Ikuhara, and T. Yamamoto, Phys. Rev. B **68**, 205213 (2003)

[45] J. M. De Teresa, A. Barthélémy, A. Fert, J. P. Contour, R. Lyonnet, F. Montaigne, P. Seneor, and A. Vaurès, Phys. Rev. Lett. **82**, 4288 (1999)

[46] M. Jullière, Phys. Lett. **54A**, 225 (1975)

[47] Co has a negative spin polarization at the Fermi level, as predicted by F. Batallan, I. Rosenman, and C. B. Sommers, Phys. Rev. B **11**, 545 (1975), and by Andreev reflection experiments [S. K. Upadhyay, A. Palanisami, R. N. Louie, and R. A. Buhrman, Phys. Rev. Lett. **15**, 3247 (1998)] it was measured to be 0.37.

[48] D. R. Lide, *Handbook of Chemistry and Physics*, 72nd Edition (CRC Press, Boca Ratón FL, USA), pages 12-97

[49] W. F. Brinkman, R. C. Dynes, and J. M. Rowell, J. Appl. Phys. **41**, 1915 (1970)

[50] F. Batallan, I Rosenman, and C. B. Sommers, Phys. Rev. B **11**, 545 (1975)

[51] A. M. Bratkovsky, Phys. Rev. B **56**, 2344 (1997)

[52] M. Bowen, J.-L. Maurice, A. Barthélémy, M. Bibes, D. Imhoff, V. Bellini, R. Bertacco, D. Wortmann, P. Seneor, E. Jacquet, A. Vaurés, J. Humbert, J.-P-Contour, C. Colliex, S. Blügel, and P. H Dederichs, J. Phys.: Condens. Matter **19**, 315208 (2007)

7 Appendix I

7.1 Magnetotransport propeties of (110) $La_{0.95}Ag_{0.05}MnO_3$ films

Anisotropic magnetoresistance (AMR) has been previously introduced as a major effect occurring in ferromagnetic films in Ch5 for (110) LCMO films. The AMR is defined as the change in the resistance when magnetization is parallel or perpendicular to the current flow (AMR ~ $\rho_{//} - \rho_{\perp}$). An interesting result in LCMO (110) filsm is the different [001] and [1-10] AMR ratio, which has been measured at a fixed temperature and at varied fields. It was shown that AMR along [001] was negative whereas along the [1-10] direction was positive. With the study of another kind of manganite films, in this case (110) $La_{0.95}Ag_{0.05}MnO_3$(LAMO), a more complete knowledge of the AMR change of sign and its meaning is expected to be achieved.

Putting the performed experiments into the appropriate context, generic measurements of AMR dependence on temperature present a characteristic peak when approximating T_C, which has not been still completely understood [1]. Spin–orbit coupling Hamiltonian is expressed as $H_{SO} \approx \Delta_{so}\mathbf{L}\cdot\mathbf{S}$; where **L** and **S** are the orbital and magnetic moments, respectively. As the Curie temperature is approached from below, the double-exchange mechanism is somewhat suppressed and the Jahn-Teller (JT) electron-lattice becomes more relevant. Within this picture it has been suggested the stabilization of the JT Mn^{3+} ions at the ferromagnetic to paramagnetic transition, which unquenches the orbital moment **L** ($\mathbf{L} \neq 0$), which in transition metal ions is typically **L** = 0 due to the effect of the crystal field, and increases the spin-orbit coupling.and thus

the AMR amplitude [2]. In contrast, in a ferromagnetic (FM) metallic oxide that does not include JT ions, such as $SrRuO_3$, the AMR displays a monotonic decay when approaching the Curie [3]. Unquenching of the orbital moment around T_C could give rise in manganites to the appearance of an anisotropy in H_{SO} and it could thus be expected AMR to be anisotropic.

With the purpose of studying the anisotropy of H_{SO} already observed in LCMO (110) films, different (110) manganite film have been investigated. The patterning along the [001] and [1-10] directions allowed to show not only the AMR itself but also its anisotropy. Furthermore, from the different AMR temperature dependences, it has been deduced a possible scenario for the occurrence of the different response on the basis of an anisotropic spin-orbit coupling and spin-dependent scattering effects.

7.1.1 Growth and structural characterization

Epitaxial $La_{0.95}Ag_{0.05}MnO_3$ (LAMO) films (300 nm thick) were grown onto (110) STO substrates, by two step procedure including MOCVD of $La_{0.95}MnO_3$ films at 800^{o}C and the silver vapor treatment in the oxygen containing atmosphere also at 800^{o}C as described elsewhere [4]. Also extensive structural studies have been reported in this very same reference. As this part of the work has been developed by the group of Gorbenko and Kaul, the only importance fact to recall here is that LAMO (110) films are fully relaxed and have the rhombohedral symmetry as in bulk [5]. X-ray diffraction (XRD) including symmetric and asymmetric $\theta/2\theta$ scans and rocking curves was used to generate reciprocal space mappings (RSM) providing data on the out-of plane and in-plane lattice parameters ($a = 0.551$ nm, $c = 1.342$ nm for the hexagonal setting). The partly resolved doublets were observed for pseudocubic (110) and (111) reflection zones with only singlets for (100) pseudocubic reflection zones in agreement with the rhombohedral distortion of the perovskite lattice. The strain relaxation happens during silver vapor treatment resulting in the silver and oxygen diffusion in the film. The difference between the lattice symmetry of rhombohedral LAMO films, as for Sr-doped $LaMnO_3$ ones, and that of orthorhombic LCMO films [2,6] is due to the difference in the ionic radius of Ag^+ and Sr^{2+} compared to that of Ca^{2+}($r(Ag^+) \sim r(Sr^{2+}) = 1.44$ Å and $r(Ca^{2+}) = 1.34$ Å). It is important to note that the rhombohedral symmetry of LAMO, as it happened for LSMO, is expected to suppress the long range cooperative JT orbital and charge ordering.

7.1.2 Magnetotransport

In order to perform simultaneous magnetotransport measurements on the very same film but with current along different in-plane directions, two pieces of a (10x10) mm^2 film were obtained and previously patterned in Hall bar configuration by photolithography and wet etching. Typical bar width is 1 mm. Electric measurements were performed using PPMS from Quantum Design by four probes using a low frequency (10Hz) ac current, as described for LCMO (110) films in Ch5. Magnetic measurements performed on similar unpatterned LAMO films revealed that above 10 K the magnetic loops are closed at fields above 4 kOe for field configurations either perpendicular to the film plane or in-plane.

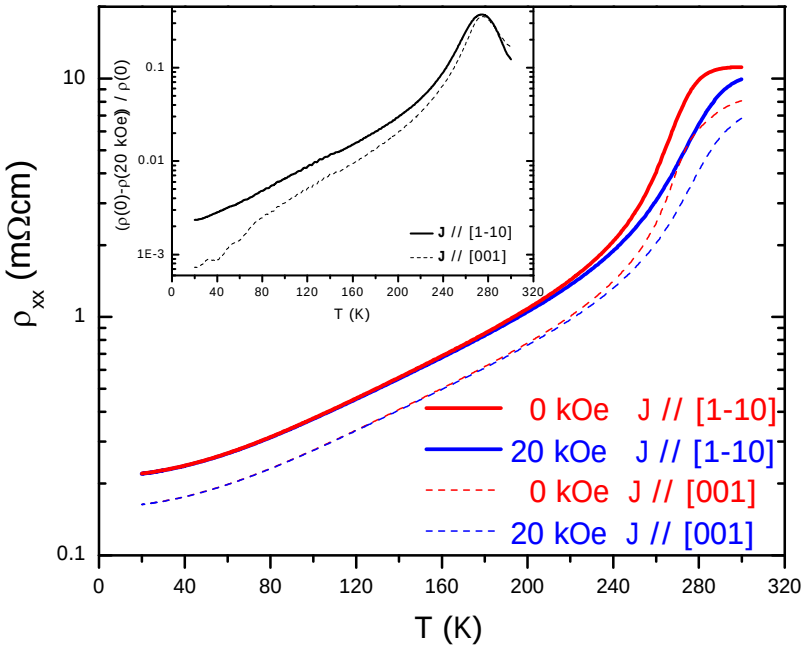

Figure 7.1. Temperature dependence down to 20 K of the resistivity (main panel) measured along [001] (dash lines) and [1-10] (dark lines) directions with H = 0 (red lines) and 20 kOe (blue lines) in-plane field. In the inset, the plot of the magnetoresistance curve obtained from these curves is shown.

First, in Figure 7.1 (main panel) the corresponding temperature dependences of longitudinal resistivty (ρ_{xx}) for current **J** parallel to [001] and [1-10] directions are shown, measured at zero-field (red lines) and under 20 kOe of in-plane magnetic field (blue lines). The onset of the metallic behaviour is well visible at about T_{MI} ~ 280 K. The measured resistivity is somewhat smaller (about a 30 % at 300 K) along [001] than along [1-10]. This anisotropic resistivity is comparable to what is measured in epitaxial

films of LCMO (110) already reported [2][6]. It can be appreciated in the inset of Figure 7.1, where the temperature dependence of the magnetoresistance MR(20 kOe) = [ρ_{xx}(0)-ρ_{xx}(20 kOe)]/ρ_{xx}(0) is plotted, that MR displays a well defined maximum at around 280 K, being almost identical the value for each direction. At lower temperature, MR displays a distinct behaviour depending on the direction of current flow, being about a 50 % larger along the [1-10] track that along the [001] one.

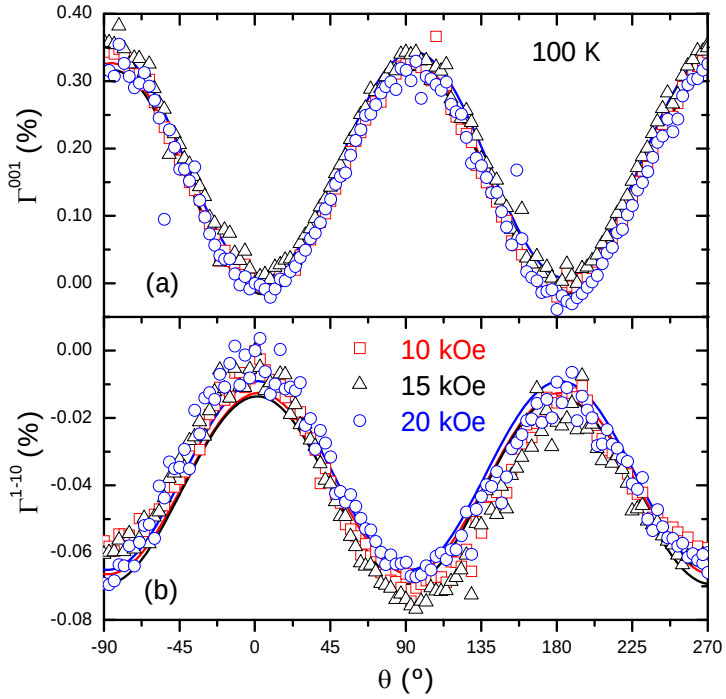

Figure 7.2. Angular dependence of the magnetoresistance Γ(θ) = [ρ(θ)-ρ(0)]/ρ(0) measured at 100 K under various in-plane magnetic fields applied at an angle θ with respect to the measuring current **J**. (a) and (b) correspond to **J** // [001] and **J** // [1-10] respectively.

Turning to AMR studies, in order to perform them, films were simultaneously measured with the current density (**J**) applied parallel to the [001] and [1-10] directions and the magnetic field was rotated in-plane.

In Figure 7.2 the angular dependence of the resistivity Γ_{hkl} = [ρ(θ)-ρ(0)]/ρ(0) are shown, being θ the angle between the applied magnetic field **H** and the current **J** and with **J** along [001] (Figure 7.2a) and [1-10] (Figure 7.2b), measured at various fields (H = 10, 15 and 20 kOe) at 100 K. For all fields, the angular dependence of Γ_{hkl} is well described by $\Gamma_{hkl} \sim \cos^2\theta$, as illustrated by the fitted solid lines through the data. It has to be noted that in general $\Gamma \approx (\rho_{//}-\rho_{\perp})\cos^2\phi$, where ϕ is the angle between **J** and the magnetization direction **M**, as explained in detail in Ch5. The goodness of the fits of

Figure 7.2 indicate that at the fields of measure (H > 10 kOe), $\theta = \phi$ and thus **M** // **H**, implying that along both directions the film magnetization is saturated and the measured AMR is not masked by single-ion anisotropy, shape anisotropy or other sources of magnetic anisotropy. Besides, comparing the amplitude of both set of AMR curves, the $\Gamma_{1\text{-}10}$ one is much smaller than that of Γ_{001}, being $\Gamma_{1\text{-}10} \sim 0.06$ % and $\Gamma_{001} \sim 0.3$ %).

Detailed inspection of data in Figure 7.2 reveals that, at 100 K the oscillations of Γ_{001} and $\Gamma_{1\text{-}10}$ have an opposite phase. That is, whereas for Γ_{001} the resistivity is at a minimum for $\theta = 0$ deg ($\rho^{001}_{//} < \rho^{001}_{\perp}$) this is not the case for $\Gamma_{1\text{-}10}$, where the resistivity is at a maximum ($\rho^{1-10}_{//} > \rho^{1-10}_{\perp}$). Therefore, data in Figure 7.2 indicate that there is an anisotropy in the AMR response of the LAMO (110) films. As the origin of the AMR traces back to the atomic spin-orbit coupling and the asymmetry of spin-up and spin-down scattering events [7] the above observation provides a new insight into the physics of manganites.

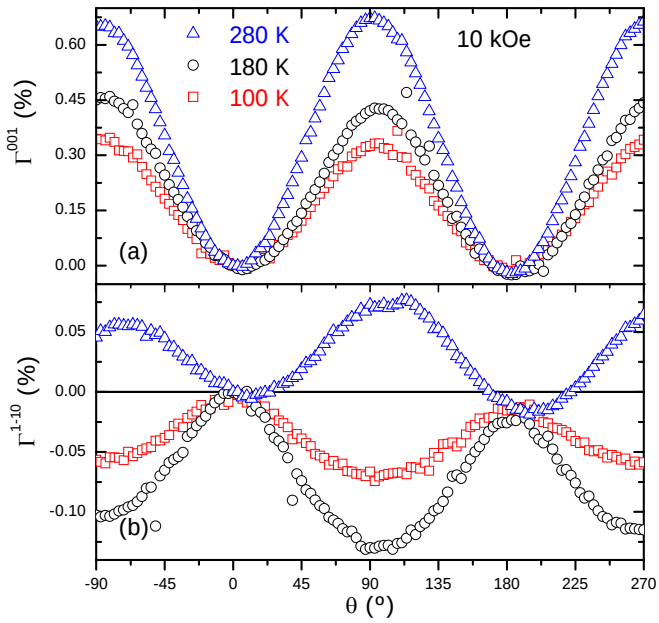

Figure 7.3. Angular dependence of the magnetoresistance Γ(θ) measured at 10 kOe at various temperatures.(a) and (b) correspond to current parallel to [001] and current parallel to [1-10] respectively.

In Figure 7.3 Γ_{001} and $\Gamma_{1\text{-}10}$ curves measured at several temperatures above 100 K are plotted. Looking at the amplitude of AMR effect along [001] direction (Figure 7.3a), the amplitude of Γ_{001} ($AMR^{001} = (\rho_{//}\text{-}\rho_{\perp})^{001}/\rho^{001}_{av}$) shows an increase when temperature drops, reaching a value of about $\Gamma_{001} \sim 0.6$ % close to the temperature

where the metal-insulator transition (T_{MI}) occurs and where the longitudinal magnetoresistance (inset of Figure 7.1) has also its maximum. At higher temperature, the amplitude of Γ_{001} is reduced (see Figure 7.4 below) as expected as the sample becomes paramagnetic. On the other hand, in Figure 7.3b the amplitude of $\Gamma_{1\text{-}10}$ ($AMR^{1\text{-}10} = (\rho_{//}\text{-}\rho_{\perp})^{1-10}/\rho^{1-10}{}_{av}$) displays a non monotonic behaviour. It is positive at 100 K, as described above, and increases upon heating; but when approaching T_{MI}, it changes its sign and becomes negative thus mimicking AMR^{001}. Figure 7.4, where a plot of AMR^{001} and $AMR^{1\text{-}10}$ data recorded at several temperatures are shown, clearly illustrates that for [1-10] it occurs a non monotonic behaviour of AMR, and thus the asymmetry for **J** // [001] and **J** // [1-10].

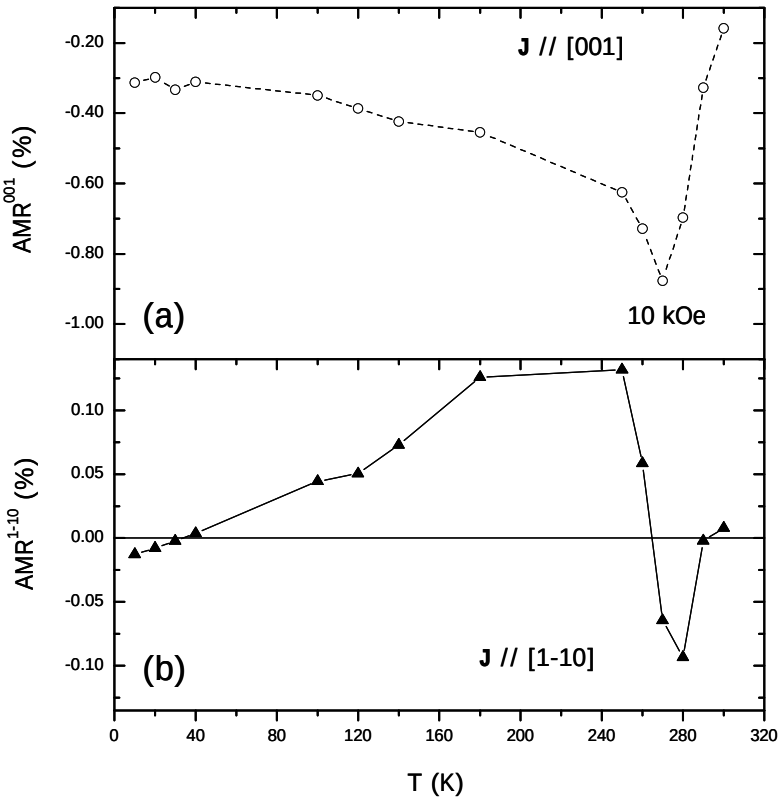

Figure 7.4. Temperature dependence of the anisotropic magnetoresistance $AMR = (\rho_{//} - \rho_{\perp})/\rho_{av}$ measured with (a) current parallel to [001] and (b) current parallel to [1-10].

The peak of AMR^{hkl} at around T_C is well visible for both orientations and it has the same sign (negative), that is $\rho^{001}{}_{//} < \rho^{001}{}_{\perp}$ and $\rho^{1-10}{}_{//} < \rho^{1-10}{}_{\perp}$. This is in agreement with reports on LCMO films [2][6]. The occurrence of a maximum of AMR which mimics that of the MR, as suggested by M. Bibes at *al.* [2] and G. Herranz et *al.* [3], can

be related to the unquenching of orbital moment **L** (**L** ≠ 0) close to the metal-insulator transition. However, the observation of a distinct sign of AMR effect for **J** along different in-plane directions, $AMR^{001} < 0$ and $AMR^{1\text{-}10} > 0$ at low temperature, and the change of sign of $AMR^{1\text{-}10}$ from positive to negative at higher temperature remains intriguing. Considering the experimental results shown in Ch5 and the simulations performed to generate the AMR temperature peak, we can generalize the conclusions obtained for LCMO to LAMO and even for future manganite films. If we consider that a one conduction channel can adequately describe the manganite conduction, using the model presented by Malozemoff [8] to this system obliges us to change the energy diagram of the system, and for instance the exchange energy should go to zero when approaching the T_C. But, although the general temperature dependence of the AMR can be described with this approximation, the different sign of the AMR measured within the (110) plane and the change of sign at different temperatures cannot be explained with this approach. We suggest that the different symmetry of the (110) plane can play a major role in the scattering events and thus in the AMR sign.

In summary, anisotropic magnetoresistance along [001] and [1-10] directions in LAMO (110) epitaxial thin films grown on (110) STO, display an anisotropic behaviour that helps to understand that of LCMO (110) films. Along the [001] the AMR^{001} amplitude is negative, indicating that $\rho^{001}_{//} < \rho^{001}_{\perp}$, in agreement with results reported for (001) LCMO films, increases with temperature and displays a maximum close to the metal-insulator transition. In contrast, $AMR^{1\text{-}10}$ is positive at low temperature, indicating that $\rho^{1-10}_{//} > \rho^{1-10}_{\perp}$, switching to $\rho^{1-10}_{//} < \rho^{1-10}_{\perp}$ at temperatures close to the meta-insulator transition. A possible explanation of the temperature dependent spin-orbit coupling and spin-dependent scattering effects is expected to be also applicable to LCMO (110) films.

References

[1] M. Ziese, and S. P. Sena, J. Phys. Condens. Matter **10**, 2727 (1998)

[2] M. Bibes, V. Laukhin, S. Valencia, B. Martínez, J. Fontcuberta, O. Yu Gorbenko, A. R. Kaul, and J. L. Martínez, J. Phys. Condens. Matter **17**, 2733 (2005)

[3] G. Herranz, F. Sánchez, M. V. García-Cuenca, C. Ferrater, M. Varela, B. Martínez, and J. Fontcuberta, J. Magn. Magn. Mater. **272-276**, 517 (2004)

[4] O.Yu. Gorbenko, A. R. Kaul, A. A. Kamenev, O. V. Melnikov, I. E. Graboy, N. A. Babushkina, A. N. Taldenkov, and A.V. Inyuskin, J. Cryst. Growth **275**, e2453 (2005)

[5] O.Yu. Gorbenko,O. V. Melnikov, A. R. Kaul, A. M. Balagurov, S. N. Bushmeleva, L. I. Koroleva, and R. V. Demin, Mater. Sci. Eng. B **116**, 64 (2005)

[6] V. S. Amaral, A.A.C.S. Lourenço, J. P. Araújo, P. M. Pereira, J. B. Sousa, P. B. Tavares, J. M. Vieira, E. Alves, M. F. da Silva, and J. C. Soares, J. Appl. Phys. **87** 5570 (2000)

[7] I. A. Campbell, and A. Fert, Ferromagnetic Materials, Vol. 3, E.P. Wohlfarth, North-Holland, 1982, p 747

[8] A. P. Malozemoff, Phys. Rev. B **34**, 1853 (1986)

8 Appendix II

8.1 $La_{2/3}Sr_{1/3}MnO_3$ (LSMO) films: epitaxial growth and magnetic properties

$La_{2/3}Sr_{1/3}MnO_3$ (LSMO) is a metallic ferromagnetic manganite [1][2] with a Curie temperature of ≈ 360 K [1]. The ferromagnetism of this material arises from the double-exchange, as explained in Ch1, where electrons from the 3d bands of Mn ions (in mixed valence state 3+/4+) hop from Mn^{3+} to Mn^{4+} through O^{2-} ions (Mn^{3+}-O^{2-}-Mn^{4+} electron hopping). Fully spin polarization of the conduction band is thus expected in this material, as for the Ca-doped manganites. Consequently, LSMO has received much attention due to its potential usefulness as electrode in spintronics devices as magnetic tunnel junctions [4].

Aiming to extent the study of the influence of the plane of growth onto the structural and functional properties of manganite films, we have grown LSMO films on (001) and (110) $SrTiO_3$ substrates and investigate the structural and magnetic properties of these films. We expect a less significant effect of the epitaxial stress in the LSMO/STO system due to the lower lattice mismatch of the LSMO and STO compared to that of LCMO and STO: LSMO pseudocubic parameter is a_{LSMO} ~ 3.890 Å and STO parameter is a_{LSMO} ~ 3.905 Å, thus the lattice mismatch is $f = (a_{LSMO} - a_{STO})/a_{LSMO}$ = -0.4 %.

In this appendix, results on the epitaxial growth and structural characterization of LSMO films on (001) and (110) STO substrates are presented. The magnetic properties of these films are also shown. We discuss the possible mechanisms of the

magnetic anisotropy in the light of the work performed on (001) and (110) LCMO films already presented as well as the origin of the differential Curie temperature and saturation magnetization values of (001) and (110) LSMO films.

8.1.1 Epitaxial growth: film thickness, morphology and structural characterization

LSMO films were grown by pulsed laser deposition (PLD) at the Dept. de Fisica Aplicada i Òptica, at the Universitat de Barcelona, using a KrF excimer laser as described in Ch2. Using a stoichiometric target, we performed a series of PLD depositions at different substrate temperature (650 C-700 C-750 C) and oxygen pressure during the deposition (pure oxygen pressure of 0.10 mbar, 0.25 mbar, and 0.40 mbar) in order to optimize the morphology of the films and to vary the oxygen stoichimetry of the films. The frequency of the laser was set to 5 Hz and the number of laser pulses was 5000; each film deposition was simultaneously performed onto (001) and (110) STO substrates. The results presented in this appendix correspond to the samples listed in Table 8.1.

Table 8.1. List of LSMO films studied in this chapter. The deposition substrate temperature (Td) and oxygen pressure [$P_d(O_2)$] are also indicated.

Sample	Substrate	Sample	Substrate	Thickness (nm)	T_d (C)	$P_d(O_2)$ (mbar)
lsmo19	STO(001)	lsmo20	STO(110)	78	700	0.10
lsmo22	STO(001)	lsmo23	STO(110)	78	700	0.25
lsmo22	STO(001)	lsmo26	STO(110)	78	700	0.40
lsmo40	STO(001)		STO(110)	78	650	0.40
		lsmo35	STO(110)	78	750	0.40

Thickness determination and surface morphology

The thickness of these films was investigated by X-ray reflectometry (XRR) measurements. Representative examples of the XRR spectra collected for all the LSMO films are shown in Figure 8.1a. The spectra present oscillations with similar period for all films, independently of the oxygen pressure or substrate temperature. With the angular position of each minimum in the XRR spectra and fitting the minimum order, we could evaluate the thickness of the films, obtaining in all cases $\sim 78 \pm 3$ nm. The films shown in Figure 8.1a are lsmo22 [(001) film grown at 0.25 mbar $P(O_2)$] and

lsmo20 [(110) film grown at 0.10 mbar of $P(O_2)$]. It is remarkable that the oscillations are observed up to θ ~ 1.4 deg, following a soft exponential decay characteristic of flat surfaces. For the case of the (110) films, we probe that flat (110) surfaces are achieved using the PLD technique, and in Figure 8.1b an atomic force microscopy (AFM) image of lsmo20 surface clearly signal a low roughness (rms = 0.4 nm) and a morphology characterized by terraces and steps.

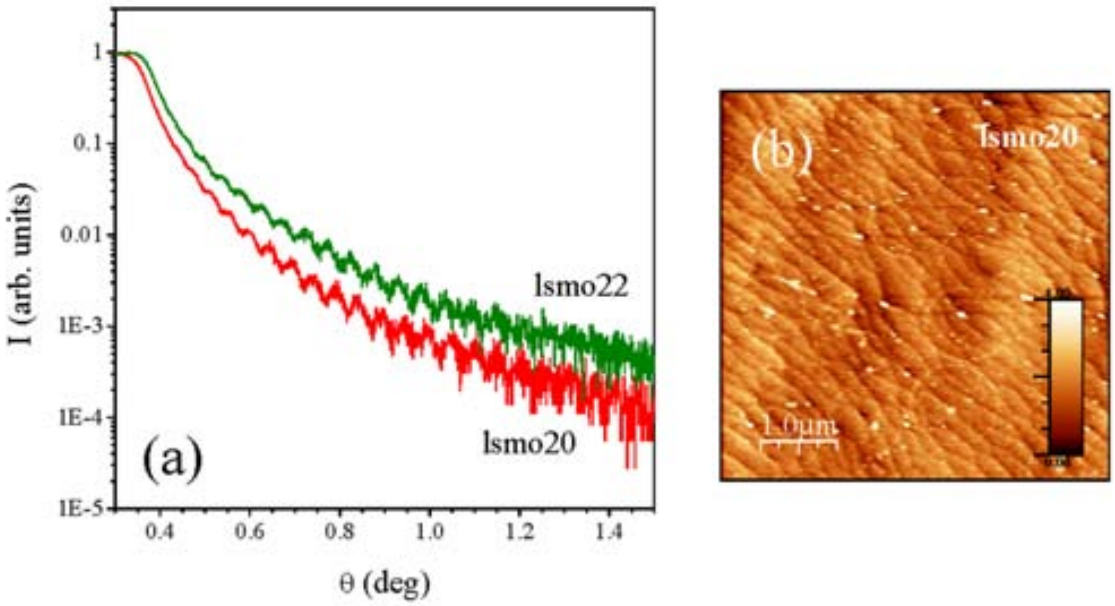

Figure 8.1. (a) Normalized XRR spectra from LSMO films: (110) LSMO film grown at 0.10 mbar of $P(O_2)$ (lsmo20) and (001) LSMO film grown at 0.25 mbar of P(O2) (lsmo22). (b) AFM (5x5) μm^2 image from lsmo20. The z-scale corresponds to 4 nm.

Structural characterization

(a) θ-2θ scans

To study the structure of these LSMO films, we first investigated the texture of the films performing θ-2θ scans. For the (001) and (110) films, the θ-2θ spectra for each film orientation included only (00*l*) and (*hk*0) peaks (being *h*, *k*, *l* the Miller indices) corresponding to the (001) and (110) texture, respectively. No traces of other phases were observed. The out-of-plane parameter of the films was calculated from the detailed zooms of the θ-2θ scans at large angle; the zooms for the 700 C (001) and (110) films are shown in Figure 8.2, being for the former around (004) peaks and for the latter around (330) peaks. We notice that for the STO single crystal but also for the LSMO films two peaks are observed for each reflection, corresponding to the two main emission lines of the Cu catode of the diffractometer. ($k_{\alpha 1}$ and $k_{\alpha 2}$). For both sets of films, for samples with increasing growth oxygen pressure, the diffraction peak shifts to

high angles. This fact is signalled in Figure 8.2a and b by arrows.The out-of-plane parameters were calculated from these spectra, and the resulting values are included in Table 8.2.

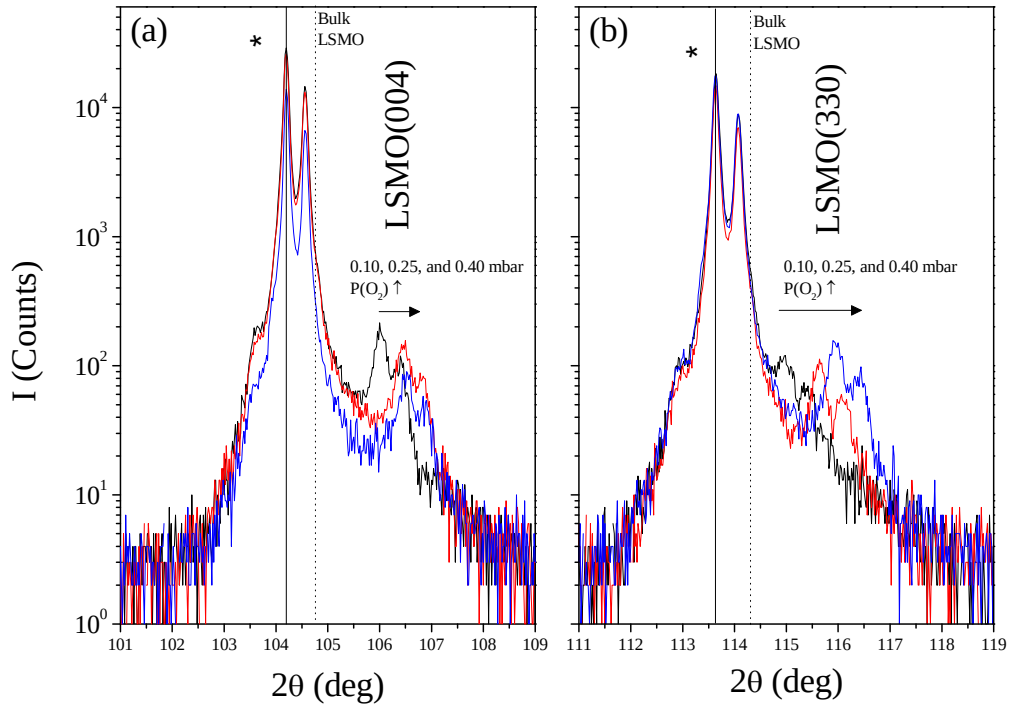

Figure 8.2. Zooms of complete θ-2θ scans, showing the substrate peaks (indicated by asterisks *) ad the film peak: (a) (004) peaks for (001) samples and (b) (330) peaks for (110) samples. The solid lines mark the angular position of the STO substrate and the dotted lines indicate the angular position corresponding to pseudocubic bulk LSMO parameter. The arrow signals the samples with increase of $P(O_2)$ during the growth.

Table 8.2. Out-of-plane parameter of LSMO films grown at 700 C (see Table 8.1) as a function of the deposition oxygen pressure [$P(O_2)$] for (001) and (110) films: d_{001} and $\sqrt{2}d_{110}$, respectively.

$P(O_2)$ (mbar)	(001)	(110)
	d_{001} (Å)	$\sqrt{2}d_{110}$ (Å)
0.1	3.857	3.875
0.25	3.847	3.862
0.4	3.845	3.855

(b) Reciprocal space maps (RSMs)

To fully characterize the LSMO unit cell of (001) and (110) films, the in-plane and out-of-plane parameter were explored performing RSMs around appropriate reflections. Similarly to the LCMO films (Ch4), for (001) films we studied the (103)

reflection and for the (110) films (130) and (222) reflections were measured. For this study, we present the results of the series of films grown at 700 C.of substrate temperature.

We start the analysis of the RSMs with the (001) samples. The RSMs on (001) samples were performed using Bruker diffractometer, working at the central area of the two dimensional detector ($\chi = 0$). In Figure 8.3, the RSMs around the (103) reflections indicate the presence of intense STO peaks and the LSMO peak appearing vertically aligned with the substrate. For these reflections, in-plane [100] direction and out-of-plane [001] direction are investigated. In all cases, the alignment of the film and substrate peaks signal that the in-pane unit cell parameter of film and substrate are equal. On the other hand, the out-of-plane parameters of the LSMO films, determined from the vertical position of the film and substrate peak, are substantially different from that of the STO. Inspecting the RSM from the different films, from Figure 8.3a to Figure 8.3b, the LSMO peak is more separated from the STO peak, a separation which is enhanced when inspecting higher oxygen pressure film RSM in Figure 8.3c. Therefore, the change in the oxygen pressure during film growth influenced the out-of-plane unit cell but not the in-plane parameter, and the films are independently of the oxygen pressure fully strained.

For the investigation of the unit cell parameters of the (110) samples, reflections with pure in-plane [1-10] and [001] directions were investigated. The study of the in-plane [1-10] direction was undertaken with (130) reflections, and that of the in-plane [001] direction wih the (222) reflections. The RSMs of these (110) samples were obtained with a MRD Philips diffractometer. In Figure 8.4 we include the RSMs of the (110) films grown under different oxygen pressure. Inspecting the in-plane parameter of the STO and LSMO peaks, in all cases we observe a complete vertical alignment of substrate and film unit cell, indicating that (110) films are fully strained along [1-10] and [001] in-plane directions. However, the LSMO peak appears at different vertical position for the samples grown under different oxygen pressure, which means that the out-of-plane distance depends on the oxygen pressure. In the low pressure film RSMs (Figure 8.4a and b), the LSMO peak is almost hidden underneath the STO peak, thus being the unit cell parameters of the LSMO film closer to those of the STO. For the intermediate oxygen pressure film (Figure 8.4c and d), the LSMO peak is more separated from the STO peak, still increasing this separation for the higher oxygen pressure film (Figure 8.4e and f).

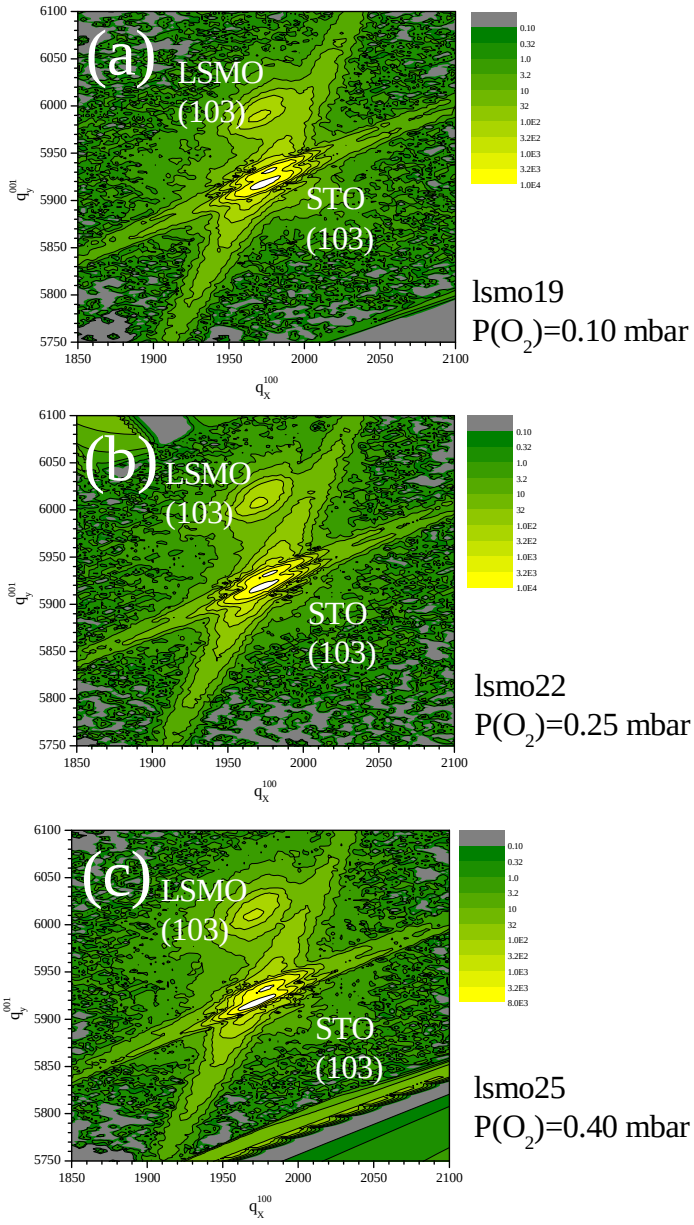

Figure 8.3. RSMs from (103) reflection of LSMO film and STO substrate for the (001) samples, being the films grown at different $P(O_2)$: (a) 0.10 mbar, (b) 0.25 mbar, and (c) 0.40 mbar.

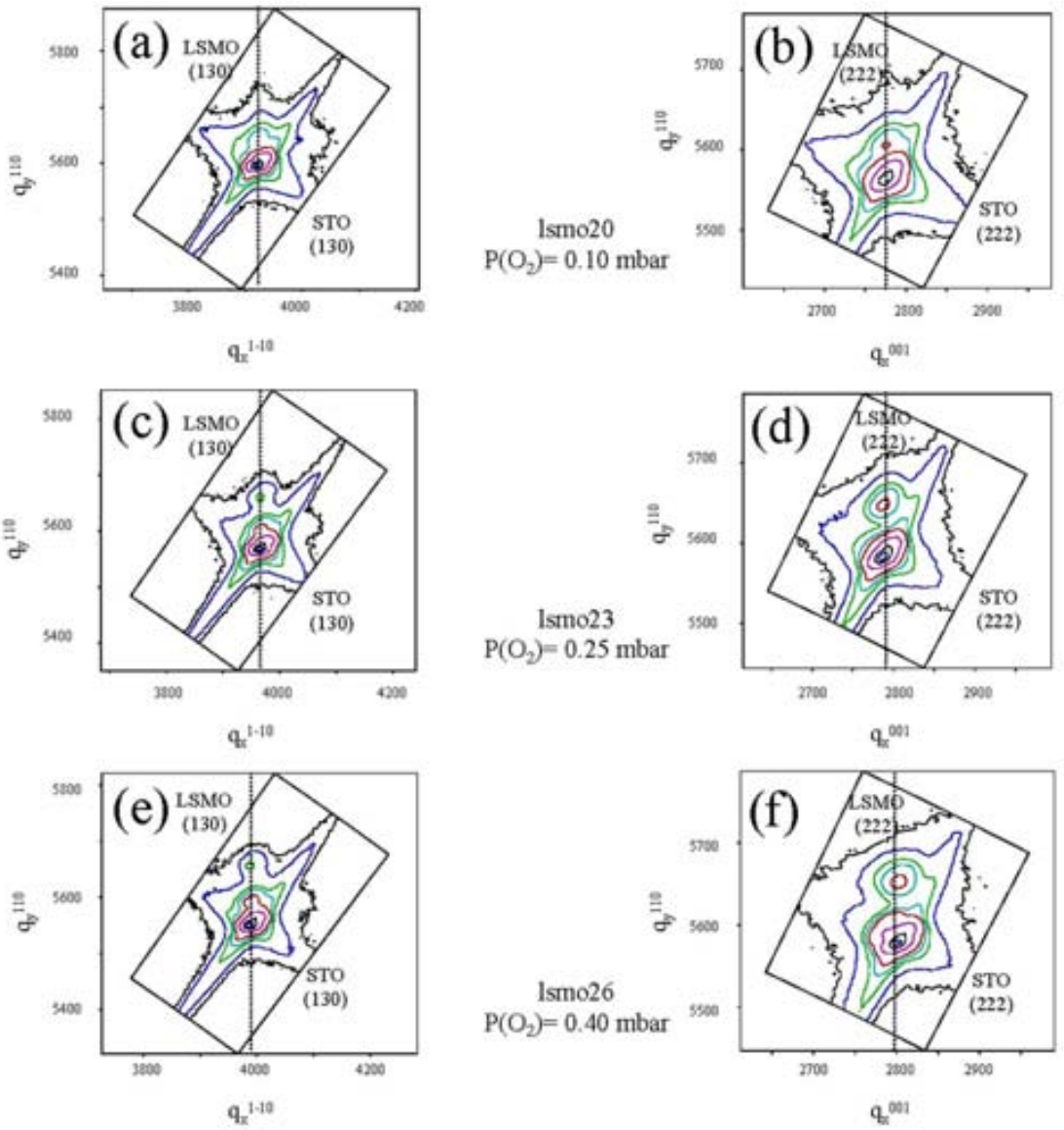

Figure 8.4. RSMs from (130) [(a), (c), and (e)] and (222) [(b), (d), and (f)] reflections of LSMO film and STO substrate for the (110) samples, being the films grown at different $P(O_2)$: [(a) and (b)] 0.10 mbar, [(c) and (d)] 0.25 mbar, and [(e) and (f)] 0.40 mbar.

We used the LSMO and STO peak positions in the RSMs from the (001) and (110) films to evaluate the unit cell interplanar distances. We recall the equivalency between the wave vectors and the crystallographic directions for the (001) and (110) films analyzed in detail for the LCMO films in Ch4 (eqs. 4.5-4.9). The resulting unit cell parameters are plotted in Figure 8.5 as a function of the oxygen pressure.

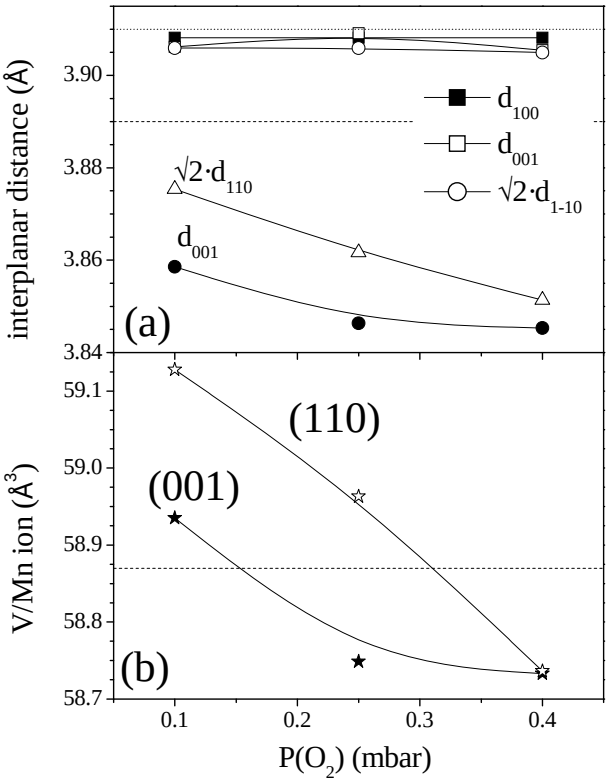

Figure 8.5. Oxygen pressure dependence of (a) the interplanar distances and (b) the unit cell volume for the (001) and (110) films. The dashed lines indicate the pseudocubic (a) unit cell parameter and (b) unit cell volume of bulk LSMO. To make interplanar distances comparable, for (001) films we plot d_{100} and d_{001} and for (110) films $\sqrt{2}d_{1\text{-}10}$, d_{001} and $\sqrt{2}d_{110}$.

The analysis of Figure 8.5 signals the results already observed from θ-2θ scans and RSMs: the out-of-plane (001) and (110) LSMO parameter depend on the oxygen pressure and the in-plane (001) and (110) LSMO parameters are clamped to those of the STO substrate. From Figure 8.5a, we note that the out-of-plane parameter of the (001) films is always lower than the corresponding value of the (110) films. This trend is conserved when computing the total unit cell volume shown in Figure 8.5b.

The mechanism underneath the changes in the out-of-plane parameter and consequentely in the unit cell volume of (001) and (110) films can be related to the oxygen content of the LSMO films. The oxygen pressure during deposition tunes the oxygen stoichiometry, thus the low oxygen pressure films may present a higher amount of oxygen vacancies. Within this scenario, with less oxygen anions on the LSMO lattice (virtually $LSMO_{3\text{-}\delta}$, being δ the concentration of vacancies) the lattice can be naturally expanded due to unbalanced charge (Coulomb repulsion), and this argument would

explain the increase of the out-of-plane parameter and unit cell volume in the low oxygen pressure films.

8.1.2 Magnetic properties

Low temperature hysteresis loops

The magnetic properties of LSMO films, and in particular, the saturation magnetization M_S and magnetic anisotropy, were investigated measuring the magnetization *vs* magnetic field. We present first the general results on the M_S measured at 10 K and the dependence on the oxygen pressure and films orientation.

Figure 8.6 the magnetic hysteresis loops obtained from (001) and (110) films indicate relevant differences among films with the same orientation but also between films gown under the same oxygen pressure. Inspecting Figure 8.6a, the (001) film grown under the lower oxygen pressure (squares) presents a strongly decreased M_S compared to the bulk value (~ 591 emu/cm^3). Upon studying films grown under higher deposition oxygen pressure, the M_S increases. For the (110) films, in the Figure 8.6b the curves indicate higher M_S for films with higher deposition oxygen pressure, although comparing the curves for the (001) and (110) films grown under 0.10 mbar of oxygen pressure (squares), the (110) film (open squares) presents higher M_S than that of the (001) film (close squares). This difference between the M_S of (001) and (110) films is also extended to the rest of samples.

Studying in detail the dependence of the magnetic hysteresis loops on the direction of applied magnetic field leads us to the knowledge of the in-plane magnetic anisotropy of (001) and (110) LSMO films. We present in Figure 8.7a in-plane magnetic hysteresis loops from a (001) film (lsmo40, see Table 8.1) and in Figure 8.7b in-plane magnetic hysteresis loops from a (110) film (lsmo35, see Table 8.1). For the (001) film (Figure 8.7a), the field was applied along the [100] and [110] directions, and the hysteresis loops indicate that coming from high field (magnetization is saturated along the applied field direction), the remnant magnetization is higher for field parallel to [110] direction (triangles) than for field along [100] direction. In fact, a square-like hysteresis loop is obtained for field along [110] direction, which signals that [110] direction corresponds to an easy magnetic axis. For the (110) film (Figure 8.7b), the differences between the loops recorded for field parallel to [1-10] or [001] direction are much evident: almost linear behavior (hard magnetic axis) at low field is obtained for

field parallel to [1-10] direction (circles), whereas a square-like loop (easy magnetic axis) is recorded when field is parallel to [001] direction (triangles). These results agree with the already shown hysteresis loops from (001) and (110) LCMO films; the anisotropy in that case was mainly caused by the magnetoelastic effects. In the LSMO films, thickness is the same for all samples, being the only variable parameter the film orientation. The (110) film loops clearly evidence the existence of a uniaxial in-plane magnetic anisotropy with easy [001] axis and hard [1-10] one. We center the discussion in the determination of easy and hard magnetic axis in the (001) samples. We note that following the same arguments as those developed in Ch5 (5.1.3 Magnetic anisotropy), the higher the stress the easier the direction. (001) films are fully strained films, the epitaxial strain along a crystallographic [*hkl*] direction (ε_{hkl}) is the same in all cases, and within the approximation of an isotropic magnetostriction ($\lambda_{hkl} = \lambda_{100}$), the relevant parameter to determine the magnetoelastic energy along a given [*hkl*] direction E^{hkl}_{me} is the Young moduli Y_{hkl}: $E^{hkl}_{me} = -3/2\ \lambda_{100} Y_{hkl}\ \varepsilon_{hkl}$. The Young moduli in manganite films are expected to depend on the crystallographic directions, as explained in detail in Ch1 (1.3.1 Elastic properties). From the Y_{hkl} values of the [100] and [110] directions, $Y_{110} > Y_{100}$, the higher stress and thus the lowest magnetoelastic energy is related to the [110] direction, where the easy magnetic axis is found.

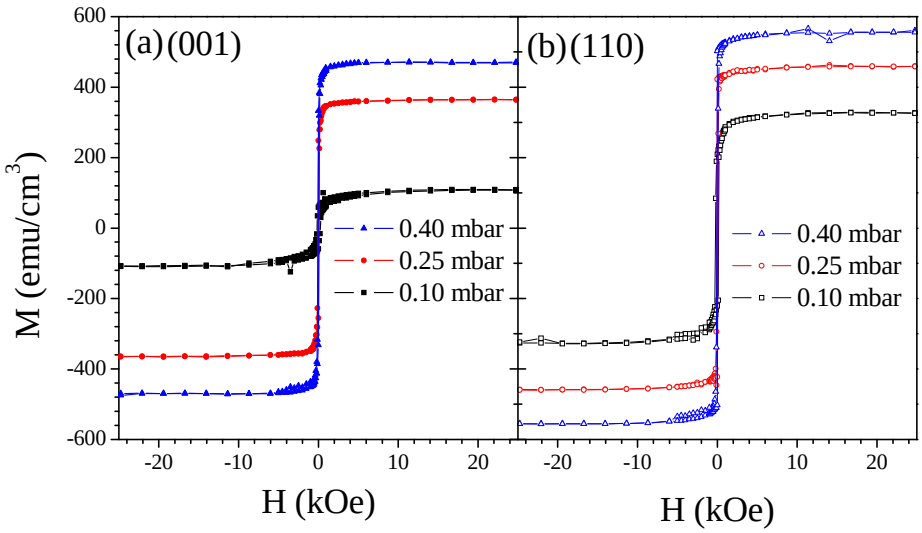

Figure 8.6. Magnetic hystresis loops measured on the 700 C samples at 10 K. Magnetic field was applied in-plane of the samples, being for the (001) samples (a) along the [100] direction and for the (110) samples (b) along the [001] direction. Films grown under different oxygen pressure are represented by squares for $P(O_2)$ = 0.10 mbar, circles for $P(O_2)$ = 0.25 mbar and triangles for $P(O_2)$ = 0.40 mbar.

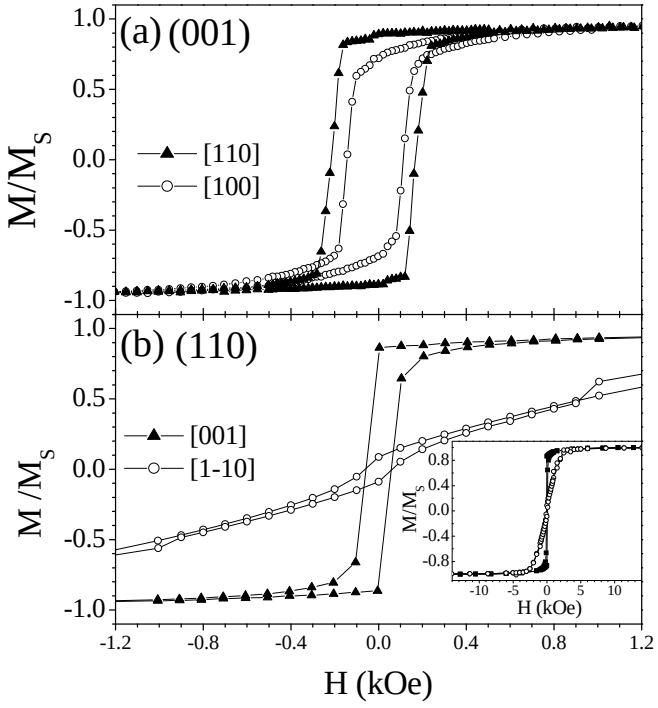

Figure 8.7. Normalized magnetic hystresis loops measured at 10 K with the magnetic field applied in-plane of the samples along different directions: (a) (001) sample (lsmo40), field applied along [100] (circles) and [110] (triangles) directions, and (b) (110) sample (lsmo35), field applied along [1-10] (circles) and [001] (triangles) direction. Inset: Same loops that those of the main (b) panel, showing the magnetization saturation at approximately 5 kOe.

Magnetization *vs* temperature curves

Ferromagnetic to paramagnetic transition in (001) and (110) LSMO films of the 700 C series was studied by recording the magnetization *vs* temperature curves at a fixed in-plane magnetic field of 1 kOe. The magnetic field was enough to saturate the (001) and (110) samples along the [100] and [001] directions, respectively. We performed these measurements after saturating the films at high field (3 kOe) and decreasing field down to the stable 1 kOe value.

In Figure 8.8 the magnetization dependence on temperature curves are shown. Starting with the low oxygen pressure curves (squares), the (001) film present a gradual transition, which cannot be related with a purely ferromagnetic film. The lack of abruptness and the low magnetization value at any temperature compare with that of the (110) film indicate that the film present a much deprimed magnetic properties. On the other hand, the (110) film grown at the same oxygen pressure presents a smooth ferromagnetic transition, but the magnetization is much higher. Comparing the pairs of (001) and (110) films grown at any oxygen pressure, the resulting remarks signal that

(110) films always present higher magnetization, with a transition that occurs much abruptically and at higher temperature.

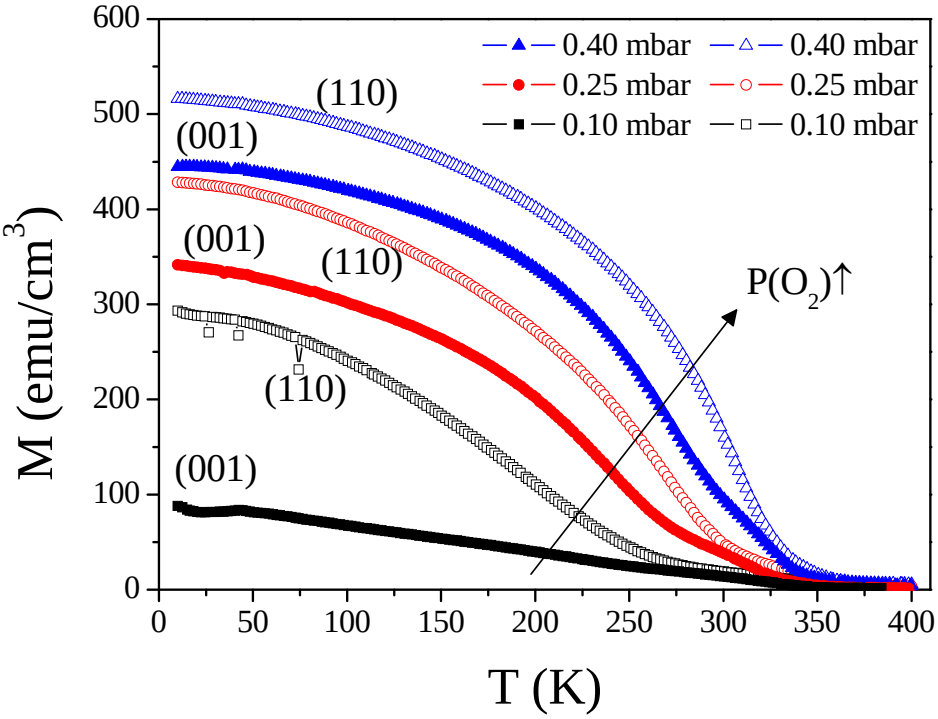

Figure 8.8. Magnetization *vs* temperature curves measured at a in-plane field of 1 kOe in (001) (close symbols) and (110) (open symbols) films grown at different oxygen pressure conditions: 0.10 mbar (squares), 0.25 mbar (circles) and 0.40 mbar (triangles).

Different methods can be used to evaluate the Curie temperature of these films. Analyzing the curvature of the data shown in Figure 8.8 it is possible to get insight into the ferromagnetic transition in these films. To perform this evaluation, we calculated the derivatives of the experimental curves and afterwards fitted them to appropriate Gaussian functions to accurately obtain the transition temperature and width of the transition. The derivative curves from data in Figure 8.7 and the corresponding Gaussian fits are plotted in Figure 8.9. Inspecting the (001) data in Figure 8.9a, we confirm that the wide transition observed for the low oxygen pressure film (squares) cannot describe any clear transition. On the other hand, for the other (001) samples, two peaks arise, with different intensity and at different temperatures: oxygen pressure dependent peak, appearing between 250 and 300 K, and a high temperature peak close to 330 K, independent of the oxygen pressure. We ascribe the first peak to the majority transition of the (001) film. In Figure 8.9b, the (110) films present in all cases an intense peak corresponding to the majority transition, increasing towards higher values as a

function of the oxygen pressure. A second peak, less intense, is found around 350 K. We confirm the observations obtained from the analysis of Figure 8.8: (110) films present higher T_C and in (001) films ferromagnetic transition is wider and occurring at lower temperature, and it is also connected to lower magnetization at any temperature.

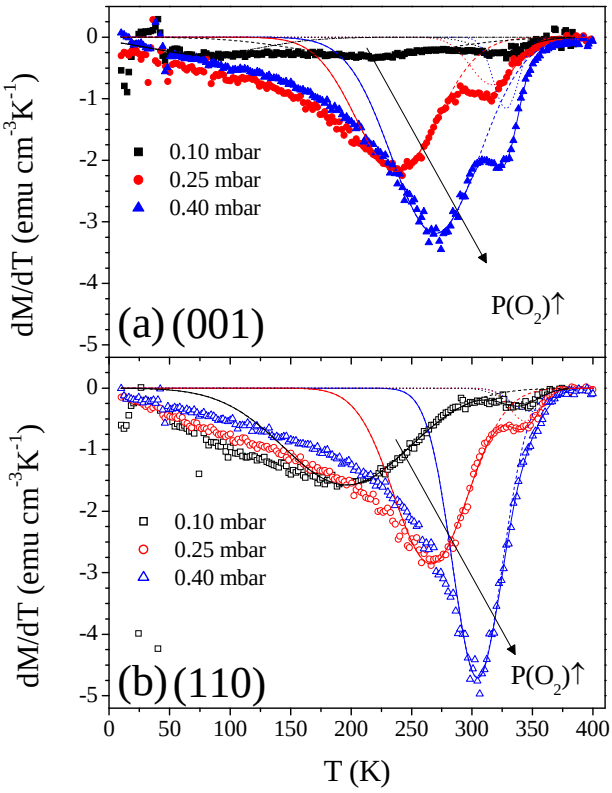

Figure 8.9. Derivative curves (symbols) calculated from data in Figure 8.8: (a) for (001) films and (b) for (110) films. Lines correspond to Gaussian fits to the experimental curves.

(c)Summary of magnetic properties and discussion

In Figure 8.10 we summarize the M_S and T_C values obtained from the curves included in Figure 8.6 and Figure 8.8. As observed when analyzing these curves, the M_S (from saturated magnetization at ~ 20 kOe) and T_C (evaluated from the majority minima of the curves shown in Figure 8.8) of all the (110) samples. The strained state of the films together with the intrinsic trend of (001) manganite films to phase separation [5] may have driven the (001) films to be magnetically depressed. On the other hand, playing with the oxygen content during the film deposition has allowed us to investigate the relevance of the oxygen stoichiometry in the magnetic properties of these films. We confirm that under the same growth conditions, (110) films present enhanced properties compared to those of the (001) films. We suggest that due to the different orientation of

the plane of growth, the amount of oxygen vacancies created during the high temperature can be different. Within his scenario, and recalling the major relevance of the oxygen ions in the double-exchange interaction, the (110) films are clearly less affected by the poor oxygen conditions, which can be related to a much probable creation of oxygen vacancies in the (001) planes. Other effects, as the polarity discontinuity in (001) STO and LSMO, absent in the (110) case, are expected to contribute to increase the magnetic properties of (001) and (110) films.

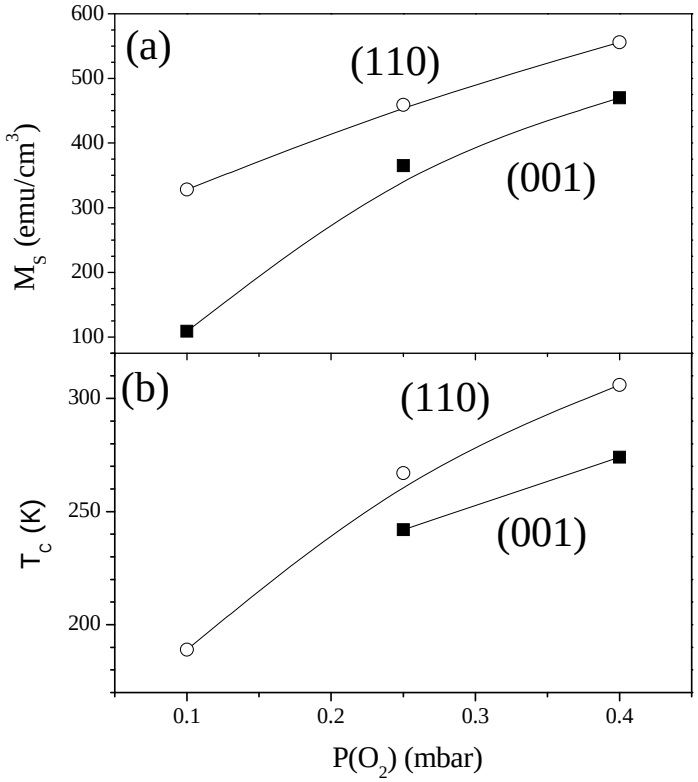

Figure 8.10. M_S (a) and T_C (b) as a function of the oxygen pressure during the film growth for (001) (close symbols) and (110) (open symbols) films.

References

[1] A. Urushibara, Y. Moritomo, T. Arima, A. Asamitsu, G. Kido, and Y. Tokura, Phys. Rev. B **51**, 14103 (1995);

[2] M. Imada, A. Fujimori, and Y. Tokura, Rev. Mod. Phys. **70**, 1039 (1998)

[3] G. Hu and Y. Suzuki, Phys. Rev. Lett. **27**, 276601 (2002); M. Bowen, M. Bibes, A. Barthélémy, J. P. Contour, A. Anane, Y. Lemaître, and A. Fert, Appl. Phys. Lett. **82,** 233 (2003)

[4] Y. B. Zhang, S. Li, C. Q. Sun, and W. Gao, Mater. Sci. Engin. B **98**, 54 (2003)

[5] M. Bibes, LL. Balcells, S. València, J. Fontcuberta, M. Wojcik, E. Jedryka, and S. Nadolski, Phys. Rev. Lett. **87**, 67210 (2001); M. Bibes, S. Valencia, Ll. Balcells, B. Martínez, J. Fontcuberta, M. Wojcik, S. Nadolski, and E. Jedryka, Phys. Rev. B **66**, 134416 (2002)

Outlook

During the last years, the research on complex oxides, especially in those used into epitaxial heterostructures, has signaled that these materials can display a wide variety of unexpected physical phenomena. For instance, it has been shown that an induction of a stable electric polarization into the naturally paraelectric $SrTiO_3$ occurs when $SrTiO_3$ thin layers are combined into thin film heterostructures with the ferroelectric $PbTiO_3$. It has been also discovered that radically different properties from those of the bulk properties can be generated at the interfaces in epitaxial heterostructures. As an example, the insulating perovskites $SrTiO_3$ and $LaAlO_3$ can lead to an interface with high mobility electrons confined into a two-dimensional region, which can display superconductivity at low temperature. Besides, the research into spintronics devices, as magnetic tunnel junctions based in manganites, has shown that the control of the interface properties and especially the interface spin polarization tune the functionality of the devices.

Within the exposed framework, this thesis has faced the challenge of understating the physical phenomena occurring in the epitaxially grown $La_{2/3}Ca_{1/3}MnO_3$ ferromagnetic manganite films and $SrTiO_3/La_{2/3}Ca_{1/3}MnO_3$ heterostructures on $SrTiO_3$ substrates with (001) and (110) orientation. In general, La-manganite layers have repetitively displayed depleted ferromagnetic and transport properties when grown in (001) substrates, whereas as presented in this thesis the use of (110) orientation can help to obtain closer to bulk properties. The physical origin of this effect has been related to the different structural and electronic characteristics of the (001) and (110) planes which leads to the development of electronic phase separation in the (001) case. Exploitation of the anisotropy of the mechanical properties of (110) planes allows obtaining in-plane

uniaxial magnetic anisotropy in (110) films, which can be tuned by the epitaxial strain. The transport properties of these (110) films is also observed to be highly sensitive to this uniaxial magnetic anisotropy, being possible to obtain abrupt changes in the transverse magnetoresistance along the in-plane hard axis. This is not the case for (001) films, where the biaxial in-plane anisotropy does not strongly influence the sinusoidal shape of the measured magnetoresistance. The comparative analysis of structural, electronic and chemical properties together with the magnetic and transport properties of bare (001) and (110) electrodes motivated their integration into oxide heterostructures. Growing $SrTiO_3$ insulating layers on these (001) and (110) manganite electrodes, we could investigate the influence of the insulator layers on the properties of these electrodes, thus providing an insight into the role of the interface phenomena in oxide functional properties.

The limited functional properties of current applications based on oxide heterostructures are known to be closely linked to the interface phenomena. Charge redistribution and electronic and chemical phase separation occur and limit the properties of the explored interfaces, although it is not clear whether the origins of these effects are intrinsic to the material, caused by the interface electronic and chemical mismatch, or originated by the different elastic properties. Being still unclear the role of each contribution, we suggest to extend the comparative study on (001) and (110) LCMO films and STO/LCMO bilayers to other manganites, for instance $La_{2/3}Sr_{1/3}MnO_3$, and other insulators, as $LaAlO_3$. Several combinations are available, being possible to tune the epitaxial stress, the symmetry of the electronic wavefunctions or the polarity of the interface planes. By playing with the epitaxial stress and the electronic and chemical discontinuities, it would be possible to determine the specific role of each of these factors and to tune the interface properties and thus those of further applications.

List of publications and oral presentations

List of publications

- *Critical effects of substrate terraces and steps morphology on the growth mode of epitaxial $SrRuO_3$ films*. F. Sánchez, G. Herranz, I. C. Infante, J. Fontcuberta, M.V. García-Cuenca, C. Ferrater, M. Varela. Applied Physics Letters **85**, 1981 (2004)

- *Self-organization in complex oxide thin films: from 2-D to 0-D nanostructures of $SrRuO_3$ and $CoCr_2O_4$.* F. Sánchez, U. Lüders, G. Herranz, I. C. Infante, J. Fontcuberta, M.V. García-Cuenca, C. Ferrater, M. Varela. Nanotechnology **16**, S190-S196 (2005)

- *Planar Hall effect in epitaxial (110) $La_{0.67}Ca_{0.33}MnO_3$ films.* I. C. Infante, V. Laukhin, F. Sánchez, J. Fontcuberta. Materials Science and Engineering B **126**, 283-286 (2006)

- *Control of the surface roughening in the epitaxial growth of manganite films.* F. Sánchez, I. C. Infante, Ll. Abad, U. Lüders, Ll. Balcells, B. Martínez, J. Fontcuberta. Thin Solid Films **495**, 154-158 (2006)

- *Electronic phase separation in epitaxial $La_{2/3}Ca_{1/3}MnO_3$ films on (001) and (110) SrTiO3 substrates.* J. Fontcuberta, I. C. Infante, V. Laukhin, F. Sánchez, M. Wojcik, and E. Jedryka. Journal of Applied Physics **99**, 08A701 (2006)

- *Anisotropic magnetoresistance in epitaxial (110) manganite films.* I. C. Infante, V. Laukhin, F. Sánchez, J. Fontcuberta, O. Melnikov, O. Yu Gorbenko, A.R. Kaul. Journal of Applied Physics **99**, 08C502 (2006)

- *Magnetic switching in epitaxial (110) $La_{2/3}Ca_{1/3}MnO_3$ films.* I. C. Infante, D. Hrabovský, V. Laukhin, F. Sánchez, J. Fontcuberta. Journal of Applied Physics **99**, 08C503 (2006)

- *Surface roughening by anisotropic adatom kinetics in epitaxial growth of $La_{0.67}Ca_{0.33}MnO_3$.*. F. Sánchez, I. C. Infante, U. Lüders, Ll. Abad, J. Fontcuberta. Surface Science **600**, 1231-1239 (2006)

- *Growth modes and self-organization in the epitaxy of ferromagnetic $SrRuO_3$ on $SrTiO_3(001)$.* F. Sánchez, G. Herranz, I. C. Infante, C. Ferrater, M.V. García-Cuenca, M. Varela, J. Fontcuberta. Progress in Solid State Chemistry **34**, 213-221 (2006)

- *Controlled magnetic anisotropy of $SrRuO_3$ thin films grown on nominally exact $SrTiO_3(001)$ substrates*. G. Herranz, F. Sánchez, N. Dix, D. Hrabovsky, I. C. Infante, J. Fontcuberta, M.V. García-Cuenca, C. Ferrater, M. Varela. Applied Physics Letters **89**, 152501 (2006)

- *Functional characterization of $SrTiO_3$ tunnel barriers by conducting atomic force microscopy*. I. C. Infante, F. Sánchez, V. Laukhin, A. Pérez del Pino, J. Fontcuberta, K. Bouzehouane, S. Fusil, A. Barthélémy. Applied Physics Letters **89**, 172506 (2006)

- *Structural and functional characterization of (110)-oriented epitaxial $La_{2/3}Ca_{1/3}MnO_3$ electrodes and $SrTiO_3$ tunnel barriers*. I. C. Infante, F. Sánchez, J. Fontcuberta, S. Fusil, K. Bouzehouane, G. Herranz, A. Barthélémy, S. Estradé, J. Arbiol, F. Peiró, R.J.O. Mossanek, M. Abbate, M. Wojcik. Journal of Applied Physics **101**, 93902 (2007)

- *Strain-driven elastic and orbital-ordering effects on thickness-dependent properties of manganite thin films*. I. C. Infante, F. Sánchez, J. Fontcuberta, M. Wojcik, E. Jedryka, S. Estradé, J. Arbiol, F. Peiró, V. Laukhin, J. P. Espinós, Journal of Applied Physics **101**, 93902 (2007)

- *Step formation, faceting and bunching in atomically flat $SrTiO_3$ (110) surfaces.* R. Bachelet, F. Valle, I. C. Infante, F. Sánchez, J. Fontcuberta, Applied Physics Letters **91**, 251904 (2007)

- *Elastic and orbital effects on thickness-dependent properties of manganite thin films*. I.C. Infante, F. Sánchez, J. Fontcuberta, M. Wojcik, E. Jedryka, S. Estradé, F. Peiró, J. Arbiol, V. Laukhin, J. P. Espinós, Physical Review B **76**, 224415 (2007)

- *Tuning in-plane magnetic anisotropy in (110) $La_{2/3}Ca_{1/3}MnO_3$ films by anisotropic strain relaxation*. I. C. Infante, J. O. Ossó, F. Sánchez, J. Fontcuberta, Applied Physics Letters **92**, 012508 (2008)

- *Effects of $SrTiO_3$ capping in $La_{2/3}Ca_{1/3}MnO_3$ electrodes of different orientation.* I. C. Infante, F. Sánchez, J. Fontcuberta, S. Estradé, F. Peiró, J. Arbiol, M. Wojcik, E. Jedryka, Journal of Applied Physics**103**, 07E302 (2008)

List of oral presentations

- Journées de la Matière Condensée, Nancy (France) 2004. *Dissimilar magnetic properties in strained $La_{2/3}Ca_{1/3}MnO3$ epitaxial films on $SrTiO_3(001)$ and $SrTiO_3(110)$.* I. C. Infante, F. Sánchez, J. Fontcuberta.

- Workshop on Oxides at the Nanoscale (WON 2005), Zaragoza (Spain) 2005. *Reduced electronic phase separation in La2/3Ca1/3MnO3/SrTiO3(110) interfaces.* I. C. Infante, V. Laukhin, F. Sánchez, S. Estradé, J. Arbiol, F. Peiró, M. Wojcik; E. Jedryka, J. Fontcuberta.

- European Materials Research Society Spring Meeting (E-MRS), Nice (France) 2006. *Conductive atomic force microscopy characterization of $SrTiO_3$ tunnel barriers on (001) and (110) oriented $La_{2/3}Ca_{1/3}MnO_3$ ferromagnetic electrodes.* I. C. Infante, F. Sánchez, K. Bouzehouane, S. Fusil, A. Pérez del Pino, V. Laukhin, J. Fontcuberta

- Thin films for novel oxide devices (5th meeting), Sant Feliu de Guíxols, (Spain) 2007. *Correlation of Chemical and Electronic Phase Separation and Strain State in Epitaxial (001) and (110) Manganite Films.* I. C. Infante, F. Sánchez, V. Laukhin, J. Fontcuberta, S. Estradé, J. Arbiol, F. Peiró, M. Wojcik, S. Jedryka, J. P. Espinós.

- 52nd Magnetism and Magnetic Materials conference, Tampa (United States of America) 2007. *Probing interface phenomena in $SrTiO_3$ capped $La_{2/3}Ca_{1/3}MnO_3$ interfaces: STO(110) versus STO(001) orientation.* I. C. Infante, F. Sánchez, J. Fontcuberta, S. Estradé, F. Peiró, J. Arbiol, M. Wojcik, E. Jedryka

Acknowledgements

The work presented here is actually the product of a constant interaction and collaboration of a list of people from different institutes. It is my pleasure to have worked with them, and to continue doing it for long time. I just want to devote to them a couple of words of thanks to this priceless support.

First, I have to express my gratitude to my directors Prof. Josep Fontcuberta and Dr. Florencio Sánchez. They have created an active and motivating atmosphere of scientific research. I have leant many experimental and theoretical things thanks to their capability to guide me through my thesis, especially when facing any problem. I want to express my gratitude to Prof. Jordi Pascual of the Universitat Autònoma de Barcelona, my PhD tutor, who has helped me with the PhD program and with the administration.

No matter the order of reference, next words are devoting my gratitude to a number of people that helped me in my work, especially in the characterization and analysis of thin films and heterostructures.

I thank Dr. Gervasi Herranz, who has been a constant aid whenever he was, in Barcelona or in Paris, and also because of his scientific spirit. I want to express my acknowledgement also to Prof. Vladimir Laukhin, for his great accuracy in magnetotransport measurements and performance of electric contacts. Also I want to specially thank Dr. David Hrabovský, who developed the Stoner-Wohlfarth fittings to magnetotransport measurements. Your helping discussions on magnetic anisotropy resolved so many doubts I had on this topic. Thanks also to Prof. Vassil Skumryev, he has been a helping hand with the SQUID and our discussions provide me always a deeper knowledge in the topic of magnetism. I need to thanks the priceless help and support of Dr. Ulrike Anne Lüders, who developed her thesis in my group. She guided me with great patience the first days at the ICMAB and everywhere! Her knowledge of a variety of techniques, materials and, most of all, physics motivated me to develop my research. To Nico Dix, thanks a lot, because nobody but you has done the great work of facing LabView programs and a variety of experimental problems of the sputtering chamber with such a great smile. Thanks for the accurate work developed by María Jesús Polo and Dr. Ángel Pérez in the performance of AFM tapping measurements, and for spending some of their free time in doing them. To Dr. J. Oriol Ossó, thanks for his disposal to perform nanoindentation eperiments on our samples at any time, and his ideas and suggestions for analyzing their mechanical properties from these experiments.

I want to thank José-Manuel Pérez for his efficiency in managing the low temperature laboratory, with the SQUIDs and the PPMS, who always found some time to measure my samples.

Thanks to the group of Dr. Francesca Peiró in the Universitat de Barcelona, who performed and analyzed HRTEM and EELS measurements, and especially to Sonia Estradé, who is developing her PHD thesis, and have worked so hardly on the structural and chemical analysis of my samples. To Dr. Marek Wojcik, of the Institut of Physics of Warsaw, I would like to express my gratitude for his NMR measurements and analysis. I know it has been a great difficulty to work with such a long distance in between, but it worked! I thank also Dr. Juan Pedro Espinós in the Instituto de Ciencia de Materiales de Sevilla for performing XPS measurements, and for his collaboration in the analysis. Also thanks to Prof. MaCarmen Asensio, who has helped me to evaluate my XPS results. Besides, I want to acknowledge XAS measurements and analysis performed by Prof. Miguel Abbate and his group, of Campinhas, Brazil. Although from such far away place, your sincere support by e-mail was greatly received. To the group of Prof. A. R. Kaul of the Departement of Chemistry in Moscow, who provided us some (110) LAMO films, which we found so useful to confirm the findings in AMR of our (110) LCMO. I want to thank the group of Dr. Sebastian Gönnenwein, especially to the phD student Andreas Brandlmaier, who used their FMR setup to observe the magnetic anisotropy of my samples.

Special thanks also for Prof. Agnés Barthélémy, who made it possible my stages in UMR-Thales and discussed so long about spintronics. I would want to thank also to Dr. Karim Bouzehouane and Dr. Stéphane Fusil, who taught me many things on Conducting-AFM and on transport measurements. My thanks to all them for allowing me the performance and measurement of magnetic tunnel junctions with my samples. I would also like to thank Dr. Manuel Bibes for his discussions. Many thanks to the group of Prof. Enric Bertrán, from the Universitat de Barcelona, and especially to the PhD student Miquel Rubio, because of their priceless work on the development of electron beam lithography, who worked with me in the performance of magnetic tunnel junctions in Barcelona.

I remark also the invaluable help on the laboratory of Dr. Lluis Balcells and Llibertat Abad, specially those days when the pressure was on the sputtering chamber schedule. To Prof. Benjamín Martínez, I would want also to express my gratitude for teaching me how to use the SQUID and the understanding of their measurements.

Thanks also to PhD student “professor” Xavi Martí and to Dr. José Santiso, for making it easy to use the new diffractometer GADDS, otherwise it would have been quite more difficult to obtain pole figures. To Dr. Diego Rubí and PhD student Franco Rigato because they have made it easy to use and understand some of the laboratory set-up. Thanks also to Dr. Josep Bassas and Dr. Xavier Alcobé, from the X-ray diffraction laboratory, and to Aránzazu Villuendas and Dr. Lorenzo Calvo, from the X-ray photoelectron spectroscopy facility, all them working at the Serveis Científicotècnics of the Universitat de Barcelona. I have enjoyed my XRD and XPS sessions as well as our discussions, somwtimes also on the phone. Also to the personal of the clean room of the Universitat Autònoma de Barcelona, who help me with the optical lithography.

Thanks to César Moreno, always wanting to discuss about manganites,, and to Joffre Gutiérrez, with whom I managed to use the PPMS without any trouble. I want to thank also Patricia Abellán for her disposal to take a break and continue discussing about anything, including about the work! Also thanks to my PhD colleagues, who have created a great atmosphere of work. To the people at the ICMAB administration and technical services: Thanks! I do not have words (or space) to thank all them, but they have helped me so many times…!

To my dear friends since the university, “les floretes”, our meetings are a source of energy. To all them, my best: Marta, doctor STM-“maquinota” now at Holland; in Sweden, Núria, living in Kalmar with her cellular motors, and Gemma, surviving to the synchrotrons and sometimes resting in Stockholm; and in New York (maybe), Laia, making a great carrier in informatics. Thanks to the friends I found in Paris, because I enjoyed so much my time there because of their company: Martin, Dani, Guillermo and Maria. And also very special thanks to Olivier.

And most of all, thanks to my family, who has given me the support to continue my research. Inside of a universe in constant movement, they are always my point of reference, over anything else and at any moment.